

**Ministry of Higher Education and Scientific Research
University of Baghdad
Institute of Laser for Postgraduate Studies**



**Design and Numerical Verification of a Chip-
Integrated Single-Photon Source Based on
Quantum Plasmonics**

A Thesis

**Submitted to the Institute of Laser for Postgraduate
Studies, University of Baghdad in Partial Fulfillment
of Requirements for the Degree of Doctor of
Philosophy in Laser Applications, Electronic and
Communications Engineering**

By:

Farooq Abdulghafoor Khaleel

Supervised by:

Asst. Prof. Dr.

Shelan Khasro Tawfeeq

2022 AD

1443 AH

Certification

I certify that this thesis was prepared under my supervision at the Institute of Laser for Postgraduate Studies, University of Baghdad, as partial fulfillment of requirements for the degree of Doctor of Philosophy in Laser Applications/Electronic and Communications Engineering.

Signature:

Name: **Dr. Shelan Khasro Tawfeeq**

Title: **Asst. Prof.**

Address: Institute of Laser for Postgraduate Studies, University of Baghdad

Date : / / 2022

Given the available recommendation, I forward this thesis for debate by the Examining Committee.

Signature:

Name: **Dr. Hanan Jaafar Taher**

Title: **Asst. Prof.**

Address: Head of the Scientific Committee,
Institute of Laser for Postgraduate Studies,
University of Baghdad

Date: / / 2022

Examining Committee Certification

We certify that we have read the thesis entitled “Design and Numerical Verification of a Chip-Integrated Single-Photon Source Based on Quantum Plasmonics” and as the examining committee we examined the student in its contents and our opinion it is adequate with standards as a thesis for the degree of Doctor of Philosophy in Laser Applications, Electronic and Communications Engineering.

Signature:

Signature:

Name: **Dr. Hussein Ali Jawad**

Title: **Professor**

Address: Institute of Laser for
Postgraduate Studies, University of
Baghdad

Date: / / 2022

(Chairman)

Name: **Dr. Raad Sami Fyath**

Title: **Professor**

Address: College of Engineering, Al-
Nahrain University

Date: / / 2022

(Member)

Signature:

Signature:

Name: **Dr. Jassim Kadhim Hmood**

Title: **Professor**

Address: Laser and Optoelectronics
Engineering Dept., University of
Technology

Date: / / 2022

(Member)

Name: **Dr. Tahreer Safa'a Mansoor**

Title: **Assistant Professor**

Address: Institute of Laser for
Postgraduate Studies, University of
Baghdad

Date: / / 2022

(Member)

Signature:

Signature:

Name: **Dr. Mohammed Nadhim Abbas**

Title: **Assistant Professor**

Address: College of Engineering,
University of Baghdad

Date: / / 2022

(Member)

Name: **Dr. Shelan Khasro Tawfeeq**

Title: **Assistant Professor**

Address: Institute of Laser for
Postgraduate Studies, University of
Baghdad

Date: / / 2022

(Supervisor)

Approved by the Dean of Institute of Laser for Postgraduate Studies, University of Baghdad.

Signature:

Name: **Prof. Dr. Hussein Ali Jawad**

Title: **Dean**

Address: Institute of Laser for Postgraduate
Studies, University of Baghdad

Date: / / 2022

Dedication

To my greatest teacher and support, **my mother**,

To my role model, my father,

And to all my teachers in the elementary school, the secondary school, the Undergraduate courses, the M.Sc. courses, and the Ph.D. courses, with love and respect

(To all, your debt can never be returned)

Acknowledgment

I would like to thank my principal supervisor, **Asst. Prof. Dr. Shelan Khasro Tawfeeq**, for her support and encouragement. It was certainly a privilege to be her student. She was a powerhouse of positivity with the ability to address difficult workplace situations immediately and keep me fully motivated to deliver results regularly. The presented thesis could never be done without her efforts and guidance.

Great appreciation to **Prof. Dr. Hussein Ali Jawad**, Dean of the Institute of Laser for Postgraduate Studies, for his advice and support during my academic years at the institute. I am thankful for **Asst. Prof. Dr. Tahreer Safa'a Mansoor**, Head of the Department of Engineering and Industrial Applications for her support and encouragement.

I thank my group members, **Dr. Ahmed I. Khalil, Dr. Adel Fadhel, and Colleague Salwa Marwan**. Our discussions in the lab and during the courses and the research work were very beneficial to my research and have been an interesting part of my journey.

I thank the **Department of Electrical Engineering / College of Engineering / University of Baghdad** for offering the Ph.D. scholarship to the Institute of Laser for Postgraduate Studies, University of Baghdad, where I spent the most beautiful days in my academic life.

I would like to express my gratitude to **all my teachers** from the elementary school to the Ph.D. level, they built the man I am and I can never return their debt. Many thanks from my heart.

Finally, I would like to thank **my great mother**, my father, and my sister for their full support and continuous encouragement throughout my years of study. This accomplishment would not have been possible without them. Thank you.

Abstract

Nowadays, most of the on-chip (integrated) plasmonic single-photon sources emit an unpolarized stream of single photons that demand a subsequent polarizer stage in a practical quantum cryptography system. Therefore, this thesis achieved the specification of the polarization states of the emitted photons by studying three main topics.

Firstly, the coupling of the light emitted from a quantum emitter at 700 nm wavelength to the propagation mode supported by an on-chip hybrid plasmonic waveguide polarization rotator is numerically demonstrated. The results proved that the light emitted is linearly polarized at 0° , 45° /- 45° , and 90° with propagation lengths of 5 μm , 3.3 μm , and 3.9 μm , respectively. Moreover, high power-conversion efficiency was obtained from an applied transverse magnetic mode (0° -polarization) to a transverse electric (90° -polarization) and a linearly polarized light at 45° /- 45° of 97% and a 98%, respectively. The proposed work obtained almost a 3-fold enhancement of the total decay rate of the QE with high emission coupling efficiency (β -factor) of 88%, 80%, and 87% to the corresponding waveguide mode for 0° , 45° /- 45° , and 90° , respectively. The proposed methodology paves the way towards more efficient and less complicated on-chip plasmonic single-photon sources with a specified output polarization. To the best of our knowledge, this is the first work that presents a polarized on-chip single-photon source based on HPWs at the transmitter side for a QKD system to achieve a specific polarization of the output photons at the wavelength of QE emission with a high β -factor.

Secondly, the numerical techniques required to prove the single-photon emission from any type of quantum emitter after being coupled to any nanostructure are presented. Purcell effect modifies the emission characteristics of QEs, such as Color Centers in Nanodiamonds, for example, Nitrogen-Vacancy centers, Silicon-Vacancy centers, etc., or semiconductor

quantum dots. The proposed numerical approach is based on the unique QEs' experimental photophysics parameters and numerical analysis software, which are MATLAB and Quantum Toolbox in Python (QuTiP). The results show a comparable $g^{(2)}(\tau)$ behavior between the proposed numerical model and the other two experimental results for the QE before and after coupling to a plasmonic waveguide with subwavelength dimensions. The proposed methodology is essential to prove the single-photon emission of modeled single-photon source in an on-chip polarization-dependent quantum key distribution system.

Finally, a double-layer approach is proposed to design a compact four-state polarization-independent grating coupler. The proposed polarization-independent GC is designed to couple a 700 nm polarized light propagating in a 150 nm Gallium Phosphide waveguide to a polarization-maintaining fiber. The double-layer approach is based on the deposition of GaP gratings designed to couple the TM light over the GaP gratings designed to couple the TE light. The two layers are separated by a Hydrogen silsesquioxane with an optimum thickness of 20 nm. The proposed method resulted in relatively high coupling efficiencies of 39.2%, 31.1%, and 23.3% for the TE, TM, and 45°/-45° linearly polarized light, respectively. The polarization-dependent loss is 1 dB, 1.26 dB, and 2.26 dB corresponding to TE-TM, TM-45°/-45°, and TE-45°/-45°, respectively. The performance of the double-layer approach is numerically verified by the two-dimensional finite element algorithm using COMSOL software. The proposed method suggests a novel and simple approach to design a compact four-state polarization-independent GC that could be used in integrated photonic and quantum communication circuits.

List of Abbreviations

2D	Two Dimensional
3D	Three Dimensional
Ag	Silver
Al	Aluminum
Au	Gold
B	External Magnetic Field
BOX	Buried Oxide
C	Carbon
CdS	Cadmium Sulfide
CdSe	Cadmium Selenide
CE	Coupling Efficiency
DLSP	Dielectric Loaded Surface Plasmon Polariton
EM	Electromagnetic
ewfd	Electromagnetic Waves Frequency Domain
FDTD	Finite Difference Time Domain
FEM	Finite Element Method
GaP	Gallium Phosphide
GC	Grating Coupler
GeV	Germanium Vacancy
GUI	Graphical User Interface
HBT	Hanbury Brown and Twiss
HPW	Hybrid Plasmonic Waveguide
HSQ	Hydrogen Silsesquioxane
Intop	Integration Probe
LDOS	Local Density of States
LOQCs	Linear Optical Quantum Computers
NA	Numerical Aperture
NV	Nitrogen Vacancy
PCE	Power Conversion Efficiency
PDE	Partial Differential Equations
PDL	Polarization-dependent Loss
PICs	Photonic Integrated Circuits
PMF	Polarization-maintaining Fiber
PML	Perfectly Matched Layer
PMT	Photomultiplier Tube
PSB	Phonon Sideband
PW	Plasmonic Waveguide
QE	Quantum Emitter
QD	Quantum Dot
QKD	Quantum Key Distribution
QuTiP	Quantum Toolbox in Python
Si	Silicon
SiO ₂	Silicon Oxide
SiV	Silicon Vacancy
SOI	Silicon on Insulator
SPAD	Single-photon Avalanche Detector
SPEs	Single-photon Emitters
SPPs	Surface Plasmon Polaritons

SPS	Single-photon Source
TE	Transverse Electric
TEM	Transverse Electromagnetic
TM	Transverse Magnetic
V	Volume
WCP	Weak Coherent Pulses
ZPL	Zero Phonon Line

List of Symbols

\vec{N}	A general vector
\vec{n}_d	A unit vector of the dipole moment
ω	Angular frequency (rad/s)
\vec{r}_d	Another position in space (m)
α	Attenuation factor (Neper/m)
$\nabla \times$	Curl operation
\vec{J}	Current density (A/m ²)
γ	Damping frequency (rad/s)
d	Dielectric
θ_c	Diffraction angle to the cladding region
μ_D	Dipole moment (A.s.m)
$\nabla \cdot$	Divergence operation
n_{eff}	Effective index
\vec{E}	Electric field intensity (V/m)
\vec{D}	Electric flux density (C/m ²)
R	Excitation strength
k_0	Free-space wavenumber (rad/m)
∇	Gradient operation
Λ	Grating coupler's period
\vec{G}	Green's function
∇^2	Laplacian operation
σ	Lowering operator
\vec{H}	Magnetic field intensity (A/m)
\vec{B}	Magnetic flux density (Tesla)
m	Metal, number of photons
\vec{n}	Normal unit vector
n	Number of photons
NA	Numerical Aperture
r_{core}	Optical fiber's radius
β	Phase constant (rad/m)
h	Planck's constant (J.s)
ω_p	Plasma frequency (rad/s)
Γ_{pl}	Plasmonic decay rate
L	Polarization conversion length
\vec{S}	Poynting vector (W/m ²)
γ	Propagation factor
$\Omega(t)$	Rabi frequency
\hbar	Reduced Planck's constant (J.s)
n	Refractive index of a material
θ	Rotation angle
H_r	Simplified Hamiltonian
\vec{r}	Space (m)
c	Speed of light (m/s)
m_s	Spin quantum number
S	Surface area (m ²)
k_{xy}	The decay rate from level x to level y

Γ_0	The decay rate in a vacuum
τ_x	The decay time of level x
γ_e	The gyromagnetic ratio of electrons
t_{shift}	The mean value of the pulse
μ_0	The permeability of free-space (H/m)
ϵ_0	The permittivity of free-space (F/m)
ρ_x	The population of the electrons at level x
ρ_{pl}	The projected LDOS to the plasmonic waveguide's mode
β -factor	The ratio of Γ_{pl} to Γ_{tot}
μ_r	The relative permeability of the material
ϵ_r	The relative permittivity of the material
$g^{(2)}(\tau)$	The second-order intensity correlation function as a function of time delay
$G^{(2)}(t, \tau)$	The second-order optical coherence function
p_f	The Signal/Noise ratio
t_p^2	The variance of the pulse
t	Time (s)
T_{\pm}	Time operators
Γ_{tot}	Total decay rate
P_0	Total radiated power in a vacuum (W)
P_{tot}	Total radiated power in medium (W)
\vec{I}	Unit dyad
V	Volume (m^3)
ρ_v	Volume charge density (C/m^3)
λ	Wavelength (m)

Table of Contents

Acknowledgment	i
Abstract	ii
List of Abbreviations	iv
List of Symbols	vi
Table of Contents	viii
List of Figures	x
List of Tables	xvii
Chapter 1	1
Introduction	1
1.1. General Introduction and Motivation	1
1.2. Integrated optical circuits	3
1.3. Computational nanophotonics	4
1.4. Electrodynamics	5
1.4.1. Maxwell's equations	6
1.4.2. Poynting's theorem	7
1.4.3. Dyadic Green's function	8
1.5. Coupling theory	8
1.5.1. PW's decay rate	9
1.5.2. The QE's total decay rate	11
1.5.3. The β -factor	11
1.6. Photon statistics	12
1.7. Types of Quantum Emitters	20
1.7.1. Quantum Dots	20
1.7.2. Defect centers in diamonds	21
1.8. General relations of waveguide propagation	29
1.9. Surface plasmon polaritons (SPPs)	34
1.10. Literature survey	39
1.11. Aim of the thesis	43
1.12. The layout of the thesis	44
Chapter 2	44
Polarization control of a QE coupled with an HPW	44
2.1. Introduction	44
2.2. The proposed HPW	45
2.2.1. Selection of the HPW's materials	45
2.2.2. Selection of the HPW's geometries	49

2.3. Polarization control mechanism	53
2.4. The QE's spontaneous emission enhancement	57
2.5. Tuning the output polarization	71
Chapter 3	76
The modeling techniques of the second-order correlation function $g^{(2)}(\tau)$ for a quantum emitter.....	76
3.1. Introduction	76
3.2. The NV emission dynamics with unity quantum yield	77
3.3. The NV emission dynamics with less than unity quantum yield	82
3.4. The emission modeling of a two-level QE.....	88
Chapter 4	98
Design and numerical verification of a four-state polarization-independent GC...	98
4.1. Introduction	98
4.2. The GC's principles	99
4.3. The TE GC simulation framework.....	103
4.3.1. The 2D COMSOL simulation framework in [118]	105
4.3.2. Changing the Si waveguide with a GaP waveguide	110
4.4. The polarization-independent GCs.....	121
4.4.1. Tuning θ_c and Λ method	121
4.4.2. The Λ intersection and union method [95]	123
4.5. The proposed GC design	126
4.5.1. The modifications to COMSOL's 2D simulation framework	126
4.5.2. The proposed GC design methodology	128
4.5.3. The excitation requirements	140
Chapter 5	140
Conclusions and Suggestions for Future Work.....	140
5.1. Conclusions	140
5.2. Future work	141
Appendices	141
A. Graphical literature survey.....	A-1
B. The MATLAB code for Section (3.2).....	B-1
C. The MATLAB code for Section (3.3).....	C-1
D. The QuTiP code for Section (3.4).....	D-1
E. MATLAB code to generate the contour plots	E-1
F. Publications:	F-1
Referencess	

List of Figures

Figure 1.1: The delay times against the feature size [15]	4
Figure 1.2: Several technologies for on-chip integrated circuits [17].....	4
Figure 1.3: the three decay channels for a QE near a PW [25].....	8
Figure 1.4: The implementation of Equation (1.14) to calculate Γ_{pl}/Γ_o in a a) Wire made of silver, b) Two nearby silver wires, c) V-groove waveguide, and d) Wedge waveguide [25].....	10
Figure 1.5: β -factor for the waveguide structure presented in Figure (1.4.b) [25]	12
Figure 1.6: $p(m)$ distribution for (a) a thermal light source (lamp), (b) a coherent light source (laser light), and (c) an ideal single-photon source [28].....	13
Figure 1.7: A schematic of the HBT experiment using a classical light source [29].....	14
Figure 1.8: A time-dependent simulation shows the intensity fluctuation to τ_c of a chaotic light source [29].....	14
Figure 1.9: $g(2)\tau$ for (a) bunched (chaotic), (b) coherent, and (c) antibunched light sources [30]	16
Figure 1.10: A HBT experiment with a stream of photons input [29].....	17
Figure 1.11: The photon stream for a (a) thermal light, (b) laser light, and (c) quantum light [29].....	17
Figure 1.12: (a) Fock state with unity mean photon number, (b) A two-level QE emits a single photon [27]	18
Figure 1.13: The photon emission sequence from a QE [29]	18
Figure 1.14: The schematic of a general set-up used to characterize the emission from systems with QEs [30]	19
Figure 1.15: The time correlator's graph under (a) continuous, (b) pulsed excitation [29]	19
Figure 1.16: (a) A QD composed of a CdSe core with a CdS shell exhibited a blinking behavior of its emission at a core radius of 1.1 nm and 2.4 nm shell thickness. (b-e) The photoluminescence (red) and absorption (blue) curves for four different core radii of 1.35 nm, 1.7 nm, 2.2 nm, and 2.7 nm, respectively [32]	20
Figure 1.17: (a) NV-center's atomic structure, electronic structure for (b) NV^0 , and (c) NV^- [36]	22
Figure 1.18: Emission spectra of an (a) NV^0 , (b) NV^- excited by a 532 nm laser [25] ..	23
Figure 1.19: (a) The synthetic type IV diamond [48], (b) The microscopic NV center [50].....	23

Figure 1.20: The experimental setup of pumping NV centers in a diamond performed in [52].....	24
Figure 1.21: The fluorescence spectrum of the NV center [50].....	24
Figure 1.22: The simplified transitions and energy levels for both types of the NV center, Red and Green represent red and green excitation, respectively [50].....	25
Figure 1.23: A three-level model for the emission dynamics of the NV center [52].....	25
Figure 1.24: The detailed energy levels schematic for NV ⁻ center [50]	26
Figure 1.25: The fluorescence counts against the excitation power for the single NV ⁻ center [52]	28
Figure 1.26: SiV's (a) atomic structure, (b) electronic structure (negatively charged) [53].....	29
Figure 1.27: SiV- emission spectra at different temperatures [55]	29
Figure 1.28: A waveguide with random and uniform cross-section along the direction of propagation [54]	30
Figure 1.29: SPPs propagating at a metal-dielectric boundary [62]	35
Figure 1.30: SPPs dispersion relation at the ideal metal-air and metal-silica interfaces [60].....	38
Figure 1.31: Aim of the thesis diagram	44
Figure 2.1: The general structure of an HPW at a wavelength of 1.55 μm	45
Figure 2.2: The two orthogonal modes supported by the HPW for each case of output polarization for Au, Ag, and Al materials at 700 nm.....	47
Figure 2.3: The HSQ's geometries in DLSPP waveguides used as on-chip plasmonic single-photon sources. (a) [73], (b) [78], (c) [80]	50
Figure 2.4: The orthogonal modes field distribution when the width and height of the GaP region is (a), (b) 250, 180 nm, (c), (d) 200, 150 nm, (e), (f) 190, 150 nm, and (g), (h) 200, 145 nm, respectively.....	51
Figure 2.5: The orthogonal modes field distribution with Al bar's height of (a), (b) 45 nm, and (c), (d) 50 nm	52
Figure 2.6: The schematic of a QE coupled to an HPW that acts as a polarization rotator. The inset shows the transversal cross-section of the proposed structure at the QE's position	52
Figure 2.7: The variation of θ against the Al width for different HSQ thickness.....	55
Figure 2.8: $ \mathbf{H}_{\text{norm}} $ in the case of the a) first effective mode index. b) second effective mode index. Arrows indicate the magnetic field distribution.....	55

Figure 2.9: (a) $ E_x $ (b) $ E_y $ for 0° output polarization. Arrows indicate the magnetic field distribution.	56
Figure 2.10: The field distributions for the (a) TM (E_x), (b) TM (E_y), (c), TM (E_z), (d) TM (H_x), (e) TM (H_y), (f) TM (H_z), (g) TM (E_x), (h) TM (E_y), (i) TM (E_z), (j) TM (H_x), (k) TM (H_y), and (l) TM (H_z).....	57
Figure 2.11: The normal magnetic field distribution for the second orthogonal mode ..	58
Figure 2.12: COMSOL's variables section that defines Equation (1.14)	58
Figure 2.13: (a) The Integration (intop1) Nonlocal Coupling in the Definitions tree of the Model builder, (b) The Global Variable Probe that monitors the Purcell variable, (c) The transversal distribution of the Purcell factor calculated by Equation (1.14)	59
Figure 2.14: The 2D analysis for the Purcell factor calculation in (a) [25], (b) [73], the reproduced 2D analysis for the Purcell factor calculation in (c) [25], and (d) [73]	60
Figure 2.15: The schematic of the 3D model used to calculate the total decay rate	60
Figure 2.16: The total decay rate evaluation (Equation (2.3)'s numerator). (a) The QE's location in the 3D model (indicated by the Green line), (b) The edge probe settings for the corresponding QE's line geometry	61
Figure 2.17: β -factor and Purcell enhancement factor as a function of (a) y-coordinate. (b) x-coordinate for 0° output polarization	66
Figure 2.18: The β -factor and Purcell enhancement factor versus x- and y- directions for (a), (b) [73] and (c), (d) reproduced results, respectively	68
Figure 2.19: β -factor and Purcell enhancement factor as a function of y- and x-coordinates, respectively, (a) and (b), for 90° output polarization, (c) and (d), for 45° output polarization, and (e) and (f), for -45° output polarization.	69
Figure 2.20: The mesh configuration for the (a) 2D and (b) 3D models	70
Figure 2.21: The $ H_{\text{norm}} $ when Al width is (a) 110 nm ($\theta = 45^\circ$), (b) 70 nm ($\theta = 22.5^\circ$), (c) 70 nm ($\theta = -22.5^\circ$), (d) Schematic of the structure when θ is -22.5° . Arrows represent the magnetic field distribution	71
Figure 2.22: The electric field components distribution at 90° output polarization (Al width equals 110 nm) (a) E_x , (b) E_y	72
Figure 2.23: (a) PCE against the variation in Al width at the designed conversion length for 90° output polarization, (b) The $ E_x $, and E_y variations against Al width for $45^\circ/-45^\circ$ output polarization	73
Figure 2.24: The distribution of the electric field components against z-coordinate for (a) 0° . (b) 90° . (c) 45° . and (d) -45° output polarization.....	75

Figure 2.25: The input and output electric field distribution for both x and y components, respectively, for 0°, 90°, 45°, and -45° output polarization. The figures are arranged as a) $ E_x $,input at 0°, b) $ E_y $,input at 0°, c) $ E_x $,output at 0°, d) $ E_y $,output at 0°, e) $ E_x $,output at 90°, f) $ E_y $,output at 90°, g) $ E_x $,output at 45°, h) $ E_y $,output at 45°, i) $ E_x $,output at -45°, j) $ E_y $,output at -45°	76
Figure 3.1: The experimental $g^{(2)}(\tau)$ under excitation power of (a) 0.16, (b) 1.6, and (c) 30 of the saturation power P_{sat} [52].....	78
Figure 3.2: The values of (a) $\tau_{2,3}$ and (b) $c_{2,3}$ obtained from the least square fitting of the data shown in Figure (3.1) [52].....	79
Figure 3.3: The fitting of the experimental $g^{(2)}(\tau)$ data in [73] using the model in [52].	79
Figure 3.4: The $g^{(2)}(\tau)$ versus time delay plots by (a) experimental fitting [73], (b) theoretical modeling of the experimental values in [52]	81
Figure 3.5: The $g^{(2)}(\tau)$ of the proposed structure in Chapter 2 with an output polarization of (a) 0°, (b) 90°, (c) 45°, and (d) -45° using Section (3.2)'s methodology	82
Figure 3.6: The diagram for the calculation of $g^{(2)}(\tau)$ after coupling an NV center to an HPW	82
Figure 3.7: (a) The modified NV center's emission dynamic [112], (b) The SiV center's emission dynamic in [111].....	83
Figure 3.8: The $g^{(2)}(\tau)$ experimental graphs for different excitation powers from 0.2 mW to 10 mW for (a) NV^0 , and (b) NV^- [112].....	84
Figure 3.9: γ_1 , γ_2 , and β for NV^0 (green) and NV^- (red) for different excitation powers [112].....	84
Figure 3.10: Continued.	85
Figure 3.11: $g^{(2)}(\tau)$ comparison between (a) The experimental fitting of $g^{(2)}(\tau)$ data for NV^- under 0.5 mW excitation power, (b) The modeling of $g^{(2)}(\tau)$ by direct approach (Blue) and using k-parameters approach (dotted red), (c) The experimental fitting of $g^{(2)}(\tau)$ before (Black) and after (Blue) of NV center to a nanoantenna [113], (d) The modeling of the $g^{(2)}(\tau)$ before (Black) and after (Blue) coupling the NV center in [113] to a nanoantenna	86
Figure 3.12: The $g^{(2)}(\tau)$ of the proposed structure in Chapter 2 with an output polarization of (a) 0°, (b) 90°, (c) 45°, and (d) -45° using Section (3.3)'s methodology ..	87
Figure 3.13: The emission dynamics of a two-level QE [114]	88
Figure 3.14: The two-level emission shape for Exponential and Gaussian pulses before and after coupling to a nanostructure	90

Figure 3.15: Visualization of the $G^{(2)}(\tau)$ for the QE's emission under short and long excitation pulse, (a), (b) before coupling [115], (c), and (d) after coupling	91
Figure 3.16: The integrated $G^{(2)}(\tau)$ before and after the coupling of the QE for short and long excitation pulses.....	91
Figure 4.1: A summary of the polarization-independent GC design steps	98
Figure 4.2: A general cross-section of a 2D GC [117]	99
Figure 4.3: The GC's principle with (a) GC's period equals optical wavelength ($\Lambda = \lambda_o/n_{eff}$), and two diffraction modes, (b) GC's period is larger than the optical wavelength ($\Lambda > \lambda_o/n_{eff}$), and only a single diffraction mode [117].....	100
Figure 4.4: An illustration of Bragg's condition [117], (a) without considering the diffracted wave and for m grating periods, (b) without considering the diffracted wave into space (air region) and considering the 1 st -order diffraction grating, (c) considering the diffracted wave into space, (d) considering the diffracted wave into both space and BOX regions	101
Figure 4.5: The 3D TE GC proposed in [118]. The blue area represents the waveguide's material while the green area represents the substrate material and the red arrows are the light's propagation direction	104
Figure 4.6: The 2D simulation framework proposed by [118]	105
Figure 4.7: The PML layer used in [118] is highlighted in violet	107
Figure 4.8: (a) The three ports used in [118] highlighted with red and the scattering boundary conditions highlighted with blue, (b) The ports settings in COMSOL.....	107
Figure 4.9: A boundary mode analysis at each port [118]	108
Figure 4.10: The mesh structure for (a) the entire simulation domain and (b) a zoomed area near the optical fiber source [118].....	109
Figure 4.11: The reproduced CE following the modeling steps of [118]	110
Figure 4.12: The z-component of the electric and magnetic field for (a) and (b) unetched GaP waveguide, (c) and (d) etched GaP waveguide, respectively, and their corresponding effective index	111
Figure 4.13: The CE against the x-shift in the GC position.....	113
Figure 4.14: The CE against the etching depth.....	114
Figure 4.15: The CE against Λ	114
Figure 4.16: The CE against the operation wavelength for a TE polarization incidence	115
Figure 4.17: The scattering of $ E_{norm} $ at 700 nm TE-polarized light from the optical fiber source to the output of port 2. The GC is composed of a 150 nm GaP waveguide	

and 20 nm HSQ layer. (a) The entire 2D simulation framework, (b) Zoomed 2D simulation framework to show the propagation in the GaP waveguide	115
Figure 4.18: The CE against the PML thickness for (a) the Si waveguide in Section (4.3.1) and (b) the GaP waveguide	116
Figure 4.19: The z-component of the electric and magnetic field for (a) and (b) unetched GaP waveguide, (c) and (d) etched (80 nm) GaP waveguide, respectively, and their corresponding effective index	116
Figure 4.20: The (a) electric field and (b) magnetic field components in the propagation direction (x-axis) in the GaP waveguide when a TE polarized light is applied on the GC	118
Figure 4.21: The CE against the Λ for a TM polarized light	119
Figure 4.22: The (a) electric field and (b) magnetic field components in the propagation direction (x-axis) in the GaP waveguide when a TM polarized light is applied on the GC	119
Figure 4.23: The CE against the operation wavelength for a TM polarization incidence	120
Figure 4.24: The $ \theta_{inc} $ against the Λ for the GC in (a) [99], (b) Section (4.3.2)	122
Figure 4.25: The 3D GC proposed in [99], (a) The schematic, (b) The Bragg's conditions	122
Figure 4.26: (a) The θ_{inc} against Λ , (b) The CE against the Λ for a θ_{air} of 17.75° on the 150 nm GC described in Section (4.3.2)	123
Figure 4.27: Contour plots showing the CE for (a) Intersection, and (b) Union methods based on a 220 nm Si waveguide performed by [95], (c) Intersection, and (d) Union methods based on a 150 nm GaP waveguide, where the solid line is the TE's CE and the dashed line is the TM's CE	124
Figure 4.28: The scattering of the normal electric field in Section (4.3.1)'s simulation framework with a 2nd-order scattering boundary condition instead of the PML layer	127
Figure 4.29: The proposed double-layer GC	128
Figure 4.30: The separation of the GC into two slab waveguides to estimate the effective index for the full channel and etched channel waveguides	129
Figure 4.31: The new separation of the GC into four slab waveguides	130
Figure 4.32: The proposed double-layer GC's design strategy	131
Figure 4.33: The CE against the x-shift in the GC position (1 st layer only)	132
Figure 4.34: The CE against the etch depth of the 1 st layer only	133
Figure 4.35: The CE against Λ_1	133

Figure 4.36: The CE against the operation wavelength for a TE polarization excitation from the right port.....	134
Figure 4.37: The CE of a GC against the x-coordinate to a fixed position of a PMF in the simulation domain.....	134
Figure 4.38: The CE spectra of the proposed GC with (a) a single-layer approach, (b) a double-layer approach.....	135
Figure 4.39: The CE spectra of the four polarization cases for the optimum double-layer GC	136
Figure 4.40: The PDL performance of the optimum double-layer GC for different polarization cases	137
Figure 4.41: The intensity distribution in the simulation domain for (a) a TE excitation, (b) a TM excitation, (c), and (d) a 45° linear excitation.	137
Figure 4.42: The intensity distribution of the excitation light source in the simulation domain for (a) a TE excitation, (b) a TM excitation, (c), and (d) a 45° linear excitation.	142

List of Tables

Table 2.1: The refractive indices information for different materials [104]	46
Table 2.2: Al dimensions for output polarization of 0° , $45^\circ/-45^\circ$, and 90°	54
Table 2.3: The β -factor calculation for 0° , 90° , 45° , and -45° output polarization when the QE has varied along the y-axis and x-axis	62
Table 2.4: The optimum position of the QE for each output polarization and the corresponding Purcell enhancement factor and β -factor	69
Table 3.1: The experimental pf values for different excitation power [112]	85
Table 4.1: A summary of the simulation performance of the polarization-independent GCs approaches	140
Table 4.2: The two orthogonal modes effective indices for the four HPWs designed at Chapter 2 at 532 nm	141
Table 4.3: The CE of the GC after being excited by a 532 nm laser light having 0° , 90° , and $45^\circ/-45^\circ$ (Green) and the output power at the end of HPWs mentioned in Table (4.2) (Orange)	141

Chapter One

Introduction

Chapter 1

Introduction

1.1. General Introduction and Motivation

In 1900, Max Planck proposed that light is composed of a stream of discrete energies. This proposal developed the quantum mechanics context and led to the first quantum rising that developed the laser, the atomic clock, and the transistor. Nowadays, a second quantum rising is seen by the development of quantum sensors, quantum computing, and quantum simulators. The physics laws at the quantum scale including—entanglement, no-cloning theorem, the principle of superposition, and non-commuting operators, formed the basis of quantum computing and quantum communications. The broad commercialization of the latter led to the development of quantum cryptography [1].

The light-matter interaction is a substantial phenomenon in nature and, therefore, it has been under study for decades. In 1946, Edward M. Purcell found out that the rate of emission from an atom is partially extrinsic and could be affected by the atom's environment considerably [2]. Purcell discovered that when an atom is coupled to a resonator, the probability of photon emission is improved in comparison to the uncoupled atom. Consequently, Purcell found a major field of study that investigates the interaction of light with matter under quantum electrodynamics and quantum mechanics contexts [3].

The process of stimulated emission defines the quantum emitter's (QE) spontaneous emission. The stimulation resulted from a pool of photonic quantum fluctuations, which are temporarily generated and annihilated photons, in the local energy as defined by the uncertainty principle proposed by Werner Heisenberg. Maxwell's equations determined specific possible optical modes in an environment, such as a dielectric

waveguide, where the photonic quantum fluctuations and, hence, the generated photons are propagating. The QE's environment engineering improves the emission into a specific optical mode.

For example, an optical resonator or waveguide is an example of the QE's environment engineering that is used to control and improve the vacuum quantum fluctuations. Furthermore, a confined optical mode to small dimensions can considerably increase the photonic quantum fluctuations such that the emitter could emit a considerable number of photons into the confined mode, directly. A proper design of the dielectric waveguide achieves a strongly confined optical mode and, consequently, a considerable amount of the spontaneously emitted photons are directly coupled to the waveguide mode [3].

Several quantum information processing protocols depend on the intensive photon flux and the emission of spontaneously emitted photons into a single optical waveguide mode [4,5]. Efficient coupling of the QE to a single optical waveguide mode realized on-demand single photons [6], nonlinear gate operations based on few photons [4], and linear optical quantum computers (LOQCs) [7].

The single-photon source is an essential building block to realize several quantum cryptography protocols. A brighter single-photon source increases the data rate and, consequently, improves the performance of quantum cryptography systems [8]. Single-photon emitters (SPEs) could be coupled to several types of plasmonic or dielectric nanostructures to enhance their decay rate and, consequently, achieve a high rate of single-photon emission. For example, the photonic crystal waveguide [9], photonic crystal cavity [10], and high refractive index dielectric waveguide [11] had been used to enhance the decay rate and channel the QE's emission. In dielectric-based nanostructures, the light confinement is restricted to the diffraction limit. However, the plasmonic nanostructures permit the confinement of the

light much beyond the diffraction limit [12]. Plasmonic waveguides (PWs) improve the decay rate of the QE besides the channeling and routing of the propagated PW's modes [13].

1.2. Integrated optical circuits

The scaling-down of semiconductor electronic devices has been a trend in the last 60 years. This doubled the number of electronic components onto a single chip every two years as stated by Moore's law [14]. Consequently, both speed and memory are nearly 2^{58} times as much as in 1965. The miniaturization of the electronic components, i.e., transistors, resulted in a shorter gate delay, which is the required time to switch the transistor off or on. As a result, the transistor's speed improves. Nonetheless, this increases the interconnect delay, which is the on-chip time required for a signal to transfer from the source to the destination. This is because of the metallic interconnects' inherent resistances and the dielectrics' capacitances [15]. As the interconnect size decreases below $0.5\text{ }\mu\text{m}$, the interconnect delay surpasses the gate delay as shown in Figure (1.1).

Consequently, the speed is restrained by the metal interconnects. One of the encouraging solutions is the exchange of the metal interconnect by on-chip optical waveguides. This results in a mixed electronic-photonics system [16]. Photonic interconnects support a wide bandwidth compared to metallic interconnects. Nonetheless, the metallic interconnects scale is smaller than photonic interconnects because of the diffraction limit. However, the utilization of plasmonic-based nanophotonic components solved the size mismatching issues between the electronic and photonic circuits as shown in Figure (1.2) [17].

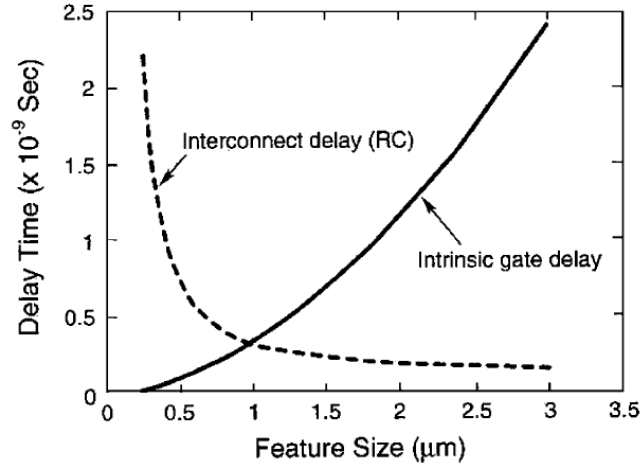


Figure 1.1: The delay times against the feature size [15]

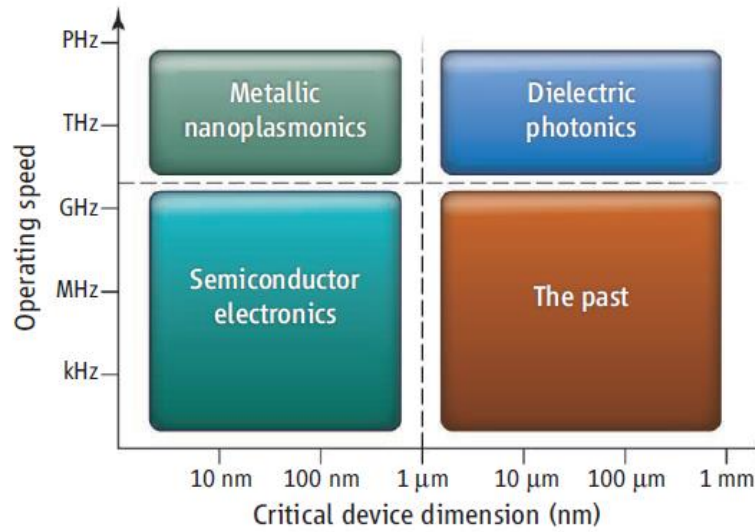


Figure 1.2: Several technologies for on-chip integrated circuits [17]

1.3. Computational nanophotonics

Most of the practical nanophotonic structures have sophisticated geometries such that Maxwell's equations are difficult to be solved mathematically. Consequently, the design and analysis of such complex nanostructures rely on numerical solutions [18]. The finite-difference time-domain (FDTD) method is the major standard for numerical computation of nanophotonic structures and has been considered a reference for other methods and approaches [19]. The FDTD method utilizes the point form of Maxwell's equations with a discrete grid of time and spatial geometry to numerically compute the electromagnetic fields [20]. The algorithms and formulations of the FDTD are simple and robust to complicated deformations and shapes of

the structures. However, it consumes a huge amount of memory and space when analyzing 3D structures. The most popular commercial FDTD software is Lumerical solutions.

Another numerical solution that is based on the frequency domain to solve the point form of Maxwell's equations is the modal technique [21]. It is based on dividing the nanostructure into uniform multilayers along a specific propagation direction. Using a scattering matrix algorithm, the electromagnetic fields are computed locally within each layer and then merged. The computational complexity relies on the transverse layers along the propagation direction. This method is efficient in analyzing long waveguide structures. Moreover, it is efficient and widely used in computing the Bloch modes in periodic systems such as photonic crystals. However, this method loses its performance when different propagation directions exist within the nanostructure [22]. One of the commercial software that implements the modal analysis is Harminv.

A widely used numerical technique that is used in several scientific branches to solve partial differential equations is the finite element method (FEM) [23]. It solves Maxwell's equations in both frequency and time domains. The structure is discretized into several mesh elements and Maxwell's equations are solved on each element of the mesh grid. FEM can apply a non-homogeneous grid of mesh with the finest resolution and it supports the solution of multiphysics problems, for example, optical, thermal, and electrical physics. The most powerful tool that relies on FEM to solve Maxwell's equations is COMSOL Multiphysics, which is used throughout this thesis due to its simplicity, accuracy, friendly graphical user interface (GUI), and powerful probes.

1.4. Electrodynamics

This thesis is related to the solution of Maxwell's equations in different geometries and with several kinds of electromagnetic sources. In

the following subsections, a brief introduction to Maxwell's equations and their resultant Poynting's and Lorentz reciprocity theorems are introduced. Furthermore, the dyadic Green's function, which is important in describing the light-matter interactions, is briefly presented. The following subsections describe the electrodynamics of the light-matter interaction in nanowaveguides [24].

1.4.1. Maxwell's equations

The point form of Maxwell's equations for time-varying fields for a homogeneous and non-magnetic medium ($\mu_r = 1$) are

$$\nabla \times \vec{E} = -\frac{\partial \vec{B}}{\partial t}, \quad (1.1. a)$$

$$\nabla \times \vec{H} = \frac{\partial \vec{D}}{\partial t} + \vec{J}, \quad (1.1. b)$$

$$\nabla \cdot \vec{D} = \rho_v, \quad (1.1. c)$$

$$\nabla \cdot \vec{B} = 0, \quad (1.1. d)$$

where \vec{E} , \vec{B} , \vec{H} , \vec{D} , \vec{J} , and ρ_v are the electric field intensity (V/m), magnetic flux density (Tesla), magnetic field intensity (A/m), electric flux density (C/m²), current density (A/m²), and volume charge density (C/m³), respectively. The general expression for any time-varying field (\vec{N}) in space (\vec{r}) is

$$\vec{N}(\vec{r}, t) = \vec{N}(\vec{r}, \omega)e^{-i\omega t}, \quad (1.2)$$

where ω is the angular frequency (rad/s). Consequently, Maxwell's equations in the frequency domain could be written as

$$\nabla \times \vec{E} = i\omega \vec{B}, \quad (1.3. a)$$

$$\nabla \times \vec{H} = \vec{J} - i\omega \vec{D}, \quad (1.3. b)$$

For linear, isotropic, and non-magnetic materials, the \vec{D} and \vec{B} could be written as

$$\vec{D} = \epsilon_0 \epsilon_r \vec{E}, \quad (1.4. a)$$

$$\vec{B} = \mu_0 \vec{H}, \quad (1.4. b)$$

where ϵ_0 is the free-space permittivity (F/m), ϵ_r is the relative permittivity of the medium, and μ_0 is the free-space permeability (H/m). By substituting Equation (1.4) into Equation (1.3), Maxwell's equations could be written as

$$\nabla \times \vec{E} = i\omega\mu_0 \vec{H}, \quad (1.5. a)$$

$$\nabla \times \vec{H} = \vec{J} - i\omega\epsilon_0 \epsilon_r \vec{E}, \quad (1.5. b)$$

$$\epsilon_0 \nabla \cdot (\epsilon_r \vec{E}) = \rho_v, \quad (1.5. c)$$

$$\nabla \cdot \vec{H} = 0, \quad (1.5. d)$$

which shall be solved by COMSOL Multiphysics to calculate the field components in the proposed structures.

1.4.2. Poynting's theorem

A direct result of frequency-domain Maxwell's equations is Poynting's theory,

$$\int_S \vec{S} \cdot \vec{n} \, dA = -0.5 \int_V \text{Re}(\vec{J}^* \cdot \vec{E}) \, dV, \quad (1.6. a)$$

$$\vec{S} = 0.5 \text{Re}(\vec{E} \times \vec{H}^*), \quad (1.6. b)$$

where \vec{S} is the time average of the Poynting vector, and \vec{n} is a unit vector directed perpendicularly outside the closed boundary of a surface (S) or a volume (V). Equation (1.6.a) states that the perpendicularly radiated power through a closed surface equals the current density inside a closed volume. Moreover, Equation (1.6.a) and Equation (1.6.b) define the radiated power from a dipole in an environment, which will be used to model the QE.

1.4.3. Dyadic Green's function

By applying the curl operator to both sides of Equation (1.5.a) and using Equation (1.5.b) to eliminate $\nabla \times \vec{H}$ from the resultant expression, the resultant wave equation could be written as

$$\nabla \times \nabla \times \vec{E} - k_0^2 \epsilon \vec{E} = i\omega\mu_0 \vec{J}, \quad (1.7)$$

where $k_0 (=2\pi/\lambda)$ is the free-space wavenumber (rad/m). The QE in the proposed structures is modeled as a point source (dipole) located at a position \vec{r}_D with a current density equals

$$\vec{J}(\vec{r}) = \vec{J}_D \delta(\vec{r} - \vec{r}_D), \quad (1.8)$$

For a Dyadic Green's function that satisfies radiation condition, the Dyadic Green's function is defined as

$$\nabla \times \nabla \times \vec{G}(\vec{r}, \vec{r}_D) - k_0^2 \epsilon \vec{G}(\vec{r}, \vec{r}_D) = \vec{I} \delta(\vec{r} - \vec{r}_D), \quad (1.9)$$

where \vec{I} is a unit dyad. Hence, the \vec{E} at any position \vec{r} due to a dipole in \vec{r}_D is given by

$$\vec{E}(\vec{r}) = i\omega\mu_0 \vec{G}(\vec{r}, \vec{r}_D) \vec{J}_D \quad (1.10)$$

1.5. Coupling theory

If a QE is placed nearby a PW, three decay channels are available, which are the radiative emission (Γ_{rad}), emission into the PW (Γ_{pl}), and the nonradiative emission ($\Gamma_{\text{non-rad}}$) that is converted to heat. The aforementioned decay channels are shown in Figure (1.3) [25].

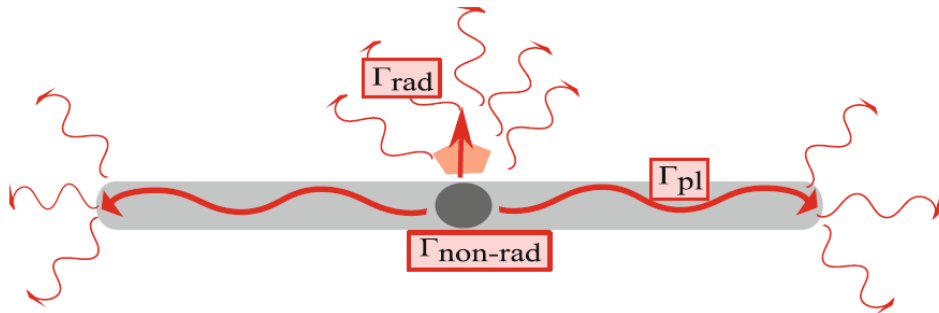


Figure 1.3: the three decay channels for a QE near a PW [25]

The most useful decay channel is Γ_{pl} . The β -factor is determined by dividing the Γ_{pl} by the QE's total decay rate (Γ_{tot}), which is the summation of the aforementioned decay channels. In this section, the numerical calculation of the Γ_{pl} is presented. Then, the corresponding equations of the Γ_{tot} are explained. Finally, the calculation of the β -factor completes this section.

1.5.1. PW's decay rate

The local density of states (LDOS) of the system defines the possible states that the system occupies at a certain energy. The LDOS projected to the PW's mode $\rho_{pl}(\vec{r}, \omega)$ are derived from the Green's function as [26]

$$\rho_{pl}(\vec{r}, \omega) = \frac{6\omega |\vec{n}_D \cdot \text{Im}(\vec{G}(\vec{r}, \vec{r}_D) \cdot \vec{n}_D)|}{\pi c^2} = \frac{6|\vec{E}(x, y) \cdot \vec{n}_D|^2}{2\pi \text{Re}\{\int_A (\vec{E} \times \vec{H}^*) \cdot \vec{a}_z dA\}}, \quad (1.11)$$

where c is the speed of light in a vacuum (m/s), \vec{n}_D is the unit vector of the dipole moment, $\vec{E}(x, y)$ is the distributions of the electric field in the transversal plane, A is the area of the transversal plane, and \vec{a}_z is a unit vector perpendicular to the transversal plane.

The QE's decay rate, when embedded in a medium, could be expressed as a function of the LDOS as [26]

$$\Gamma_{pl}(\vec{r}) = \frac{\pi\omega_o |\mu_D|^2 \rho_{pl}(\vec{r}, \omega)}{3\hbar\epsilon_o}, \quad (1.12)$$

where \hbar is the reduced Planck's constant (J.s), and μ_D is the QE's (dipole) moment (A.s.m). However, the QE's decay rate in a vacuum (Γ_o) could be expressed as [26]

$$\Gamma_o = \frac{\omega^3 |\mu_D|^2}{3\pi\hbar\epsilon_o c^3}, \quad (1.13)$$

Consequently, the ratio of the Γ_{pl} to the Γ_o (i.e. the Purcell factor) could be expressed as [26]

$$\frac{\Gamma_{pl}}{\Gamma_o} = \frac{3\pi c \epsilon_o |\vec{E}(x, y) \cdot \vec{n}_D|^2}{\text{Re}\{k_o^2 \int_A (\vec{E} \times \vec{H}^*) \cdot \vec{a}_z dA\}}, \quad (1.14)$$

Figure (1.4) shows several examples that utilize Equation (1.14) to calculate Γ_{pl}/Γ_o utilizing different waveguide topologies [25]. Figure (1.4) indicates that more confinement of the PW's mode results in a higher Γ_{pl} , which is the most useful channel as mentioned in the introduction of Section (1.5). Moreover, the QE's orientation should follow the more intense (brighter) point in the transverse plane shown in Figure (1.4) for each PW.

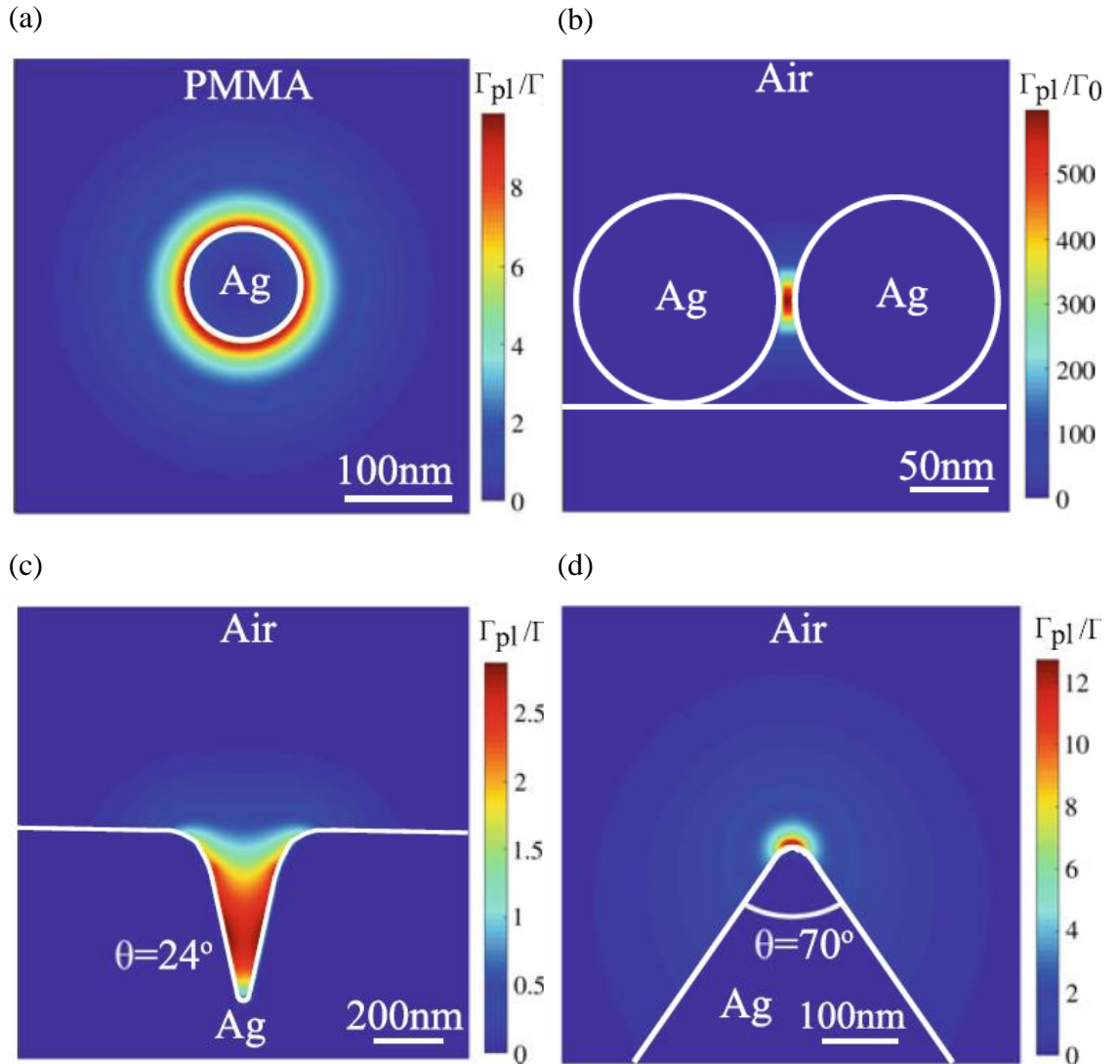


Figure 1.4: The implementation of Equation (1.14) to calculate Γ_{pl}/Γ_o in a a) Wire made of silver, b) Two nearby silver wires, c) V-groove waveguide, and d) Wedge waveguide [25]

1.5.2. The QE's total decay rate

The calculation of Γ_{tot} requires a 3D model for the nanostructure to consider all the quantities of plasmonic, radiative, and nonradiative decay channels. Equation (1.7) is numerically evaluated by COMSOL with a proper truncation for the computational domain. The $\Gamma_{\text{tot}}/\Gamma_o$ could be obtained by calculating the total power radiated by the QE in a medium divided by the QE's radiated power in a vacuum as [25]

$$\frac{\Gamma_{\text{tot}}}{\Gamma_o} = \frac{P_{\text{tot}}}{P_o}, \quad (1.15)$$

where

$$P_{\text{tot}} = 0.5 \iiint \text{Re}(\vec{J}^* \cdot \vec{E}) dV, \quad (1.16)$$

$$P_o = 0.5 \iiint \text{Re}(\vec{J}^* \cdot \vec{E}_o) dV, \quad (1.17)$$

and \vec{E} and \vec{E}_o are the radiated electric field by the QE in a medium and a vacuum, respectively. Since the QE has the same geometry in every medium, the \vec{J}^* could be omitted in Equation (1.15). The power probes in COMSOL Multiphysics can be used to calculate Equation (1.15).

1.5.3. The β -factor

Figure (1.5) shows the β -factor distribution for the waveguide presented in Figure (1.4.b) with a maximum value of 90% [25]. It is clear that the spatial position of the maximum β -factor in Figure (1.5) does not coincide with the spatial position of maximum Γ_{pl} shown in Figure (1.4.b). Therefore, the trade-off between the β -factor and the Γ_{pl} depends on the QE position in the waveguide's geometry.

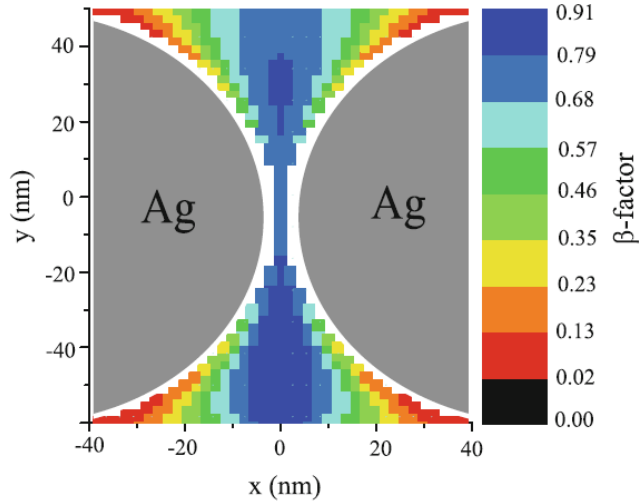


Figure 1.5: β -factor for the waveguide structure presented in Figure (1.4.b) [25]

1.6. Photon statistics

The coherent (Glauber) states were discovered by Roy Glauber. That is, the coherent state of a classical light source was generated by a classical harmonic oscillator. Afterward, a quantum harmonic oscillator was proposed as a single-mode resonator with a specified phase and amplitude relevance, i.e, a laser resonator that emits (generates) coherent states of light [27]. In a coherent state of light, the photon distribution follows Poisson's statistics, which is defined by [28]

$$p(m) = \frac{e^{-\langle m \rangle} \langle m \rangle^m}{m!}, \quad (1.18)$$

where m is the number of photons in a fixed intensity coherent light, $\langle m \rangle$ is the average of photon numbers and $p(m)$ is the probability of finding m photons. The chaotic (thermal) sources of light show a wider distribution of the photons number that corresponds to a super-Poissonian distribution while quantum sources of light have a narrower distribution of photons number that corresponds to a sub-Poissonian distribution. The difference in the light's statistical distribution enabled the light's classification into three types (thermal, coherent, and single-photon sources) as shown in Figure (1.6) [28].

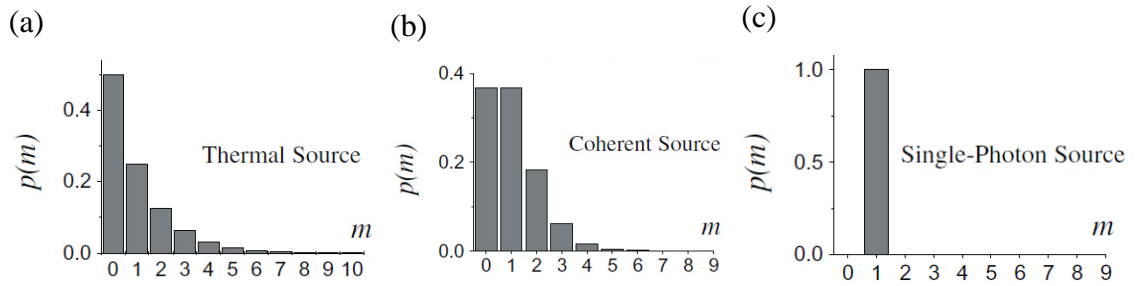


Figure 1.6: $p(m)$ distribution for (a) a thermal light source (lamp), (b) a coherent light source (laser light), and (c) an ideal single-photon source [28]

Therefore, the light could be classified according to the intensity or m fluctuations (i.e., time-dependent separation) and a specific coherence time (τ_c), which defines the period by which the phase of the wave train remains stable. Photon bunching refers to a high probability of detecting closely time-spaced photons. Thermal light, blackbody radiation, or incandescence radiation (incoherent sources) are all examples of bunched light sources. The bunched light sources follow the Bose-Einstein (Super-Poissonian) distribution of their photons.

Hanbury Brown and Twiss (HBT) performed an experiment using a mercury lamp projected to a 50:50 beam splitter as shown in Figure (1.7). They aimed to study the relationship of the classical light's intensity fluctuations to its τ_c . The split lights were applied to separate photomultiplier tubes (PMT1 and PMT2) that generate photocurrents (i_1 and i_2). The photocurrents (i_1 and i_2) are applied to AC-coupled amplifiers that generate an output proportional to the photocurrent fluctuations (Δi_1 and Δi_2). The Δi_2 was connected to a time delay generator of a time (τ). A multiplier-integrator device multiplies Δi_1 and Δi_2 and averages them over a long time. The multiplier-integrator device's output is proportional to $\langle \Delta i_1(t) \Delta i_2(t + \tau) \rangle$ because $I_1(t)$ and $I_2(t)$ generated $\Delta i_1(t)$ and $\Delta i_2(t)$ [29], where $\langle \dots \rangle$ is the average operation.

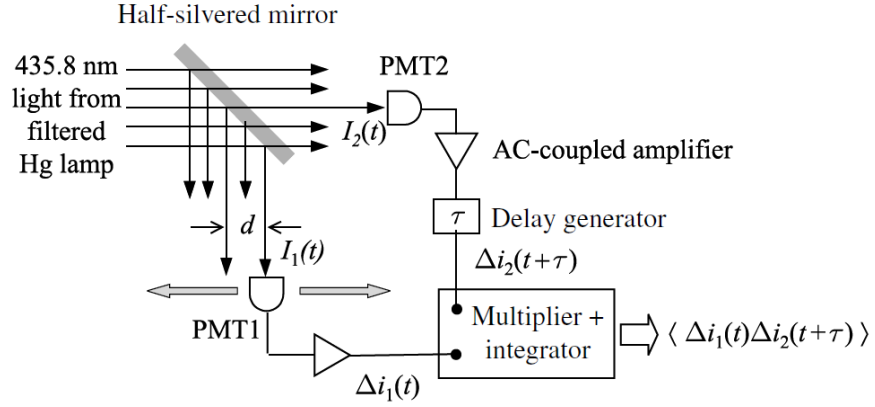


Figure 1.7: A schematic of the HBT experiment using a classical light source [29]

Several different atoms in the mercury lamp generate a fluctuated intensity light on a time-scale near τ_c . The random fluctuation of the emitting atoms results in discontinuities in the emitted phase by each atom. The random emission events from millions of atoms at a microscopic scale refer to the chaotic behavior of the emitted light. The chaotic behavior results in intensity fluctuations of the emitted light below and above the average intensity ($\langle I \rangle$) on a time-scale near τ_c because of the random collisions of the atoms as shown in Figure (1.8) [29].

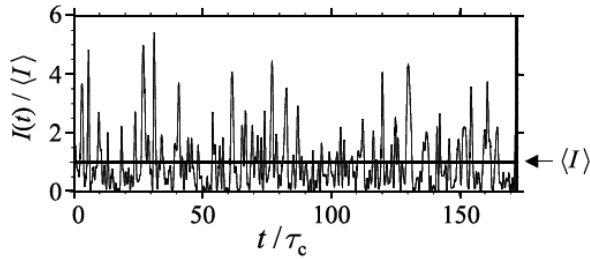


Figure 1.8: A time-dependent simulation shows the intensity fluctuation to τ_c of a chaotic light source [29]

The light's coherence properties are concluded from the measurement of the intensity's fluctuations correlation as shown in Figure (1.8). If d is at the initial position ($d = 0$), the applied time-varying intensity on the detectors could be written as [29]

$$I_1(t) = I_2(t) = I(t) = \langle I \rangle + \Delta I(t), \quad (1.19)$$

where $\Delta I(t)$ is the light's fluctuation around $\langle I \rangle$, and $I(t)$ is the output intensity from the beam splitter at each branch. The HBT experiment's

output is proportional to $\langle \Delta I(t) \Delta I(t + \tau) \rangle$ if the applied intensities on the detectors are identical. If τ is zero, then

$$\langle \Delta I(t) \Delta I(t + \tau) \rangle_{\tau=0} = \langle \Delta I(t)^2 \rangle, \quad (1.20)$$

Hence, the output is not zero at $\tau = 0$. If τ is larger than τ_c , the $\Delta I(t) \Delta I(t + \tau)$ randomly fluctuates with time and the average approaches zero because these intensities will not be correlated. Hence,

$$\langle \Delta I(t) \Delta I(t + \tau) \rangle_{\tau \gg \tau_c} = 0, \quad (1.21)$$

The τ_c could be determined directly by observing the output with τ variation. A similar approach to studying the spatial coherence of light was performed by varying d [29].

The light's second-order correlation function $g^{(2)}(\tau)$ is defined as [29]

$$g^{(2)}(\tau) = \frac{\langle E^*(t) E^*(t + \tau) E(t + \tau) E(t) \rangle}{\langle E^*(t) E(t) \rangle \langle E^*(t + \tau) E(t + \tau) \rangle} = \frac{\langle I(t + \tau) I(t) \rangle}{\langle I(t) \rangle \langle I(t + \tau) \rangle}, \quad (1.22)$$

where $E(t)$ is the light's electric field (V/m).

Since the fluctuations in the intensity at times t and $t + \tau$ are completely uncorrelated for $\tau \gg \tau_c$, the numerator of Equation (1.22) could be obtained as [29]

$$\begin{aligned} \langle I(t) I(t + \tau) \rangle_{\tau \gg \tau_c} &= \langle (\langle I \rangle + \Delta I(t)) (\langle I \rangle + \Delta I(t + \tau)) \rangle = \\ &= \langle I \rangle^2 + \langle I \rangle \langle \Delta I(t) \rangle + \langle I \rangle \langle \Delta I(t + \tau) \rangle + \langle \Delta I(t) \Delta I(t + \tau) \rangle \\ &= \langle I \rangle^2, \end{aligned} \quad (1.23)$$

Therefore, the value of $g^{(2)}(\tau)$ is [29]

$$g^{(2)}(\tau \gg \tau_c) = \frac{\langle I(t) I(t + \tau) \rangle}{\langle I(t) \rangle^2} = \frac{\langle I(t) \rangle^2}{\langle I(t) \rangle^2} = 1, \quad (1.24)$$

For $\tau = 0$, the value of $g^{(2)}(0)$ is [29]

$$g^{(2)}(0) = \frac{\langle I(t)^2 \rangle}{\langle I(t) \rangle^2} \geq 1, \quad (1.25)$$

The plot of $g^{(2)}(\tau)$ for a chaotic light source is shown in Figure (1.9.a).

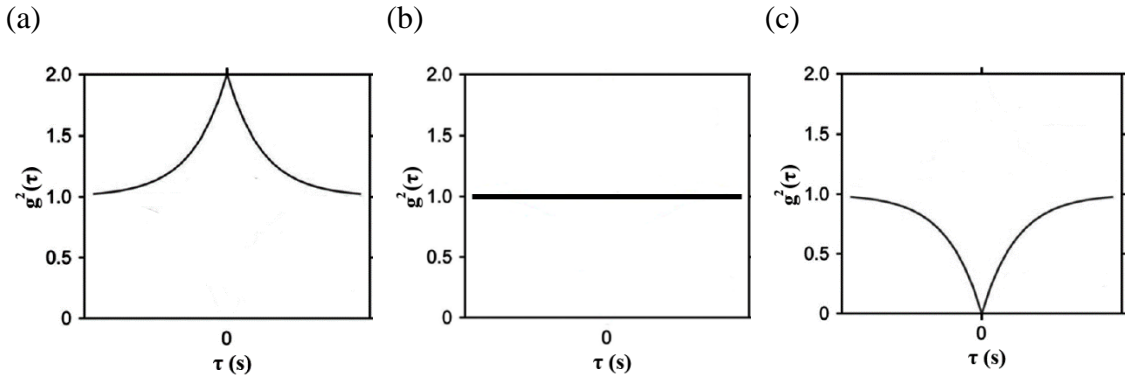


Figure 1.9: $g^{(2)}(\tau)$ for (a) bunched (chaotic), (b) coherent, and (c) antibunched light sources [30]

For a perfectly coherent light source with a constant and time-independent intensity of I_0 , the value of $g^{(2)}(\tau)$ equals unity at all τ because [29],

$$g^{(2)}(\tau) = \frac{\langle I(t)I(t+\tau) \rangle}{\langle I(t) \rangle^2} = \frac{I_0^2}{I_0^2} = 1, \quad (1.26)$$

as shown in Figure (1.9.b). The coherent light source shows random arrival times of its photons and, consequently, they are not correlated. They follow Poissonian's distribution of their photons [27,29].

A quantum light source, such as the emitted light from quantum dots or defect centers, suppresses the number of photons (intensity) variations. The emitted photons have a fixed time separation between them (anti bunched light). They follow Sub-Poissonian statistics and this is a pure quantum phenomenon. The intensity of the light is linearly proportional to the number of photons in the light beam. Hence, the $g^{(2)}(\tau)$'s equation could be modified as [29]

$$g^{(2)}(\tau) = \frac{\langle n_1(t)n_2(t+\tau) \rangle}{\langle n_1(t) \rangle \langle n_2(t+\tau) \rangle}, \quad (1.27)$$

where $n_i(t)$ is the photons number counted by detector i (1 and 2). The setup of the HBT experiment, where a stream of photons is applied to the beam splitter, is modified as shown in Figure (1.10) [29].

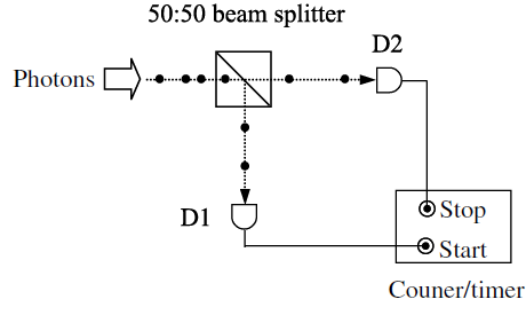


Figure 1.10: A HBT experiment with a stream of photons input [29]

The $g^{(2)}(\tau)$ becomes proportional to the conditional probability that D2 detects a second photon at τ if D1 detected a photon at $t = 0$. The timer in Figure (1.10) does not record events at $\tau = 0$ since there is no probability that two photons are detected at the same time for a quantum light source. The timer records events only when one of the output branches of the beam splitter is delayed by τ . Consequently, the $g^{(2)}(\tau)$ could be plotted as shown in Figure (1.9.c) for a quantum light source.

Figure (1.11) shows the distribution of the photons for various light sources [29].

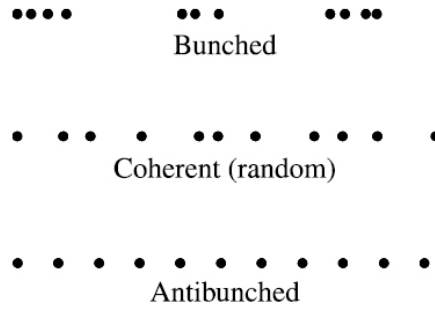


Figure 1.11: The photon stream for a (a) thermal light, (b) laser light, and (c) quantum light [29]

The photon antibunching results from the fact the QE emits a single photon when the energy is relaxed from the upper state $|e\rangle$ to the lower state $|g\rangle$ in a two-level quantum system as shown in Figure (1.12) [27,29].

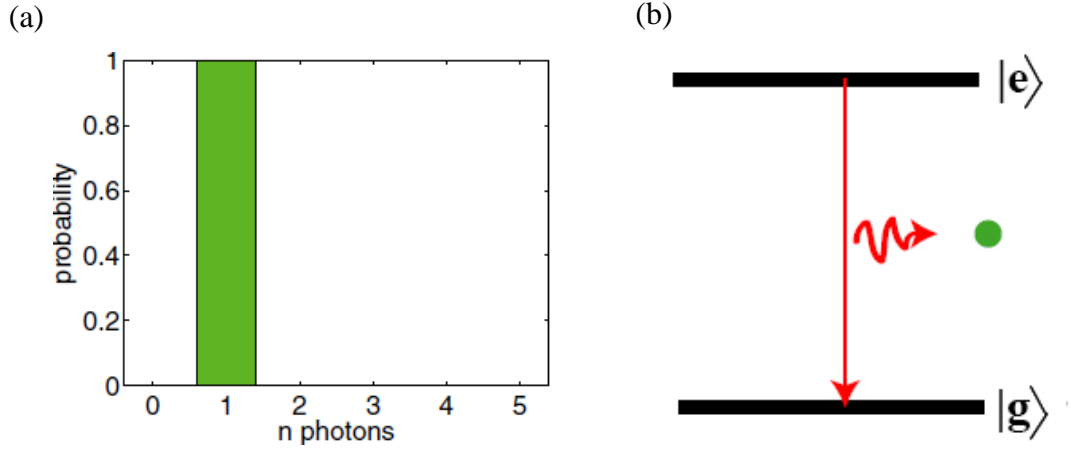


Figure 1.12: (a) Fock state with unity mean photon number, (b) A two-level QE emits a single photon [27]

Accordingly, the incoherent light sources exhibit a $g^2(0)$ greater than one, the coherent light sources exhibit a unity $g^2(0)$, and the quantum light sources exhibit a zero value for the $g^2(0)$ as shown in Figure (1.9) [30].

The QE requires a finite time (radiative lifetime (τ_R)) to be elapsed before the re-excitation of the QE. As a result, a finite time between the consecutive emission events occurs as shown in Figure (1.13) [29].

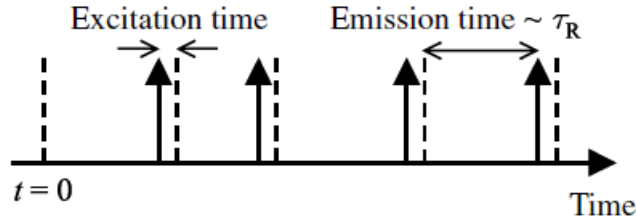


Figure 1.13: The photon emission sequence from a QE [29]

The control of the single-photon generation (on-demand) by an external trigger (optical or electrical) plays an important role in quantum communication technologies [28,31].

Figure (1.14) shows a typical experimental setup that is widely used by many researchers to characterize the emission of QEs either alone or coupled to different nanostructures [30]. The applied excitation light on the objective could be pulsed or continuous depending on the QE properties. The emission is collected by the same objective and applied to an HBT setup.

One SPAD triggers the start button of the correlator's counter and the other SPAD stops the correlator's counter and registers an event [25,29].

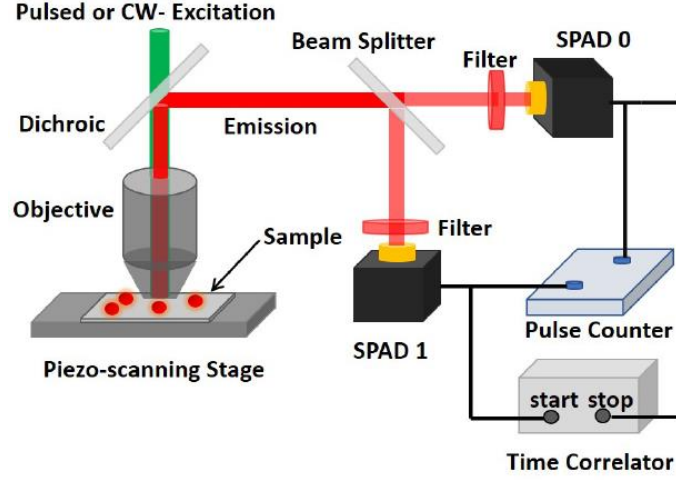


Figure 1.14: The schematic of a general set-up used to characterize the emission from systems with QEs [30]

Consequently, the time correlator draws a histogram of the arrival periods of photon pairs which are proportional to the $g^2(\tau)$. Only a zero photons coincidence at τ equals zero proves that the QE acts as a single-photon source for both continuous and pulsed excitation as shown in Figure (1.15). This is true for different experimental environments i.e. temperature, coupling, etc. For every single excitation pulse, a single photon is emitted resulting in a zero value of $g^2(\tau)$ at $\tau = 0$. The pulse excitation rate should be longer than τ_R to prevent the overlapping of the generated photons by two consecutive pulses [25,29].

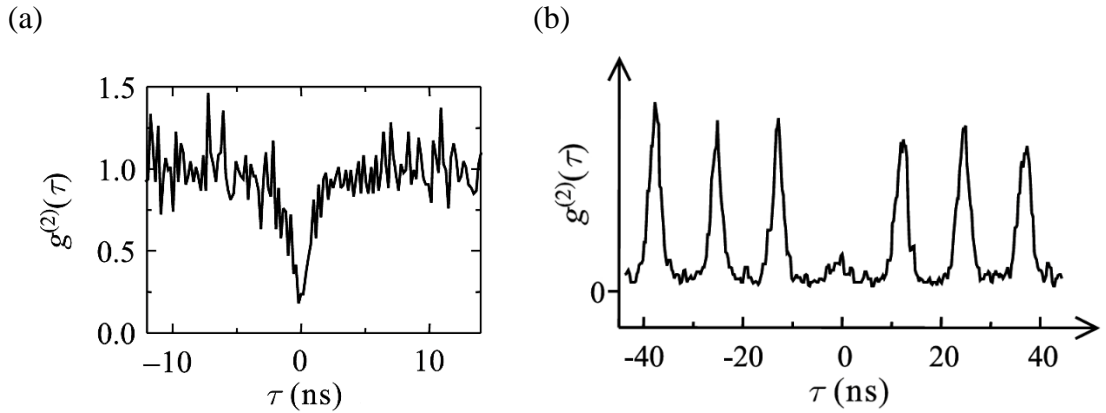


Figure 1.15: The time correlator's graph under (a) continuous, (b) pulsed excitation [29]

1.7. Types of Quantum Emitters

The most important types of single-photon emitters are a single atom, an ion, a single molecule, a quantum dot (QD), and a defect center in a diamond. A single atom or an ion demands a complicated experimental setup to produce them. On the other hand, the molecules suffer from fast bleaching. Moreover, QD or defect center in a diamond has a long lifetime. In this section, a brief introduction about QEs (QD and Defect center in diamond, specifically nitrogen-vacancy (NV) center, and silicon-vacancy (SiV) center) that are usually coupled to a PW is presented.

1.7.1. Quantum Dots

A 3D confinement of semiconductor structures by higher bandgap materials results in artificial atoms known as QDs, which radiate single photons [32–34]. The QD's size and structure specify the emission wavelength. The synthesis of the QDs could be achieved using several techniques, for example, chemical synthesis in a solution yields colloidal QDs [32]. The CdSe QD exhibited a blinking behavior, i.e. random switching between ON and OFF states under continuous excitation as shown in Figure (1.16.a). Moreover, the CdSe/CdS QDs measurements are shown in Figure (1.16. (b-e)) indicating that as the QD's size increases, the emission wavelength increases, too [32]. Other QDs suffer from bleaching, i.e. suppress their emission after a relatively long time of excitation.

(a)

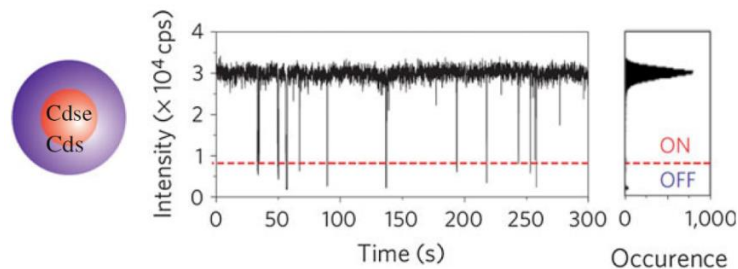


Figure 1.16: (a) A QD composed of a CdSe core with a CdS shell exhibited a blinking behavior of its emission at a core radius of 1.1 nm and 2.4 nm shell thickness. (b-e) The photoluminescence (red) and absorption (blue) curves for four different core radii of 1.35 nm, 1.7 nm, 2.2 nm, and 2.7 nm, respectively [32]

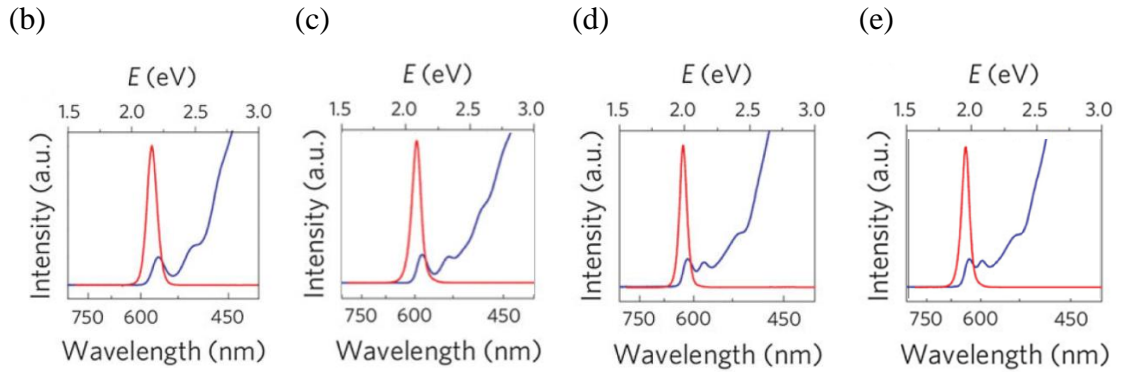


Figure 1.16: Continued.

Another QDs synthesis approach is by utilizing the lattice difference between the QD material and the substrate to form QDs islands. This synthesis approach is known as the Stranski-Krastanov approach [33]. The advantage of using colloidal QDs is that they can be positioned more easily within the PW than other types of semiconductor QDs [34,35]. Molecular beam epitaxy and lithography techniques could also be used to fabricate QDs.

1.7.2. Defect centers in diamonds

Among many types of defect centers in diamonds that act as perfect single-photon sources, the most popular two types are discussed briefly in the following subsections.

1.7.2.1. NV center

It is composed of an alternative nitrogen atom close to a vacancy as shown in the atomic structure presented in Figure (1.17.a). If the vacancy has a neutral charge, then it is named an NV^0 center, while if the vacancy is negatively charged then it is called an NV^- center. Both types are stable single-photon emitters at room temperature. The electronic structures for both NV^0 and NV^- centers are presented in Figure (1.17.b,c), respectively.

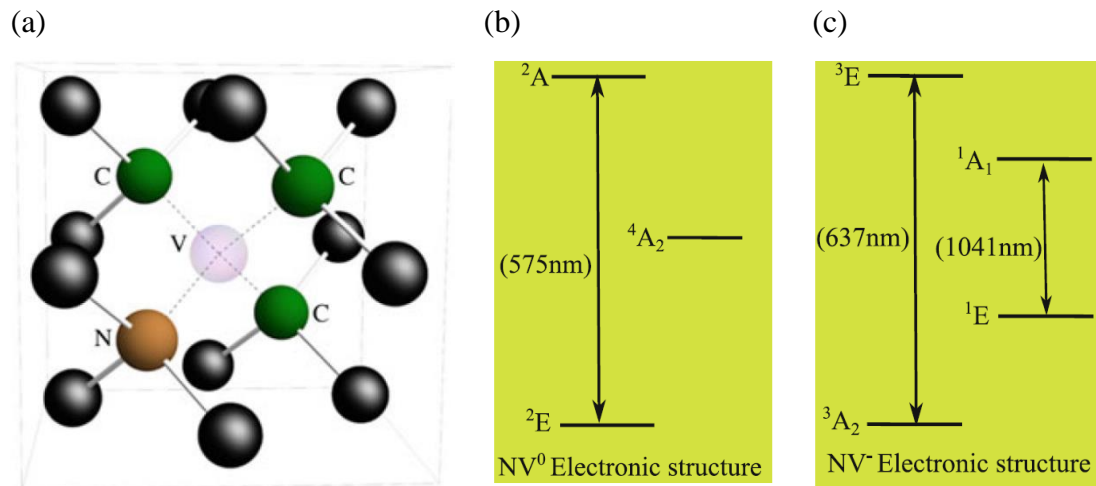


Figure 1.17: (a) NV-center's atomic structure, electronic structure for (b) NV^0 , and (c) NV^- [36]

The zero phonon lines are at 575 nm and 637 nm for NV^0 and NV^- , respectively. Several optical measurements at room temperature could be done before the decoherence of the NV^- center because of the long coherence time of its triplet ground level [36]. NV^- had been extensively used in quantum information, electric and magnetic field sensing, and temperature measurement research because of its stability and electronic structure properties [37–46]. Both NV^0 and NV^- centers have a disadvantage of a broadband emission over 100 nm because of phonons optical transitions as shown in their emission spectrum in Figure (1.18) [25]. The excited-state lifetime of the NV^- is around 11.6 ns in a bulk diamond and it changes considerably depending on the states' optical densities at the QE's site. Moreover, the quantum efficiency of the NV center embedded in a nanodiamond is smaller than that when embedded in a bulk diamond [47].

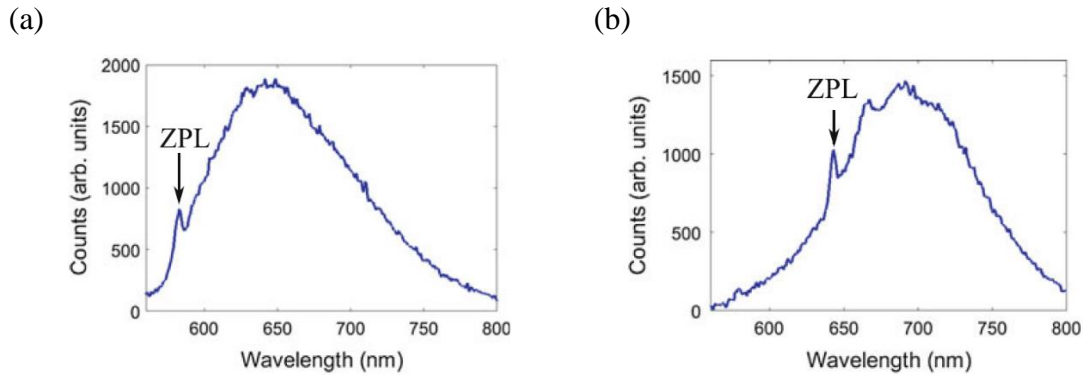


Figure 1.18: Emission spectra of an (a) NV^0 , (b) NV^- excited by a 532 nm laser [25]

The most popular QE among various color centers is the NV center due to its stability and efficient single-photon emission at room temperature [25]. The NV centers could be created by trapping a substitutional N atom and a vacancy at adjacent positions inside the diamond's lattice (Carbon (C) atoms). The synthetic diamond-type Ib, as shown in Figure (1.19) [48], was used to prepare the NV centers by homogeneously dispersing single N impurities. The neutron or electron irradiation creates further vacancies that could be diffused to nitrogen atoms after annealing the diamond sample at 900 C°. Creating more vacancies allows the observation of brighter luminescence from the diamond's sample [49].

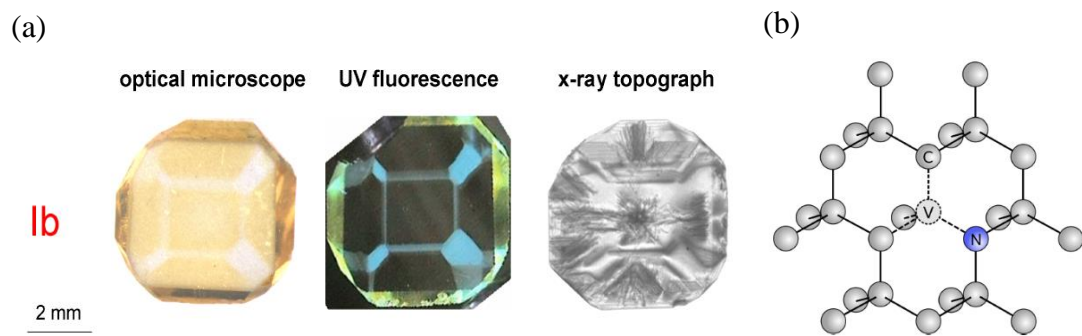


Figure 1.19: (a) The synthetic type IV diamond [48], (b) The microscopic NV center [50]

The high quantum efficiency and the short decay time of the excited state for the NV centers make them ideal for the generation of single photons [51]. Diamond samples were formed and pumped by a 532 nm ND: YVO₄ (diode-pumped) laser as shown in Figure (1.20) [52].

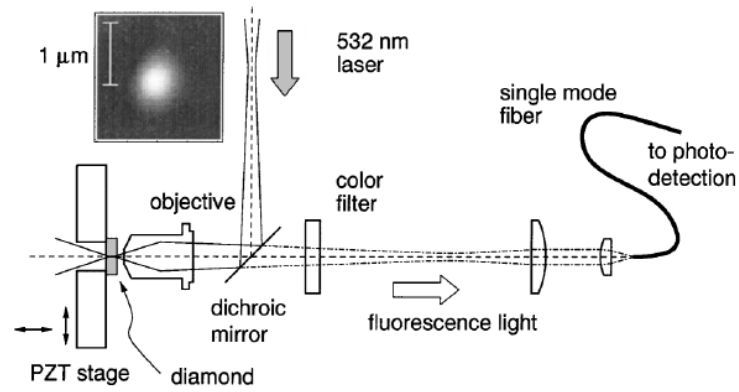


Figure 1.20: The experimental setup of pumping NV centers in a diamond performed in [52]

The fluorescence light was focused into single-photon avalanche detectors (SPADs) by a confocal microscope. The spectrum analysis of the fluorescence emission of the NV center is shown in Figure (1.21) [50].

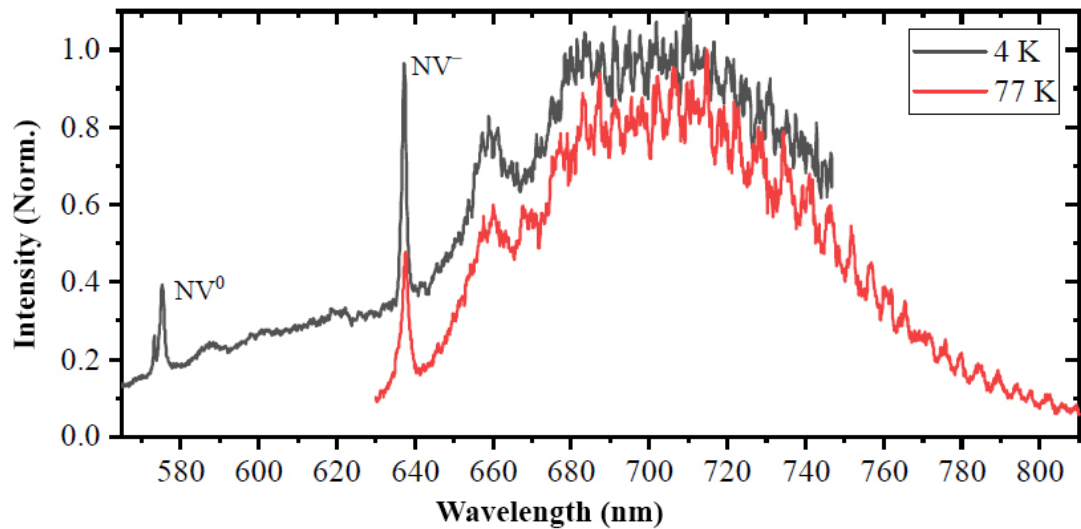


Figure 1.21: The fluorescence spectrum of the NV center [50]

The NV center could be formed in neutrally (NV^0) or negatively (NV^-) charged states. Both NV^0 and NV^- could be optically excited to emit single photons. The NV^0 is composed of free triple electrons from the relaxed bonds of the C atoms nearby the vacancy and double electrons from the N atoms. The NV^0 could accept an electron from a surrounding donor impurity to form an NV^- center. The zero phonon line (ZPL), which is the energy difference between the ground and excited states, of the NV^0 and NV^- are at 2.156 eV (575 nm) and 1.945 eV (637 nm), respectively. The NV center switches its state (NV^0 or NV^-) according to the excitation

wavelength. A 75% maximum steady-state population was obtained for the NV^- under excitation wavelength between 510 to 540 nm. Consequently, the NV^- is switched to NV^0 for 25% of the time under 532 nm excitation while red excitation converts the NV^- to an NV^0 state. The simplified energy transitions and levels for both (NV^0 and NV^-) are shown in Figure (1.22) [50].

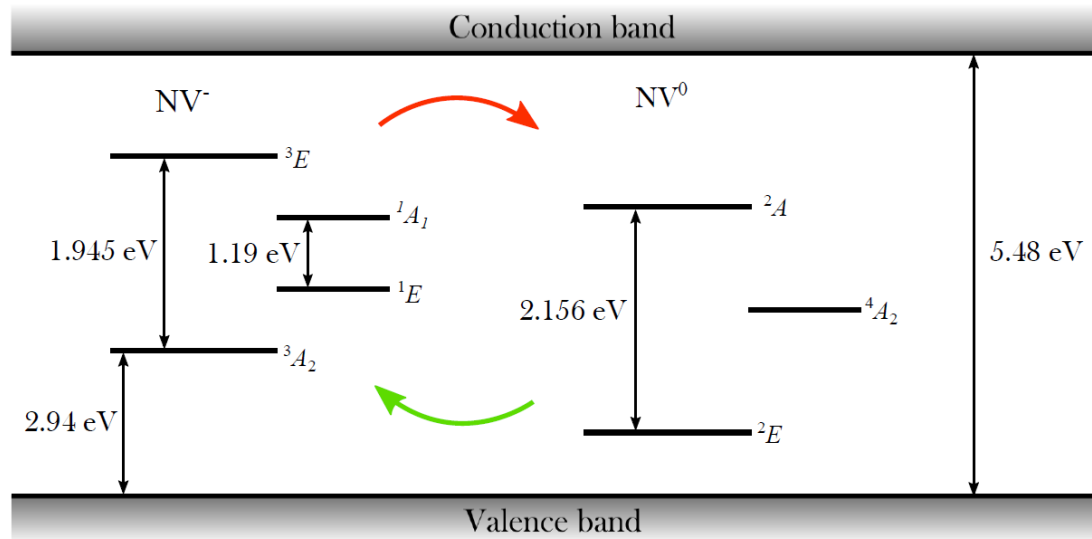


Figure 1.22: The simplified transitions and energy levels for both types of the NV center, Red and Green represent red and green excitation, respectively [50]

The diamond material has the largest energy bandgap (5.48 eV) compared to any other material and, hence, no free electrons occupy any energy level in this range. However, the N impurities in the diamond's lattice form discrete energy states within the diamond's bandgap. The three-level system of the uncoupled NV center is modeled as a ground-level, $|1\rangle$, an excited-level, $|2\rangle$, and a shelving level (because of its relatively long lifetime of 300 ns), $|3\rangle$ as shown in Figure (1.23) [52].

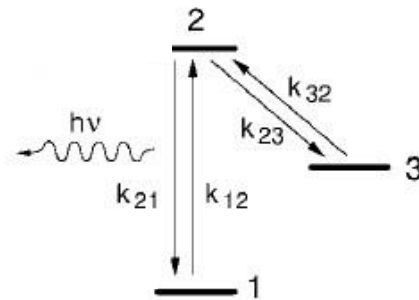


Figure 1.23: A three-level model for the emission dynamics of the NV center [52]

The NV⁻'s $|1\rangle$ is situated at 2.94 eV over the valence band and 2.54 eV under the conduction band. Also, the $|2\rangle$ is over the $|1\rangle$ by 1.945 eV as shown in Figure (1.22). After being optically excited, the NV's $|2\rangle$ radiatively coupled to the $|1\rangle$ with a single-photon emission as shown in Figure (1.23). However, the NV's $|2\rangle$ could be non radiatively coupled to $|3\rangle$. The $|2\rangle$ (3E) and the $|1\rangle$ (3A_2) states are split into three sub-level, i.e. spin-triplet states. One of the sub-levels has a zero spin quantum number ($m_s = 0$) while the other two have almost degenerate levels with m_s of +1 and -1. Without any external magnetic field (B), the 0 and ± 1 levels are split by $5.9 \mu\text{eV}$ and $12 \mu\text{eV}$ in the $|2\rangle$ and $|1\rangle$ states, respectively. If any external magnetic field is applied, the splitting between 0 and ± 1 levels increases by a factor of $2\gamma_e B$ according to the Zeeman effect, where γ_e is the gyromagnetic ratio of electrons, as shown in Figure (1.24) [50].

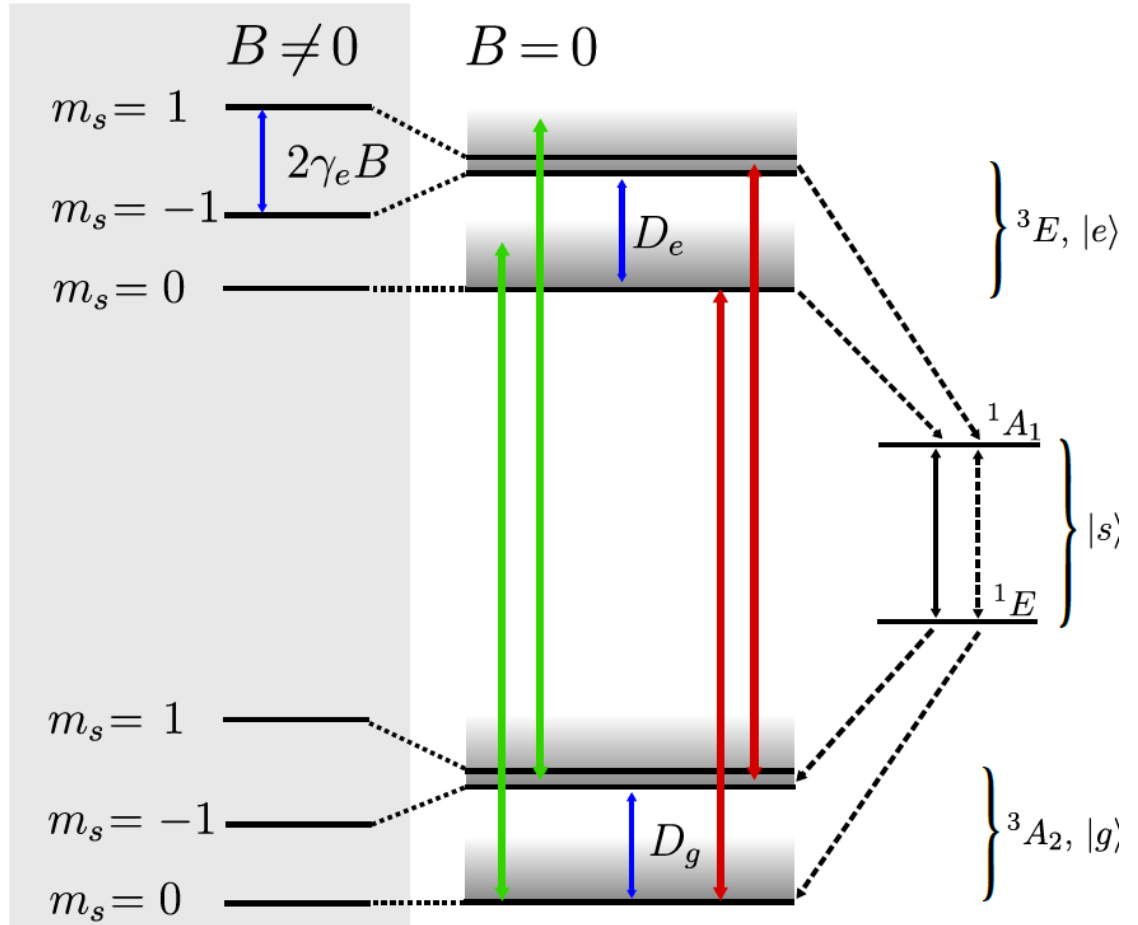


Figure 1.24: The detailed energy levels schematic for NV center [50]

The $|3\rangle$ has $m_s = 0$ and it is a spin-singlet level with two sublevels 1E and 1A_1 . The green arrows represent an off-resonant excitation to vibrational states. The red and black arrows represent spin-conserving transitions (radiative transitions), while the dashed black arrows represent non-conserving spin transitions (nonradiative transitions). The radiative emission in the singlet-state could be mitigated from the radiative emission in spin-triplet states by external optical filters[50]. A resonant excitation occurs by absorbing energy larger than or similar to 1.945 eV (637 nm). However, most of the excitation sources utilize a 532 nm (2.3 eV) laser source (off-resonance excitation) as shown in Figure (1.20). The fluorescence spectrum of the NV center under 532 nm laser excitation is shown in Figure (1.21). The fluorescence spectrum had a ZPL at 637 nm and a wide phonon sideband (PSB) with a peak at 700 nm and broadened over 600 to 800 nm. Under 532 nm laser excitation, the electron is excited to the vibrational level of $|2\rangle$. Then, it relaxed to the ground level of the vibrational state $|2\rangle$ at a timescale of ps. The transition from the vibrational ground state of $|2\rangle$ corresponds to the ZPL. The PSB occurred because the system (lattice structure) can simultaneously absorb (gain energy) and excite (lose energy) vibrational lattice modes known as phonons. Figure (1.21) showed wider phonon excitation because the PSB has lower energy than ZPL. The limitation of using the NV center as a single-photon source is its narrow ZPL of about 3-5% of the total fluorescence spectrum. However, the ZPL could be enhanced by coupling the NV⁻ center to nanophotonic structures. If $|2\rangle$ has $m_s = 0$, it radiatively decays to the $|1\rangle$ at $m_s = 0$ in about 12 ns. However, if the $|2\rangle$ has $m_s = \pm 1$ then it decays to the $|1\rangle$ that has $m_s = \pm 1$ although the decay has an increased probability to occur through the singlet state compared to the triplet state with $m_s = 0$. Consequently, the fluorescence intensity is spin-state-dependent, i.e. brighter emission for $m_s = 0$ than that of $m_s = \pm 1$ [50].

Figure (1.25) shows the fluorescence counts against the excitation power for the NV⁻ center. The background fluorescence (grey line) increased linearly with excitation power while the NV⁻ center's intensity (dashed line) was saturated with 3.6 E9 W/m^2 saturation intensity for a 1.3 mW excitation power. The solid line represented the total fluorescence contribution from the NV⁻ center and the background emission [52].

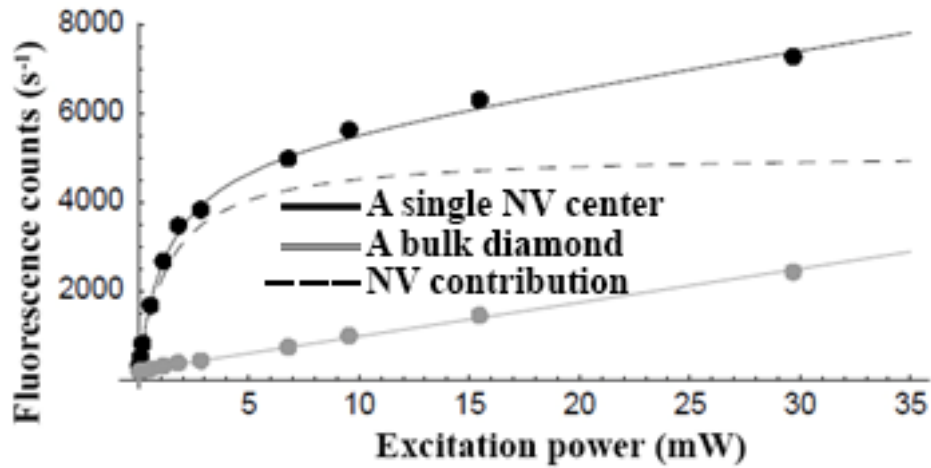


Figure 1.25: The fluorescence counts against the excitation power for the single NV center [52]

1.7.2.2. SiV center

It is composed of a SiV center situated between two removed closely carbon atoms as shown in Figure (1.26.a) [53]. The SiV defect could be neutrally or negatively charged with an emission wavelength of 946 nm or 737 nm, respectively [54]. However, the SiV⁰ did not perform as a single-photon source, yet [25]. The electronic structure of the SiV⁻ is presented in Figure (1.26.b). Figure (1.27) shows the emission spectra of the SiV⁻ at different operating temperatures excited by a 671 nm laser. The spectra show that as the temperature increases, the emission spectrum widened [55]. The major advantage of SiV⁻ is that 70% or more of its emission is at the ZPL [55]. Moreover, the SiV⁻ emitted indistinguishable photons that are important in quantum communication networks [56,57]. The major limitation of SiV⁻ is its low quantum efficiency [58].

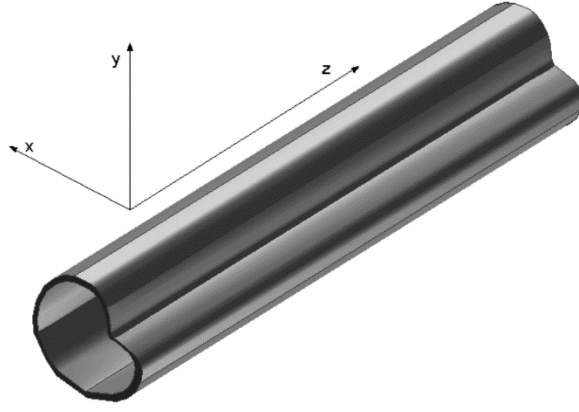


Figure 1.28: A waveguide with random and uniform cross-section along the direction of propagation [54]

The time-harmonic propagating fields in the z -direction are independent of the transversal coordinates x - and y - axes inside the medium that has a certain ϵ and μ . Such fields are represented by the factor [54]

$$e^{i\omega t} e^{-\gamma z} = e^{\alpha z} e^{i(\omega t - \beta z)}, \quad (1.28)$$

where γ is the propagation factor and equals [54]

$$\gamma = \alpha + i\beta, \quad (1.29)$$

where α is the attenuation constant (Neper/meter) and β is the phase constant (rad/m). For example, the electric field component, which is a part of the total electromagnetic wave, propagating in such a waveguide could be represented as [54]

$$\vec{E}(x, y, z, t) = \vec{E}(x, y, z) e^{i\omega t} = \vec{E}(x, y) e^{i\omega t - \gamma z}, \quad (1.30)$$

with $\vec{E}(x, y)$ changes with the transversal x - and y - coordinates, only. The electromagnetic wave equation is derived by implementing the curl operator to both sides of Equation (1.1.a) and substituting Equation (1.1.b) in the resultant expression, assuming zero current flow in the propagation direction ($\vec{J} = 0$, $\rho_v = 0$), to get [60]

$$\nabla \times \nabla \times \vec{E} = -\mu_0 \frac{\partial^2 \vec{D}}{\partial t^2}, \quad (1.31)$$

By using Equation (1.1.c) and the identities shown in Equations (1.32.a) and (1.32.b), the wave equation could be written as shown in Equation (1.33).

$$\nabla \times \nabla \times \vec{E} \equiv \nabla(\nabla \cdot \vec{E}) - \nabla^2 \vec{E}, \quad (1.32. a)$$

$$\nabla \cdot (\epsilon \vec{E}) \equiv \vec{E} \cdot \nabla \epsilon + \epsilon \nabla \cdot \vec{E}, \quad (1.32. b)$$

$$\nabla \left(-\frac{\vec{E} \cdot \nabla \epsilon}{\epsilon} \right) - \nabla^2 \vec{E} = -\mu_o \epsilon \frac{\partial^2 \vec{E}}{\partial t^2}, \quad (1.33)$$

It is assumed that the field (light) is propagating in a homogeneous (constant refractive index (n)) medium. Hence, the term $\nabla \epsilon = 0$, since $n = \sqrt{\epsilon}$. Consequently, Equation (1.33) is reduced to

$$\nabla^2 \vec{E} - \frac{\epsilon}{c^2} \frac{\partial^2 \vec{E}}{\partial t^2} = 0, \quad (1.34)$$

where

$$c = \frac{1}{\sqrt{\epsilon_o \mu_o}}, \quad (1.35)$$

From Equation (1.30), it is clear that

$$\frac{\partial}{\partial t} = i\omega, \quad (1.36. a)$$

$$\frac{\partial}{\partial z} = -\gamma, \quad (1.36. b)$$

Hence, Equation (1.34) is reduced to

$$\nabla^2 \vec{E} + k^2 \vec{E} = 0, \quad (1.37)$$

Equation (1.37) is known as the Helmholtz equation. Similarly, if the propagating wave is composed of a magnetic field only, hence, the Helmholtz equation could be written as

$$\nabla^2 \vec{H} + k^2 \vec{H} = 0, \quad (1.38)$$

where $k = (\omega/v)$ is the wavenumber (m^{-1}) and v ($1/\sqrt{\epsilon\mu}$) is the electromagnetic wave's velocity (m/s).

The Laplacian operator ∇^2 is expanded in the cartesian coordinate system as [54]

$$\nabla^2 = \frac{\partial^2}{\partial x^2} + \frac{\partial^2}{\partial y^2} + \frac{\partial^2}{\partial z^2}, \quad (1.39)$$

By applying the Laplacian operator on Equation (1.30) and substituting in Equation (1.37), Helmholtz's equation for the electric field could be written as

$$\frac{\partial \vec{E}^2}{\partial x^2} + \frac{\partial \vec{E}^2}{\partial y^2} + (\gamma^2 + k^2)\vec{E} = 0, \quad (1.40. a)$$

$$\nabla_{x,y}^2 \vec{E} + h^2 \vec{E} = 0, \quad (1.40. b)$$

where

$$h^2 = (\gamma^2 + k^2), \quad (1.41)$$

The electromagnetic (light) wave is composed of both electric and magnetic fields. Hence, Equations (1.5.a) and (1.5.b) constitute a set of six partial differential equations for the electric and magnetic fields as shown in Equation (1.42).

$$\frac{\partial E_z}{\partial y} + \gamma E_y = -i\omega\mu H_x, \quad (1.42. a)$$

$$-\gamma E_x - \frac{\partial E_z}{\partial x} = -i\omega\mu H_y, \quad (1.42. b)$$

$$\frac{\partial E_x}{\partial y} - \frac{\partial E_y}{\partial x} = -i\omega\mu H_z, \quad (1.42. c)$$

$$\frac{\partial H_z}{\partial y} + \gamma H_y = i\omega\epsilon E_x, \quad (1.42. d)$$

$$-\gamma H_x - \frac{\partial H_z}{\partial x} = i\omega\epsilon E_y, \quad (1.42. e)$$

$$\frac{\partial H_y}{\partial x} - \frac{\partial H_x}{\partial y} = i\omega\epsilon E_z, \quad (1.42. f)$$

By multiplying Equation (1.42.a) with the factor $i\omega\epsilon$ and Equation (1.42.e) by the factor γ , these equations could be written as

$$i\omega\epsilon \frac{\partial E_z}{\partial y} + i\omega\epsilon\gamma E_y = \omega^2\mu\epsilon H_x \quad (1.43. a)$$

$$-\gamma^2 H_x - \gamma \frac{\partial H_z}{\partial x} = i\omega\epsilon\gamma E_y \quad (1.43. b)$$

By substituting Equations (1.41) and (1.43.b) into Equation (1.43.a) and simplifying the result, the x-component of the magnetic field could be written as

$$H_x = \frac{-1}{h^2} \left(\gamma \frac{\partial H_z}{\partial x} - i\omega\epsilon \frac{\partial E_z}{\partial y} \right), \quad (1.44)$$

Furthermore, by multiplying Equation (1.42.a) by the factor γ and Equation (1.42.e) by the factor $-i\omega\mu$, these equations could be written as

$$-i\omega\mu\gamma H_x - i\omega\mu \frac{\partial H_z}{\partial x} = -\omega^2\epsilon\mu E_y, \quad (1.45. a)$$

$$\gamma^2 E_y + \gamma \frac{\partial E_z}{\partial y} = -i\omega\mu\gamma H_x, \quad (1.45. b)$$

By substituting Equations (1.41) and (1.45.b) into Equation (1.45.a) and simplifying the result, the y-component of the electric field could be written as

$$E_y = \frac{-1}{h^2} \left(\gamma \frac{\partial E_z}{\partial y} - i\omega\mu \frac{\partial H_z}{\partial x} \right), \quad (1.46)$$

The x- and y- components of the electric field intensity and the magnetic field intensity, respectively, could be determined by implementing the same steps on Equation (1.42.b) and Equation (1.42.d) to get

$$E_x = \frac{-1}{h^2} \left(\gamma \frac{\partial E_z}{\partial x} + i\omega\mu \frac{\partial H_z}{\partial y} \right), \quad (1.47)$$

$$H_y = \frac{-1}{h^2} \left(\gamma \frac{\partial H_z}{\partial y} + i\omega\epsilon \frac{\partial E_z}{\partial x} \right), \quad (1.48)$$

Consequently, all electromagnetic field components could be solved by analyzing Helmholtz's equations (Equation (1.40)) for the longitudinal components and Equations ((1.44), (1.46), (1.47), and (1.48)) for the transversal components. Accordingly, the electromagnetic wave could be classified into three types according to its z-component as [60]

1. A transverse electric (TE) wave that has no electric field in the z-direction.
2. A transverse magnetic (TM) wave that has no magnetic field in the z-direction.
3. A transverse electromagnetic (TEM) wave that has no electric and magnetic field components in the z-direction.

1.9. Surface plasmon polaritons (SPPs)

Metals have free electrons that define their interaction with EM fields at near-infrared and optical frequencies. The free electrons exhibit a 180° out of phase oscillation to the applied optical fields and result in a negative dielectric constant. The free electrons are described by the Drude model as a plasma, i.e. a gas that contains negatively charged particles that move against the corresponding positive ion cores. The quantization of the plasma oscillations is known as a plasmon. The corresponding dielectric constant as a function of ω was derived as [60]

$$\epsilon(\omega) = 1 - \frac{\omega_p^2}{\omega^2 + i\gamma\omega}, \quad (1.49)$$

where ω_p is the plasma frequency (rad/s), and γ is the damping term (collision frequency) measured in (rad/s). Both parameters depend on the material and were measured for many noble metals [61]. At the metal-dielectric boundary, the coupling of the plasmons with EM fields results in SPPs. The coupling results from the approximate matching of the wavevectors and frequencies for both plasmons and the EM field. By utilizing the boundary conditions at the interface, the material's parameters ($\epsilon(\omega)$), and Maxwell's equations, the SPPs can be proved to exist as a confined EM surface wave at the metal-dielectric boundary as shown in Figure (1.29) [62].

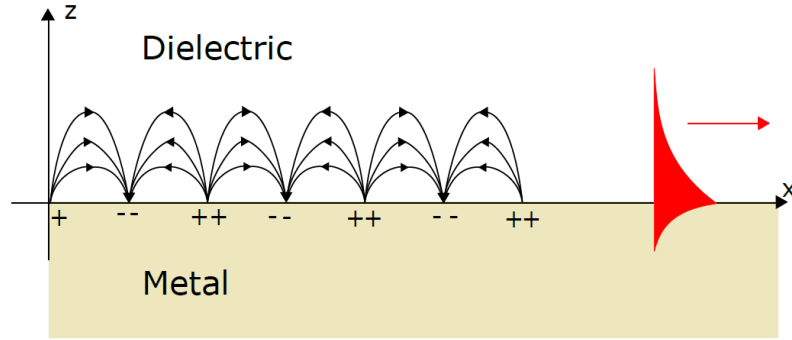


Figure 1.29: SPPs propagating at a metal-dielectric boundary [62]

By assuming that the propagating field in the x-direction has a harmonic time-dependence of the following form [63]

$$\vec{E}(\vec{r}, t) = \vec{E}(\vec{r})e^{ik_x x}e^{-i\omega t}, \quad (1.50)$$

Hence, the corresponding Helmholtz's equation is reduced to

$$\frac{\partial^2 \vec{E}(z)}{\partial z^2} + (k_0^2 \epsilon - k^2) \vec{E} = 0, \quad (1.51.a)$$

$$\frac{\partial^2 \vec{H}(z)}{\partial z^2} + (k_0^2 \epsilon - k^2) \vec{H} = 0, \quad (1.51.b)$$

By substituting Equation (1.50) in Equations (1.1.a) and (1.1.b) and considering a y-direction field invariance ($\frac{\partial}{\partial y} = 0$) with $\frac{\partial}{\partial x} = ik$ and $\frac{\partial}{\partial t} = -i\omega$, are valid, the corresponding TM field equations are

$$E_x = \frac{-i}{\omega\epsilon_0\epsilon} \frac{\partial H_y}{\partial z}, \quad (1.52. a)$$

$$E_z = \frac{-k}{\omega\epsilon_0\epsilon} H_y, \quad (1.52. b)$$

$$\frac{\partial^2 H_y}{\partial z^2} + (k_0^2\epsilon - k^2)H_y = 0, \quad (1.52. c)$$

and the TE field equations could be expressed as

$$H_x = \frac{i}{\omega\mu_0} \frac{\partial E_y}{\partial z}, \quad (1.53. a)$$

$$H_z = \frac{k}{\omega\mu_0} E_y, \quad (1.53. b)$$

$$\frac{\partial^2 E_y}{\partial z^2} + (k_0^2\epsilon - k^2)E_y = 0, \quad (1.53. c)$$

For the TM case, the solution of Equation (1.52) yields [60]

$$H_y(z) = A_d e^{ikx} e^{-k_d z} \quad (1.54. a)$$

$$E_x(z) = \frac{iA_d k_d}{\omega\epsilon_0\epsilon_d} e^{ikx} e^{-k_d z}, \quad (1.54. b)$$

$$E_z(z) = \frac{-A_d k}{\omega\epsilon_0\epsilon_d} e^{ikx} e^{-k_d z}, \quad (1.54. c)$$

In the dielectric region, and

$$H_y(z) = A_m e^{ikx} e^{k_m z}, \quad (1.55. a)$$

$$E_x(z) = \frac{-iA_m k_m}{\omega\epsilon_0\epsilon_m} e^{ikx} e^{k_m z}, \quad (1.55. b)$$

$$E_z(z) = \frac{-A_m k}{\omega\epsilon_0\epsilon_m} e^{ikx} e^{k_m z}, \quad (1.55. c)$$

In the metal region. The $z = (k_m)^{-1}$ (m) and $z = (k_d)^{-1}$ (m) are the field's evanescent normal decay length in the metal and dielectric regions,

respectively, which quantify the field's confinement. The boundary conditions at the interface require that the electric flux densities and the magnetic field intensities should follow [62]

$$(\vec{D}_m - \vec{D}_d) \cdot \vec{n} = 0, \quad (1.56.a)$$

$$(\vec{B}_m - \vec{B}_d) \cdot \vec{n} = 0, \quad (1.56.b)$$

Hence, H_y and $\epsilon_{m,d}E_z$ should be continuous at the interface implying that $A_m = A_d$. Hence,

$$\frac{k_m}{k_d} = \frac{-\epsilon_m}{\epsilon_d}, \quad (1.57)$$

Consequently, the confinement of the SPPs requires opposite signs for the dielectric constants at the boundary and this could be achieved at a metal-dielectric boundary, only. The H_y expressions in Equations (1.54.a) and (1.55.a) should satisfy Equation (1.51.b) in both regions. Hence,

$$k_m^2 = \beta^2 - k_o^2 \epsilon_m, \quad (1.58.a)$$

$$k_d^2 = \beta^2 - k_o^2 \epsilon_d, \quad (1.58.b)$$

By plugging Equation (1.58) into Equation (1.57), the propagating SPPs dispersion relation at the boundary yield

$$\beta = k_o \sqrt{\frac{\epsilon_m \epsilon_d}{\epsilon_m + \epsilon_d}}, \quad (1.59)$$

For a TE case, the continuity conditions of E_y and H_z at the boundary results in

$$A_m(k_m + k_d) = 0 \quad (1.60)$$

Since both k_m and k_d are positive at the interface, this implies that $A_m = A_d = 0$. Hence, the SPPs could exist only with TM polarization. Figure (1.30) shows the dispersion curves plotted by Equation (1.51) for an ideal

metal (i.e, $\gamma = 0$) bounded by air ($\epsilon_d = 1$) or silica ($\epsilon_d = 2.25$) dielectrics [60].

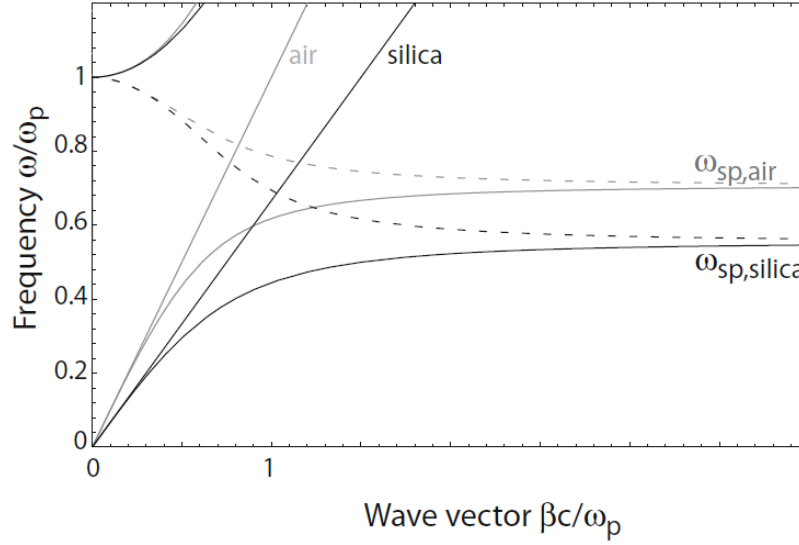


Figure 1.30: SPPs dispersion relation at the ideal metal-air and metal-silica interfaces [60]

The dispersion's curve section with high values of the wave vector (at the right side of the light's line) corresponds to the SPPs excitations because of their bound behavior. By substituting Equation (1.41) into Equation (1.51), the SPP frequency could be derived as [60]

$$\omega_{sp} = \frac{\omega_p}{\sqrt{1 + \omega_d}} \quad (1.61)$$

At the SPPs's frequency, the β is ∞ and, hence, the group velocity ($v_g = \partial\omega/\partial\beta$) is zero, and the mode shows a static behavior known as surface plasmons. Furthermore, the phase-matching techniques, such as prisms and grating couplers, should be utilized to excite SPPs by 3D waves. When the frequency is higher than the plasma frequency, then transparency is achieved and radiation into metal occurs. Between the radiative and bound modes, a pure imaginary β region exists that suppresses the propagation of the mode. Moreover, the Sommerfeld-Zenneck SPP modes are defined in the range of lower than mid-infrared frequency range. It is worth mentioning that $\gamma \neq 0$ for real metal. Hence, the ϵ_m and β are complex and the propagating SPPs exhibit an attenuation (propagation) length calculated as $L_{eff} = 1/(2\text{Im}(\beta))$.

1.10. Literature survey

This section summarizes the related work in the literature on the single-photon sources based on weak coherent pulses (WCP) and HPWs, and the grating couplers (GCs). In addition, Appendix (A) graphically summarizes each presented structure.

The single-photon source is one of the main building blocks in any quantum cryptography system performing a certain encryption protocol such as the BB84 protocol [64,65]. Experimentally, the generation of weak coherent pulses (WCP) mimics the behavior of single-photon pulses [66,67]. However, the probability of generating multi-photon in WCP results in leakage of information, decrement in the transmission rate, and reduction in the security of the system [68]. Therefore, highly efficient quantum key distribution (QKD) systems prefer the utilization of a truly efficient single-photon source instead of WCP [8]. Nowadays, the use of quantum photonic circuits enables the implementation of complex quantum algorithms, miniaturizing of the transmitter circuits, and routing and processing of the transmitted photons [69].

Recently, the most efficient single-photon sources with pure single-photon emission used different types of QEs including quantum dots [70,71], defect centers in diamonds [72,73], and molecules [74,75]. The integration possibility of the single-photon sources on silicon chips urged the use of “plug and play” single-photon sources in QKD transmitters. In the QKD transmitter, the coupling techniques between the waveguide mode and the optical fiber are used to simplify the alignment and extract the single-photon efficiently for free-space transmission [76].

The spontaneous emission rate of on-chip QEs can be changed by varying the QE environment via the Purcell effect [77]. Many recent published works simulated the enhancement of the Purcell factor as well as

the enhancement of the radiative emission coupling efficiency (β -factor) by coupling the QE emission to a PW due to the high confinement of its fundamental propagation mode.

For example, Siampour et al. (2017) proposed an on-chip single-photon source and achieved a 42-fold enhancement of the spontaneous emission for a nitrogen-vacancy (NV) coupled to a dielectric-loaded surface plasmon polariton (DLSPP) waveguide with β equals 63% [78].

Furthermore, Kumar et al. (2019) obtained a 37 total decay rate enhancement and β -factor of 87% when they coupled quantum dots emission to the proposed HPW for on-chip single-photon applications [79].

A recent work by Siampour et al. (2020) achieved an outstanding performance of 10-fold Purcell enhancement for a germanium vacancy (GeV) center and 12-fold Purcell enhancement for an NV center coupled to their proposed DLSPP waveguide structure, which can also act as an efficient on-chip single-photon source for QKD systems [80]. The polarization of the output light for the aforementioned single-photon emitters follows the excited propagation mode of the waveguide, which is, typically, the fundamental TM mode.

On another hand, T. Heindel et al. (2020) proposed an on-chip QKD system where the extracted photons from the single-photon source demand polarizers and half-lambda waveplates to prepare polarized photons at 0° , 45° /- 45° , and 90° at the transmitter side [81].

However, the drawback of using a polarizer stage is the reduction of QKD system efficiency by at least 50% [82]. Several published on-chip polarizers aimed to absorb or reflect the unwanted polarization component of unpolarized incident electromagnetic (EM) wave at C-band (1550 nm) to obtain a specific polarization at the output [83,84].

Another approach by **M. Mojahedi et al. (2012, 2013)** rotated the polarization of the polarized incident EM wave at the C-band to get a specific polarization of the emission at the output [85,86].

In addition, the novel polarization rotators with high coupling efficiency proposed by **M. Qi et al. (2015)** [87,88] encouraged the utilization of their technique to control the emitted photon's polarization from a QE coupled to an HPW.

The HPW exhibited outstanding performance in terms of subwavelength confinement of the propagating light along with ultra-low propagation losses that allow long-range propagation of the light [89–91]. Therefore, the following chapters investigate the coupling of the QE into an HPW structure. However, two main issues should be exhaustively elaborated, which are proving the single-photon emission from the QE before and after the coupling to an HPW and extracting the single photons from the HPW.

Several design strategies had been proposed to design a polarization-independent GC. For example, **H.K. Tsang (2011) et al.** suggested tuning the fill factor and the grating period in the x and y directions. They achieved a 64% polarization-independent CE in their proposed 2D GC proposed simulated by the 2D finite-difference time-domain (FDTD)[92]. The tuning equalized the different effective indices for TE and TM transmitted light in a 340 nm Si waveguide for maximum CE at the operation wavelength.

Another approach by **P. Cheben et al. (2012)** simulated with FDTD tool to decrease the difference in the effective index for TE and TM polarization [93]. They suggested and numerically proved that the increase of the Si channel thickness decreased the difference in the effective indices for TE and TM transmitted light and, consequently, a dual-polarization CE of 52.5% was achieved.

Moreover, a different complicated design strategy proposed by **F. Luan et al. (2012)** resulted in a simulated CE of 60% for dual output polarization. They suggested corrugating the top and bottom surfaces of the 370 nm Si waveguide embedded in silicon oxide (SiO_2) to form the 1D TE and TM grating periods. The tuning of the etch depths of the TE and TM gratings in the top and bottom of the Si channel resulted in a common maximum CE for both polarization cases. Despite the outstanding design and numerical performance, the sophisticated photonic structures found difficulties in the experimental fabrication[94].

Another design strategy by **F.R. Libsch et al. (2015)** [95] simulated a CE of 20% for TE and TM light polarization. Their strategy was based on the geometrical union or intersection for the designed TE and TM 1D grating periods in a 220 nm Si waveguide. Although this outstanding approach solved the grating's polarization dependency, however, it results in a nonuniform gratings (apodized) periodicity with thin grooves or summits in the Si waveguide. Consequently, the apodization of the GCs adds to the complexity of the fabrication when it is desired to use this approach in other different wavelengths since smaller operating wavelengths result in thinner grating grooves or summits.

A recent study by **S. Chang et al. (2015)** on a 400 nm thick silicon waveguide channel aimed to design a subwavelength 1D polarization-independent GC [96]. Their approach was based on the equalization of the effective refractive indices for TE and TM modes and a simulated CE of 50% for dual output polarization was obtained. The same approach was performed on a 460 nm thick silicon waveguide and a simulated CE of 60% was achieved [97].

A recent approach by **W.N. Ye et al. (2019)** utilized a 220 nm Si waveguide channel to design a dual-polarization 1D GC [98]. This approach deposited secondary subwavelength gratings in the lower index region of the

primary grating, whereas the high index region of the primary grating was filled with Si completely. By optimizing the filling factors and grating periods for both the primary and secondary gratings, a maximum CE of 32.5% was simulated for both TE and TM modes.

Finally, a 2D subwavelength GC based on a 220 nm Si waveguide was recently proposed by **W.N. Ye et al. (2020)** [99]. Their new approach modified the etch depths, grating periods, and fill factors of the gratings in 2D to achieve a shared effective index of the grating for TE and TM modes and in dual operation wavelengths of 1330 nm and 1550 nm. They simulated a maximum CE of 35.5% for both polarization cases and efficiently acted as a wavelength demultiplexer.

All the aforementioned highly informative publications operated at C-band or O-band wavelengths. Recently emerged nanophotonic applications urged the need for polarization-independent GCs at different wavelengths. For example, the single-photon emitter embedded in a DLSP or hybrid plasmonic waveguide [73] requires a polarization-insensitive GC to support the emission of photons with different output polarization. This is important in designing on-chip quantum key distribution systems based on polarization-dependent protocols such as the BB84 protocol. The on-chip BB84 protocol requires the GC to support the emission of four states of polarization, which are 0° , 45° , -45° , and 90° [100,101].

1.11. Aim of the thesis

This thesis aims to design and numerically analyze a miniaturized plasmonic chip-integrated transmitter with a single-photon source for a quantum cryptography system with a specified output polarization to be used in QKD systems based on BB84 protocol or other polarization-dependent protocols. The aim is achieved by realizing the three important design steps in the diagram shown in Figure (1.31).

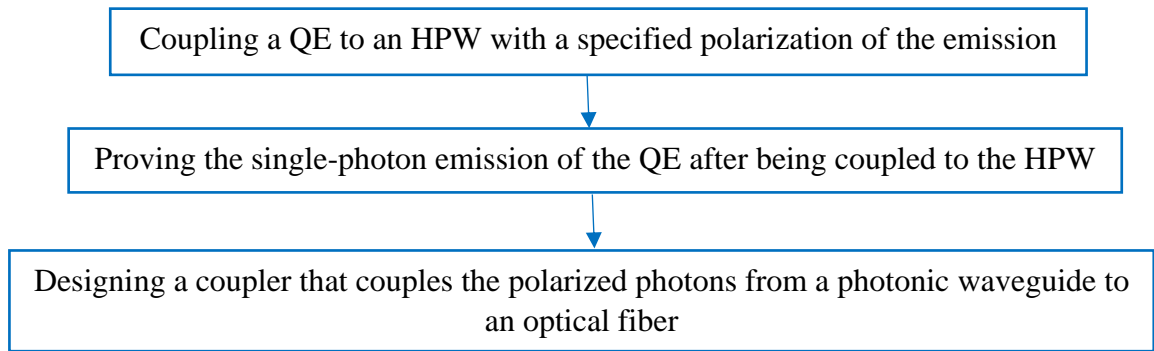


Figure 1.31: Aim of the thesis diagram

Firstly, the attempt to obtain polarized output photons by coupling the QE to an HPW is demonstrated. The HPW is based on a 150 nm GaP waveguide, HSQ dielectric, and an Al metal.

Secondly, it is important to predict the emission behavior of the QE and the effects of the QE's environment on the emission characteristics before the experimental fabrication. The presented work aims to develop a theoretical model to calculate $g^{(2)}(\tau)$ before and after coupling the QE to a nanostructure.

Finally, a novel and simple approach is proposed to design a compact four-state polarization-independent GC based on a double-layer approach utilizing a 150 nm GaP waveguide.

1.12. The layout of the thesis

This thesis is divided into five chapters.

Chapter One gives a general introduction to the properties of the integrated optical circuits, computational nanophotonics softwares that are used to simulate the integrated optical circuits, the electrodynamics principle that the simulation softwares rely on, i.e., solving Maxwell's equations, the coupling theory of the QE to a nanostructure, photon statistics principles, several types of QEs, waveguide propagation principles to determine the directions of polarization inside the waveguide, SPPs physical origin, literature survey including recent relative publications, and, finally, the aim of this thesis.

Chapter Two presents a comprehensive analysis and detailed performance investigation for an HPW with embedded QE. The reasons for choosing the dimensions and the materials used. Moreover, the Purcell enhancement factor and tuning the output polarization for 0° , 90° , 45° , and -45° output polarization cases are demonstrated.

Chapter Three gives a comprehensive investigation of the numerical techniques required to prove the single-photon emission from any type of QE after being coupled to any nanostructure including a PW. Both the two- and three-level models of the QE are included in this chapter.

Chapter Four demonstrates the detailed steps of design and comprehensive numerical verification of a novel integrated GC that supports four output polarization cases, which are 0° , 90° , 45° , and -45° . Two other techniques for designing polarization-independent GCs are also presented in this chapter.

Chapter Five presents the main conclusions obtained from this study and suggestions for future work.

Chapter Two

Polarization control of a QE coupled with an HPW

Chapter 2

Polarization control of a QE coupled with an HPW

2.1. Introduction

This chapter presents the detailed steps of analysis and a comprehensive investigation of a miniaturized four HPWs with an embedded QE to emit a stream of photons. Each HPW has a unique output polarization of either 0° , 90° , 45° , or -45° . The QE emits photons at a wavelength of 700 nm, which is the general emission wavelength of most QEs.

The findings of the proposed work could be used as a guideline to design a plasmonic chip-integrated single-photon source with a specified output polarization for any type of QEs. The detailed steps of analysis and the comprehensive investigation procedures for the proposed HPW are as follows:

1. Selecting the suitable materials and the optimum geometrical dimensions that support the propagation of the photons at the QE's emission wavelength.
2. Selecting the polarization control technique for the HPW, QE's orientation, and the mechanism that forces the output photons to be in 0° , 90° , 45° , and -45° polarization states in each HPW.
3. Calculating the spontaneous emission enhancement (Purcell) factor of the QE after being coupled to the proposed HPW for each case of output polarization (for each HPW).
4. Tuning of the output polarization to achieve an accurate output polarization degree.

COMSOL Multiphysics and MB-Ruler softwares were used to perform the aforementioned steps of analysis. Moreover, the spatial origin for all simulations in this chapter is $(-25, 0, z)$ nm.

2.2. The proposed HPW

In general, the HPW at telecommunication wavelengths (1.3 or 1.55) μm is composed of a thin dielectric spacer of low refractive index (silica (SiO_2)) that separates a high refractive index medium (silicon (Si)) from a metal conductor (gold (Au) or silver (Ag)) as shown in Figure (2.1).

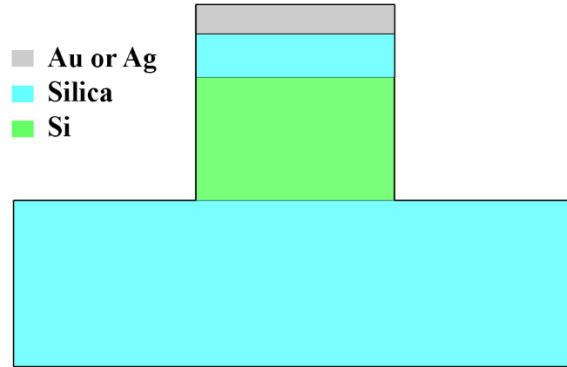


Figure 2.1: The general structure of an HPW at a wavelength of 1.55 μm

The HPW propagation modes are a combination of the photonic modes supported by the high refractive index medium (i.e. photonic waveguide) and the SPP modes at the metal-dielectric boundary (i.e. PW). The HPW combines two features—the small losses feature exhibited by a photonic waveguide and the high light confinement feature exhibited by the PW [86]. The HPW is selected as a basis for the proposed nanostructure because of its structure and features.

2.2.1. Selection of the HPW's materials

The light is attenuated when it propagates through a medium. The complex refractive index of the material includes a real part (n) that determines the light's phase velocity and an imaginary part that determines the extinction coefficient (κ).

The material's complex refractive index is a function of the light's wavelength. Because the QE's emission wavelength (700 nm) is different from the telecommunication band's wavelengths (1.3 or 1.55) μm , the HPW's materials should be selected properly.

Table (2.1) shows the n and κ for different materials. The Si material shows a considerable value of κ at 700 nm and, hence, the light propagating in the Si material is significantly attenuated as the Beer-Lambert law implies. Recently, gallium phosphide (GaP) played an important role in many modern photonic integrated circuits (PICs) [102]. GaP supports strong light confinement and small mode volume due to its high refractive index at 700 nm [103]. Consequently, the alternative material at 700 nm that shows a comparable refractive index for the Si at 1550 nm is the GaP as shown in Table (2.1).

Moreover, the SiO_2 and the hydrogen silsesquioxane (HSQ) materials show a comparable refractive index at a wide range of wavelengths as shown in Table (2.1). However, the HSQ material is selected as a basis for the proposed HPW because it is a widely used material in on-chip plasmonic single-photon sources and it could be experimentally converted to SiO_2 with the same performance [73,80].

Table 2.1: The refractive indices information for different materials [104]

Material	n	κ	n	κ	n	κ	The model
	@ 700 nm		@ 1.3 μm		@ 1.55 μm		
Si	4.0679	0.25109	3.5226	0	3.48	0	Pierce and Spicer
SiO ₂	1.4553	0	1.4469	0	1.444	0	Malitson
Au	0.131	4.0624	0.38797	8.7971	0.52406	10.742	Johnson and Christy
Ag	0.041	4.8025	0.10898	9.4317	0.14447	11.366	Johnson and Christy
GaP	3.2992	0	3.1447	0	3.128	0	Adachi
HSQ	1.41	0	1.41	0	1.41	0	Dow Corning® XR-1541 E-Beam Resist [105]
Al	1.9214	8.142	1.3481	12.917	1.5785	15.658	Rakić

The reasons for choosing the Al as a plasmonic material include its strong plasmonic resonance, simple manufacturing processes, and low cost [106]. The Al could be fabricated down to a 5 nm scale, which makes it easily handled during the manufacturing process [107,108]. Both gold and silver exhibit high plasma wavelength and, therefore, weak plasmonic resonance in contrast to Al at the operation wavelength (700 nm). Although the Au and Ag have approximately comparable refractive indices as shown in Table (2.1), Au and Ag failed to achieve the polarization rotation at a wavelength of 700 nm. The polarization rotation requires that the GaP photonic waveguide supports two orthogonal propagation modes for each case of output polarization, which was achieved by using Al (strong plasmonic resonance) instead of Au and Ag (weak plasmonic resonance) as shown in Figure (2.2).

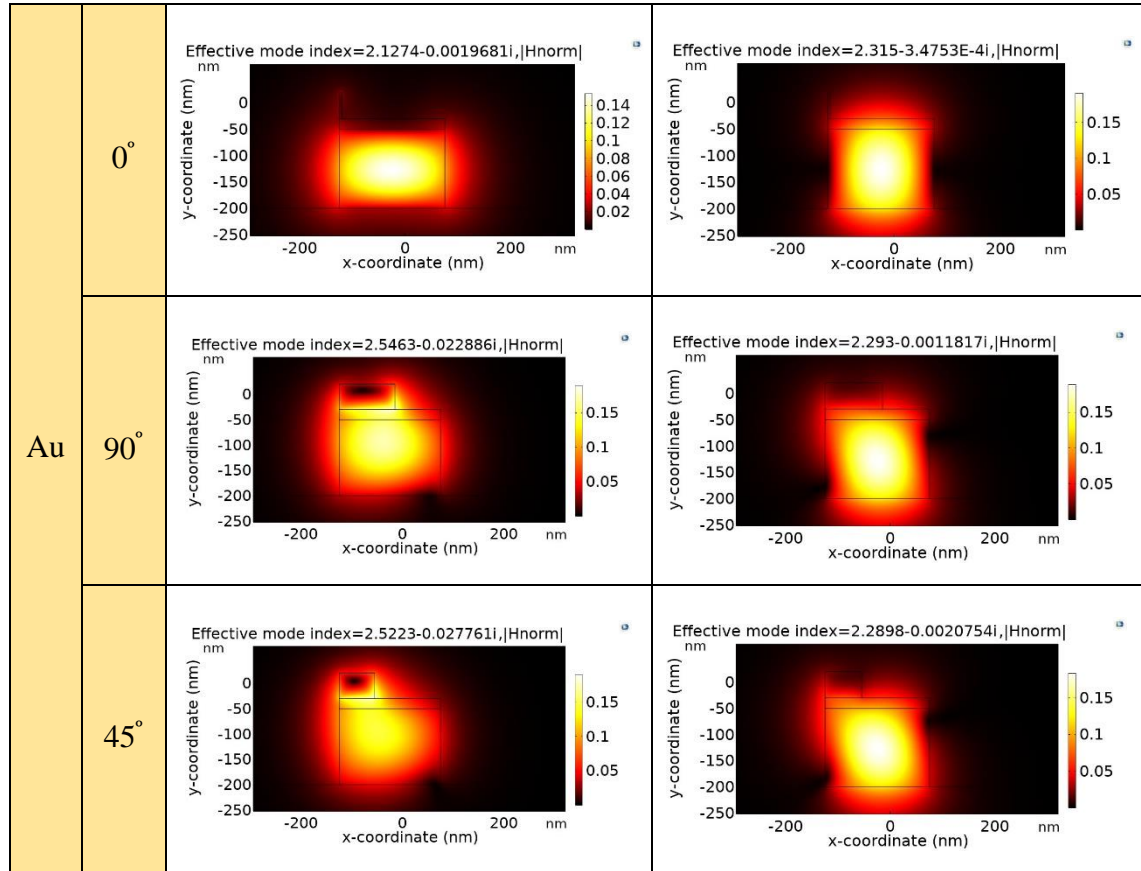


Figure 2.2: The two orthogonal modes supported by the HPW for each case of output polarization for Au, Ag, and Al materials at 700 nm

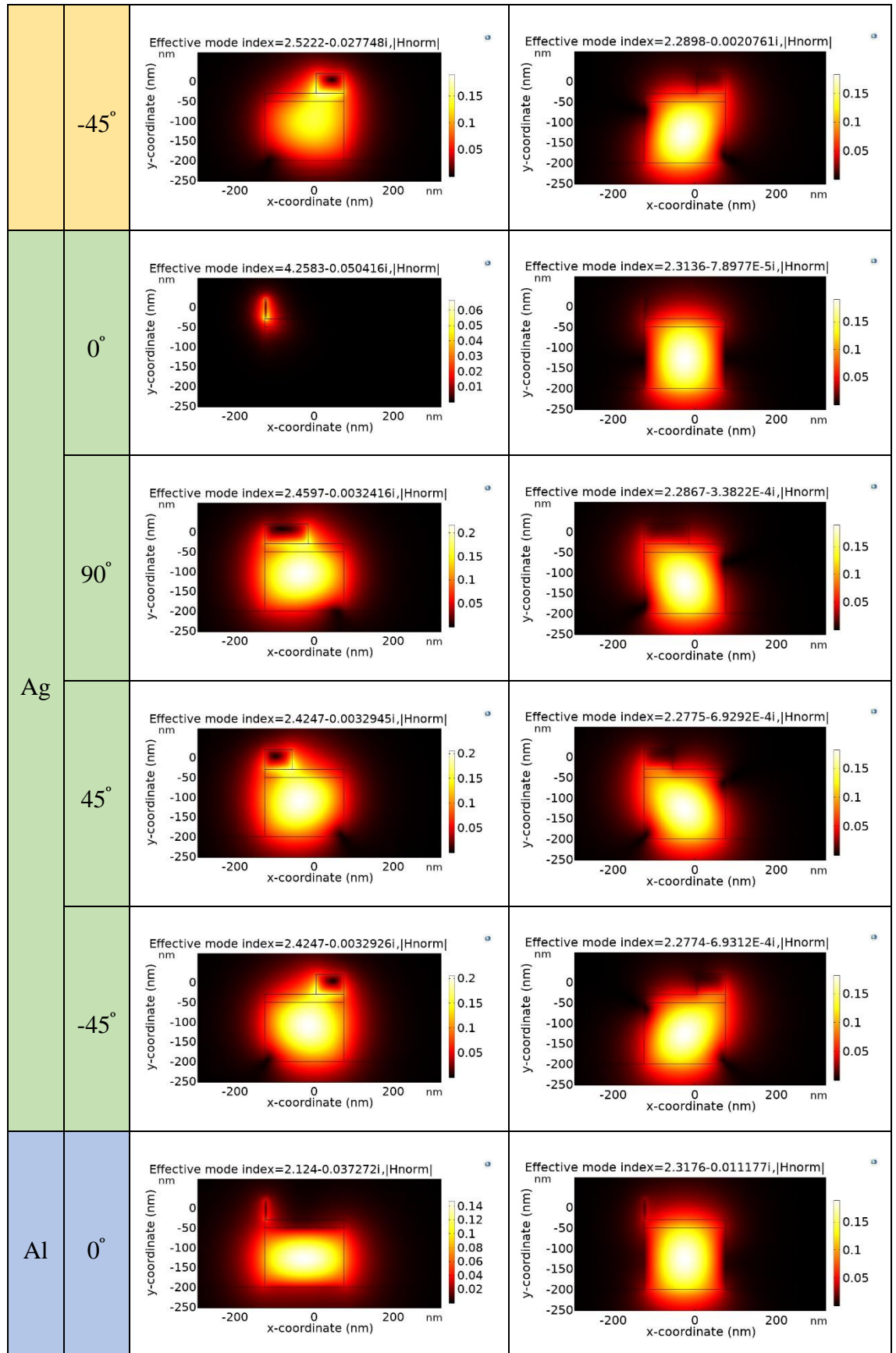


Figure 2.2: Continued.

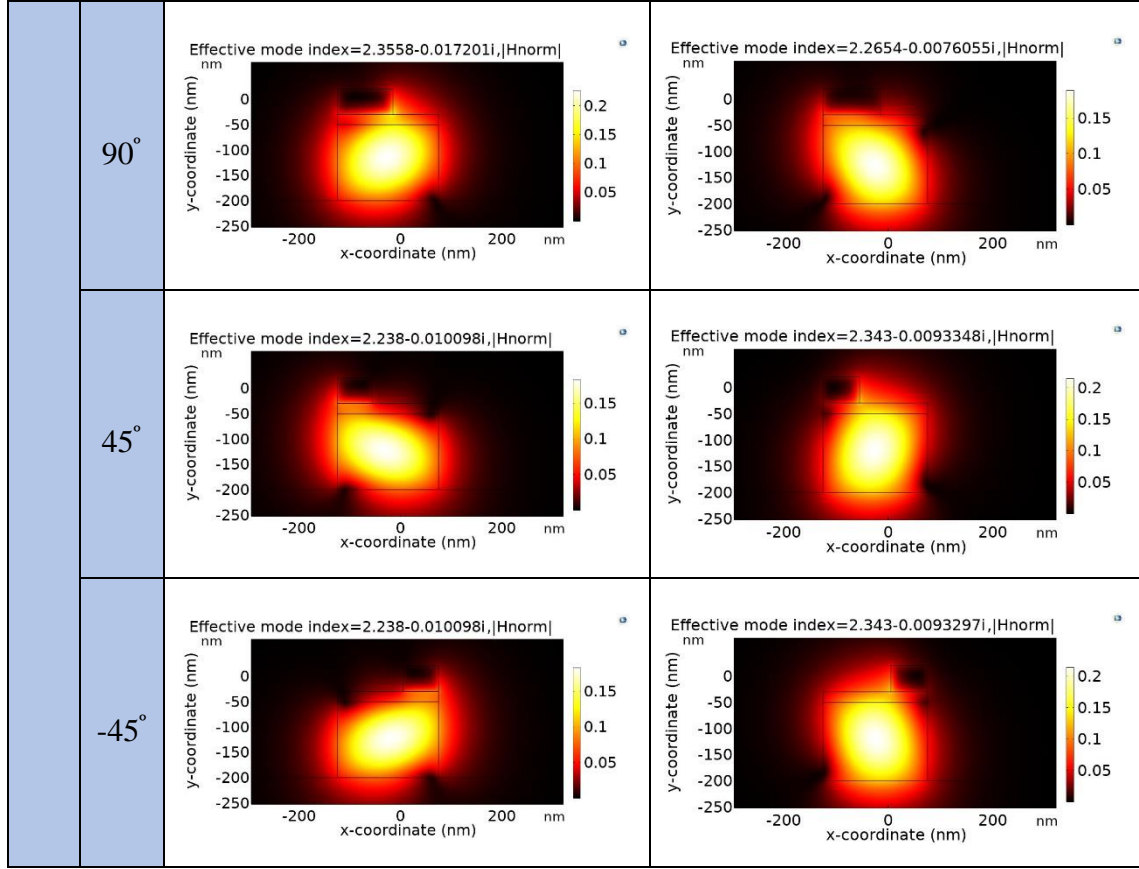


Figure 2.2: Continued.

In the following simulations, the refractive index information for Al and GaP are based on RakiA and Aspnes and Studna models, respectively, that are defined in the COMSOL's material library. Consequently, the refractive indices for the Al and GaP are $1.9214 + 8.142i$ and 3.2543 at 700 nm, respectively.

2.2.2. Selection of the HPW's geometries

A mandatory requirement to control the output polarization of the HPW is that the HPW's geometrical dimensions should support the propagation of two orthogonal modes. The dimensions of the proposed HPWs are determined by the local search algorithm. Most of the on-chip plasmonic single-photon sources in the literature survey used 250 nm (width) and 180 nm (height) for the HSQ pattern deposited above silver or gold as shown in Figure (2.3).

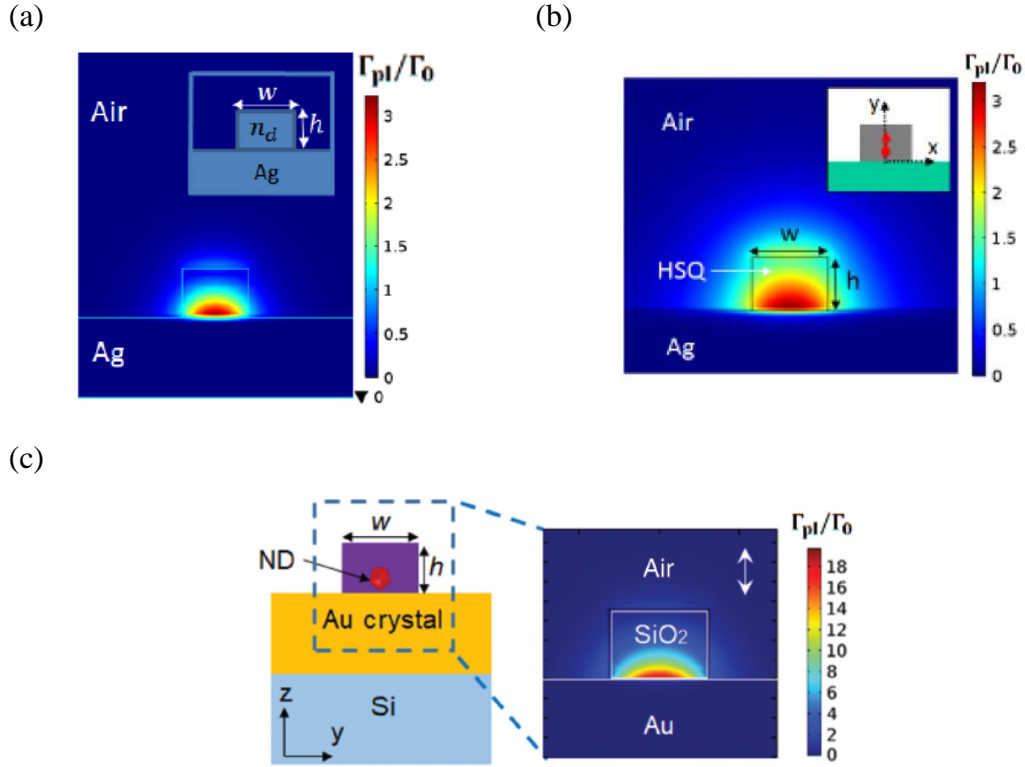


Figure 2.3: The HSQ's geometries in DLSP waveguides used as on-chip plasmonic single-photon sources. (a) [73], (b) [78], (c) [80]

The 250 nm (width) and 180 nm (height) dimensions were considered as a reference to select the GaP photonic channel dimensions in the proposed HPW, which achieved the orthogonality of the propagation modes condition in the GaP region as shown in Figure (2.4.a). However, the proposed work tends to miniaturize the dimensions of the HPW to save space on the integrated circuit. Hence, the width and the height of the GaP photonic waveguides decreased while keeping the Al bar and the HSQ spacer heights fixed at 50 nm and 20 nm, respectively, as will be justified later. The minimum dimensions of the GaP region that supports the propagation of two orthogonal modes are 200 nm (width) and 150 nm (Height) as shown in Figure (2.4.d).

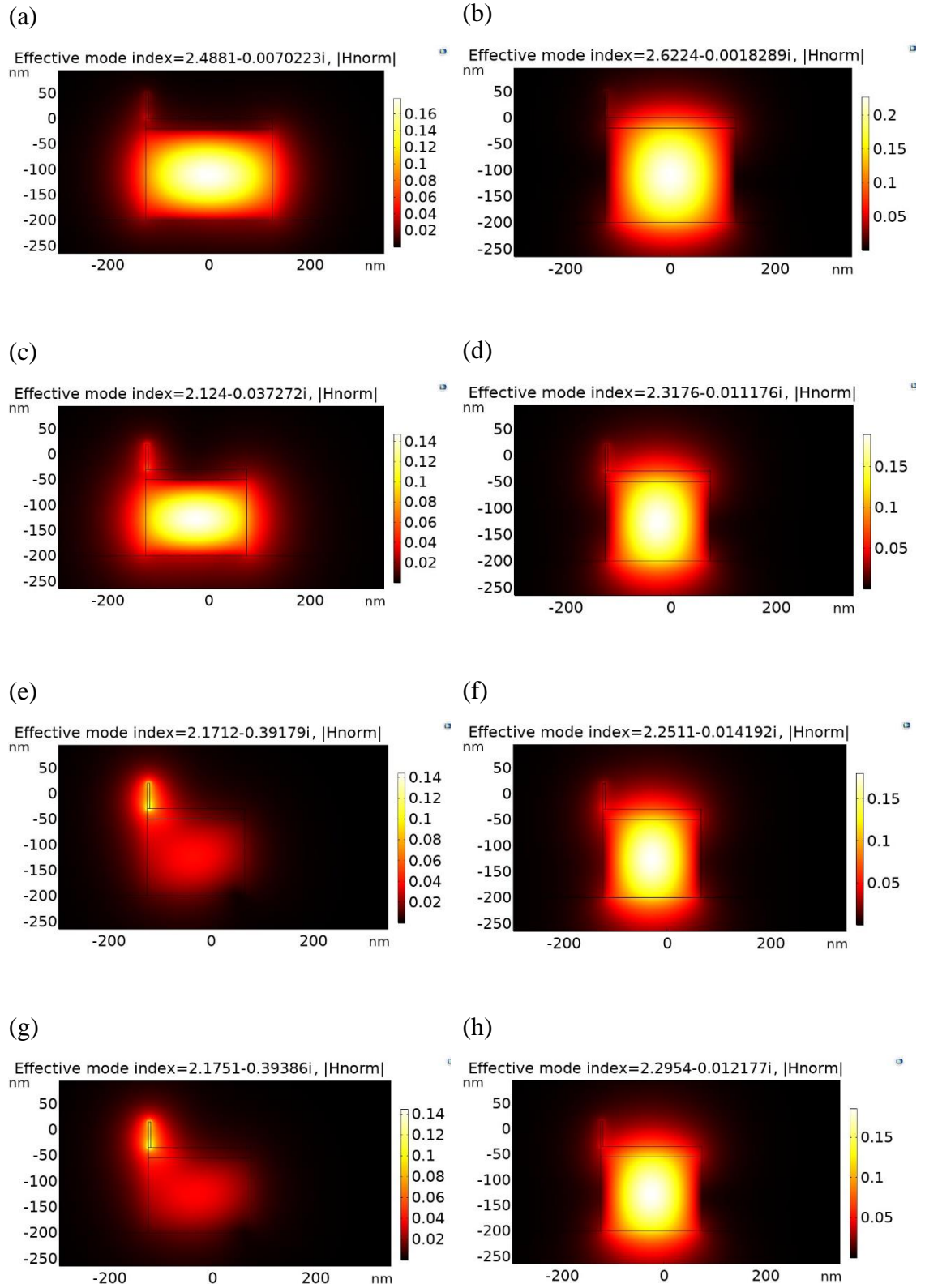


Figure 2.4: The orthogonal modes field distribution when the width and height of the GaP region is (a), (b) 250, 180 nm, (c), (d) 200, 150 nm, (e), (f) 190, 150 nm, and (g), (h) 200, 145 nm, respectively

The HSQ spacer covers the GaP and, consequently, has the same width as the GaP layer. However, the HSQ spacer's height and the Al bar's width

affect the mechanism of the polarization control technique, and, consequently, their optimum values are justified in Section (2.3). Finally, the minimum Al bar height that enables the GaP region to support the propagation of two orthogonal modes is 50 nm as shown in Figure (2.5).

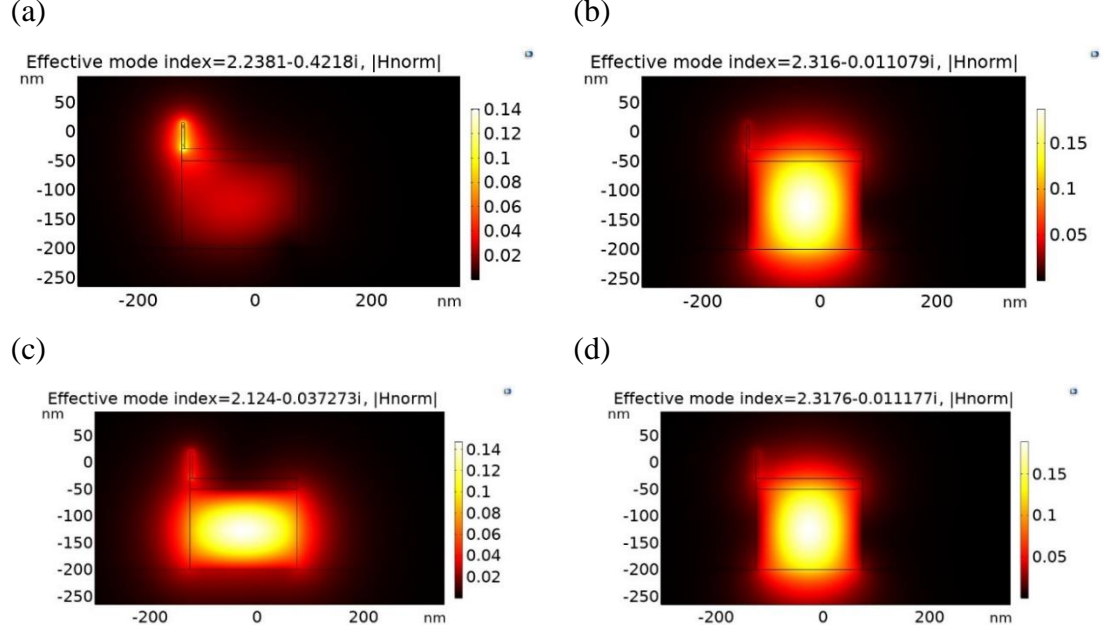


Figure 2.5: The orthogonal modes field distribution with Al bar's height of (a), (b) 45 nm, and (c), (d) 50 nm

Figure (2.6) shows the optimum dimensions for the materials of the HPW structure. The HPW acts as a polarization rotator to control the polarization of the output light and, consequently, the polarization of the photons at the output of the structure, over a silicon (Si) substrate.

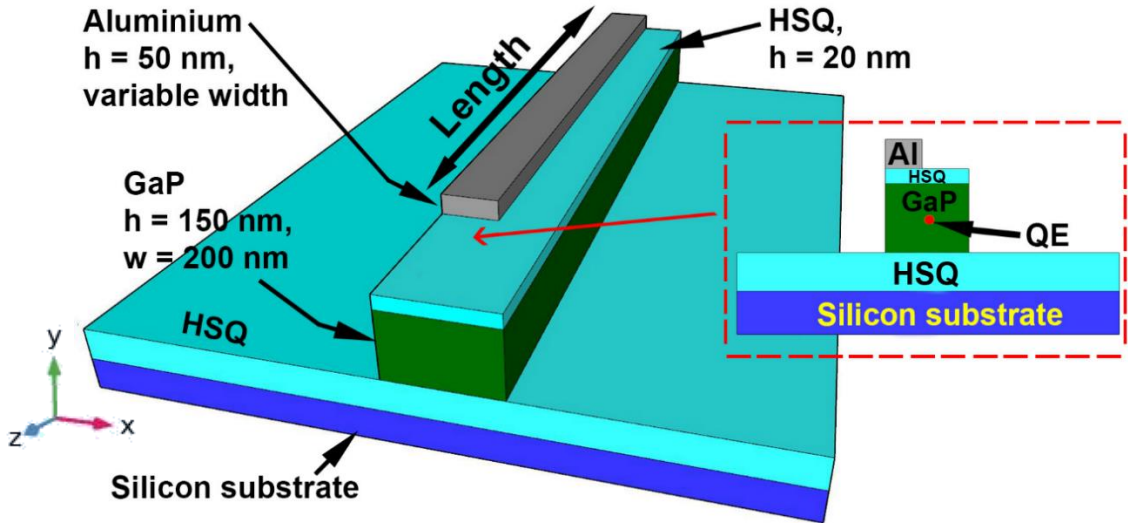


Figure 2.6: The schematic of a QE coupled to an HPW that acts as a polarization rotator. The inset shows the transversal cross-section of the proposed structure at the QE's position

The QE was modeled as a 1 nm line current of 1 A [26] positioned directly underneath the Al bar in the GaP material. The photonic waveguide with a length of 500 nm preceding the QE allows probing the electric field distributions scattered from the QE in both photonic and hybrid plasmonic waveguides.

2.3. Polarization control mechanism

Any manipulation in plasmonic mode properties affects the properties of the photonic mode including its polarization because of the mode interference. The change of the HPW geometry breaks the symmetry and achieves this manipulation and, consequently, results in the desired polarization. The QE embedded in GaP excites the TM mode in the HPW as justified later in this section. The polarization of the excited TM mode and the propagating photons are similar, i.e., 0° . The aim is to rotate the excited mode in the other three different HPW structures to obtain 90° , 45° , and -45° polarization for the output intensity, i.e. photons. By varying the Al width, the HPW symmetry breaks. Consequently, the rotation angle of the two-hybrid orthogonal propagation modes supported by the HPW varies. The optical axes of the hybrid modes are chosen to have a rotation angle (θ), which is the direction of the normal magnetic field to a vertical line in the transversal plane, of 45° and 22.5° to achieve 90° and $45^\circ/-45^\circ$ polarization, respectively. The rotation angle is defined as [109]

$$\tan(\theta) = \frac{\iint \epsilon(x,y) E_y^2(x,y) dx dy}{\iint \epsilon(x,y) E_x^2(x,y) dx dy}, \quad (2.1)$$

where $\epsilon(x,y)$ is the distribution of the permittivity in the x-y plane, $E_x(x,y)$ and $E_y(x,y)$ are the horizontal and vertical electrical components of the EM wave, respectively. Moreover, the HPW conversion length (L) is calculated from [109]

$$L = \frac{\lambda}{2|n_{\text{eff}1} - n_{\text{eff}2}|}, \quad (2.2)$$

where $n_{\text{eff}1}$ is the real part of the effective index of the first orthogonal mode, $n_{\text{eff}2}$ is the real part of the effective index of the second orthogonal mode, and λ is the QE's emission wavelength. If the propagating EM wave has a polarization of 0° or 90° and the rotation angle is set to be 0° or 90° , respectively, then the polarization of the propagating EM wave is kept fixed.

Table (2.2) shows the optimum dimensions for the Al and the corresponding effective indices of the two-hybrid orthogonal modes to get an output polarization of 0° , 45° /- 45° , and 90° . As the width of the Al and the thickness of the underlying HSQ layer vary, the value of θ will change. Figure (2.7) shows the variation of θ against the Al width for different HSQ thickness.

Table 2.2: Al dimensions for output polarization of 0° , 45° /- 45° , and 90°

Output polarization angle associated with $n_{\text{eff}2}$	Width (nm)	θ	$n_{\text{eff}1}$	$n_{\text{eff}2}$	$L_{\text{eff}2}$ (μm)	L (μm)
0° (*)	5	0°	$2.124 - 0.037272i$	$2.3176 - 0.011177i$	5	5
45°	70	22.5°	$2.2380 - 0.010098i$	$2.343 - 0.0093348i$	6	3.333
-45° (**)	70	22.5°	$2.2380 - 0.010098i$	$2.343 - 0.0093297i$	6	3.333
90°	110	45°	$2.3558 - 0.017199i$	$2.2654 - 0.0076055i$	7.3	3.872

(*) The propagation length, in this case, is calculated from $1/\text{Im}(2 n_{\text{eff}2} k_0)$.

(**) In this case, the Al bar has the same width of 45° but has a different position as explained in Figure (2.21.d).

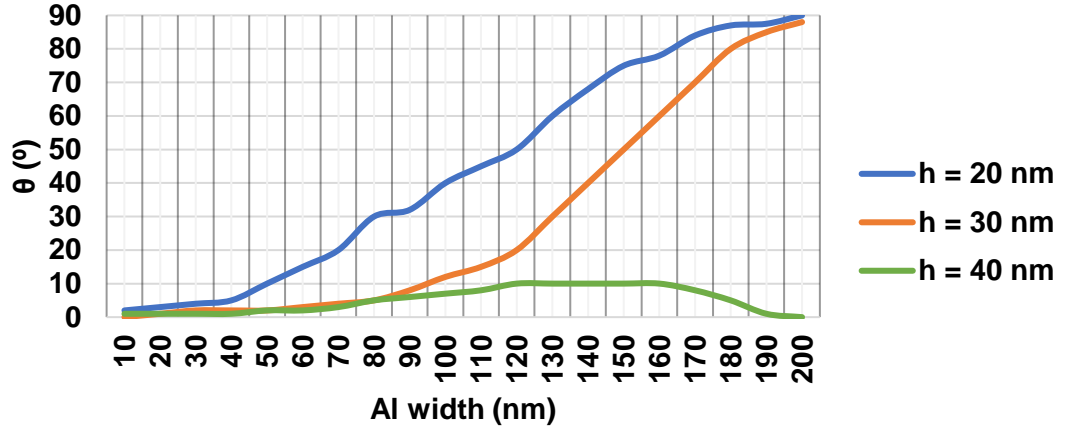


Figure 2.7: The variation of θ against the Al width for different HSQ thickness

Figure (2.7) clearly shows that the best angle variation, that achieves a linear relationship between θ and the Al width values between 40° to 180° , can be obtained when the HSQ thickness is 20 nm compared to a thickness of 30 nm or 40 nm. Accordingly, the thickness of the HSQ layer is set to 20 nm.

It is necessary to define the essence of 0° output polarization, which will be the reference for other output polarization cases. The 2D mode analysis shows the two orthogonal modes supported by the HPW in the case of 5 nm Al thickness, i.e. θ is 0° , where the light is confined with subwavelength dimensions inside the GaP region as shown in Figure (2.8). The rotation angle for the arrows was measured using MB-Ruler software.

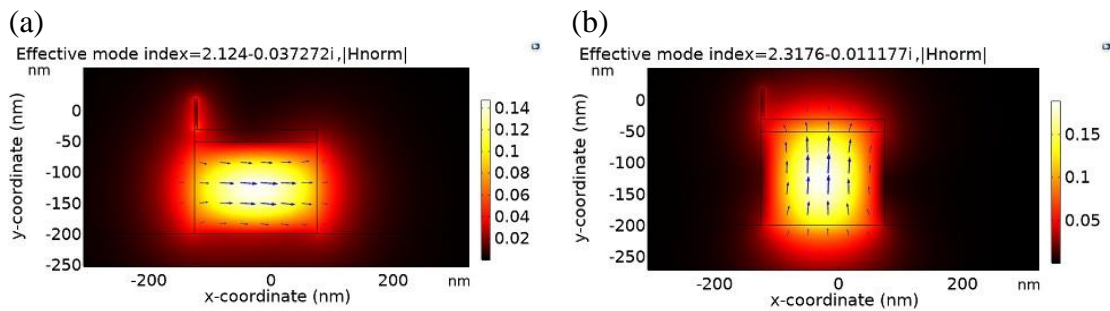


Figure 2.8: $|H_{\text{norm}}|$ in the case of the a) first effective mode index. b) second effective mode index. Arrows indicate the magnetic field distribution.

The rotation angle (θ°) is the angle between the normal magnetic field ($|H_{\text{norm}}|$) and a vertical line in the transversal plane at the center of the GaP region. The first mode supports 90° output polarization as shown in Figure (2.8.a), while the second orthogonal mode supports 0° output polarization as shown in Figure (2.8.b). To determine the orientation of the QE, the electric

field distribution supported by HPW in the case of 0° output polarization should be observed. Figure (2.9) shows the electric field distribution in x and y directions for 0° output polarization.

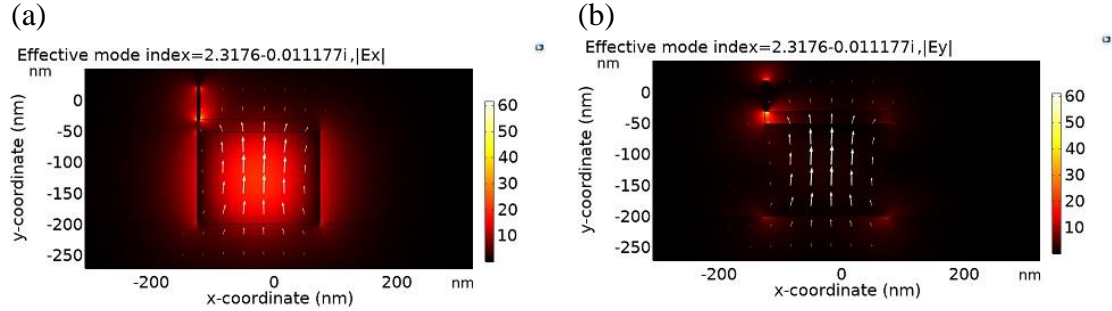


Figure 2.9: (a) $|E_x|$ (b) $|E_y|$ for 0° output polarization. Arrows indicate the magnetic field distribution.

The HPW supports the propagation of the electric field oriented in the x-direction, while, the electric field in the y-direction is concentrated in the corners of the GaP region, only. Consequently, the QE should be oriented toward a higher electric field value. Hence, the QE is positioned in the x-direction at the coordinates of the maximum electric field. In the following sections, the QE's orientation is fixed along the x-axis, however, its position follows the maximum electric field in the GaP region for maximum Purcell enhancement factor and β -factor as explained in Section (2.4). Furthermore, it is worth mentioning that both orthogonal modes are TM modes. The second orthogonal mode was selected as a reference to the QE's orientation because it is more intense than the first orthogonal mode. Consequently, the excitation of the second orthogonal mode leads to maximum Purcell and β -factor as demonstrated in Section (2.4). Furthermore, the excitation of the second orthogonal mode generates a polarization field that coincides with the normal of the transversal plane, i.e. 0° polarization. Figure (2.10) shows the electric and magnetic field distributions of both TM modes.

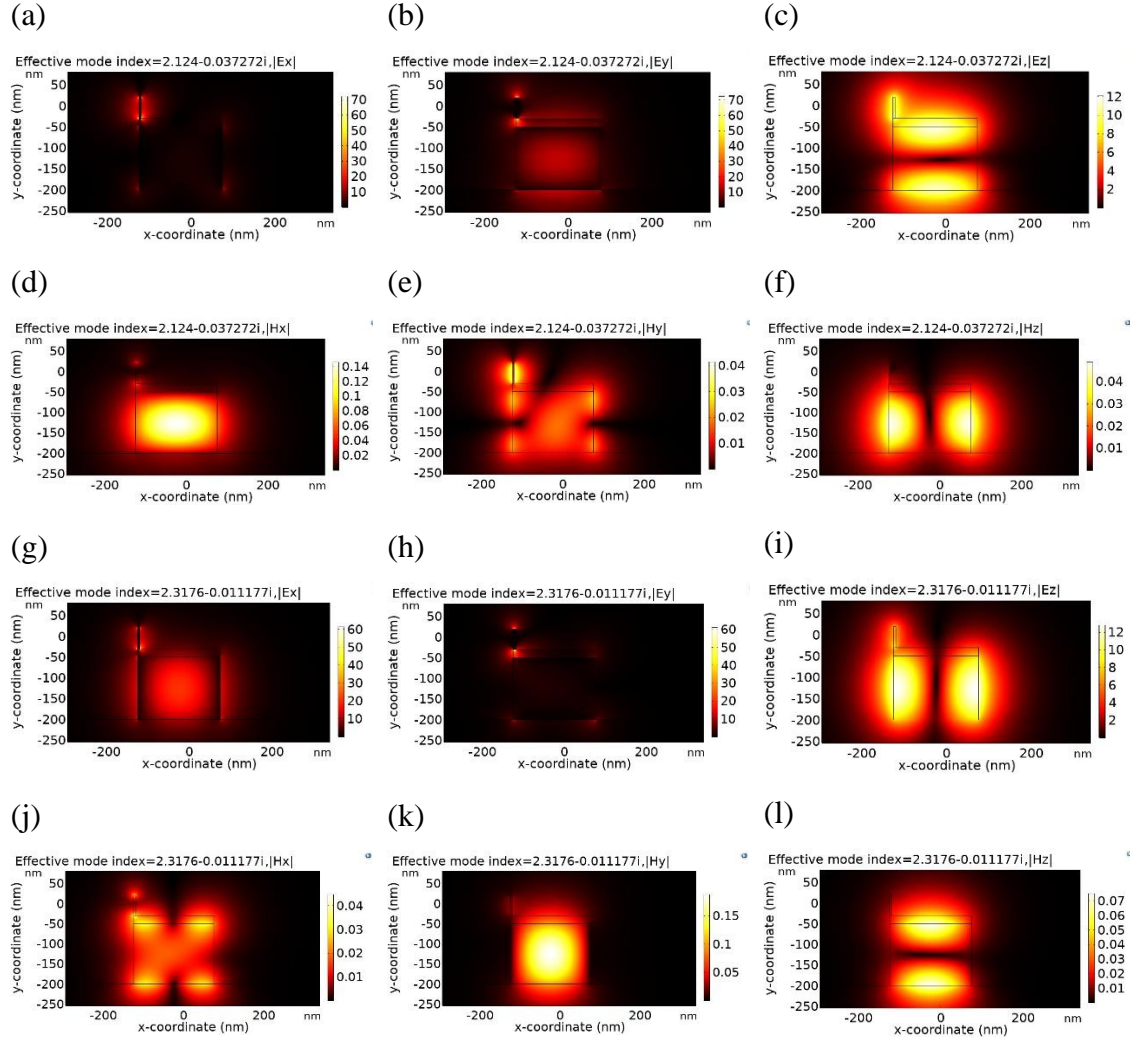


Figure 2.10: The field distributions for the (a) TM (E_x), (b) TM (E_y), (c), TM (E_z), (d) TM (H_x), (e) TM (H_y), (f) TM (H_z), (g) TM (E_x), (h) TM (E_y), (i) TM (E_z), (j) TM (H_x), (k) TM (H_y), and (l) TM (H_z)

2.4. The QE's spontaneous emission enhancement

By controlling the interference between photonic and plasmonic modes, accurate control of the output intensity polarization will be achieved. As a result, a uniform polarization field over a uniform intensity mode profile could be realized. The polarization field in plasmonic mode (between HSQ and Al) is random and its direction can not be controlled easily because of the high confinement of the electric field in a small area. However, the photonic mode in GaP has a uniform intensity mode profile and uniform polarization field. This is why the location of the quantum emitter is chosen to be in the GaP region, where it can excite both modes in HPW as shown in Figure (2.11).

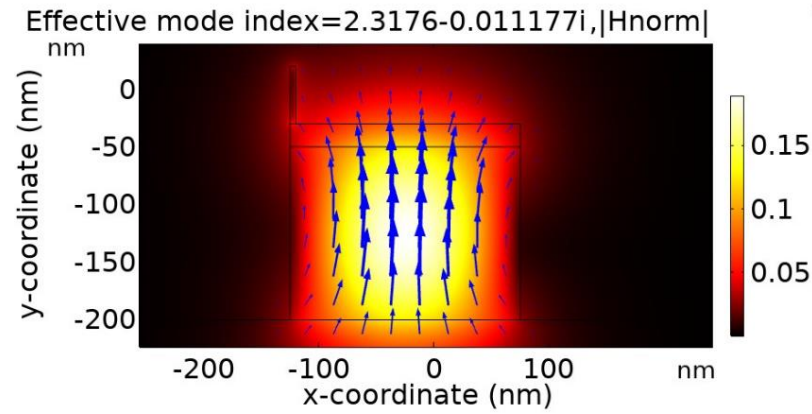


Figure 2.11: The normal magnetic field distribution for the second orthogonal mode

The spontaneous emission of the QE is improved due to the coupling of its emission into a GaP photonic mode in the HPW via the Purcell effect. The emitted energy couples to the photonic mode of the HPW with high efficiency, i.e. high β -factor, and could be obtained as

$$\beta = \frac{\Gamma_{pl}}{\Gamma_{radiative} + \Gamma_{nonradiative} + \Gamma_{pl}} = \frac{\frac{\Gamma_{pl}}{\Gamma_o}}{\frac{\Gamma_{tot}}{\Gamma_o}} \quad (2.3)$$

The 2D mode analysis estimates the ratio of the plasmonic decay rate (Γ_{pl}) to the decay rate of the emitter in a vacuum (Γ_o). The corresponding equations for the numerator and the denominator of Equation (1.14) are defined in the variables section of the model builder tree as shown in Figure (2.12).

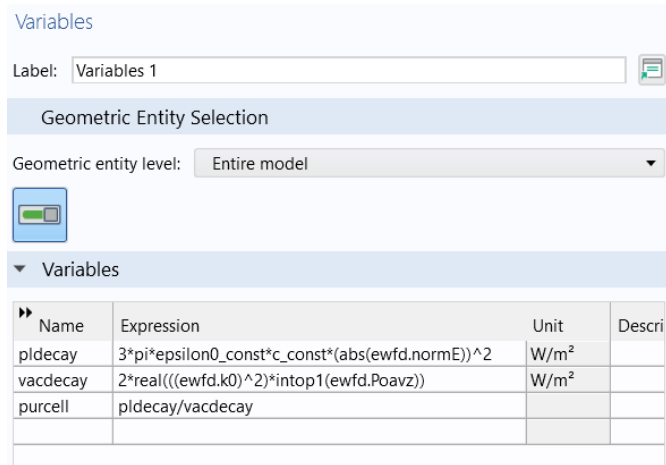


Figure 2.12: COMSOL's variables section that defines Equation (1.14)

The integration probe (intop1) is set to the total 2D plane. A Global variable probe is set to monitor the distribution of the resultant Purcell factor across the transversal plane as shown in Figure (2.13).

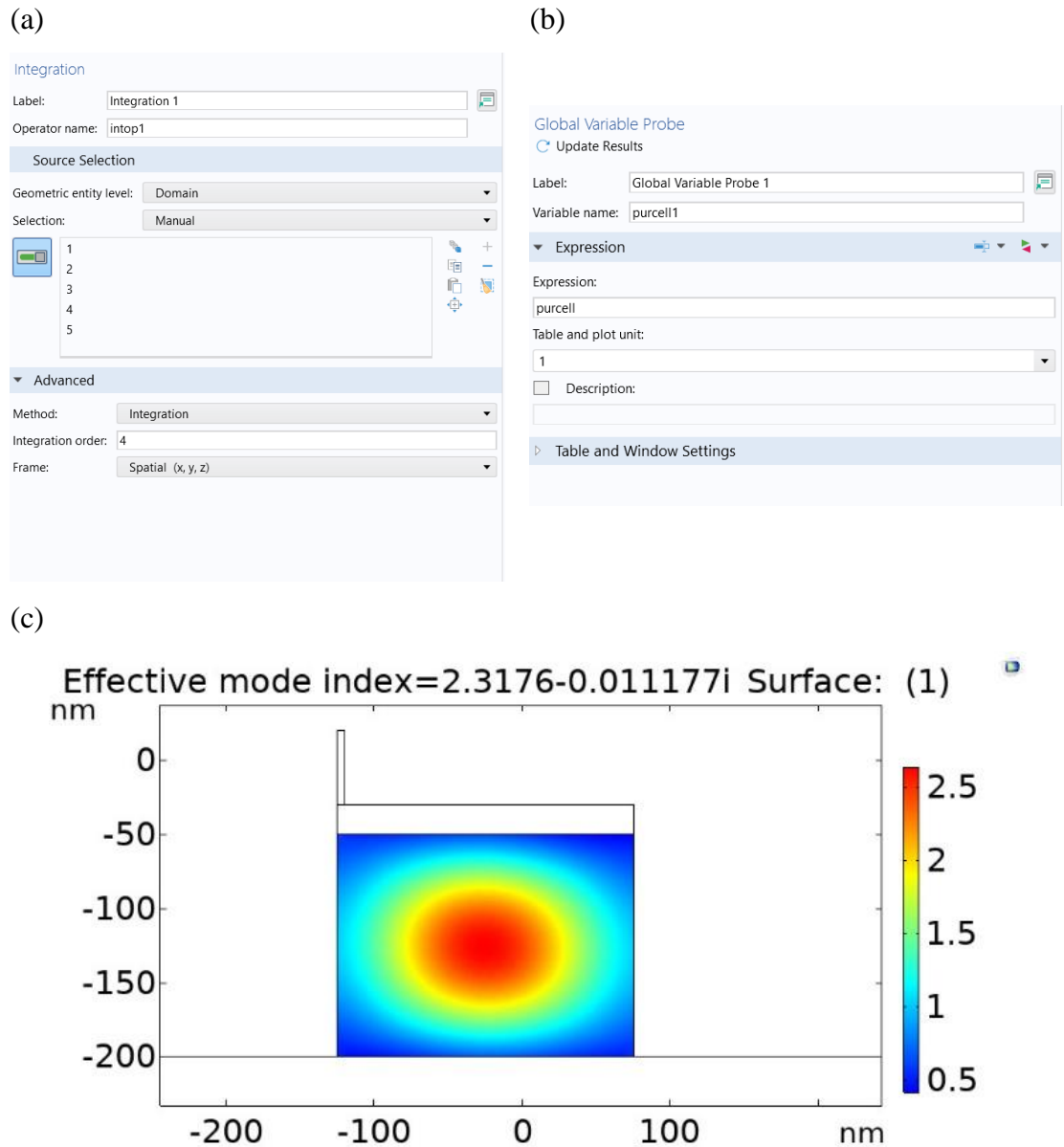


Figure 2.13: (a) The Integration (intop1) Nonlocal Coupling in the Definitions tree of the Model builder, (b) The Global Variable Probe that monitors the Purcell variable, (c) The transversal distribution of the Purcell factor calculated by Equation (1.14)

The 2D analysis procedure was confirmed by reproducing the result of Figure (1.4.b) as shown in Figure (2.14).

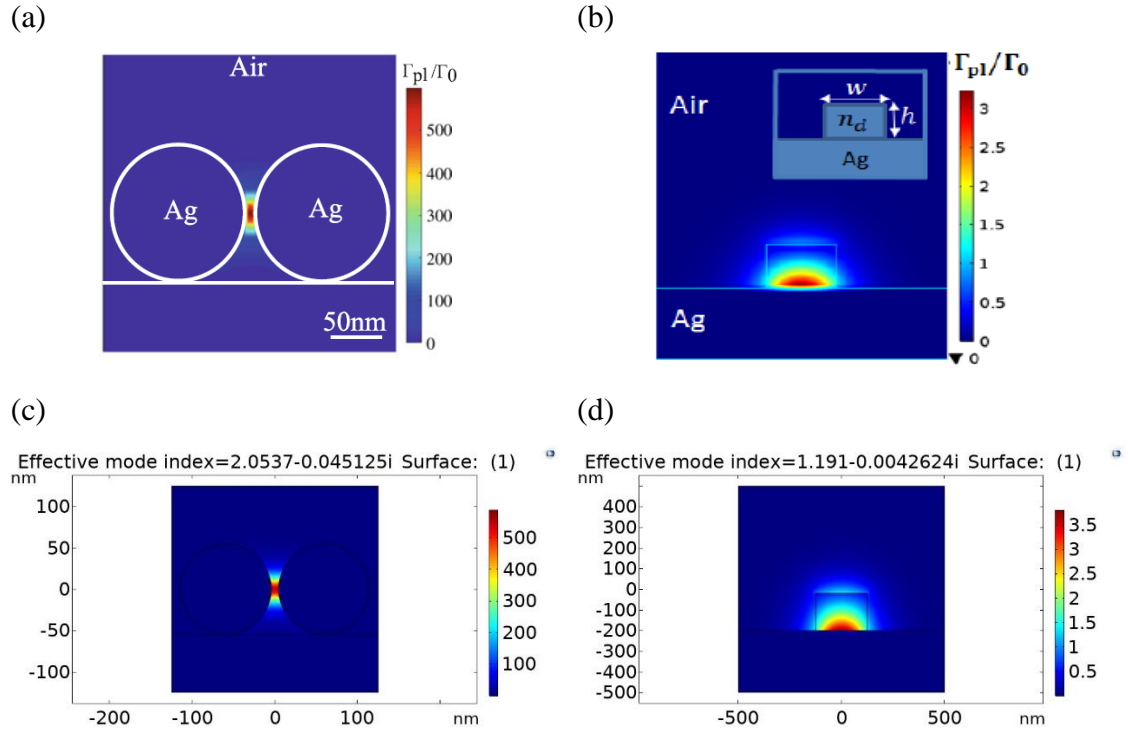


Figure 2.14: The 2D analysis for the Purcell factor calculation in (a) [25], (b) [73], the reproduced 2D analysis for the Purcell factor calculation in (c) [25], and (d) [73]

A 3D analysis of the proposed HPWs was performed to obtain the ratio of the total decay rate of the emitter to the decay rate of the QE in a vacuum and, consequently, solve Equation (1.15) as shown in Figure (2.15).

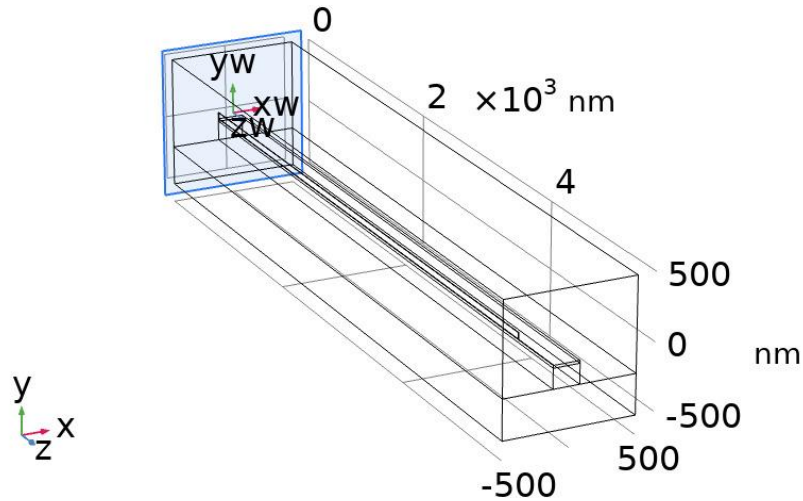


Figure 2.15: The schematic of the 3D model used to calculate the total decay rate

Equation (1.15) could be simplified as [110]

$$\frac{\Gamma_{\text{tot}}}{\Gamma_o} = \frac{0.5 \iiint \text{Re}(\vec{J}^* \cdot \vec{E}_x) dV}{0.5 \iiint \text{Re}(\vec{J}^* \cdot \vec{E}_{ox}) dV} = \frac{\int \text{Re}(\vec{E}_x) d\vec{l}}{\int \text{Re}(\vec{E}_{ox}) d\vec{l}}, \quad (2.4)$$

where \vec{J}^* (A/m²) is the complex current density produced by the QE and crosses the transversal plane perpendicularly, \vec{E}_{ox} (V/m) is the electric field intensity in the x-direction in a vacuum, and $d\vec{l}$ is the one-dimensional line integral across the QE's length. The \vec{J}^* is constant and could be omitted because the transversal area, the QE's current (1 A), and the QE's length (1 nm) are constant.

The numerator of Equation (2.4) could be calculated by setting an Integral edge probe at the QE's line geometry as shown in Figure (2.16).

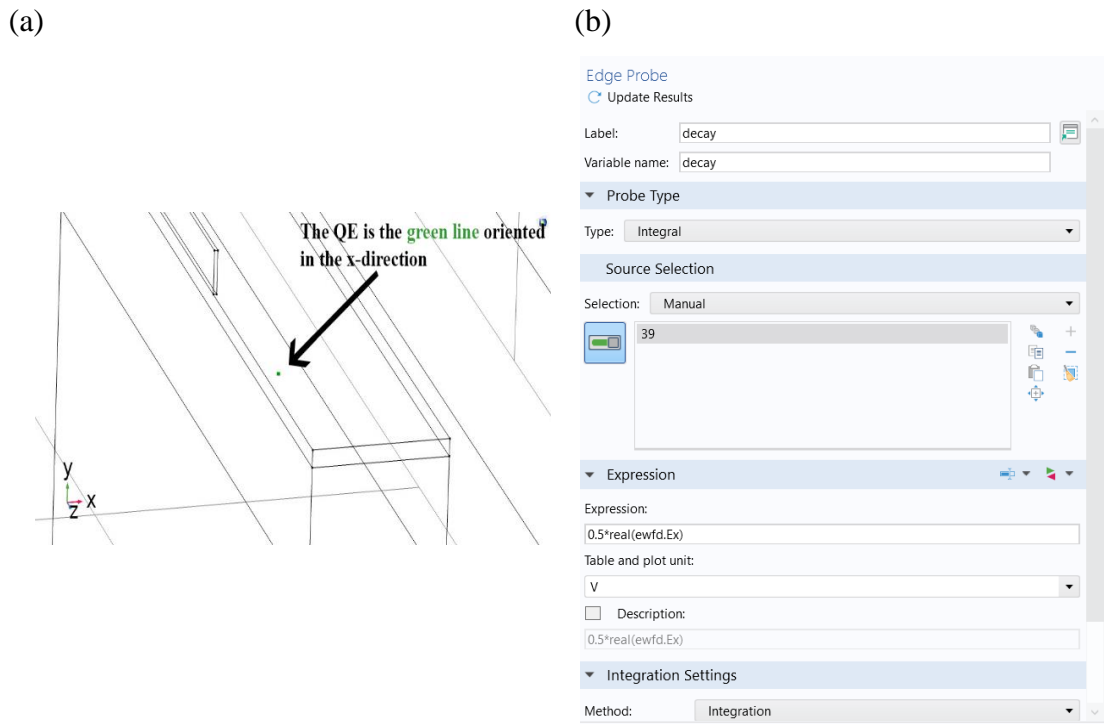


Figure 2.16: The total decay rate evaluation (Equation (2.3)'s numerator). (a) The QE's location in the 3D model (indicated by the Green line), (b) The edge probe settings for the corresponding QE's line geometry

The total decay rate of the emitter in a vacuum (Equation (2.4)'s denominator) could be calculated by setting all the domains' material to air and calculating the value of the Integral edge probe. The calculated values of Equations (1.14), (2.3), and (2.4) are listed in a separate Excel sheet for each case of output polarization (Al's width).

Table (2.3) lists the values of Γ_{pl}/Γ_o , Γ_{tot}/Γ_o and β -factor that correspond to 0°, 90°, 45°, and -45° output polarization. If θ is set to 0°, then

no change occurs to EM wave polarization at the HPW's output. For 0° output polarization, the QE's spatial position in the GaP region is varied along the y-axis around the maximum E_x point in Figure (2.9.a) to find the optimum y-coordinate that corresponds to the maximum Purcell factor. Then, the QE's optimum y-coordinate is kept fixed while sweeping the x-position of the QE to find the optimum x-coordinate that corresponds to the maximum Purcell factor.

Table 2.3: The β -factor calculation for 0° , 90° , 45° , and -45° output polarization when the QE has varied along the y-axis and x-axis

Output polarization	y	Γ_{pl}/Γ_o	Γ_{tot}	Γ_o	Γ_{tot}/Γ_o	β -factor
0°	-175.556	1.561470	-0.0033614	-0.00080984	4.150696	0.3761948
	-170.000	1.762240	-0.0032985	-0.00080984	4.073027	0.4326612
	-165.556	1.910550	-0.0032204	-0.00080984	3.976588	0.4804496
	-160.000	2.089423	-0.0030966	-0.00080984	3.823718	0.5464376
	-155.556	2.213669	-0.0029898	-0.00080984	3.691840	0.5996113
	-150.000	2.356845	-0.0028379	-0.00080984	3.504272	0.6725633
	-145.556	2.447281	-0.0027292	-0.00080984	3.370048	0.7261857
	-140.000	2.543832	-0.0026028	-0.00080984	3.213968	0.7914926
	-135.556	2.593331	-0.0025234	-0.00080984	3.115924	0.8322830
	-130.000	2.636048	-0.0024557	-0.00080984	3.032327	0.8693150
	-126.667	2.640792	-0.0024343	-0.00080984	3.005902	0.8785354
	-125.556	2.640611	-0.0024312	-0.00080984	3.002074	0.8795955
	-120.000	2.626410	-0.0024384	-0.00080984	3.010965	0.8722818
	-115.556	2.585537	-0.0024758	-0.00080984	3.057147	0.8457353
	-110.000	2.515765	-0.0025614	-0.00080984	3.162847	0.7954115
	-105.556	2.432455	-0.0026471	-0.00080984	3.268670	0.7441727
	-100.000	2.312675	-0.0027827	-0.00080984	3.436111	0.6730502
	-95.556	2.193202	-0.0029004	-0.00080984	3.581448	0.6123786
	-90.000	2.032815	-0.0030518	-0.00080984	3.768399	0.5394374
	-85.556	1.886325	-0.0031656	-0.00080984	3.908920	0.4825693
	-80.000	1.697939	-0.0032874	-0.00080984	4.059320	0.4182816
	x	Γ_{pl}/Γ_o	Γ_{tot}	Γ_o	Γ_{tot}/Γ_o	β -factor
	-75.000	1.973581	-0.0013686	-0.00080984	1.689963	1.1678248
	-70.000	2.076290	-0.0015423	-0.00080984	1.904450	1.0902304
	-65.000	2.191791	-0.0017087	-0.00080984	2.109923	1.0388016
	-60.000	2.279609	-0.0018640	-0.00080984	2.301689	0.9904071
	-55.000	2.380386	-0.0020059	-0.00080984	2.476909	0.9610308
	-50.000	2.446304	-0.0021320	-0.00080984	2.632619	0.9292282
	-45.000	2.525393	-0.0022368	-0.00080984	2.762027	0.9143258

	-40.000	2.564090	-0.0023222	-0.00080984	2.867480	0.8941965
	-35.000	2.616156	-0.0023836	-0.00080984	2.943297	0.8888522
	-30.000	2.624341	-0.0024215	-0.00080984	2.990097	0.8776775
	-25.000	2.646029	-0.0024343	-0.00080984	3.005902	0.8802777
	-20.000	2.622711	-0.0024225	-0.00080984	2.991332	0.8767703
	-15.000	2.612903	-0.0023856	-0.00080984	2.945767	0.8870025
	-10.000	2.559414	-0.0023245	-0.00080984	2.870320	0.8916825
	-5.000	2.519344	-0.0022428	-0.00080984	2.769436	0.9096957
	0.000	2.439235	-0.0021373	-0.00080984	2.639163	0.9242455
	5.000	2.372362	-0.0020107	-0.00080984	2.482836	0.9555047
	10.000	2.271139	-0.0018709	-0.00080984	2.310209	0.9830880
	15.000	2.182914	-0.0017131	-0.00080984	2.115356	1.0319369
	20.000	2.067598	-0.0015466	-0.00080984	1.909760	1.0826479
	25.000	1.965081	-0.0013730	-0.00080984	1.695397	1.1590683
90°	y	Γ_{pl}/Γ_o	Γ_{tot}	Γ_o	Γ_{tot}/Γ_o	β -factor
	-180.000	1.709269	-0.0031092	-0.000810	3.839893	0.4451346
	-175.556	1.848900	-0.0031147	-0.000810	3.846686	0.4806476
	-170.000	2.022552	-0.0030852	-0.000810	3.810253	0.5308184
	-165.556	2.143589	-0.0030347	-0.000810	3.747885	0.5719463
	-160.000	2.289287	-0.0029462	-0.000810	3.638587	0.6291694
	-155.556	2.380529	-0.0028612	-0.000810	3.533611	0.6736816
	-150.000	2.485706	-0.0027462	-0.000810	3.391585	0.7329040
	-145.556	2.538820	-0.0026534	-0.000810	3.276976	0.7747449
	-140.000	2.594624	-0.0025459	-0.000810	3.144212	0.8252066
	-135.556	2.604596	-0.0024729	-0.000810	3.054056	0.8528316
	-132.222	2.607081	-0.0024278	-0.000810	2.998357	0.8695031
	-130.000	2.606436	-0.0024034	-0.000810	2.968223	0.8781132
	-125.556	2.572012	-0.0023692	-0.000810	2.925986	0.8790242
	-120.000	2.519928	-0.0023565	-0.000810	2.910301	0.8658651
	-115.556	2.443671	-0.0023705	-0.000810	2.927591	0.8347037
	-110.000	2.342321	-0.0024169	-0.000810	2.984896	0.7847245
	-105.556	2.230381	-0.0024743	-0.000810	3.055785	0.7298878
	-100.000	2.088589	-0.0025658	-0.000810	3.168789	0.6591127
	-95.556	1.950148	-0.0026521	-0.000810	3.275370	0.5953977
	-90.000	1.780142	-0.0027638	-0.000810	3.413321	0.5215279
	-85.556	1.626695	-0.0028537	-0.000810	3.524348	0.4615591
	x	Γ_{pl}/Γ_o	Γ_{tot}	Γ_o	Γ_{tot}/Γ_o	β -factor
	-85.000	1.954950	-0.0010359	-0.000810	1.279347	1.5280841
	-80.000	2.063580	-0.0012178	-0.000810	1.503995	1.3720654
	-75.000	2.176854	-0.0013991	-0.000810	1.727903	1.2598247
	-70.000	2.268318	-0.0015766	-0.000810	1.947117	1.1649622
	-65.000	2.364034	-0.0017462	-0.000810	2.156575	1.0961985
	-60.000	2.431843	-0.0019043	-0.000810	2.351830	1.0340216
	-55.000	2.504098	-0.0020481	-0.000810	2.529424	0.9899875

	-50.000	2.543664	-0.0021745	-0.000810	2.685529	0.9471742
	-45.000	2.588335	-0.0022809	-0.000810	2.816934	0.9188481
	-40.000	2.597167	-0.0023662	-0.000810	2.922281	0.8887466
	-35.000	2.612086	-0.0024278	-0.000810	2.998357	0.8711724
	-30.000	2.589866	-0.0024650	-0.000810	3.044300	0.8507265
	-25.000	2.574897	-0.0024769	-0.000810	3.058996	0.8417456
	-20.000	2.523355	-0.0024642	-0.000810	3.043312	0.8291477
	-15.000	2.480240	-0.0024243	-0.000810	2.994035	0.8283937
	-10.000	2.402924	-0.0023611	-0.000810	2.915982	0.8240530
	-5.000	2.335100	-0.0022747	-0.000810	2.809277	0.8312104
	0.000	2.236964	-0.0021669	-0.000810	2.676143	0.8358908
	5.000	2.149180	-0.0020396	-0.000810	2.518927	0.8532127
	10.000	2.036241	-0.0018952	-0.000810	2.340591	0.8699689
	15.000	1.934284	-0.0017370	-0.000810	2.145212	0.9016746
45°	y	Γ_{pl}/Γ_o	Γ_{tot}	Γ_o	Γ_{tot}/Γ_o	β -factor
	-170.000	1.564638	-0.0032142	-0.000810	3.966630	0.3944503
	-165.556	1.690822	-0.0031384	-0.000810	3.873086	0.4365567
	-160.000	1.846287	-0.0030182	-0.000810	3.724747	0.4956811
	-155.556	1.955875	-0.0029090	-0.000810	3.589984	0.5448144
	-150.000	2.086369	-0.0027666	-0.000810	3.414249	0.6110769
	-145.556	2.170783	-0.0026568	-0.000810	3.278745	0.6620774
	-140.000	2.266535	-0.0025344	-0.000810	3.127692	0.7246669
	-135.556	2.319215	-0.0024542	-0.000810	3.028717	0.7657415
	-130.000	2.373127	-0.0023856	-0.000810	2.944058	0.8060733
	-125.556	2.389978	-0.0023584	-0.000810	2.910491	0.8211597
	-120.000	2.398182	-0.0023627	-0.000810	2.915798	0.8224789
	-115.556	2.377832	-0.0023970	-0.000810	2.958127	0.8038301
	-110.000	2.339956	-0.0024751	-0.000810	3.054510	0.7660661
	-105.556	2.283910	-0.0025627	-0.000810	3.162617	0.7221582
	-100.000	2.203124	-0.0026959	-0.000810	3.326998	0.6621956
	-95.556	2.115687	-0.0028147	-0.000810	3.473609	0.6090747
	-90.000	1.998472	-0.0029690	-0.000810	3.664030	0.5454302
	-85.556	1.886359	-0.0030891	-0.000810	3.812245	0.4948159
	-80.000	1.742127	-0.0032236	-0.000810	3.978231	0.4379150
	-75.556	1.614026	-0.0033121	-0.000810	4.087448	0.3948737
	-70.000	1.454844	-0.0033881	-0.000810	4.181239	0.3479456
	x	Γ_{pl}/Γ_o	Γ_{tot}	Γ_o	Γ_{tot}/Γ_o	β -factor
	-85.000	1.529149	-0.0009931	-0.000810	1.225593	1.2476809
	-80.000	1.644436	-0.0011696	-0.000810	1.443398	1.1392808
	-75.000	1.769190	-0.0013465	-0.000810	1.661710	1.0646807
	-70.000	1.875969	-0.0015198	-0.000810	1.875578	1.0002081
	-65.000	1.990989	-0.0016859	-0.000810	2.080562	0.9569477
	-60.000	2.080193	-0.0018415	-0.000810	2.272587	0.9153412
	-55.000	2.176733	-0.0019833	-0.000810	2.447582	0.8893402

	-50.000	2.240883	-0.0021088	-0.000810	2.602461	0.8610631
	-45.000	2.311838	-0.0022152	-0.000810	2.733769	0.8456596
	-40.000	2.345732	-0.0023007	-0.000810	2.839284	0.8261705
	-35.000	2.386262	-0.0023627	-0.000810	2.915798	0.8183907
	-30.000	2.387382	-0.0024012	-0.000810	2.963310	0.8056470
	-25.000	2.395331	-0.0024153	-0.000810	2.980711	0.8036105
	-20.000	2.363953	-0.0024038	-0.000810	2.966519	0.7968776
	-15.000	2.339845	-0.0023677	-0.000810	2.921968	0.8007772
	-10.000	2.278774	-0.0023076	-0.000810	2.847799	0.8001877
	-5.000	2.225598	-0.0022247	-0.000810	2.745492	0.8106369
	0.000	2.139726	-0.0021198	-0.000810	2.616036	0.8179269
	5.000	2.062458	-0.0019959	-0.000810	2.463131	0.8373315
	10.000	1.958213	-0.0018554	-0.000810	2.289741	0.8552115
	15.000	1.863308	-0.0017006	-0.000810	2.098703	0.8878381
-45°	y	$\Gamma_{\text{pl}}/\Gamma_o$	Γ_{tot}	Γ_o	$\Gamma_{\text{tot}}/\Gamma_o$	β -factor
	-170.000	1.552613	-0.0032863	-0.000810	4.056259	0.3827697
	-165.556	1.679170	-0.0032086	-0.000810	3.960354	0.4239949
	-160.000	1.835460	-0.0030847	-0.000810	3.807426	0.4820737
	-155.556	1.945694	-0.0029720	-0.000810	3.668321	0.5304045
	-150.000	2.077463	-0.0028267	-0.000810	3.488978	0.5954360
	-145.556	2.162957	-0.0027134	-0.000810	3.349132	0.6458262
	-140.000	2.260372	-0.0025874	-0.000810	3.193611	0.7077793
	-135.556	2.314475	-0.0025057	-0.000810	3.092770	0.7483503
	-130.000	2.370347	-0.0024352	-0.000810	3.005752	0.7886038
	-125.556	2.388830	-0.0024074	-0.000810	2.971438	0.8039305
	-120.000	2.399151	-0.0024119	-0.000810	2.976993	0.8058976
	-115.556	2.380536	-0.0024470	-0.000810	3.020316	0.7881743
	-110.000	2.344784	-0.0025268	-0.000810	3.118813	0.7518194
	-105.556	2.290455	-0.0026164	-0.000810	3.229406	0.7092497
	-100.000	2.211639	-0.0027528	-0.000810	3.397763	0.6509103
	-95.556	2.125786	-0.0028744	-0.000810	3.547854	0.5991751
	-90.000	2.010382	-0.0030320	-0.000810	3.742378	0.5371937
	-85.556	1.899729	-0.0031536	-0.000810	3.892468	0.4880525
	-80.000	1.756973	-0.0032892	-0.000810	4.059839	0.4327691
	-75.556	1.630206	-0.0033770	-0.000810	4.168210	0.3911045
	-70.000	1.472505	-0.0034514	-0.000810	4.260041	0.3456552
	x	$\Gamma_{\text{pl}}/\Gamma_o$	Γ_{tot}	Γ_o	$\Gamma_{\text{tot}}/\Gamma_o$	β -factor
	-75.000	1.643088	-0.0013589	-0.000810	1.677282	0.9796135
	-70.000	1.748228	-0.0015317	-0.000810	1.890568	0.9247105
	-65.000	1.863457	-0.0016973	-0.000810	2.094967	0.8894926
	-60.000	1.958360	-0.0018520	-0.000810	2.285912	0.8567086
	-55.000	2.062613	-0.0019924	-0.000810	2.459207	0.8387309
	-50.000	2.139878	-0.0021163	-0.000810	2.612136	0.8192061
	-45.000	2.225752	-0.0022207	-0.000810	2.740996	0.8120233

	-40.000	2.278927	-0.0023040	-0.000810	2.843812	0.8013635
	-35.000	2.339992	-0.0023642	-0.000810	2.918117	0.8018843
	-30.000	2.364101	-0.0024005	-0.000810	2.962922	0.7978952
	-25.000	2.395474	-0.0024118	-0.000810	2.976869	0.8046959
	-20.000	2.387523	-0.0023985	-0.000810	2.960453	0.8064720
	-15.000	2.386400	-0.0023603	-0.000810	2.913303	0.8191388
	-10.000	2.345861	-0.0022981	-0.000810	2.836530	0.8270179
	-5.000	2.311971	-0.0022128	-0.000810	2.731245	0.8464897
	0.000	2.241011	-0.0021070	-0.000810	2.600657	0.8617095
	5.000	2.176866	-0.0019820	-0.000810	2.446370	0.8898352
	10.000	2.080323	-0.0018402	-0.000810	2.271347	0.9158981
	15.000	1.991129	-0.0016847	-0.000810	2.079414	0.9575430
	20.000	1.876104	-0.0015190	-0.000810	1.874892	1.0006465
	25.000	1.769328	-0.0013459	-0.000810	1.661236	1.0650671

Figure (2.17) shows both β - and Purcell enhancement factors plots (plotted with the same Excel sheet's values) as the location of the QE around the y-coordinate and x-coordinate is varied.

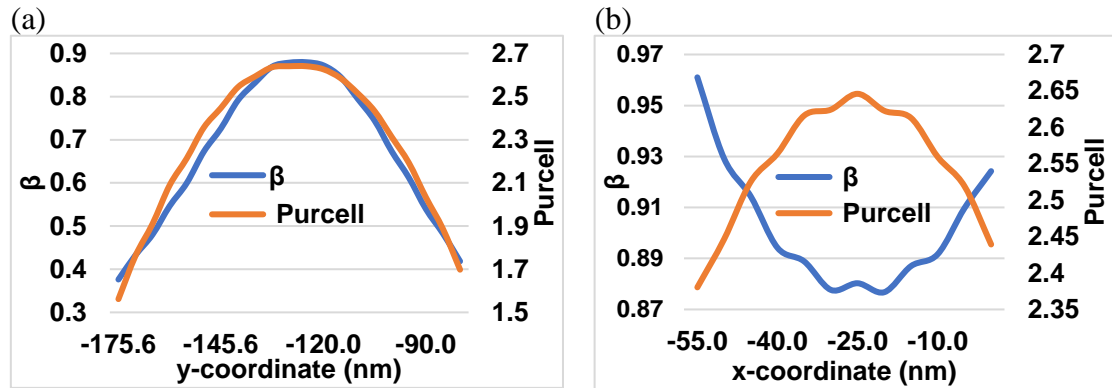


Figure 2.17: β -factor and Purcell enhancement factor as a function of (a) y-coordinate. (b) x-coordinate for 0° output polarization

The maximum Purcell enhancement factor is located at $y = -126.6$ nm with a value of 2.64 as shown in Figure (2.13.c) and Figure (2.17.a). The moderate value of the Purcell enhancement factor is due to the relatively wide transversal area of the high refractive index (GaP) material at the QE's emission wavelength. However, a high β -factor of 88% at this optimum position was achieved because the QE position is relatively far away from the Al bar that is responsible for the coupling losses. The Al bar is a lossy material because of the imaginary part of its refractive index at the QE's emission wavelength.

To find the optimum position at the x-coordinate, the optimum position ($y = -126.6$ nm) of the QE is fixed and the x-coordinate is varied. Figure (2.17.b) shows both β - and Purcell enhancement factors as a function of the x-coordinate variations. Figure (2.17.b) shows an optimum position of x-coordinate at -25 nm (the Highest Purcell enhancement factor) and a β -factor of 88%. If the QE is shifted around the optimum position in the x-coordinate or the y-coordinate, the Purcell enhancement factor decreases according to the decrease of the QE's emission coupling to the associated HPW mode as shown in Figures (2.9.a), (2.17.a), and (2.17.b). Moreover, the total decay rate increases as the QE is shifted in the y-coordinate. This is why the β factor decreases as the QE is shifted in both $+y$ and $-y$ directions as shown in Figure (2.17). The decrease of β -factor in $+y$ is due to the increment in the non-radiative decay rate that appears in the denominator of β -factor, while the β -factor in $-y$ -direction decreases because the QE becomes far away from the HPW region and approaches the grounded substrate region. The β -factor increases as the QE is shifted from the optimum position at y-coordinate by $-x$ and $+x$ as shown in Figure (2.17.b). This is because the total decay rate includes the radiative and nonradiative decay rates excluding the plasmonic decay rate due to the decrement of the electric field in both $-x$ and $+x$ shifts as shown in Figure (2.9.a). This fact is true for each polarization as will be shown in Figure (2.19). Hence, the optimum position for the emitter in the case of 0° output polarization in x- and y- coordinates is -25 nm and -126.6 nm, respectively. The calculation of Γ_{pl} and β -factor methodology was verified by reproducing Γ_{pl} and β -factor in [73] as shown in Figure (2.18).

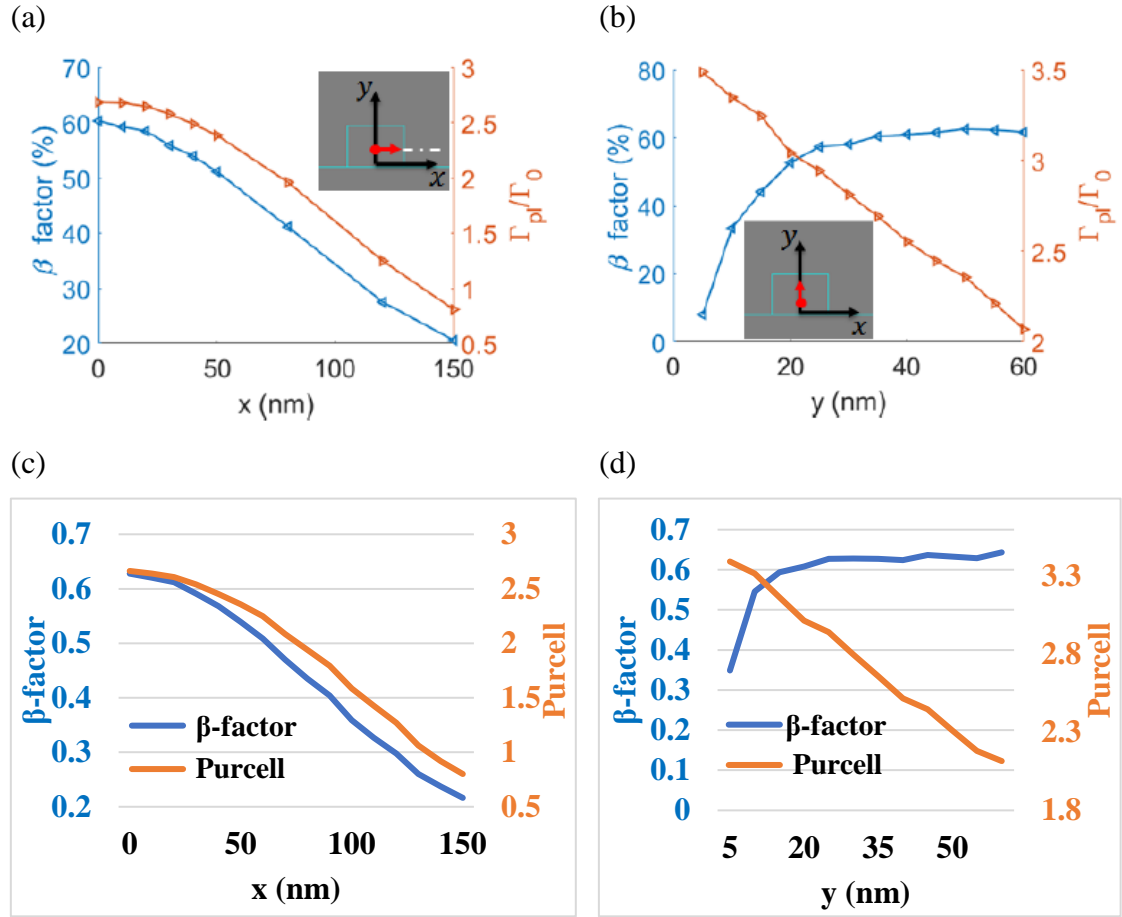


Figure 2.18: The β -factor and Purcell enhancement factor versus x - and y - directions for (a), (b) [73] and (c), (d) reproduced results, respectively

The calculation of Γ_{pl} and β -factor is performed in each case of output polarization. Because each output polarization has a specific length of Al bar, different electric field components inside the GaP region are propagated. Figure (2.19) shows the variation in β - and Purcell enhancement factors when the QE position is varied in y - and x - coordinates, respectively, for 90° , 45° , and -45° output polarization. Table (2.4) summarizes the optimal x - and y - coordinates with their corresponding Purcell and β -factor for each output polarization.

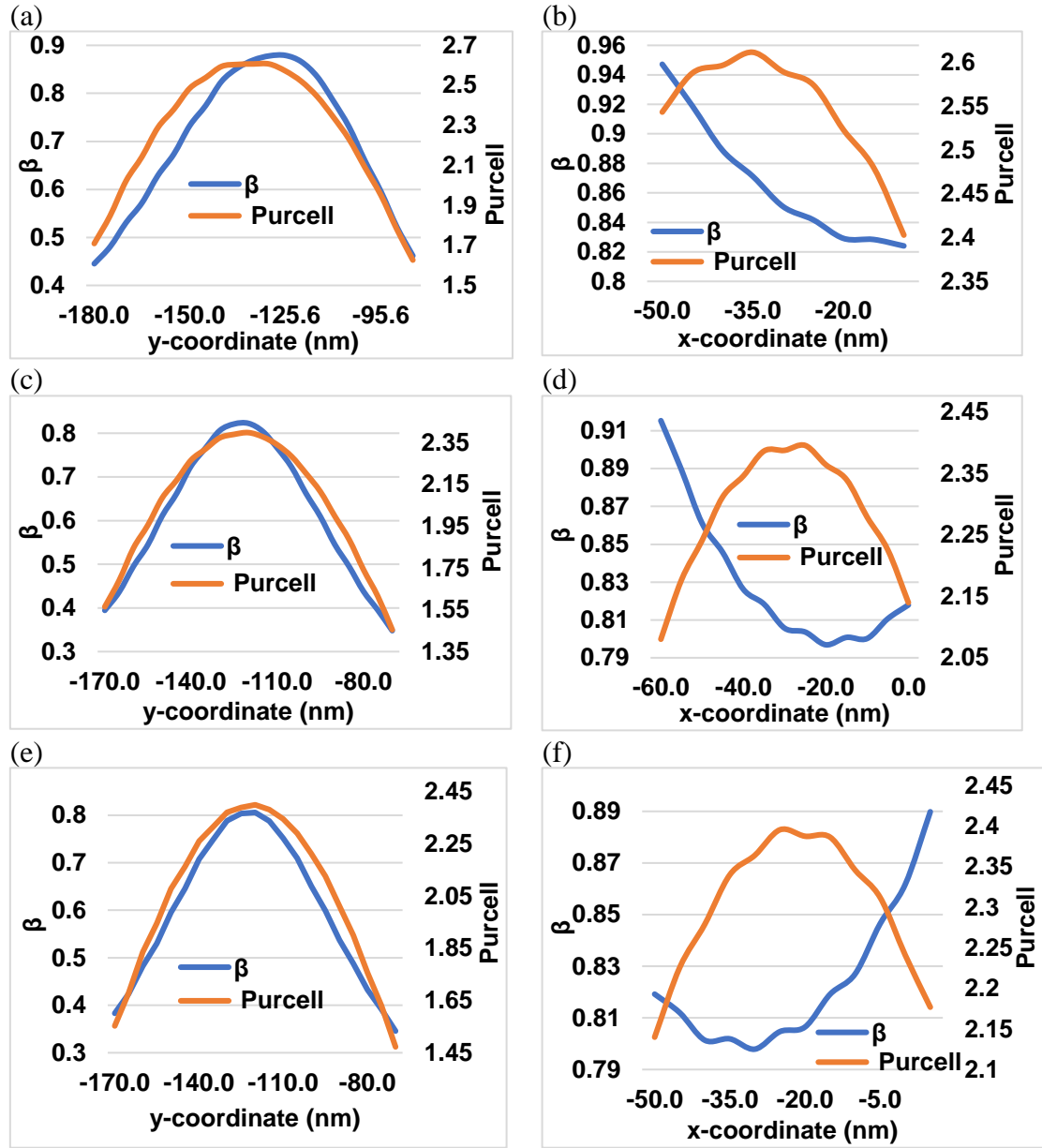


Figure 2.19: β -factor and Purcell enhancement factor as a function of y- and x-coordinates, respectively, (a) and (b), for 90° output polarization, (c) and (d), for 45° output polarization, and (e) and (f), for -45° output polarization.

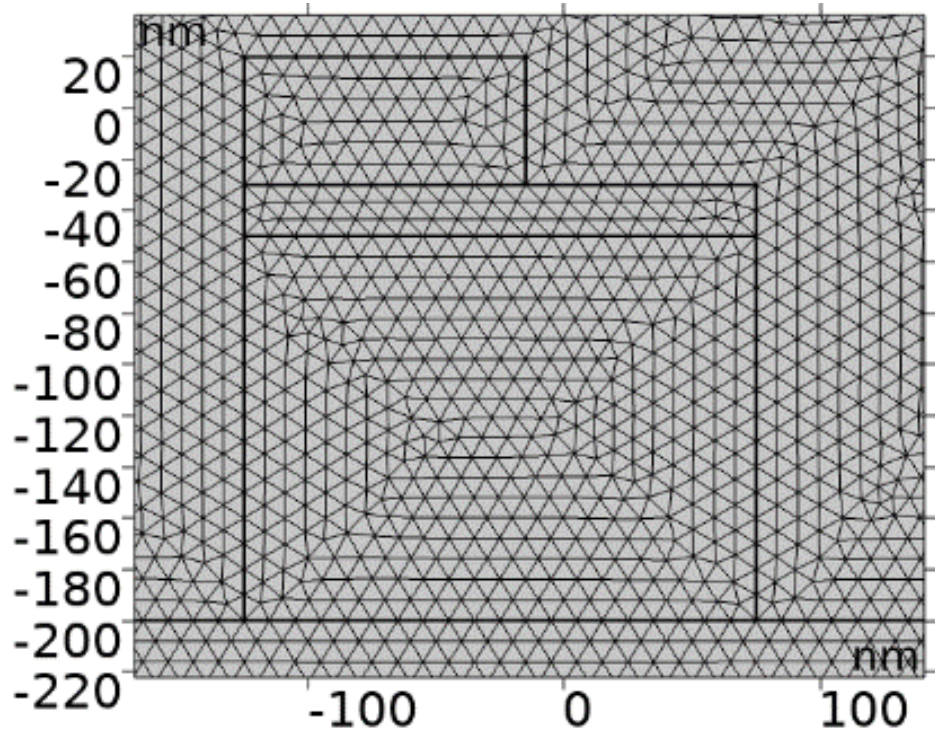
Table 2.4: The optimum position of the QE for each output polarization and the corresponding Purcell enhancement factor and β -factor

Output polarization	x-coordinate (nm)	y-coordinate (nm)	Purcell factor	β -factor
0°	-25	-126.6	2.64	88%
90°	-35	-132.2	2.6	87%
45°	-25	-120	2.4	80%
-45°	-25	-120	2.4	80%

The 2D and 3D simulation frameworks are truncated by first-order scattering boundary conditions that provide minimum reflections and more accurate

solutions. The maximum size of the used mesh is 10 nm with free triangular topology in a 2D framework. In a 3D framework, a physics-controlled mesh with an extra-fine resolution was used as shown in Figure (2.20).

(a)



(b)

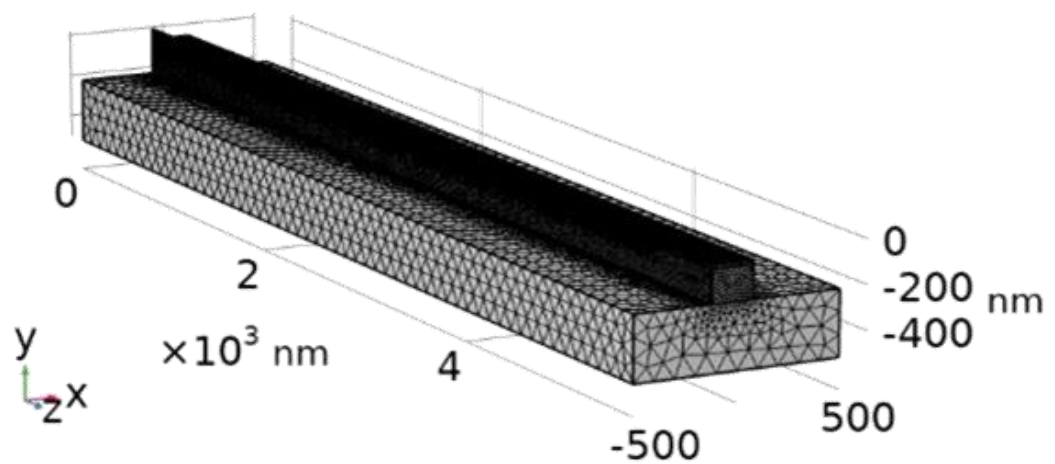


Figure 2.20: The mesh configuration for the (a) 2D and (b) 3D models

2.5. Tuning the output polarization

The first step in tuning the required output polarization is to observe its rotation degree by changing the Al width to obtain a suitable θ , i.e. 45° and $22.5^\circ/-22.5^\circ$ that gives an output polarization of 90° and $45^\circ/-45^\circ$, respectively. The values of Al width for the required θ s and the corresponding conversion lengths are shown in Table (2.2). Figure (2.21) shows the magnetic field distribution for θ equals 45° and $22.5^\circ/-22.5^\circ$. To get θ of -22.5° , the position of the Al bar is changed as shown in Figure (2.21.d).

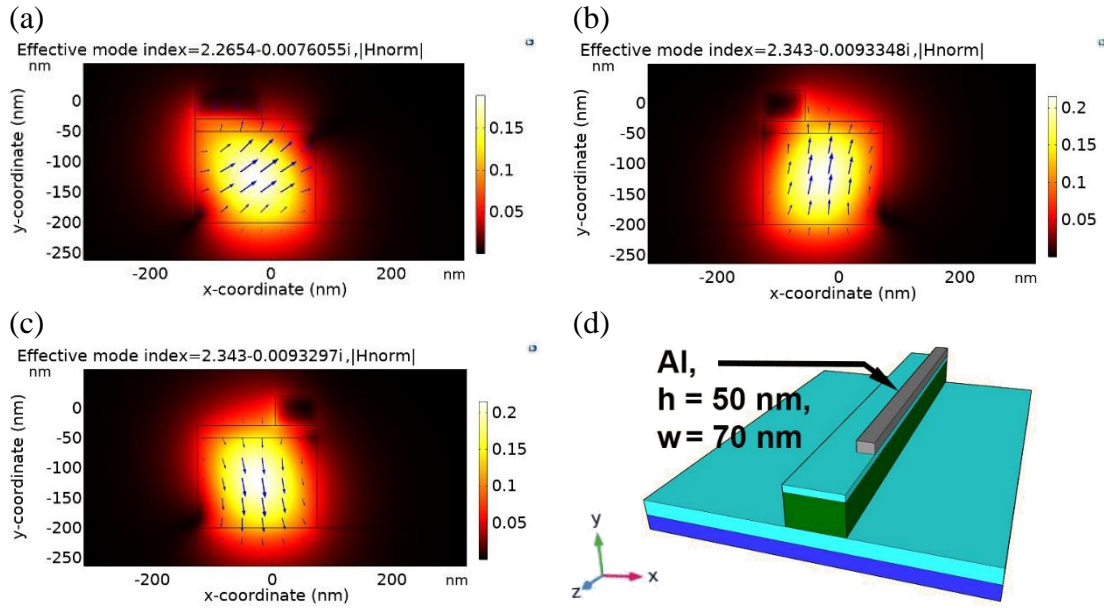


Figure 2.21: The $|H_{norm}|$ when Al width is (a) 110 nm ($\theta = 45^\circ$), (b) 70 nm ($\theta = 22.5^\circ$), (c) 70 nm ($\theta = -22.5^\circ$), (d) Schematic of the structure when θ is -22.5° . Arrows represent the magnetic field distribution

However, the designed Al width values in Table (2.4) do not yield an optimum performance as shown in Figure (2.21). The measured θ in Figure (2.21.a) shows a value of 35° , while Figure (2.21.b) and Figure (2.21.c) show θ s of 13.5° and -12.5° , respectively. The inaccurate θ s result from the high confinement of the electric field in the GaP region. Consequently, the electric field in both directions (x and y) has unsymmetrical distribution and they have a different center point for their maximum value. For example, both components of the electric field in the x and y directions for 90° output polarization are shown in Figure (2.22).

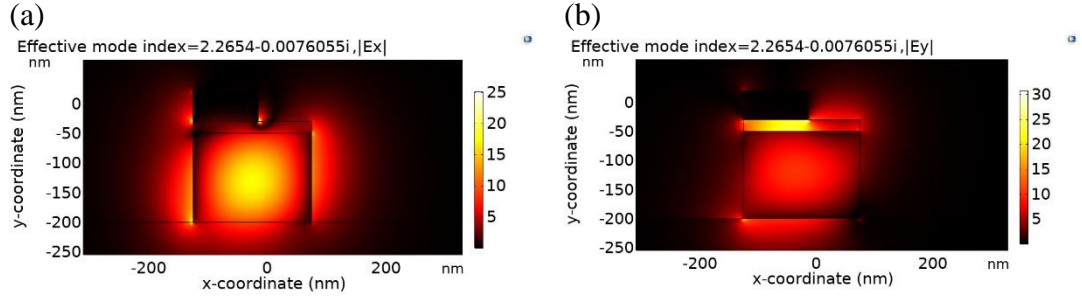


Figure 2.22: The electric field components distribution at 90° output polarization (Al width equals 110 nm) (a) E_x , (b) E_y

The power conversion efficiency from 0° output polarization to 90° output polarization is defined as [109]:

$$\text{PCE} = \frac{P_{\text{TE}}}{P_{\text{TE}} + P_{\text{TM}}} = \frac{|E_y|^2}{|E_y|^2 + |E_x|^2}, \quad (2.5)$$

where P_{TE} is the power of the TE mode, P_{TM} is the power of TM mode, E_y is the y-component of the output electric field, and E_x is the x-component of the output electric field. The PCE from TM mode to a 45°/-45° linearly polarized output light is defined as:

$$\text{PCE} = \frac{P_{\text{TE}}}{P_{\text{TM}}} = \frac{|E_{y,x}|^2}{|E_{x,y}|^2}, \quad (2.6)$$

where $E_{y,x}$ is the smallest electric field component and the $E_{x,y}$ is the opposite field component to $E_{y,x}$.

The unsymmetrical distribution of x- and y-components of the electric field shown in Figure (2.22) results in different spatial centers for the maximum of the electric field components. The mismatch in these spatial centers causes an imperfect conversion of the x-component of the electric field to the y-component of the electric field along the HPW's propagation length. Consequently, a considerable amount of the x component will remain at the HPW output resulting in a reduction in the PCE at 90° output polarization. Furthermore, this unsymmetrical distribution in the case of 45°/-45° output polarization leads to an unequal amount of the x- and y-components of the electric fields at the HPW's output that, consequently, decreases the PCE in this case. The Al bar's width can tune the x- and y-

components of the electric field to the same optimum position so that most of the x-component of the electric field can be converted to y-component in the case of 90° output polarization. Similarly, the Al width tuning can convert the x-component of the input electric field to equal amounts of x- and y-components of the electric field at the HPW's output.

To find the Al width that has a maximum PCE, the variation of the PCE against the Al width is plotted for the same designed conversion length listed in Table (2.2) as shown in Figure (2.23.a).

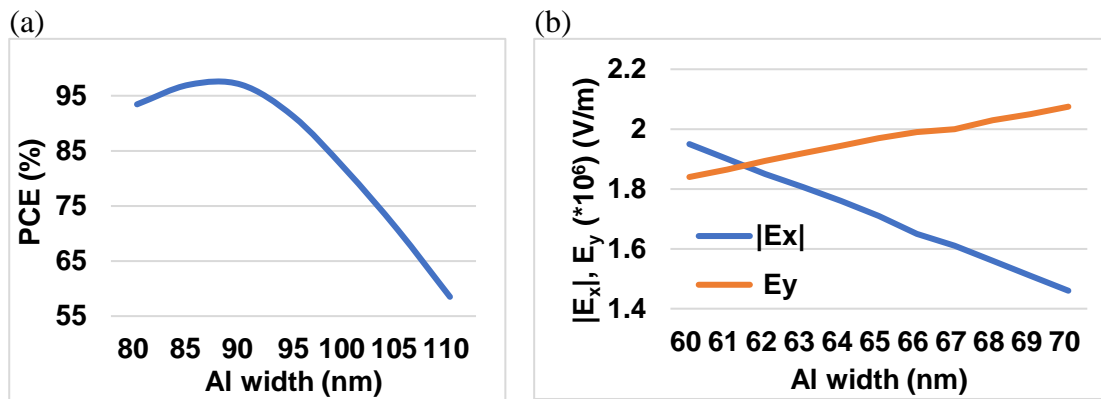


Figure 2.23: (a) PCE against the variation in Al width at the designed conversion length for 90° output polarization, (b) The $|E_x|$, and E_y variations against Al width for $45^\circ/-45^\circ$ output polarization

The Al width of 90 nm increases the PCE to 97%, where the polarization is changed from 0° to 90° as shown in Figure (2.23.a) and calculated theoretically in Figure (2.24.b).

On another hand, a 45° linearly polarized light has an equal amplitude for both x and y electric fields and they should be in phase. The designed value of 70 nm Al width does not result in an exact similar value for both electric field components in the x and y directions because of their unsymmetrical distribution in the GaP area. A slight change in Al width results in precise equal values for both electric field components in x and y directions as shown in Figure (2.23.b). Consequently, an Al width of 62 nm with the same conversion length, as listed in Table (2.2), for $45^\circ/-45^\circ$ output polarization is considered, too. The absolute value for E_x in Figure (2.23.b)

results in positive PCE for both $45^\circ/-45^\circ$ since the electric field components are antiphase as shown in Figure (2.24.b).

It is worth mentioning that the variation of the Al width value from the designed values in Table (2.2) might lead to a negligible variation in the optimum spatial coordinates of the QE obtained in Section (2.4). However, a slight change in Al width leads to a significant change in the output polarization state of the emitted photons in both cases of 90° and $45^\circ/-45^\circ$ output polarization as shown in Figure (2.23).

By placing a line probe along the propagation direction in the z-axis, i.e., at the optimum QE's position shown in Table (2.2) for each output polarization, it can be shown how the electric field components vary. The electric field distributions are continuous and show no discrete jumps along the total device's length that include both HPW and photonic waveguide. The continuity of the electric fields is a clear indication that there are negligible reflections when the electric fields travel along the entire device's length that including both the photonic and hybrid plasmonic waveguides. Figure (2.24) shows the electric field components' distribution against the propagation distance for 0° , 90° , 45° , and -45° . The intensity of the electric field in the x-direction is reduced by a factor of $1/e$, due to the plasmonic losses, at the end of the calculated plasmonic propagation length (HPW's output) as shown in Figure (2.24.a). Meanwhile, the electric field in the y-direction has a negligible contribution to the total electric field. For the case of rotating 0° (TM) to 90° (TE) output polarization, a PCE of 97% was achieved as shown in Figure (2.24.b).

On the other hand, a PCE of converting a 0° linearly polarized light to a 45° linearly polarized light, which is the power ratio of both components at the output, of 98.43% was obtained as shown in Figure (2.24.c). It is important to note that the propagation direction is in -z-direction and, therefore, the E_x and E_y seem as they are anti-phased. Although the E_x and E_y have antiphase, however, it does not contradict the fact that the output

photons are linearly polarized at 45° . The -45° output polarization has two similar values for the electric field components in the x- and y- directions but they are anti-phased as shown in Figure (2.10.d) and, consequently, have the same PCE.

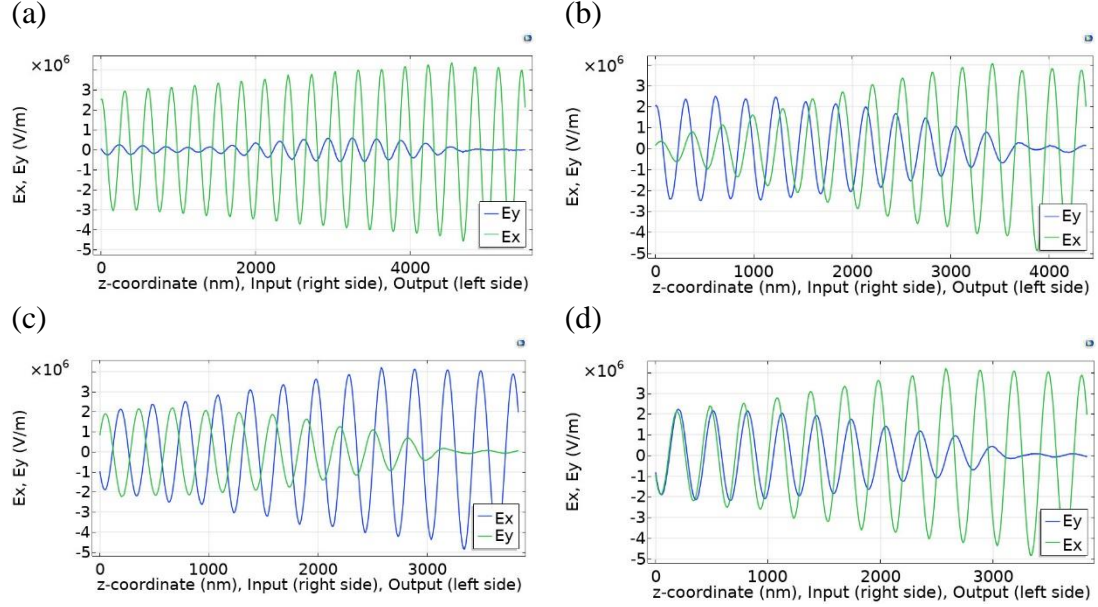


Figure 2.24: The distribution of the electric field components against z -coordinate for (a) 0° . (b) 90° . (c) 45° . and (d) -45° output polarization

Figure (2.25) visualizes the relationship between the input and output polarization when the QE is situated at the optimum positions listed in Table (2.4) for each output polarization. The input field is probed by a 2D surface plane at 300 nm (and it could be any value preceding the HPW) before the QE, while the output field is probed by a 2D surface plane at the end of the HPW conversion length.

As indicated in Figure (2.25), the polarization in the high-intensity regions at the GaP area is perfectly oriented toward the required output polarization states. Although there are spurious components of the polarization in low-intensity areas, there is a rare probability that the emitted photons from an experimental quantum emitter, i.e., NV, SiV, etc. propagate in the low-intensity path. This is because the intensity and the number of photons are linearly proportional. Thus, the majority of the emitted photons are concentrated in high-intensity regions inside the GaP area.

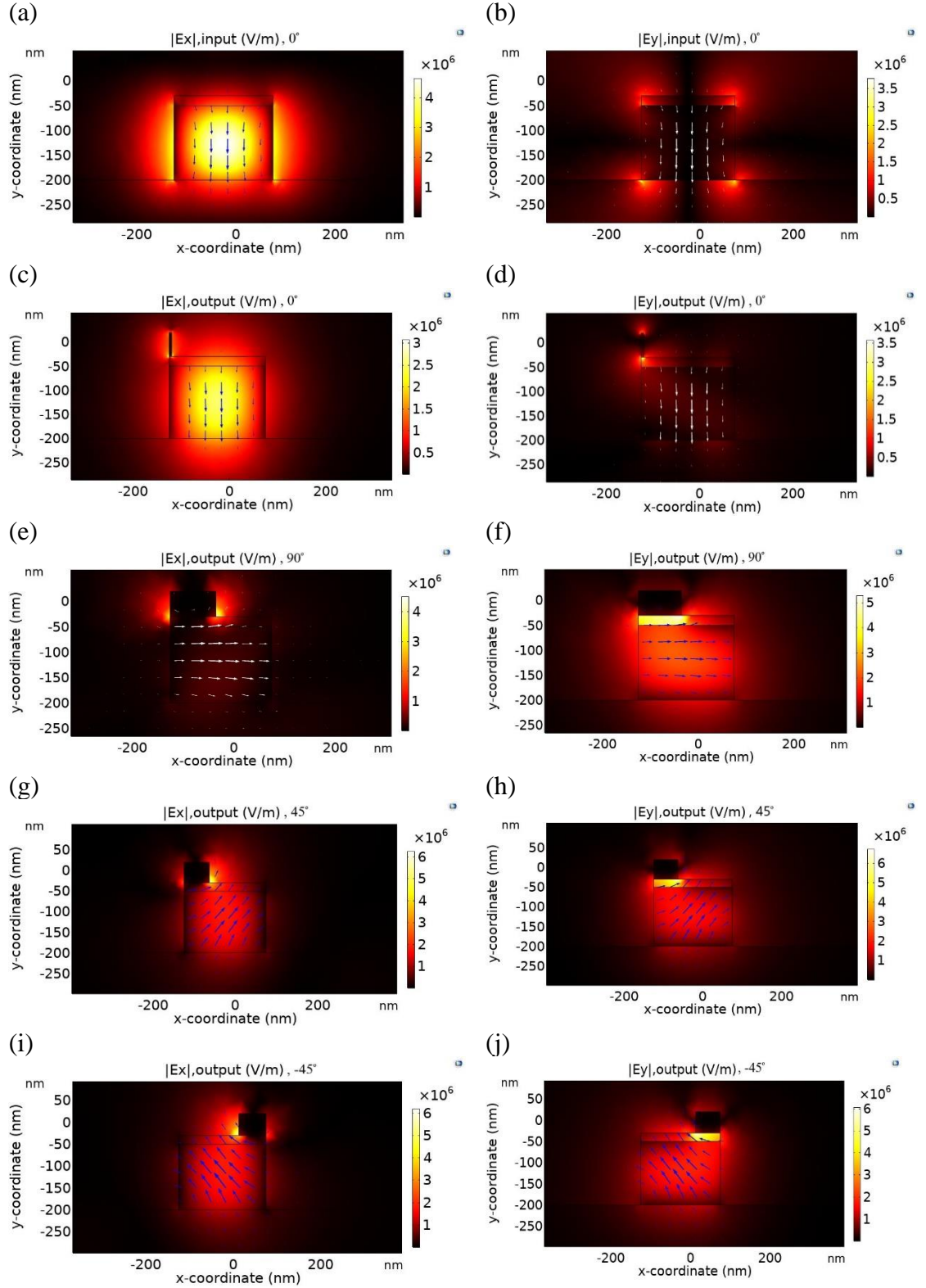


Figure 2.25: The input and output electric field distribution for both x and y components, respectively, for 0° , 90° , 45° , and -45° output polarization. The figures are arranged as a) $|E_x|_{\text{input}}$ at 0° , b) $|E_y|_{\text{input}}$ at 0° , c) $|E_x|_{\text{output}}$ at 0° , d) $|E_y|_{\text{output}}$ at 0° , e) $|E_x|_{\text{output}}$ at 90° , f) $|E_y|_{\text{output}}$ at 90° , g) $|E_x|_{\text{output}}$ at 45° , h) $|E_y|_{\text{output}}$ at 45° , i) $|E_x|_{\text{output}}$ at -45° , j) $|E_y|_{\text{output}}$ at -45° .

Chapter Three

The modeling techniques of the second-order correlation function $g^{(2)}(\tau)$ for a quantum emitter

Chapter 3

The modeling techniques of the second-order correlation function $g^{(2)}(\tau)$ for a quantum emitter

3.1. Introduction

This chapter describes the detailed steps of analysis and a comprehensive investigation of the numerical techniques required to prove the single-photon emission from any type of QE after being coupled to any nanostructure including a PW. The QE's dynamics of the excitation and emission events are considered as energy transitions considering two states (levels) of an ideal quantum yield and three states with an ideal and non-ideal quantum yield. The fundamental rate equations of modeling QEs depend on the predicted scenario of transitions between the energy levels of the QE.

The findings of the proposed work could be considered as a guideline to simulate and predict the coupling effects on the $g^{(2)}(\tau)$ behavior for a QE before the experimental fabrication. The detailed steps of the analysis presented in this chapter are as follows:

1. Observing the experimental photophysical parameters of the QE.
2. Studying the energy transition dynamics of the QE considering two different scenarios of three energy levels. Furthermore, studying the two energy levels system.
3. Modeling, plotting, and comparing the resultant $g^{(2)}(\tau)$ behavior with experimentally-based results.
4. Modeling the $g^{(2)}(\tau)$ of the proposed structure in Chapter 2 for each case of output polarization.

The experimental photophysical parameters of the NV centers are considered as a basis for the modeling steps. Moreover, MATLAB 2019 and Quantum toolbox in Python (QuTiP) softwares were used to model and verify the aforementioned steps of analysis.

3.2. The NV emission dynamics with unity quantum yield

The scenario of the transitions between the three energy levels shown in Figure (1.23) differs according to the assumption of how these three energy levels interact. Besides, the transitions are modified by the Purcell effect when the NV center is coupled to nanostructures. The excitation rate k_{12} and the spontaneous emission rate k_{21} are related to the $|1\rangle$ and $|2\rangle$ levels. The k_{32} and k_{23} couple the $|3\rangle$ and $|2\rangle$ levels, which represent the nonradiative transition rate. The population dynamics between the energy levels follow Einstein's rate equations as [52]

$$\begin{pmatrix} \dot{\rho}_1 \\ \dot{\rho}_2 \\ \dot{\rho}_3 \end{pmatrix} = \begin{pmatrix} -k_{12} & k_{21} & 0 \\ k_{12} & -k_{21} - k_{23} & k_{32} \\ 0 & k_{23} & -k_{32} \end{pmatrix} \begin{pmatrix} \rho_1 \\ \rho_2 \\ \rho_3 \end{pmatrix}, \quad (3.1)$$

where $\dot{\rho}_x = \partial \rho_x / \partial t$ is the time rate of change of the population in levels $x = 1, 2$, and 3 with an initial condition of ($\rho_1 = 1$, $\rho_2 = 0$, and $\rho_3 = 0$, $\sum \rho_x = 1$). In the following scenario, the nonradiative transition from the shelving level to the ground level (k_{31}) is omitted as it is three-fold less than all other decay rates [52]. Also, a unity quantum yield is assumed for the NV center model presented in Figure (1.23) [52].

The photon's emission probability is proportional to ρ_2 and, hence, the $g^{(2)}(\tau)$ could be deduced by normalizing the $\rho_2(t)$ to $\rho_2(t = \infty)$ to obtain [52]

$$g^{(2)}(\tau) = 1 + c_2 e^{-\frac{\tau}{\tau_2}} + c_3 e^{-\frac{\tau}{\tau_3}}, \quad (3.2)$$

where the coefficients $c_{2,3}$ and decay times $\tau_{2,3}$ are different for different excitation laser power and are defined by [52]:

$$\tau_{2,3} = \frac{2}{A \pm \sqrt{A^2 - 4B}}, \quad (3.3)$$

$$c_2 = \frac{1 - \tau_2 k_{32}}{k_{32}(\tau_2 - \tau_3)}, \quad (3.4)$$

$$c_3 = -1 - c_2, \quad (3.5)$$

$$A = k_{12} + k_{21} + k_{32} + k_{23}, \quad (3.6)$$

$$B = k_{12}k_{23} + k_{12}k_{32} + k_{21}k_{32}, \quad (3.7)$$

and the $\rho_2(t = \infty)$ is the $|2\rangle$'s population at steady-state, which equals [52]

$$\rho_2(t = \infty) = \frac{k_{23}k_{12}}{B}, \quad (3.8)$$

The $\tau_{2,3}$ and $\tilde{c}_{2,3}$ (where $c_{2,3} = \tilde{c}_{2,3}/p_f^2$) parameters are deduced from the least square fitting of Equation (3.2) with the experimentally measured $g^{(2)}(\tau)$ shown in Figure (3.1) [52]. p_f is the probability that the photon is emitted because of the NV's emission and not because of background noise ($p_f = S/(S+N)$), where S is the NV center's emission and N is the background emission. The corresponding values of the $c_{2,3}$ and $\tau_{2,3}$ are drawn for each excitation power as shown in Figure (3.2). Under high excitation power, the values of k_{21} , k_{23} , and k_{32} were obtained as $(20.1 \text{ ns})^{-1}$, $(31 \text{ ns})^{-1}$, and $(127 \text{ ns})^{-1}$, respectively [52].

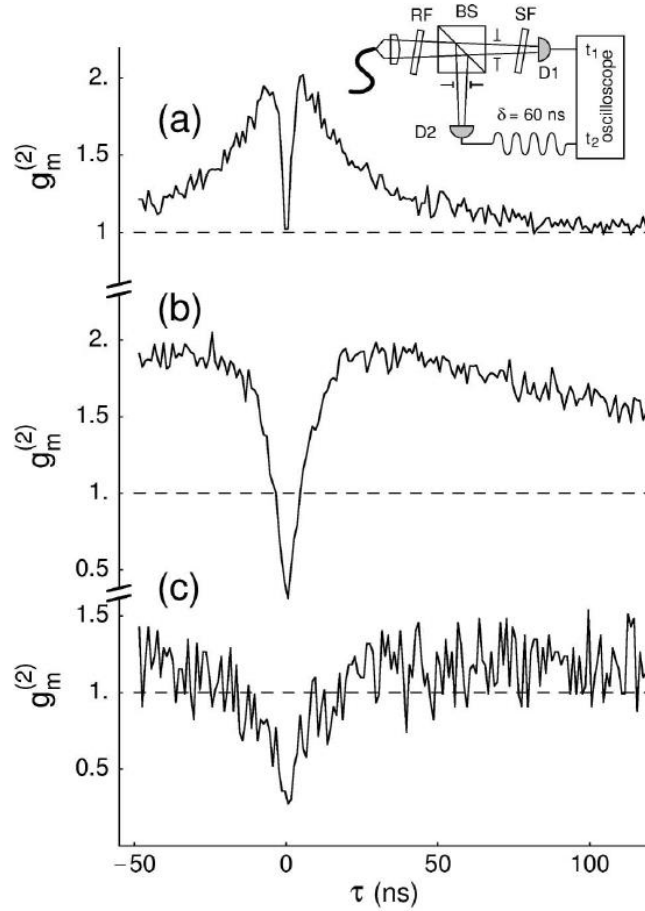


Figure 3.1: The experimental $g^{(2)}(\tau)$ under excitation power of (a) 0.16, (b) 1.6, and (c) 30 of the saturation power P_{sat} [52]

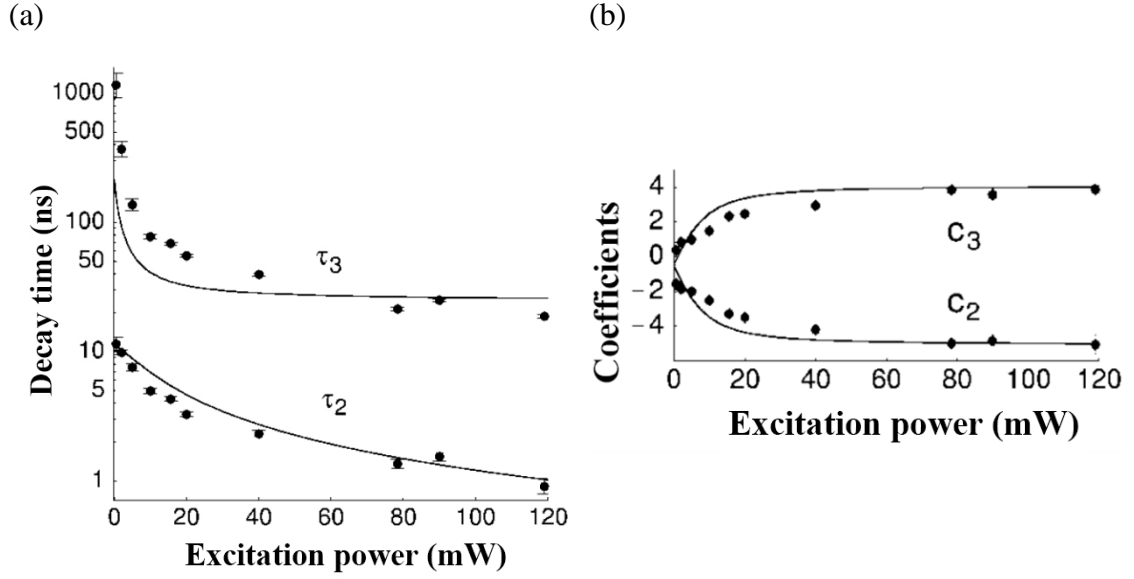


Figure 3.2: The values of (a) $\tau_{2,3}$ and (b) $c_{2,3}$ obtained from the least square fitting of the data shown in Figure (3.1) [52]

The experimental $g^{(2)}(\tau)$ data of the aforementioned NV's emission was modeled by [73] to prove the NV's single-photon emission. The $g^{(2)}(0)$ was less than 0.5 before and after coupling to a dielectric-loaded surface plasmon polariton (DLSP) waveguide as shown in Figure (3.3) [73].

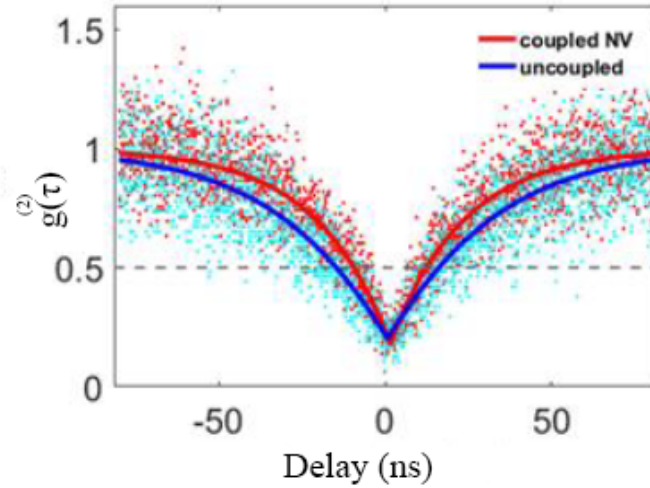


Figure 3.3: The fitting of the experimental $g^{(2)}(\tau)$ data in [73] using the model in [52]

The coupling of the NV center to a DLSP waveguide modifies the total decay rate, which is the sum of k_{21} , k_{23} , and k_{32} . This modification is interpreted by the increase of the radiative decay rate due to the Purcell enhancement factor.

For example, the Purcell enhancement factor, which is defined as the plasmonic decay rate (Γ_{pl}) to the decay rate of the NV in a vacuum (Γ_0), is

3 [73]. Consequently, this results in a 2-fold increase in the nonradiative decay rate because the total decay rate after coupling the NV to a DLSP waveguide was 5 as demonstrated in [73]. As a result, the decay rate parameters are modified as $3k_{21}$ and $2(k_{23} + k_{32})$. Moreover, the excitation laser repetition rate (k_{12}) is fixed at $(400 \text{ ns})^{-1}$ as used in [73] before and after coupling the NV to the DLSP waveguide.

Equation (3.2) lacks the consideration of p_f when it is required to plot $g^{(2)}(\tau)$ in MATLAB. Consequently, the $g^{(2)}(\tau)$ modeling equation in [111], which includes p_f , is considered instead of Equation (3.2) when the modeling results are plotted in the next steps. The modified $g^{(2)}(\tau)$ equation is [111]:

$$g^{(2)}(\tau) = 1 - p_f^2 + p_f^2 \left(1 + c_2 e^{-\frac{|\tau|}{\tau_2}} + c_3 e^{-\frac{|\tau|}{\tau_3}} \right), \quad (3.9)$$

where p_f equals 88% in comparison with the experimental value obtained in [52]. It is worth mentioning that [111] does not include the experimental values for k_{21} , k_{32} , and k_{23} because $c_{2,3}$ and $\tau_{2,3}$ were obtained by fitting the experimental data of $g^{(2)}(\tau)$, only. Also, the scenario of the population dynamics of the QE in [111] differs from the scenario demonstrated in this section because [111] investigated SiV centers, while [52] investigated NV centers. Consequently, the modified decay rate parameters cannot be plugged in [111] to plot $g^{(2)}(\tau)$ because of the missing k parameters.

To compare the theoretical (modeled) values of $g^{(2)}(\tau)$ with the experimental values obtained by [73], before and after coupling to a DLSP waveguide, both cases are plotted by MATLAB code shown in Appendix (B). The experimental and numerical $g^{(2)}(\tau)$ plots are shown in Figure (3.4).

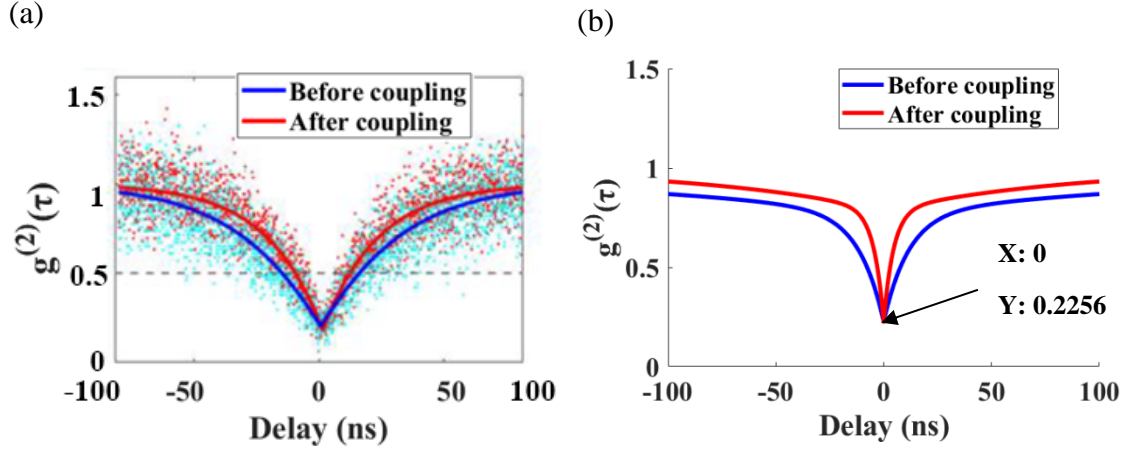


Figure 3.4: The $g^{(2)}(\tau)$ versus time delay plots by (a) experimental fitting [73], (b) theoretical modeling of the experimental values in [52]

Both Figure (3.4.a) and Figure (3.4.b) have the same behavior. However, the slight changes are due to the differences in k values between [73] and [52] because they were measured experimentally. On the other hand, the experimental $g^{(2)}(0)$ was 0.26 [52], while the theoretical $g^{(2)}(0)$ is 0.2256 as shown in Figure (3.4.b) due to the experimental mismatches and fabrication tolerance.

The $(\Gamma_{pl}/\Gamma_o, \Gamma_{tot}/\Gamma_o)$ values of the proposed structure in Chapter 2 are (2.64, 3), (2.6, 3), (2.4, 2.9), and (2.4, 3) for 0° , 90° , 45° , -45° output polarization, respectively, as shown in Table (2.3). The values of $(\Gamma_{pl}/\Gamma_o, \Gamma_{tot}/\Gamma_o)$ modify the decay rate parameters of the NV center as $(2.64 k_{21}, 0.36(k_{23} + k_{32}))$, $(2.6 k_{21}, 0.4(k_{23} + k_{32}))$, $(2.4 k_{21}, 0.5(k_{23} + k_{32}))$, and $(2.4 k_{21}, 0.6(k_{23} + k_{32}))$ for 0° , 90° , 45° , -45° output polarization, respectively. The modified k parameters are substituted in the code presented in Appendix (B) to plot the $g^{(2)}(\tau)$. Consequently, the described methodology in this section yields a $g^{(2)}(\tau)$ less than 0.5 for each case of output polarization for the proposed structure as shown in Figure (3.5). Section (3.2)'s methodology could be summarized in the diagram shown in Figure (3.6).

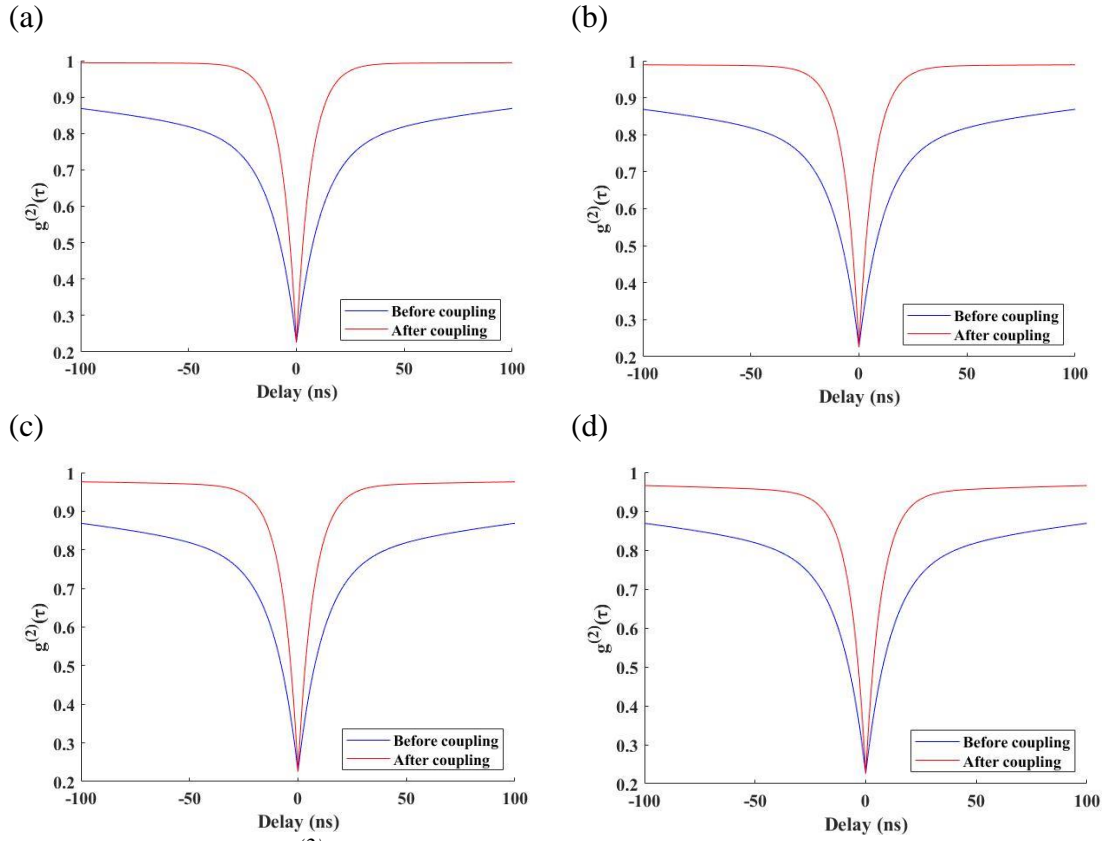


Figure 3.5: The $g^{(2)}(\tau)$ of the proposed structure in Chapter 2 with an output polarization of (a) 0° , (b) 90° , (c) 45° , and (d) -45° using Section (3.2)'s methodology

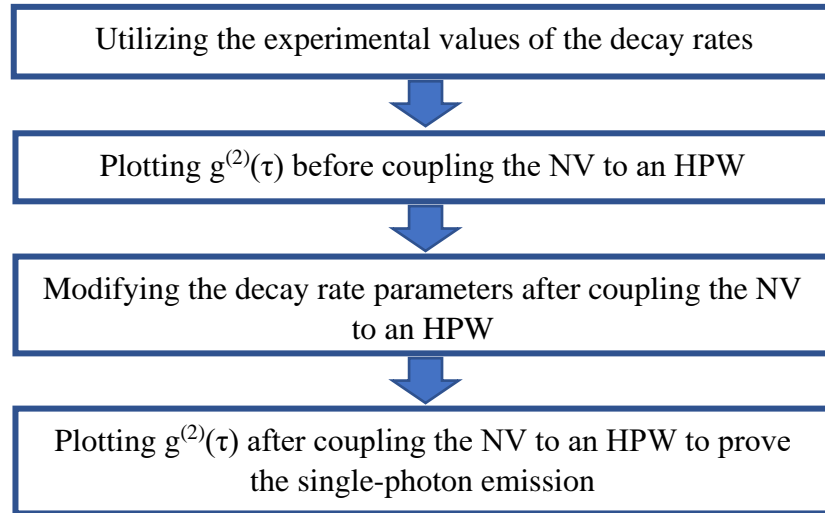


Figure 3.6: The diagram for the calculation of $g^{(2)}(\tau)$ after coupling an NV center to an HPW

3.3. The NV emission dynamics with less than unity quantum yield

The emission dynamics presented in Section (3.2) need to be modified because the NV center's quantum yield was found experimentally to be less than unity (in bulk diamonds) down to 0.6~0.7 (in nanodiamonds) [112]. The

transition rate between levels 3 to 2 and 1 to 3 is omitted because the NV center is not excited at these transition levels.

The modified NV center's emission dynamic is presented in Figure (3.7.a) [112]. The modified NV center's emission dynamic is similar to the SiV center's emission dynamics presented in [111] as shown in Figure (3.7.b).

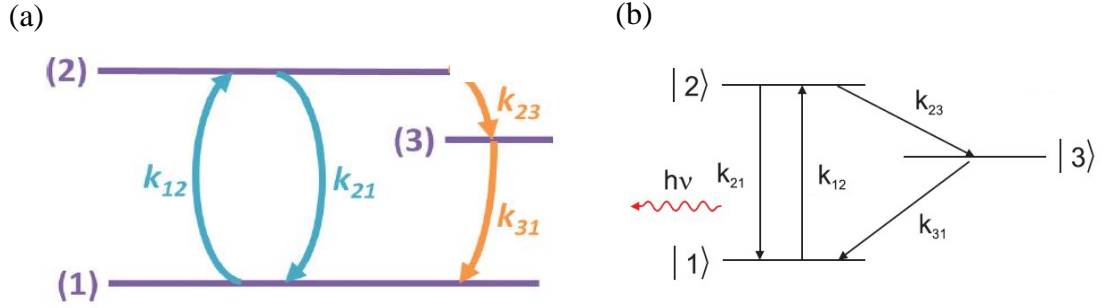


Figure 3.7: (a) The modified NV center's emission dynamic [112], (b) The SiV center's emission dynamic in [111]

Einstein's rate equations for the emission dynamics described in Figure (3.7) are [112]

$$\begin{pmatrix} \dot{\rho}_1 \\ \dot{\rho}_2 \\ \dot{\rho}_3 \end{pmatrix} = \begin{pmatrix} -k_{12} & k_{21} & k_{31} \\ k_{12} & -k_{21} - k_{23} & 0 \\ 0 & k_{23} & -k_{31} \end{pmatrix} \begin{pmatrix} \rho_1 \\ \rho_2 \\ \rho_3 \end{pmatrix}, \quad (3.10)$$

with $\sum \rho_x = 1$ and an initial condition of ($\rho_1 = 1$, $\rho_2 = 0$, and $\rho_3 = 0$). The $g^{(2)}(\tau)$ modeling equation for the dynamics shown in Figure (3.7) were derived as [112]

$$g^{(2)}(\tau) = 1 - p_f^2 + p_f^2 (1 - \beta e^{-\gamma_1 \tau} + (\beta - 1)e^{-\gamma_2 \tau}), \quad (3.11)$$

Where,

$$\gamma_1 \approx k_{12} + k_{21}, \quad (3.12)$$

$$\gamma_2 \approx k_{31} + \frac{k_{12}k_{23}}{k_{12} + k_{21}}, \quad (3.13)$$

$$\beta \approx 1 + \frac{k_{12}k_{23}}{k_{31}(k_{12} + k_{21})}, \quad (3.14)$$

and the decay rate parameters are derived as [112]

$$k_{21} = \gamma_1 - k_{12}, \quad (3.15)$$

$$k_{31} = \frac{\gamma_2}{\beta}, \quad (3.16)$$

$$k_{23} = \frac{\gamma_1 \gamma_2 (\beta - 1)}{\beta k_{12}}, \quad (3.17)$$

The determination of γ_1 , γ_2 , and β and, consequently, the k parameters was done by fitting Equation (3.11) with the experimental data of the $g^{(2)}(\tau)$ for each case of excitation power. The experimental $g^{(2)}(\tau)$ graphs for the NV^0 and NV^- are shown in Figure (3.8.a) and Figure (3.8.b), respectively [112].

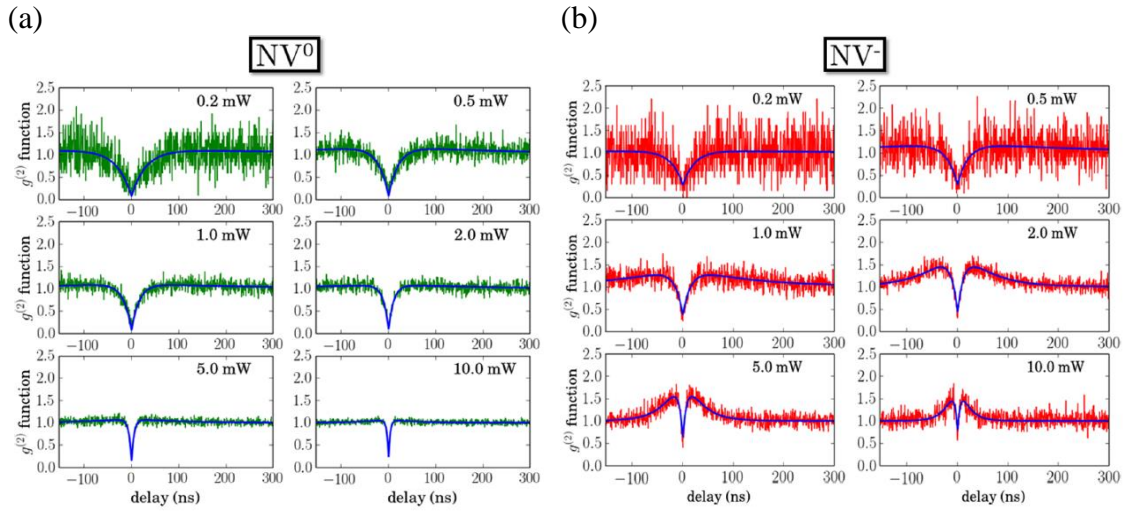


Figure 3.8: The $g^{(2)}(\tau)$ experimental graphs for different excitation powers from 0.2 mW to 10 mW for (a) NV^0 , and (b) NV^- [112]

The fitting results in the power-dependent values of γ_1 , γ_2 , and β for NV^0 and NV^- are shown in Figure (3.9.a), Figure (3.9.b), and Figure (3.9.c), respectively [112].

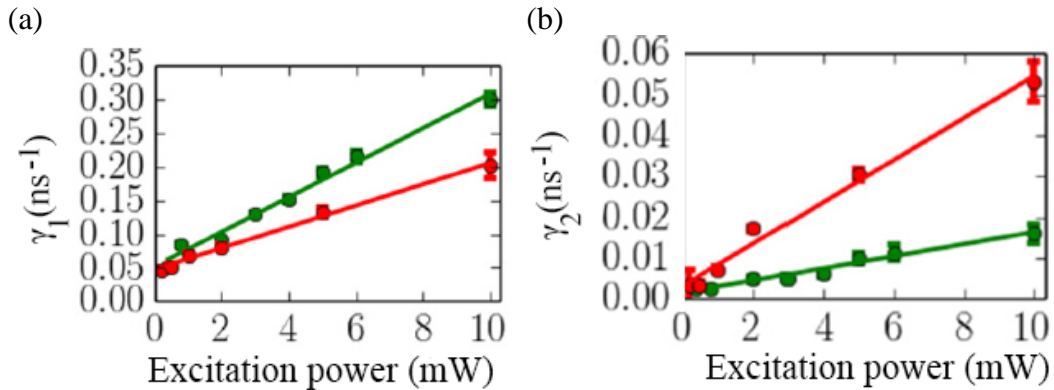


Figure 3.9: γ_1 , γ_2 , and β for NV^0 (green) and NV^- (red) for different excitation powers [112]

(c)

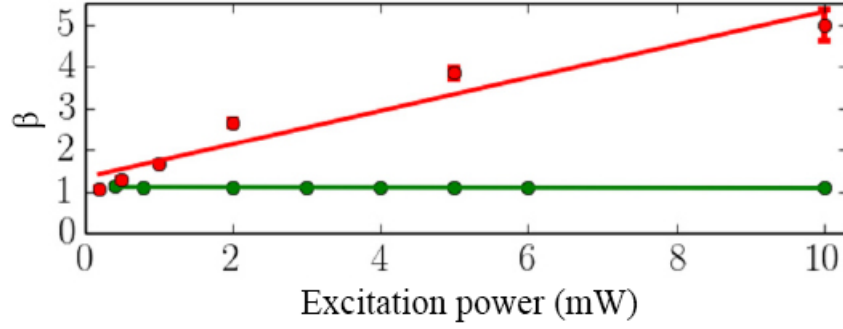


Figure 3.10: Continued.

At zero excitation power, the k_{21} parameter was determined experimentally to be $(19.231 \text{ ns})^{-1}$ and $(21.74 \text{ ns})^{-1}$ for NV^0 and NV^- , respectively [112]. This is compatible with the k_{21} parameter obtained in [52] in the case of NV^- center. However, the other decay rate parameters differ completely from [52] because of the different $g^{(2)}(\tau)$ modeling assumptions. The other decay parameters are obtained from Figure (3.9) and Equations (3.15), (3.16), and (3.17).

The Purcell factor modifies the decay rate parameters with the same rates as demonstrated in Section (3.2). The MATLAB code that presents the results of the modified $g^{(2)}(\tau)$ before and after coupling to a DLSP waveguide is available in Appendix (C).

The same rates of change in decay rate parameters as in [73] are considered in this section. Furthermore, the emission probability (p_f) is inversely proportional to the excitation power as it was measured experimentally as shown in Table (3.1) [112].

Table 3.1: The experimental p_f values for different excitation power [112]

Excitation power (mW)	p_f
0.5	0.8644
1	0.82456
2	0.722
3	0.74
5	0.63

Hence, a 0.5 mW excitation power is considered in the MATLAB code, shown in Appendix (C), to obtain a maximum p_f . The MATLAB code

implements two approaches to plot the $g^{(2)}(\tau)$. Firstly, the direct substitution of the experimental fitting values of γ_1 , γ_2 , and β in Equation (3.11). Secondly, by the substitution of the experimentally determined k_{21} parameter in Equations (3.15-3.17) to determine the remaining k parameters and then substitute them in Equation (3.11).

This scenario is also applied to model the $g^{(2)}(\tau)$ of the NV center coupled to a nanoantenna as demonstrated in [113]. The radiative decay rate enhancement in [113] was 5.8, hence, the k_{21} parameter after coupling to the nanoantenna is multiplied by 5.8. Figure (3.10) compares the plot of $g^{(2)}(\tau)$ by the first and second approaches and the $g^{(2)}(\tau)$ plot after coupling to a nanoantenna with 5.8 radiative decay enhancement [113].

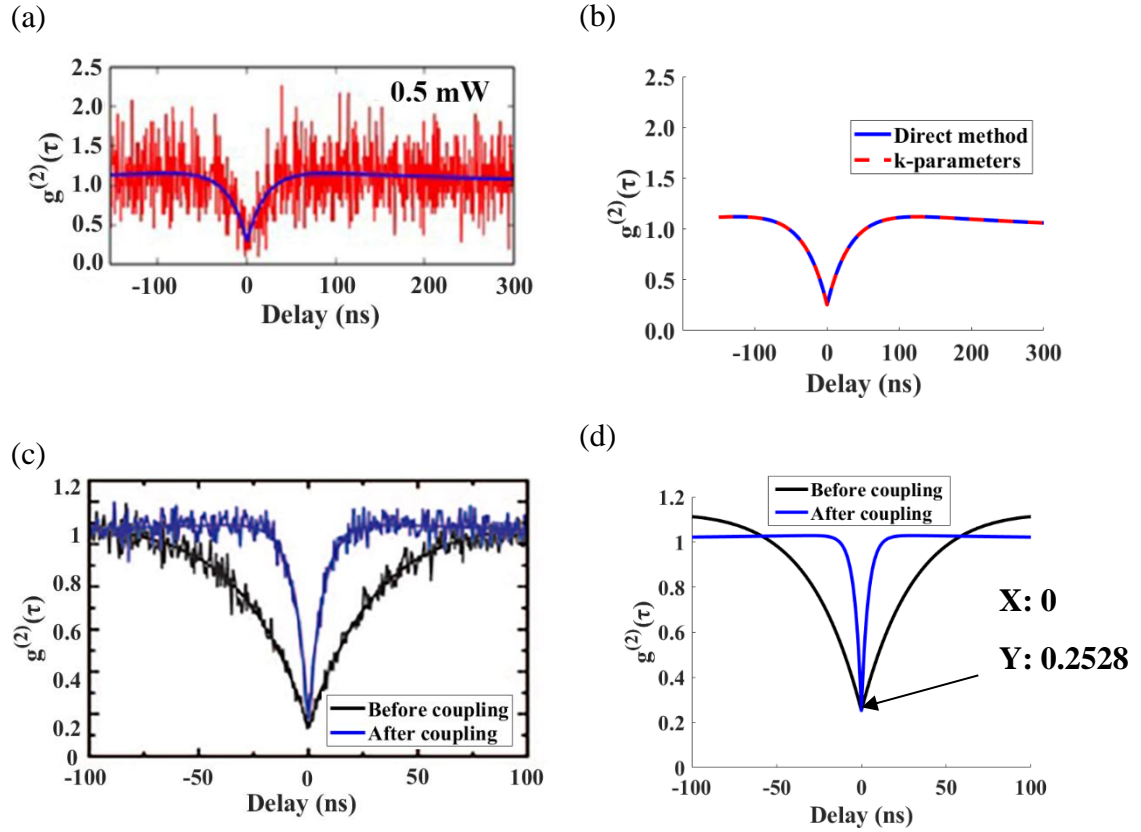


Figure 3.11: $g^{(2)}(\tau)$ comparison between (a) The experimental fitting of $g^{(2)}(\tau)$ data for NV under 0.5 mW excitation power, (b) The modeling of $g^{(2)}(\tau)$ by direct approach (Blue) and using k -parameters approach (dotted red), (c) The experimental fitting of $g^{(2)}(\tau)$ before (Black) and after (Blue) of NV center to a nanoantenna [113], (d) The modeling of the $g^{(2)}(\tau)$ before (Black) and after (Blue) coupling the NV center in [113] to a nanoantenna

The modeling of $g^{(2)}(\tau)$ by the first approach matched the $g^{(2)}(\tau)$ modeling by the second approach as shown in Figure (3.10.b). Moreover, the experimental fitting of the $g^{(2)}(\tau)$ data in Figure (3.10.a) shows an exact match to the $g^{(2)}(\tau)$ modeling plot in Figure (3.10.b).

Similarly, the experimentally fitted $g^{(2)}(\tau)$ data for NV center coupled to a nanoantenna shown in Figure (3.10.c) [113] is compared to the theoretical $g^{(2)}(\tau)$ plot shown in Figure (3.10.d) to validate the proposed $g^{(2)}(\tau)$ modeling. Both Figures (3.10.c) and (3.10.d) show a comparable behavior and this indicates the validity of this modeling approach.

The proposed structure in Chapter 2 shows $g^{(2)}(0)$ values of less than 0.5 using the corresponding k values described at the end of Section (3.3) for each case of output polarization as shown in Figure (3.11). Section (3.3)'s work could be summarized in a flow chart similar to Figure (3.6).

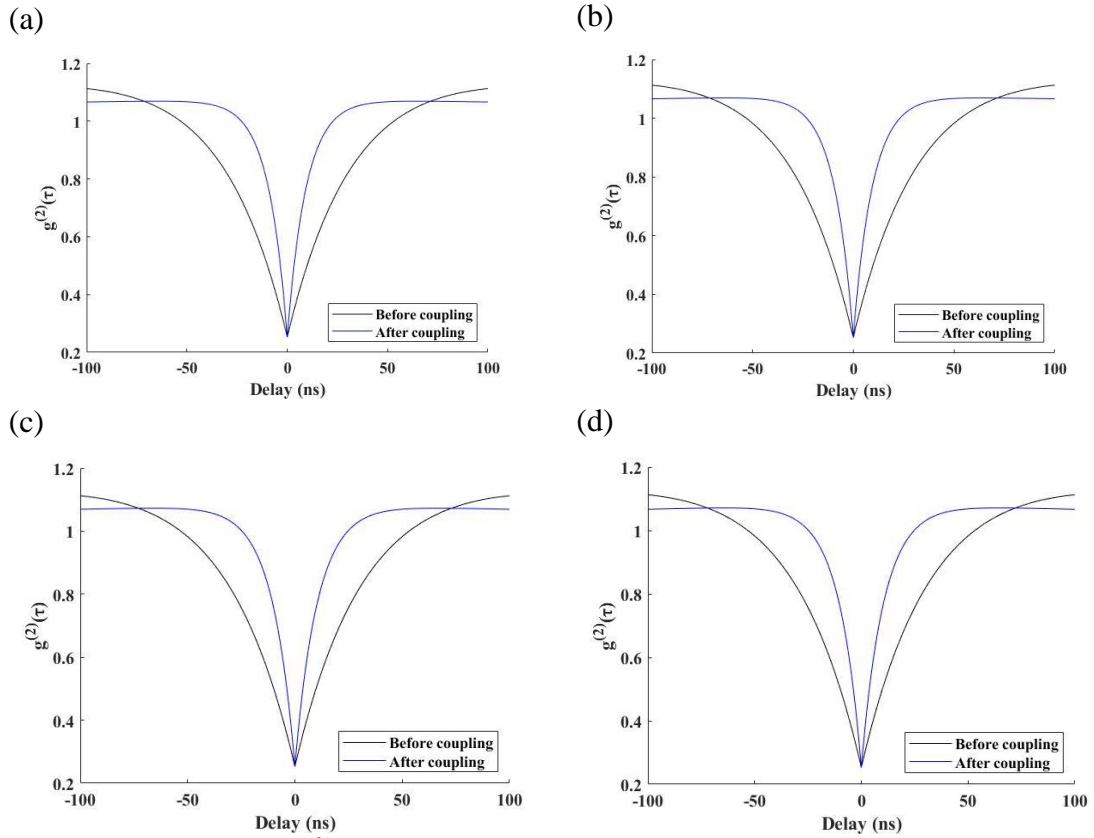


Figure 3.12: The $g^{(2)}(\tau)$ of the proposed structure in Chapter 2 with an output polarization of (a) 0° , (b) 90° , (c) 45° , and (d) -45° using Section (3.3)'s methodology

3.4. The emission modeling of a two-level QE

The NV center could also be modeled as two levels system in a low excitation power regime [112]. This section considers the effect of the QE's total decay rate on its emission dynamics described in [114]. The emission dynamics of a two-level QE could be described as shown in Figure (3.12) [114].

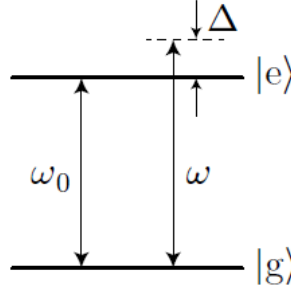


Figure 3.13: The emission dynamics of a two-level QE [114]

where ω_0 is the QE's resonance frequency, ω is the excitation laser frequency, and Δ is the difference between ω and ω_0 . If the QE is excited by a pulsed laser source, the QE-system interaction can be described by the simplified Hamiltonian with $\Delta = 0$ as [115,116]:

$$H_r = 0.5\hbar\Omega(t)(\sigma + \sigma^\dagger), \quad (3.18)$$

where \hbar is the reduced Planck's constant, σ is the QE's lowering operator, σ^\dagger is the transpose conjugate of σ , and $\Omega(t)$ is the Rabi frequency [115]. The time evolution of the QE's is studied using QuTiP software and the output emission is observed in this section for both short (exponential) and long (Gaussian) excitation pulse before and after coupling the QE to a DLSP waveguide. The excitation pulse shape is defined by the Gaussian function as [115]

$$f(t) = \frac{R}{2} e^{-\frac{(t-t_{\text{shift}})^2}{2t_p^2}}, \quad (3.19)$$

where t_p^2 is the variance of the pulse, t_{shift} is the mean value of the Gaussian pulse, and R is the excitation strength. The length of the pulse is controlled by varying the exponential function parameters. Moreover, the

Hamiltonian of the system should follow the pulse shape demonstrated in the QuTiP code shown in Appendix (D). The Hamiltonian of the system is time-evolved by using the master equation command in QuTiP.

The modeling of $g^{(2)}(\tau)$ of the two-level QE emission is obtained from the photon intensity time-dependent correlations $G^{(2)}(t, \tau)$, where τ is the time delay between two detection events. The $G^{(2)}(t, \tau)$, also known as the second-order optical coherence function, with random pulse length for a two-level QE is [115]

$$G^{(2)}(t, \tau) = \gamma^2 \langle \sigma^\dagger(t) \sigma^\dagger(t + \tau) \sigma(t + \tau) \sigma(t) \rangle, \quad (3.20)$$

where γ is the decay rate of the QE. Equation (3.20) could be interpreted as [115]

$$\langle A(t) B(t + \tau) C(t) \rangle, \quad (3.21)$$

Equation (3.21) can be solved using QuTiP correlators to calculate the QE's $G^{(2)}(t, \tau)$. The $G^{(2)}(t, \tau)$ varies widely in correspondence to the length of the pulse and by integrating over a long time, the $G^{(2)}(t, \tau)$ could be written as [115]

$$G^{(2)}(\tau, t) = \gamma^2 \int dt \langle T_- [\sigma^\dagger(t) \sigma^\dagger(t + \tau)] T_+ [\sigma(t + \tau) \sigma(t)] \rangle, \quad (3.22)$$

where the T_\pm operators indicate the time needed for a physical measurement [115]. Finally, to calculate the $g^{(2)}(0)$, the $G^{(2)}(\tau)$ should be normalized by the average number of photons ($\langle \hat{n}(t) \rangle$), which is supposed to be unity, integrated over time as [115]

$$G^{(2)}(0) = \int d\tau G^{(2)}(\tau), \quad (3.23)$$

$$g^{(2)}(\tau = 0) = \frac{G^{(2)}(0)}{(\gamma \int dt \langle \hat{n}(t) \rangle)^2}, \quad (3.24)$$

A $g^{(2)}(0)$ value less than 0.5 is a clear indication of single-photon emission. However, the plot of $g^{(2)}(\tau)$ over a large-scale time delay (τ) by this

approach demands a long computational time and complicated technical resources. Thus, the value of $g^{(2)}(0)$ is enough to indicate the single-photon emission behavior of the QE.

The time evolution of the QE was performed using QuTiP software [115]. However, the following results take into account the coupling effects on the QE behavior, which were not discussed in [115].

The QE is assumed to be excited by a short (exponential) pulse and a long (Gaussian) pulse. Moreover, the total decay rate enhancement after coupling the QE to a nanostructure was assumed to be 5 in the code shown in Appendix (D). The total decay rate enhancement could be considered to any other value according to the coupling environment.

The coupling of the QE to a nanostructure decreases the time by which the pulse is emitted. The QE's emission field under Exponential and Gaussian excitation pulses before and after coupling is shown in Figure (3.13).

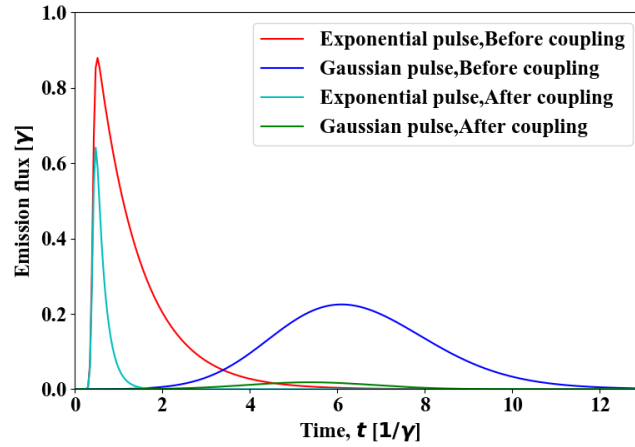


Figure 3.14: The two-level emission shape for Exponential and Gaussian pulses before and after coupling to a nanostructure

The corresponding $G^{(2)}(\tau)$ plots for short and long excitation before and after coupling the QE to a nanostructure are shown in Figure (3.14).

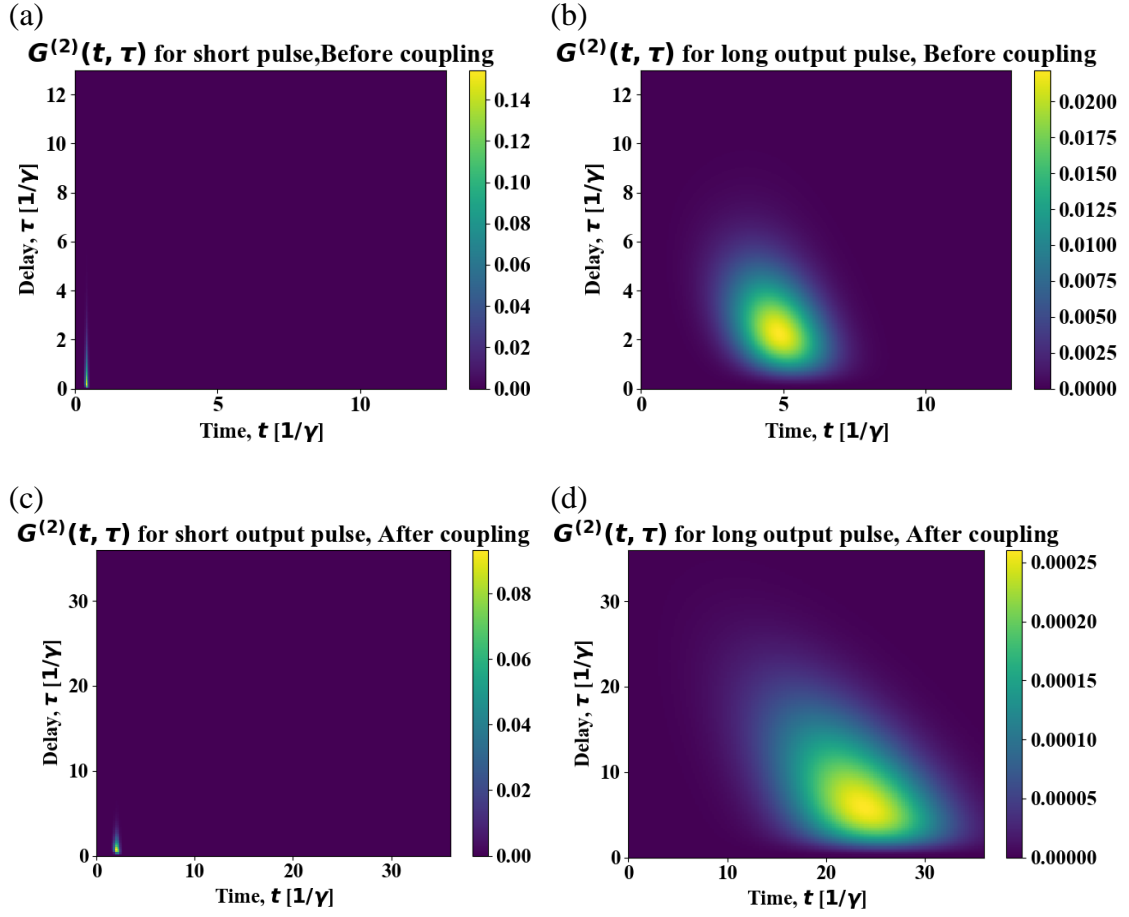


Figure 3.15: Visualization of the $G^{(2)}(\tau)$ for the QE's emission under short and long excitation pulse, (a), (b) before coupling [115], (c), and (d) after coupling

The corresponding integrated $G^{(2)}(\tau)$ before and after coupling under short and long excitation pulses is shown in Figure (3.15).

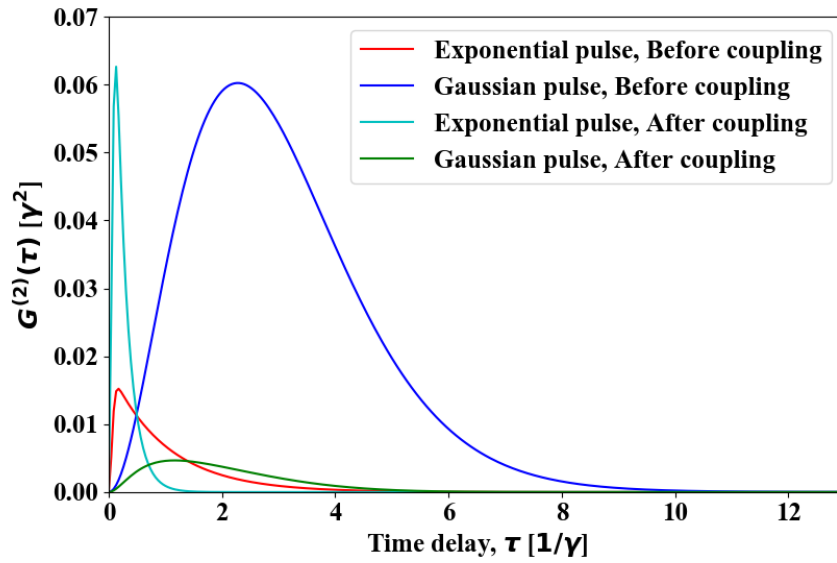


Figure 3.16: The integrated $G^{(2)}(\tau)$ before and after the coupling of the QE for short and long excitation pulses

Under short-pulse excitation of the QE, the $g^{(2)}(0)$ value is decreased from 0.034 before to 0.00541 after the coupling of QE to a nanostructure. Moreover, under long-pulse excitation, the $g^{(2)}(0)$ value is decreased from 0.436 before to 0.0034 after coupling the QE to a nanostructure. Consequently, the resultant $g^{(2)}(0)$ values showed a clear signature for the single-photon emission of the two-level QE before and after coupling to a nanostructure with a total decay rate enhancement of 5.

For the proposed structure in Chapter 2, the total decay rate is approximately 5 in all cases of output polarization. By modifying the code shown in Appendix (D) to consider a total decay rate of 5, the resultant $g^{(2)}(0)$ values showed 0.0035 and 0.00541 for long and short pulse excitation, respectively.

Chapter Four

Design and numerical verification of a four-state polarization-independent GC

Chapter 4

Design and numerical verification of a four-state polarization-independent GC

4.1. Introduction

This chapter describes the detailed steps of design and comprehensive numerical verification of a novel integrated GC that supports four output polarization cases, which are 0° , 90° , 45° , and -45° . The proposed integrated GC outcouples the polarized photons, which were emitted from a QE and propagating in the HPWs designed in Chapter 2, with maximum possible efficiency. The findings of the proposed work could be considered as a guideline to design four states of 0° , 90° , 45° , and -45° polarization-independent GC at any different QE's emission wavelength. The detailed steps of the analysis presented in this chapter are summarized in the following flowchart.

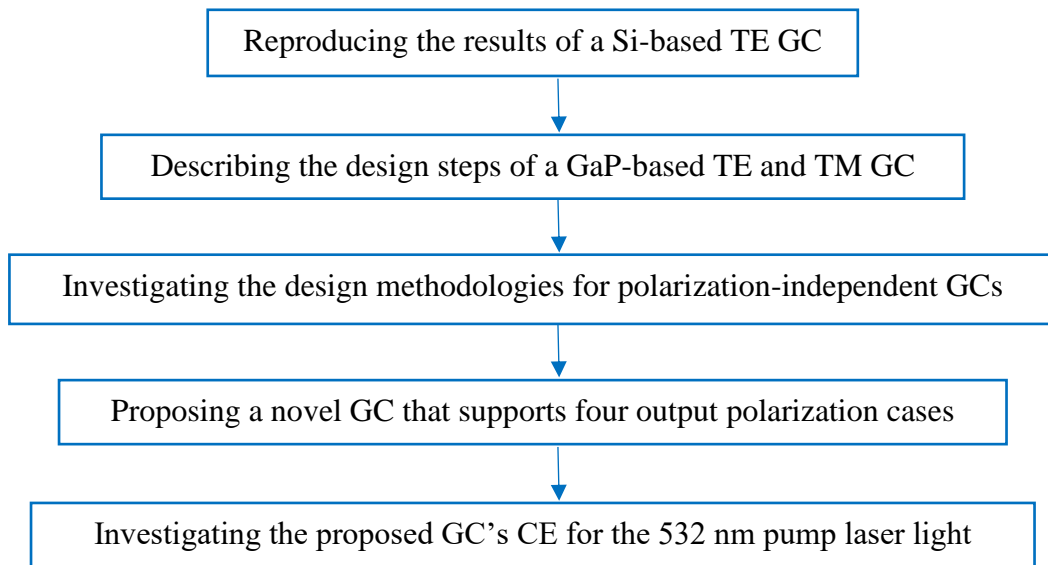


Figure 4.1: A summary of the polarization-independent GC design steps

COMSOL Multiphysics was used to perform and verify the aforementioned steps of analysis.

4.2. The GC's principles

The GC is a periodic structure that diffracts the light propagating inside the waveguide (in-plane) to free space (out-of-plane) or couples the light from free space (optical fiber) to an integrated nanowaveguide. A general cross-section of a shallow-etched 2D GC based on Silicon (Si)-On-Insulator technology (SOI) is shown in Figure (4.2) [117].

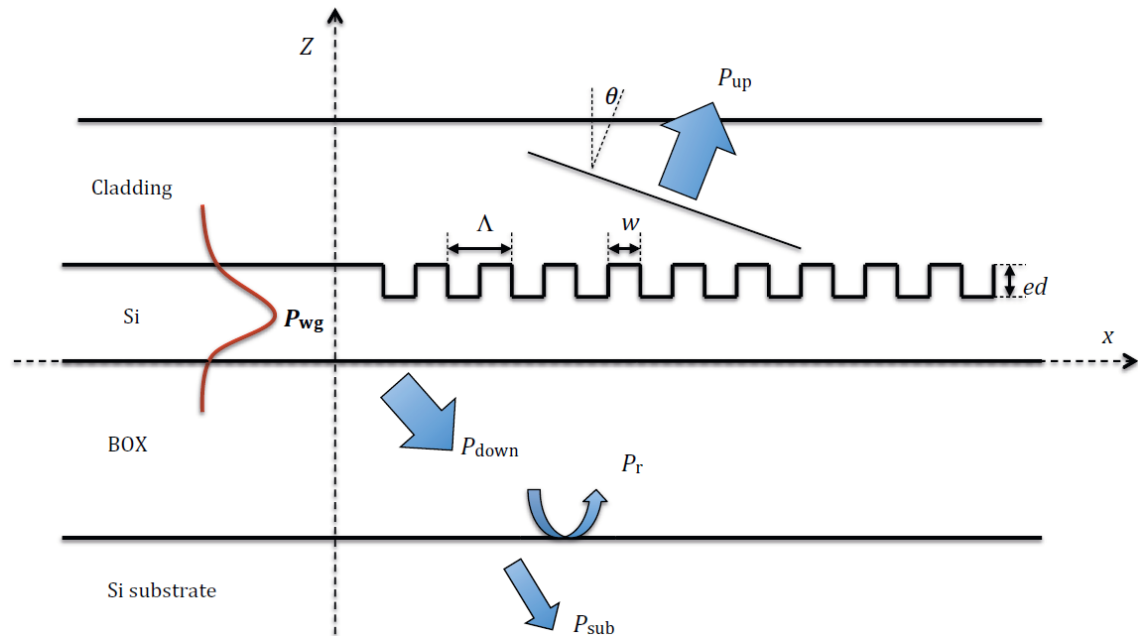


Figure 4.2: A general cross-section of a 2D GC [117]

The thickness of the Si and its corresponding buried oxide (BOX) layer depend on the fabrication processes. A cladding layer might be deposited to preserve the Si layer and allow depositing multilayers for electric interconnects. The cladding layer could be liquid or air depending on the possible applications, such as sensing or enhancing the light coupling. Because of the high refractive index difference between the cladding layer (air with $n = 1$) and the core layer (Si with $n = 3.47$ at 1550 nm), the light's propagating modes show high confinement in the Si layer with orders of several hundred nm. Therefore, a large mismatch between the Si mode and the optical fiber (which collects the diffracted light) mode occurs. For example, the core radius of a typical optical fiber is 4.5 μm and has an area of almost 600 larger than the Si nanowaveguide because a typical Si

nanowaveguide has dimensions of $500 \text{ nm} \times 220 \text{ nm}$. The mode mismatch issue has been addressed efficiently through several different approaches including the edge couplers that utilized lensed fibers or spot-size converters. However, the edge couplers exhibited alignment complexities and complicated post-fabrication processes that result in expensive fabrication costs. The GCs were considered an efficient alternative that replaced the edge couplers with no further post-fabrication processes, much easier alignment, adaptive designs, low cost, and on-chip testing [117]. Because of the GC's advantages, it is used as a basis to couple the light between the optical fiber and the nanowaveguide or vice-versa.

The principle of the GC relies on the understanding of the Huygens-Fresnel principle, i.e., the constructive and destructive interference of the light's wavefronts after being diffracted from the grating's teeth. If the optical wavelength coincides with the GC's period (Λ), the 1st-order diffraction propagates in a vertical direction (green curves) while the 2nd-order diffraction propagates in a backward direction (red curves) to the waveguide as shown in Figure (4.3.a) [117].

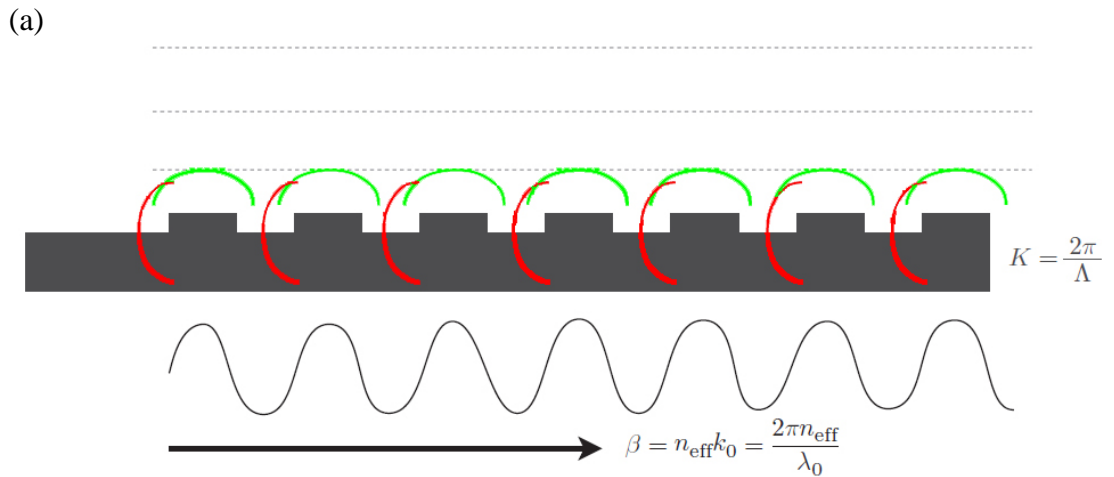


Figure 4.3: The GC's principle with (a) GC's period equals optical wavelength ($\Lambda = \lambda_0/n_{\text{eff}}$), and two diffraction modes, (b) GC's period is larger than the optical wavelength ($\Lambda > \lambda_0/n_{\text{eff}}$), and only a single diffraction mode [117]

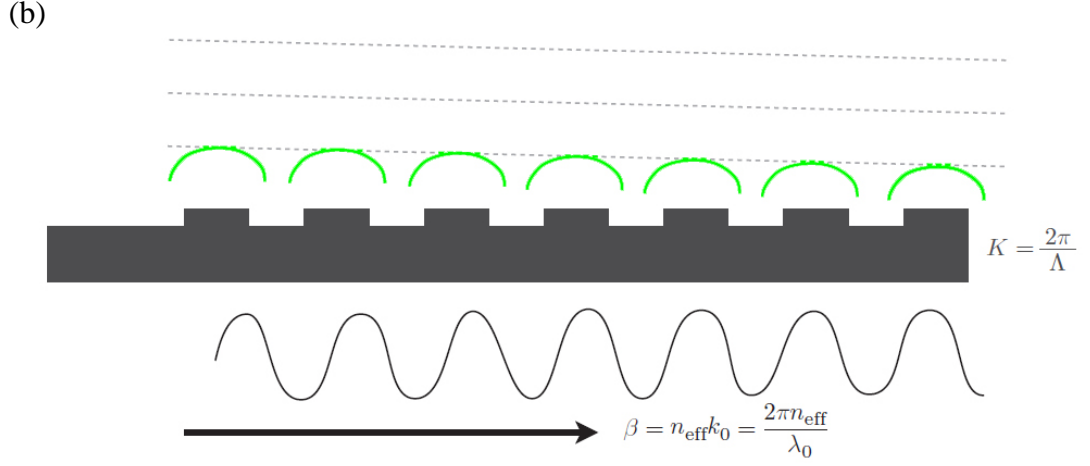


Figure (4.3): Continued.

The light's backward propagation should be mitigated since it results in a Fabry-Perot oscillation between input and output couplers. To mitigate the 2nd-order diffraction, the optical fiber is tilted to the normal on the grating's surface and the GC's period should be larger than the optical wavelength as shown in Figure (4.3.b). As a result, the light diffracted at a tilted angle (green curves) with no 2nd-order diffraction.

The GCs described in this Chapter are 1D periodic structures based on Bragg's principle as shown in Figure (4.4) [117].

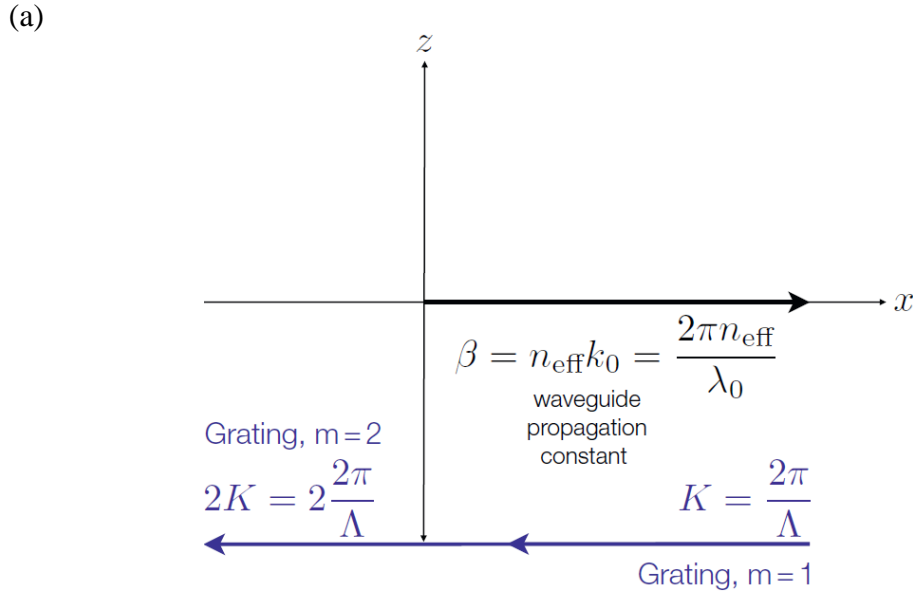


Figure 4.4: An illustration of Bragg's condition [117], (a) without considering the diffracted wave and for m grating periods, (b) without considering the diffracted wave into space (air region) and considering the 1st-order diffraction grating, (c) considering the diffracted wave into space, (d) considering the diffracted wave into both space and BOX regions

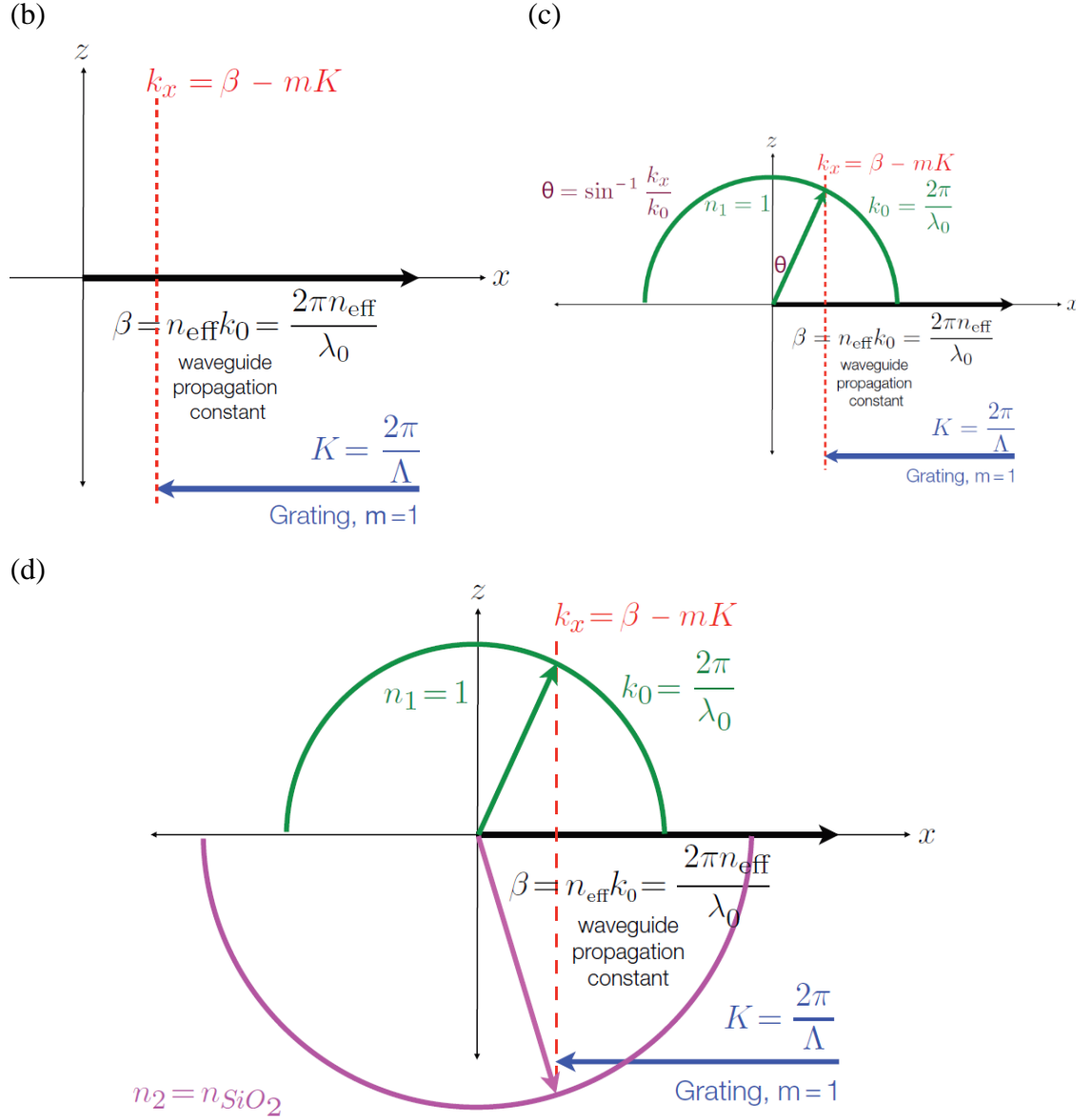


Figure 4.4: Continued.

The propagating (guided) wave in a slab waveguide has a similar propagation direction to the GC's plane and it is perpendicular to the GC's teeth as shown in Figure (4.4.a). The propagation constant (β) of the guided wave is [117]

$$\beta = \frac{2\pi n_{\text{eff}}}{\lambda_0}, \quad (4.1)$$

where $K (= 2\pi/\Lambda)$ is the GC's periodicity and the higher orders of GC's diffraction are mK , where $m = 1, 2, 3, \dots$. If k_x is defined as the diffracted wave vector's component towards the propagating wave as shown in Figure (4.4.b), then the Bragg condition could be defined as [117]

$$\beta - k_x = mK, \quad (4.2)$$

The diffracted light into the cladding region, as shown in Figure (4.4.c), has a wavevector of [117]

$$k = \frac{2\pi n_c}{\lambda_o}, \quad (4.3)$$

Hence, the diffraction angle (θ_c) is [117]

$$\sin\theta_c = \frac{k_x}{k_o}, \quad (4.4)$$

Consequently, the Bragg condition of Equation (4.2) for air cladding is reduced to [117]

$$\begin{aligned} n_{\text{eff}}k_o - k_o \sin\theta_c &= \frac{m2\pi}{\Lambda}, \\ n_{\text{eff}} \frac{2\pi}{\lambda_o} - \frac{2\pi n_c \sin\theta_c}{\lambda_o} &= \frac{2\pi}{\Lambda}, \\ n_{\text{eff}} - n_c \sin\theta_c &= \frac{\lambda_o}{\Lambda}, \end{aligned} \quad (4.5)$$

Where θ_c is the angle of incidence to the normal line in the 2D transversal plane in the cladding region. Finally, if there is considerable diffraction into the substrate, Bragg's diagram could be modified as shown in Figure (4.4.d) [117]. The diffraction angle into the oxide is smaller than that in the air as shown in Figure (4.4.d).

The 1D GCs could be designed at any desired wavelength and could also support the diffraction of different cases of polarized light. The following sections aim to describe the design of a 1D GC that supports the diffraction of different polarization cases for the propagating light.

4.3. The TE GC simulation framework

This section highlights the most important information of the simulation framework that reproduces the simulation results of the TE GC proposed in [118] and is shown in Figure (4.5).

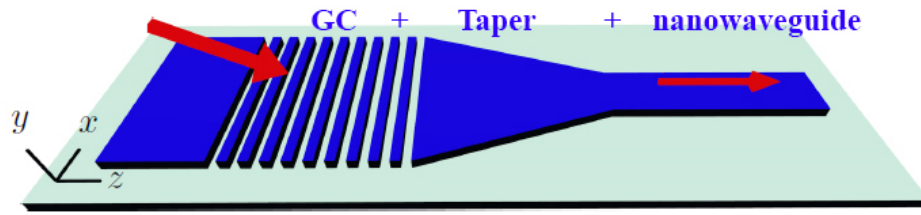


Figure 4.5: The 3D TE GC proposed in [118]. The blue area represents the waveguide's material while the green area represents the substrate material and the red arrows are the light's propagation direction

Figure (4.5) shows three integrated components that are required to couple the light from the free space (optical fiber) to the nanowaveguide. The first component is the GC, which is described in Section (4.2). The diameter of the optical fiber used to inject (or detect) the light to (or from) the nanowaveguide is typically much larger than the nanowaveguide's dimensions. Therefore, the GC's depth (in the x-direction) should approximately match the optical fiber's diameter for efficient coupling of the light. A taper coupler connects the GC to the nanowaveguide by gradually narrowing the waveguide's channel. The CE between the GC and the nanowaveguide is increased as the taper section length increases.

The mathematical design of the GC is complex and depends on a wide range of parameters. Hence, computational electrodynamic softwares based on numerical methods, such as COMSOL Multiphysics, are utilized for accurate GC designs. COMSOL Multiphysics is based on the finite-element method (FEM), which splits the simulation domain into small finite elements of 3D volumes or 2D areas that constitute a mesh. Each mesh element has a single boundary, at minimum, in common with the neighboring mesh element. The wave optics, electromagnetic waves frequency domain (ewfd) physics in COMSOL solves Maxwell's partial differential equations (PDEs) at each mesh element subjected to the boundary and initial conditions to obtain the electric and magnetic fields. The solution is more accurate with a smaller mesh element size. However, the finer mesh elements require longer computational time, larger memory, and increased processing power.

Moreover, the drawbacks of using finer mesh elements are significantly increased if a 3D simulation framework is used [118].

Alternatively, the 2D simulation framework simplifies the design process requirements. The 2D simulation framework considers an infinite depth (1 m) for the GC shown in Figure (4.5). Consequently, the 2D model is simplified and has comparable accuracy to that of the 3D model [118].

4.3.1. The 2D COMSOL simulation framework in [118]

This subsection highlights the most important notes about the 2D COMSOL simulation framework presented in [118] and reproduces the same results to compare with the modifications in the proposed work. In [118], the goal was to couple a TE-polarized incident light with a wavelength of 1550 nm from an optical fiber to a GC of 500 nm (width in the x-direction) by 220 nm (height in the y-direction). The taper section was assumed to be ideal and had been neglected in the simulation framework, which is true for long taper sections. Thus, the 2D simulation framework included the GC section, only. The 2D simulation framework proposed by [118] is shown in Figure (4.6).

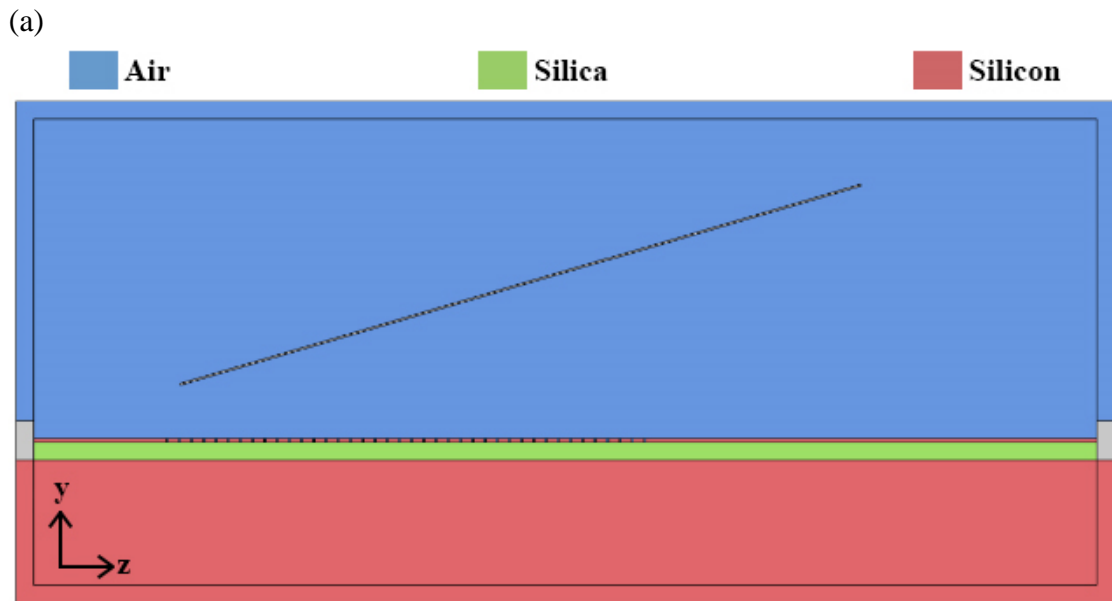


Figure 4.6: The 2D simulation framework proposed by [118]

(b)

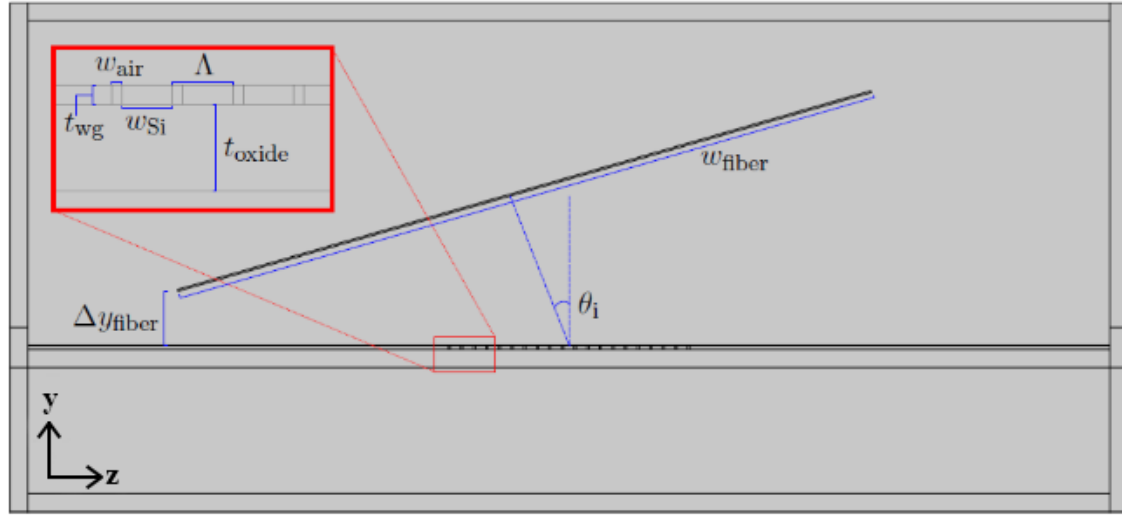


Figure 4.6: Continued.

Si, Silica (SiO_2), and air have refractive indices of 3.48, 1.45, and 1, respectively. The gray areas were not considered simulation areas and they were used as ports to monitor the propagating intensities of the light. The SiO_2 cladding had a $1\ \mu\text{m}$ thickness deposited above the $7\ \mu\text{m}$ Si layer that was sufficient to neglect the light's reflection in the substrate area. The air domain included a thin rectangle that was used to model the optical fiber. The waveguide's length (in the z -axis) was assumed to be $60\ \mu\text{m}$, which is long enough to include 40 gratings. The number of gratings was found through the trial and error process until a stable CE, which is the ratio of the output to input intensities, was achieved. The air region's height (towards the y -axis) of $18\ \mu\text{m}$ allowed a maximum tilt angle of 21° for the optical fiber. A 16.3° tilt angle was considered in [118]. Perfectly matched layer (PML) domains of $1\ \mu\text{m}$ thickness were included in the Si and air regions to absorb all the light's radiation and prevent continuous light scattering in the simulation domain as shown in Figure (4.7) [118].

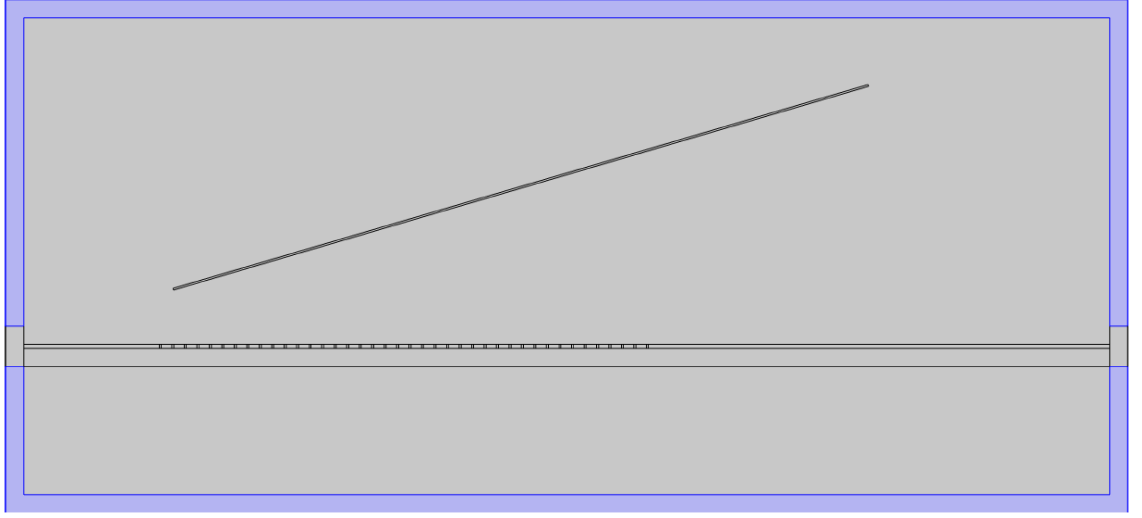


Figure 4.7: The PML layer used in [118] is highlighted in violet

One port at each waveguide's ends was used to absorb and measure the incident intensity. A third port at the bottom of the thin rectangle in the air domain was used to apply the TE-polarized light to the GC. The other three boundaries of the thin rectangle in the air region and the boundaries that surrounded the PML layers were set to scattering boundary conditions for further scattering suppression. The optical fiber's port normal was always perpendicular to the center of the GC. Moreover, the optical fiber's height to the waveguide was roughly fixed at $3\ \mu\text{m}$ because it didn't affect the CE when was varied as shown in Figure (4.8).

(a)

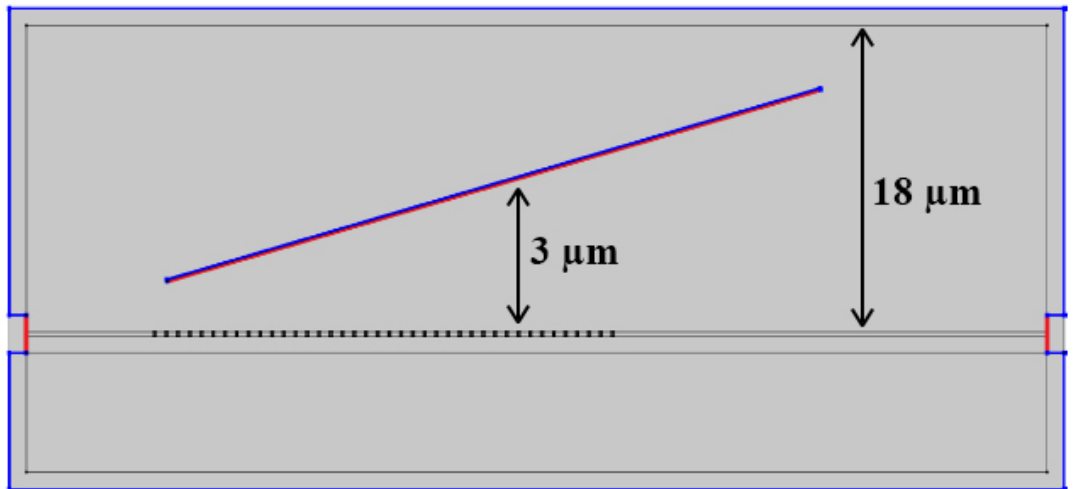


Figure 4.8: (a) The three ports used in [118] highlighted with red and the scattering boundary conditions highlighted with blue, (b) The ports settings in COMSOL

(b)

Label	Left port	Right port	Fiber port
Port name	1	2	3
Type of port	Numeric	Numeric	User defined
Wave excitation at this point	Off	Off	On
Electric mode field			$x: 0$ $y: 0$ $z: \exp(-((x-x_0)^2+(y-y_0)^2)/(w_0^2))$
Propagation constant			$2\pi/w_l$

Figure 4.8: Continued.

A boundary mode analysis corresponding to the refractive index of the port's medium was performed to make COMSOL calculates the propagation modes at the waveguide and air as shown in Figure (4.9).

Label	Left port	Right port	Fiber port
Port name	1	2	3
Mode analysis frequency	fq	fq	fq
Desired number of modes	<input checked="" type="checkbox"/> 1	<input checked="" type="checkbox"/> 1	<input type="checkbox"/>
Search for modes around	<input checked="" type="checkbox"/> n_Si	<input checked="" type="checkbox"/> n_Si	<input checked="" type="checkbox"/> n_air

Figure 4.9: A boundary mode analysis at each port [118]

The optical fiber used in [118] was Corning SMF-28 and its modeling data were based on its manual [119]. The SMF-28 has a mode field diameter of $10.4 \mu\text{m}$, a core diameter of $8.2 \mu\text{m}$, and a 0.14 numerical aperture (NA). By substituting these parameters in Equation (4.6), the single-mode operation of the optical fiber at 1550 nm was confirmed since V is less than 2.405 [120].

$$V = \frac{2\pi r_{\text{core}} \text{NA}}{\lambda_0} = 2.31 < 2.405, \quad (4.6)$$

where r_{core} is the core radius. The light's field distribution inside the optical fiber follows a Gaussian distribution, which has a maximum value at the boundary's midpoint (at the bottom line of the thin rectangle in the air region). Therefore, the optical fiber's port length of $40 \mu\text{m}$ was considered to include the majority of the field's distribution at the optical fiber's

boundary as defined in Figure (4.8.b). The MFD defines the depth of the light beam into the z-direction shown in Figure (4.8.a). The TE-polarization was specified by setting the x- and y-components of the electric field to zero and entering the Gaussian equation of the light in the z-direction as shown in Figure (4.8.b). The Gaussian equation of the TE-polarized light is defined as

$$E_z = e^{-\frac{((x-x_0)^2+(y-y_0)^2)}{w_0^2}}, \quad (4.7.a)$$

$$x_0 = 0.5 \text{ ft} \sin(\theta_{\text{in}}), \quad (4.7.b)$$

$$y_0 = -0.5 \text{ ft} \cos(\theta_{\text{in}}), \quad (4.7.c)$$

where ft is the fiber's thickness, θ_{in} is the tilt angle, w_0 is the Gaussian beam radius, x_0 is the Gaussian mean in the x-direction, and y_0 is the Gaussian mean in the y-direction. For a TM-polarized light, Equation (4.7.a) is applied to the z-component of the magnetic field intensity, and all other components are set to zero.

A free triangle mesh with maximum element size, minimum element size, maximum element growth rate, curvature factor, and the resolution of narrow regions was set to 130 nm, 8E-10, 1.1, 0.2, and 0.4, respectively. Figure (4.10) shows the resultant mesh structure of the simulation domain.

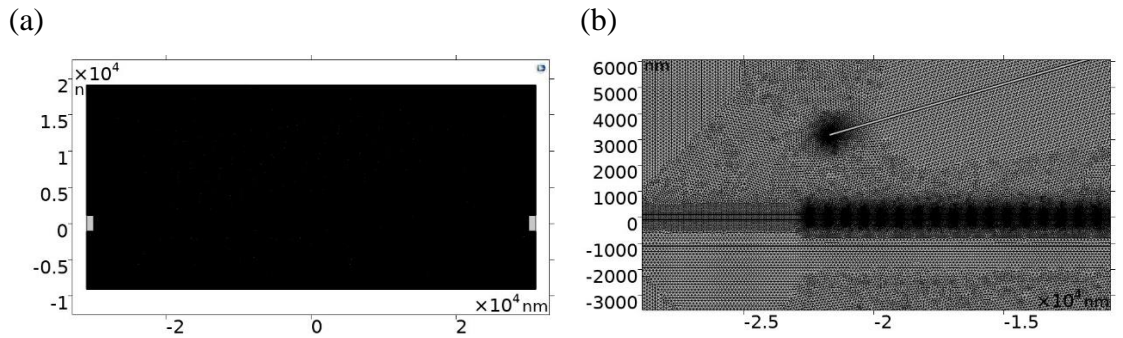


Figure 4.10: The mesh structure for (a) the entire simulation domain and (b) a zoomed area near the optical fiber source [118]

By following the above settings and further simulation instructions in [118] for a fixed uniform grating period (Λ) of 690 nm, the reproduced CE

is 44.772% as shown in Figure (4.11) compared to a CE of 44.789% simulated in [118].

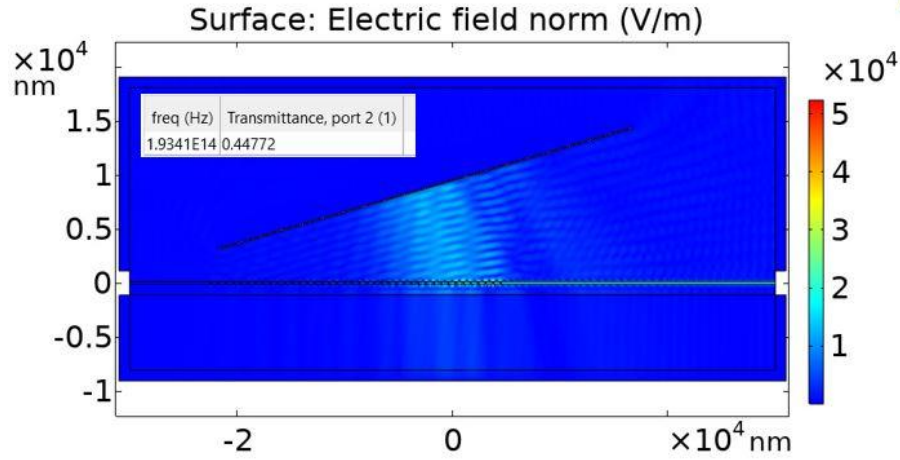


Figure 4.11: The reproduced CE following the modeling steps of [118]

4.3.2. Changing the Si waveguide with a GaP waveguide

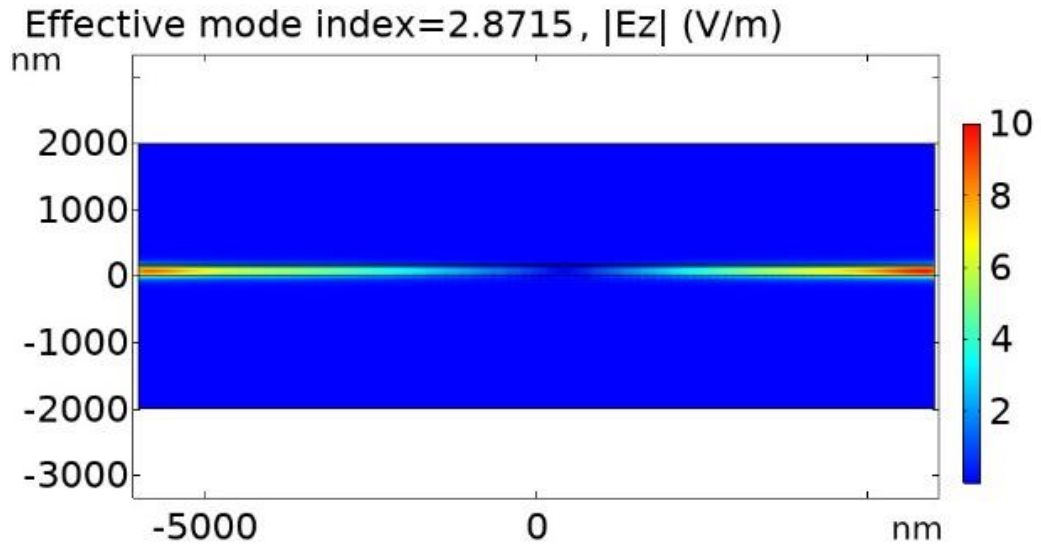
The design details of the GC based on a 220 nm Si waveguide (i.e. period, etch depth, incident angle, and polarization) in Section (4.3.1) was not explained in [118]. In this subsection, the design details of the GC based on a GaP waveguide following the design guidelines in [117] are presented. The aim is to investigate the performance of the GC based on a 150 nm GaP waveguide to couple a TE and a TM polarized light, individually. The GC's period should follow Equation (4.5) where n_{eff} is calculated by [117]

$$n_{\text{eff}} = ff n_{\text{eff1}} + (1 - ff) n_{\text{eff2}}, \quad (4.8)$$

where ff is the GC's tooth width of an unetched waveguide (fill factor), n_{eff1} is the effective index of 12 μm unetched slab waveguide, and the n_{eff2} is the effective index of a 12 μm etched waveguide as shown in Figure (4.2). The length of the slab waveguide (12 μm) could be any other much larger length than the operation wavelength. Figure (2.6) has an unetched 150 nm GaP waveguide. The etched waveguide height is taken 50% from the unetched GaP waveguide i.e. 75 nm. A 10° tilt angle for the optical fiber is assumed in the air region with an ff of 50%. The GaP waveguide is covered with an HSQ layer of 20 nm thickness. Consequently,

the n_c in Equation (4.5) has a value of 1.41. For a TE-polarized light, the effective indices for the unetched and etched slab waveguides at the GaP region are shown in Figure (4.12).

(a)



(b)

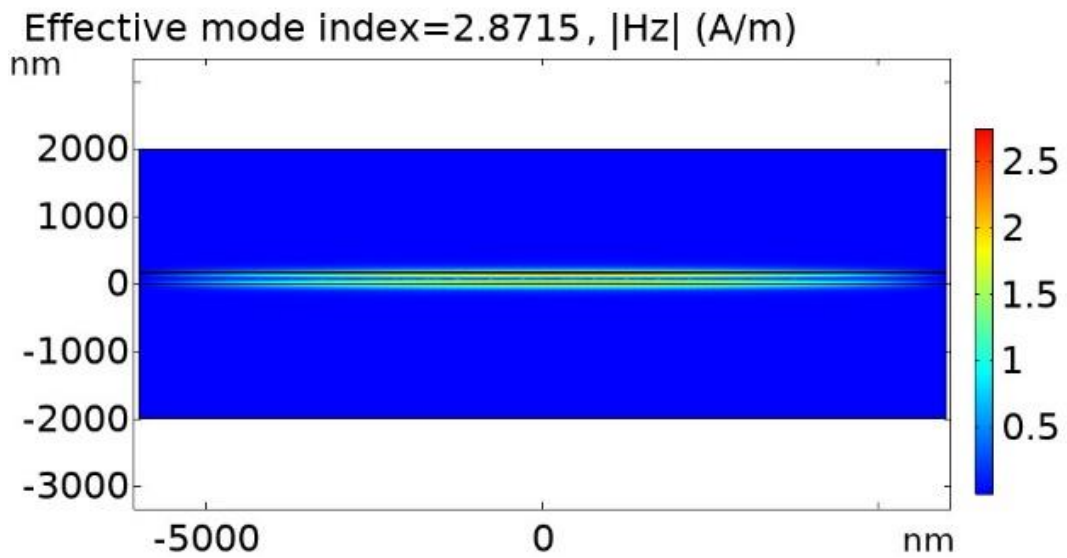
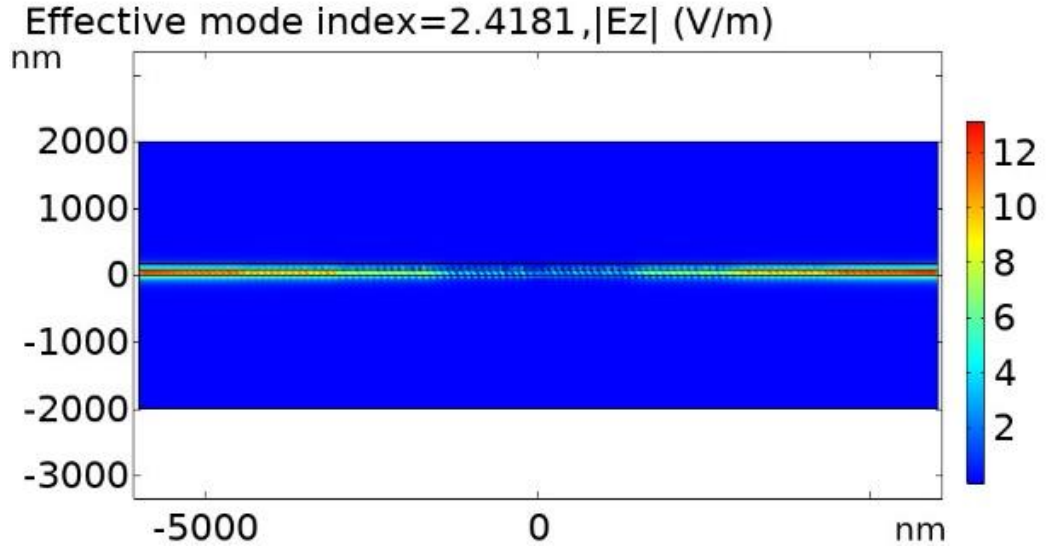


Figure 4.12: The z -component of the electric and magnetic field for (a) and (b) unetched GaP waveguide, (c) and (d) etched GaP waveguide, respectively, and their corresponding effective index

(c)



(d)

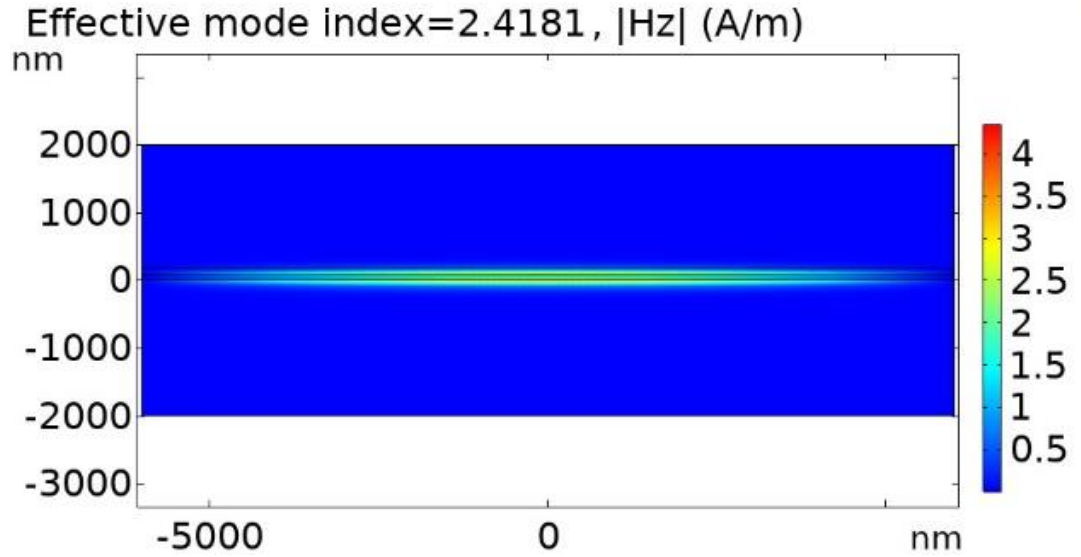


Figure 4.12: Continued.

Therefore, by applying Equation (4.8), n_{eff} equals 2.6448. θ_c in Equation (4.5) could be obtained by applying Snell's law

$$n_{\text{hsq}} \sin \theta_{\text{hsq}} = n_{\text{air}} \sin \theta_{\text{air}}, \quad (4.9)$$

where θ_{air} equals 10° (the tilt angle of the optical fiber in the air) and θ_{hsq} is the angle of the light at the HSQ layer (on top of the GaP waveguide) to the normal line on the GaP waveguide (Which equals 7.0742°). Therefore, Λ equals 283.27 nm by applying Equation (4.5). The number of gratings has been kept at 40 as in Section (4.3.1). The number of gratings could be any

number such that the entire length of the GC covers the MFD of the incident light beam for maximum collection efficiency.

The optical fiber source should be replaced because the SMF-28 supports two operation wavelengths, which are 1310 nm and 1550 nm as indicated in [119], and the GC should support the QE's wavelength, which is 700 nm. The optical fiber source should also support different polarization. Hence, the Thorlabs PM630-HP polarization-maintaining fiber (PMF) is selected to inject or detect light. The PM630-HP has an MFD of $4.5\ \mu\text{m}$ and operation wavelengths from 620 nm to 850 nm, which should be considered in the 2D simulation framework parameters in the following simulations instead of the SMF-28. It also has a $3.5\ \mu\text{m}$ core diameter and a 0.12 NA that achieves a $V = 1.885 < 2.405$, which assures the single-mode operation as indicated in Equation (4.6).

The spatial x-axis position (the center of the first grating tooth) of the GC under the optical fiber is swept from $0\ \mu\text{m}$ to $10\ \mu\text{m}$ with a 100 nm step size to align the optical fiber for maximum CE as shown in Figure (4.13).

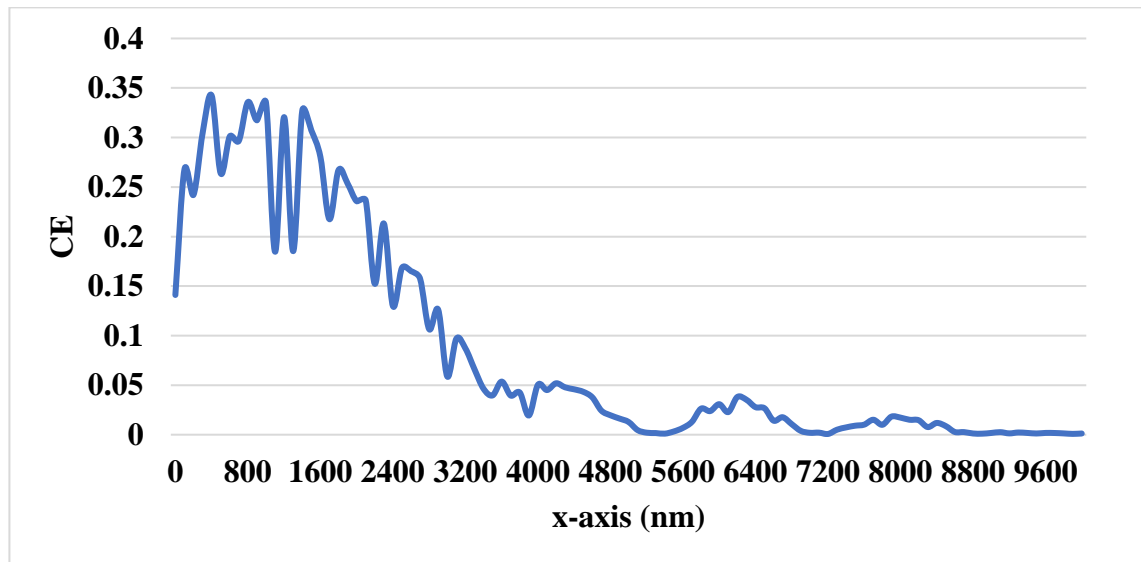


Figure 4.13: The CE against the x-shift in the GC position

Figure (4.13) shows maximum CE values at $x = 400, 800,$ and 1000 nm of 34.2%, 33.6%, and 33.5%, respectively. The x-axis position is fixed at 400 nm and the etch depth is swept from 25 nm to 95 nm with a 5 nm step size for maximum CE as shown in Figure (4.14).

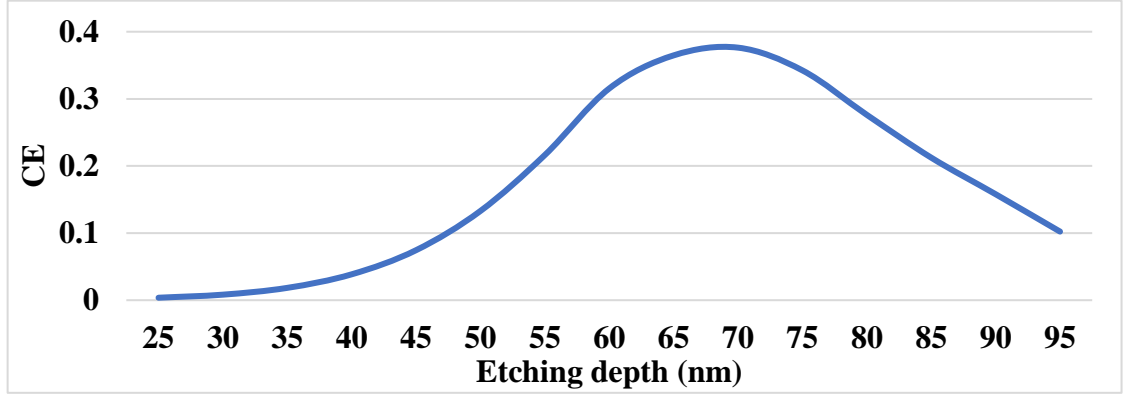


Figure 4.14: The CE against the etching depth

Figure (4.14) shows a maximum CE of 37.63% for an etching depth of 70 nm. By setting the etch depth and the x-position to their optimal values, the GC period is swept from 275 nm to 300 nm with a 5 nm step size to search for maximum CE as shown in Figure (4.15).

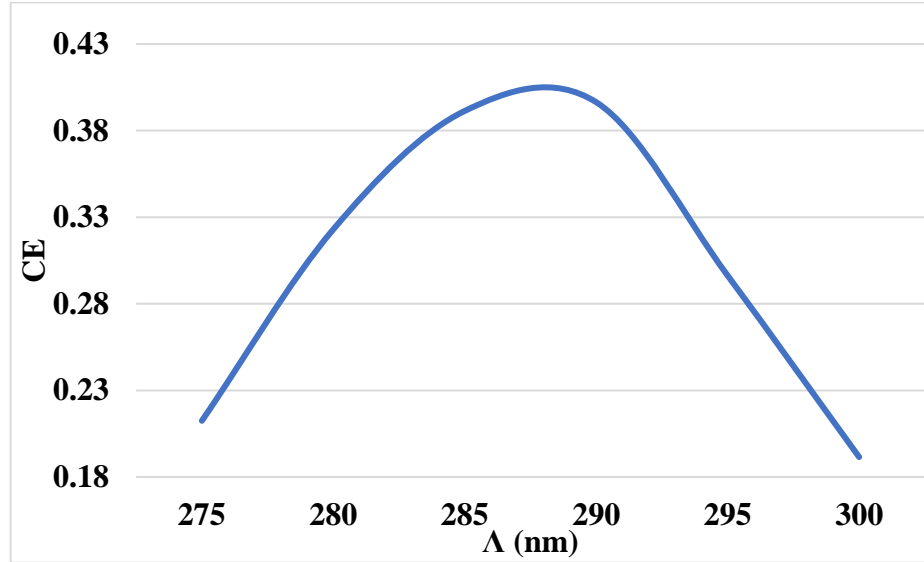


Figure 4.15: The CE against Λ

Figure (4.15) shows a maximum CE of 39.64% for a Λ equals 290 nm. The theoretical and numerical difference of Λ results from the numerical approach tolerance. By setting all the optimal parameters of Λ , etch depth, and the GC's x spatial position, the CE for a TE-polarized light against the operation wavelength is shown in Figure (4.16) with a maximum CE of 39.64% at 700 nm.

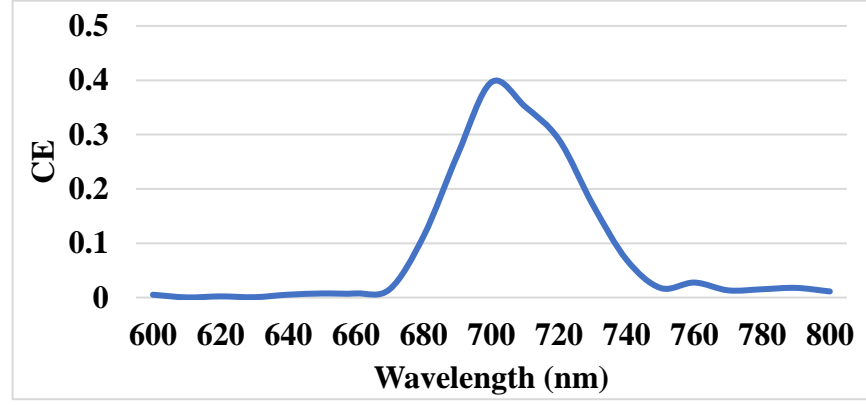
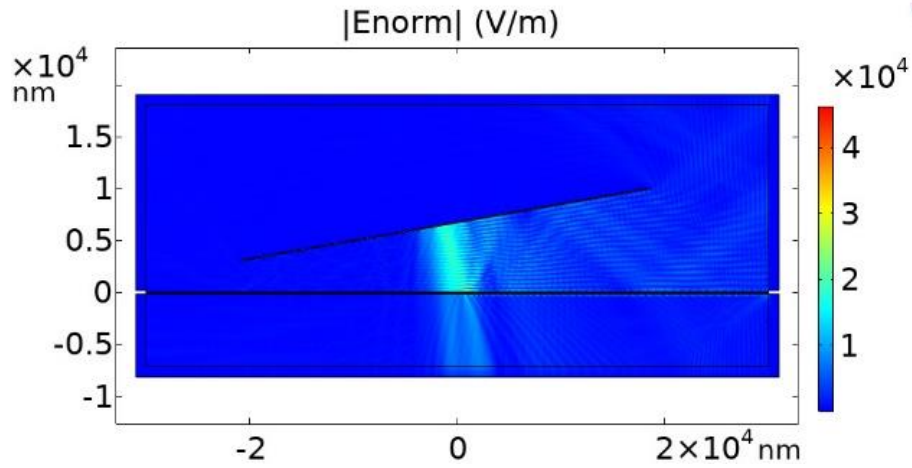


Figure 4.16: The CE against the operation wavelength for a TE polarization incidence

The normal electric field distribution for the TE light from the optical fiber source to the output of the GaP waveguide at 700 nm is shown in Figure (4.17).

(a)



(b)

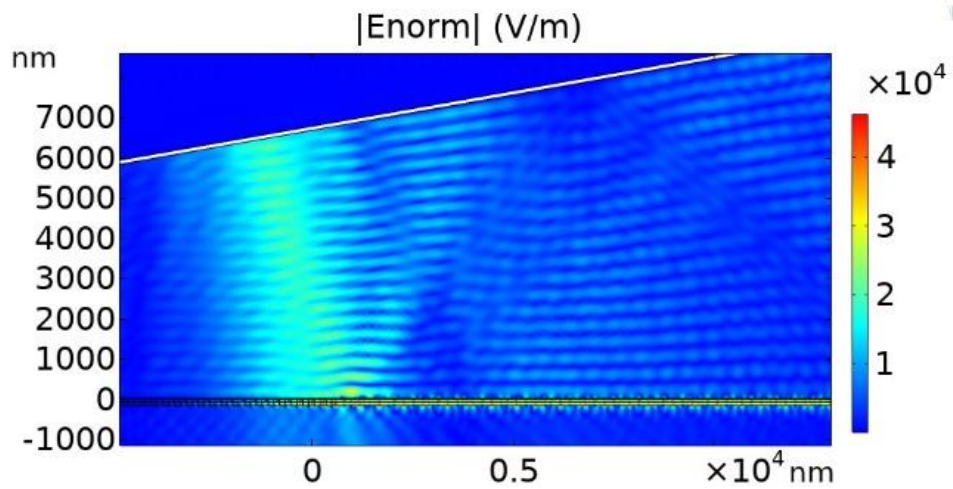


Figure 4.17: The scattering of $|E_{norm}|$ at 700 nm TE-polarized light from the optical fiber source to the output of port 2. The GC is composed of a 150 nm GaP waveguide and 20 nm HSQ layer. (a) The entire 2D simulation framework, (b) Zoomed 2D simulation framework to show the propagation in the GaP waveguide

It is worth mentioning that the thickness of the PML layer does not considerably affect the CE for the Si waveguide described in Section (4.3.1) and the GaP waveguide in Section (4.3.2) as shown in Figure (4.18).

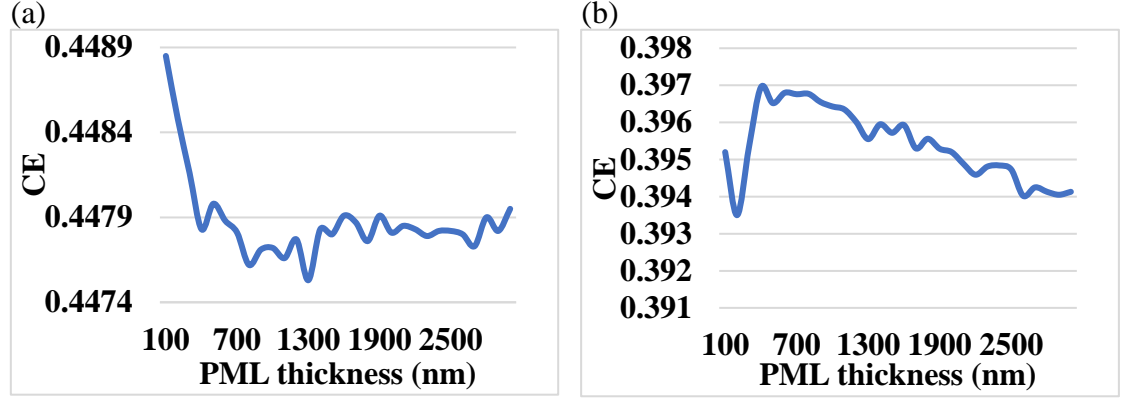


Figure 4.18: The CE against the PML thickness for (a) the Si waveguide in Section (4.3.1) and (b) the GaP waveguide

To design a GC that supports the coupling of a TM polarized light, the Λ should be changed because n_{eff} for the TM mode differs from that of the TE mode. The effective indices for the unetched (150 nm) and etched (150 – 70 = 80 nm) GaP waveguide for a TM mode are shown in Figure (4.19).

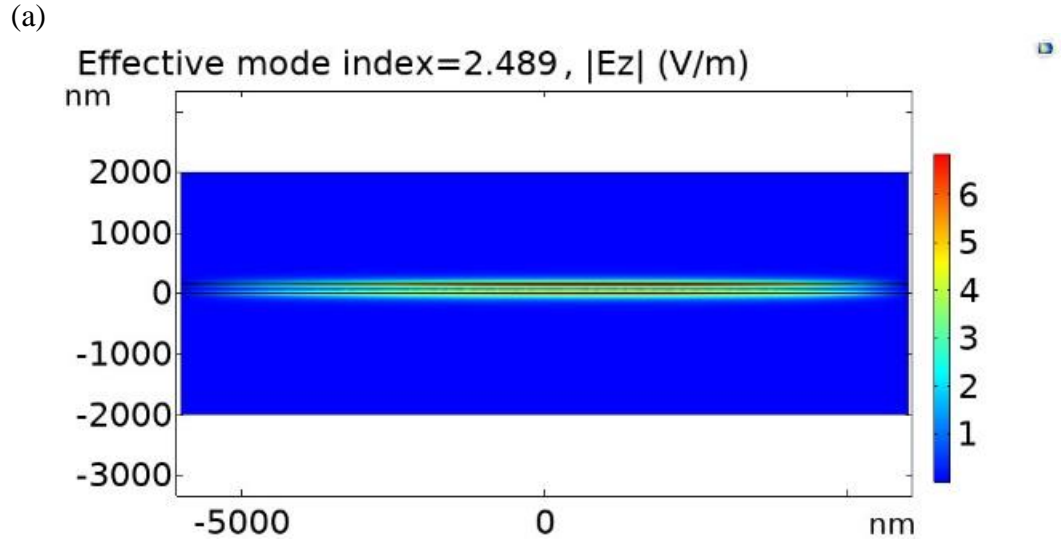
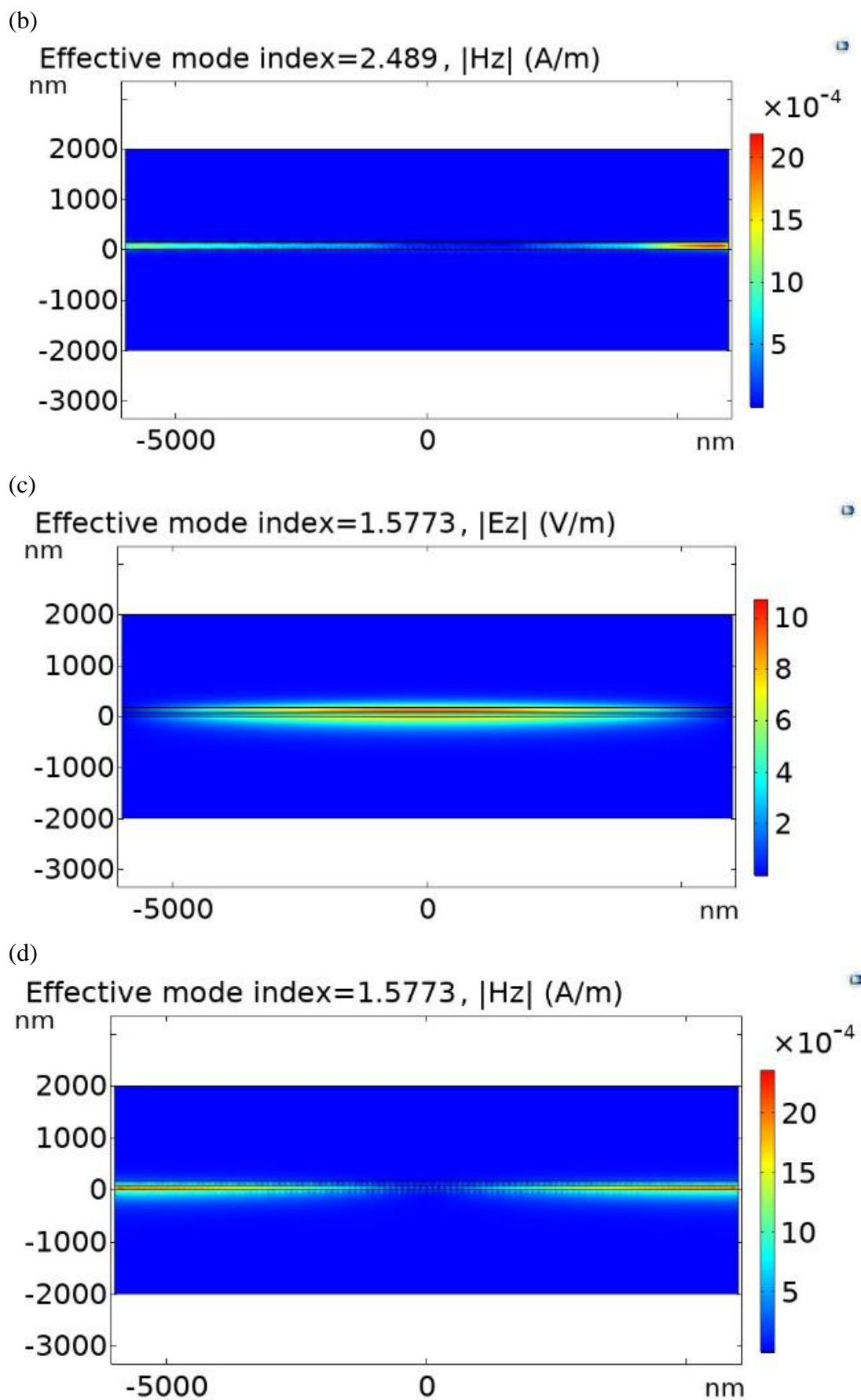
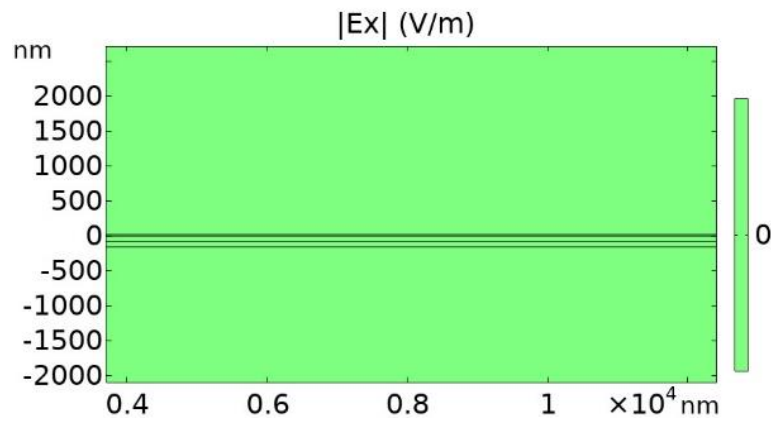


Figure 4.19: The z -component of the electric and magnetic field for (a) and (b) unetched GaP waveguide, (c) and (d) etched (80 nm) GaP waveguide, respectively, and their corresponding effective index

*Figure 4.19: Continued.*

For an ff of 50%, the Λ is obtained from Equations (4.5) and (4.8), which equals 376.45 nm. The port setting of the optical fiber source should solve for (In-plane) vectors and only the H_z component is activated by the Gaussian beam excitation shown in Equation (4.7). It is worth mentioning that the port excitation polarization differs from the waveguide propagation polarization explained in Chapter 1 – Section (1.8) and Figures (4.12) and (4.19). The difference appears in the propagation direction of the light where the light is propagating in the x-directions as shown in Figure (4.17) in the GaP waveguide. The electric and magnetic field components of the GaP waveguide in the case of TE polarization excitation are shown in Figure (4.20), which is a clear verification that the propagating light is a TE mode coupled from an optical fiber source excited by a TE light.

(a)



(b)

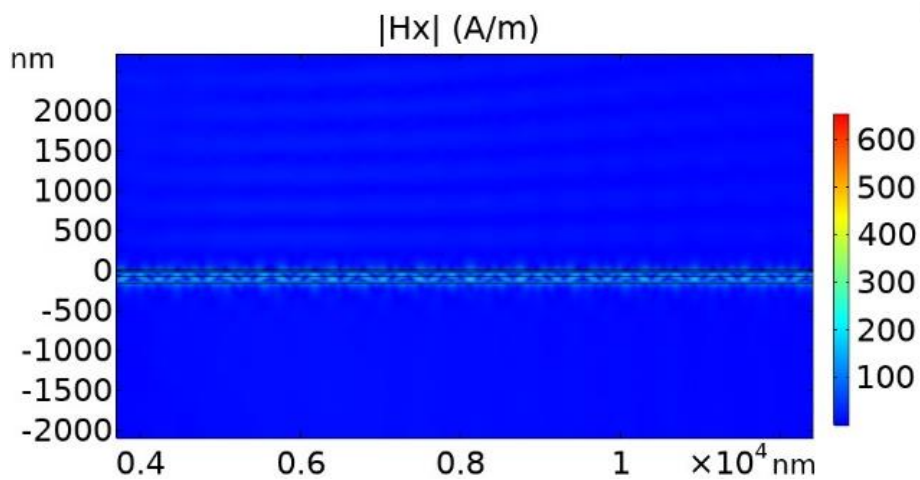


Figure 4.20: The (a) electric field and (b) magnetic field components in the propagation direction (x-axis) in the GaP waveguide when a TE polarized light is applied on the GC

The designed Λ is swept from 365 nm to 410 nm with a 5 nm step size to achieve maximum CE as shown in Figure (4.21). The etch depth and the x-position shift are kept fixed as for the TE polarization case.

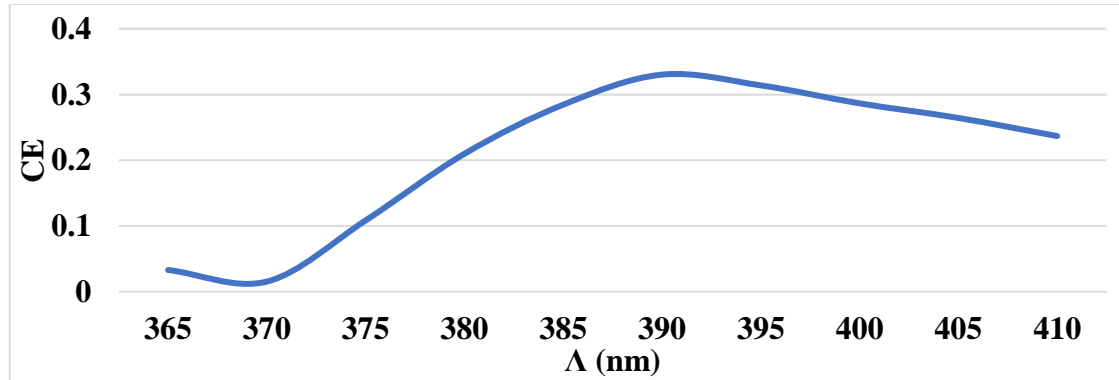


Figure 4.21: The CE against the Λ for a TM polarized light

Figure (4.21) shows a Λ of 390 nm achieves a maximum CE of 33%. The deviation between the designed and simulated Λ results from the numerical approach tolerance. The x-component of the electric and magnetic field distribution inside the GaP waveguide is shown in Figure (4.22) to verify that the propagating light is a TM polarized light.

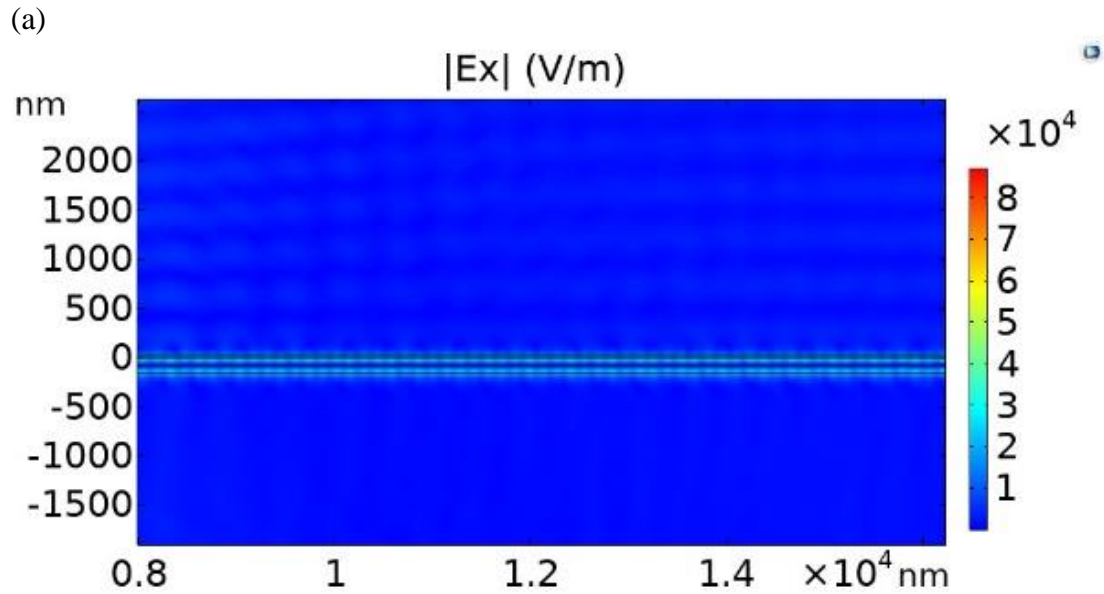


Figure 4.22: The (a) electric field and (b) magnetic field components in the propagation direction (x -axis) in the GaP waveguide when a TM polarized light is applied on the GC

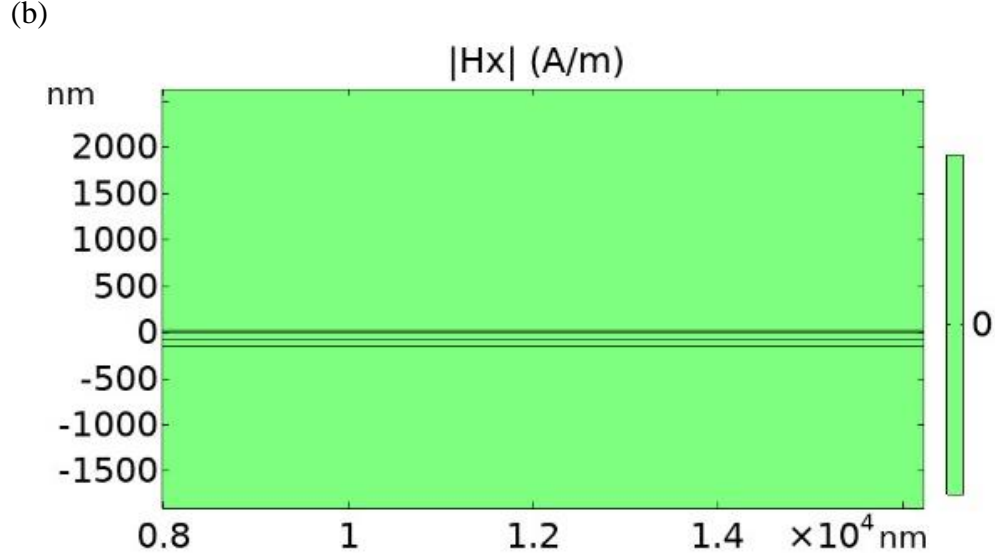


Figure 4.22: Continued.

The wavelength sweep from 600 nm to 800 nm at $\Lambda = 390$ nm shows a maximum CE of 33% at 700 nm as shown in Figure (4.23).

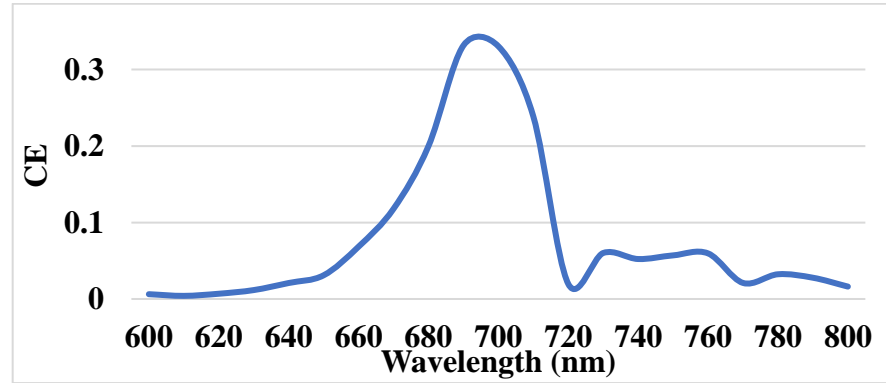


Figure 4.23: The CE against the operation wavelength for a TM polarization incidence

The GC based on a 150 nm GaP waveguide should support the coupling of a TE, TM, 45° , and -45° linearly polarized light, simultaneously, corresponding to each proposed GaP waveguide in Chapter 2. The unified GC's design for the four individual GaP waveguides simplifies the fabrication processes. The fabrication of a single GC that supports the light's coupling of four polarization cases, simultaneously, is logically more practical than designing four GCs that couple each case of the light's polarization. Hence, Section (4.4) describes two attempts to design a polarization-independent GC.

4.4. The polarization-independent GCs

The aim is to utilize the 2D simulation framework described in Section (4.3.2) to design a polarization-independent GC using the 150 nm GaP waveguide described in Chapter 2 (Figure 2.6). This section describes the implementation of the two most popular methodologies, which were used previously on different waveguide structures, to design a polarization-independent GC based on a 150 nm GaP waveguide. The first method is based on tuning the θ_c and Λ to find a unified CE for both TE and TM polarized light. The second method is based on the intersection and union of the two TE and TM Λ s. Both methodologies failed to achieve a significant value for the CE for the GC based on a GaP waveguide described in Section (4.3.2) due to several design environment differences that are mentioned in the following subsections.

4.4.1. Tuning θ_c and Λ method

The fact that each polarization case has different n_{eff} results in different Λ for each polarization case. It was found that $n_{\text{eff}} = 2.6448$ resulted in $\Lambda = 283.27$ nm for TE polarization and $n_{\text{eff}} = 2.03315$ resulted in $\Lambda = 376.45$ nm according to Bragg's laws mentioned in Equation (4.5). However, to achieve a unified GC that supports both TE and TM polarization, the Bragg's condition equation could be modified as [99]

$$n_{\text{eff-TE}} - n_c \sin(\pm\theta_{c\text{-TE}}) = \frac{\lambda_o}{\Lambda_{\text{TE}}}, \quad (4.10. a)$$

$$n_{\text{eff-TM}} - n_c \sin(\pm\theta_{c\text{-TM}}) = \frac{\lambda_o}{\Lambda_{\text{TM}}}, \quad (4.10. b)$$

Since Λ_{TE} should equal Λ_{TM} and ($n_{\text{eff-TE}} > n_{\text{eff-TM}}$ and n_c) are constants, only $\theta_{c\text{-TE}}$ and $\theta_{c\text{-TM}}$ are the remaining variables that could be changed to equalize the Λ for both polarization cases. By utilizing the same 2D simulation framework performed in Section (4.3.2), a similar behavior to [99] for the variation of $|\theta_{\text{inc}}|$ against Λ shown in Figure (4.24.a) is obtained in Figure (4.24.b) for a wavelength of 1550 nm and 700 nm, respectively.

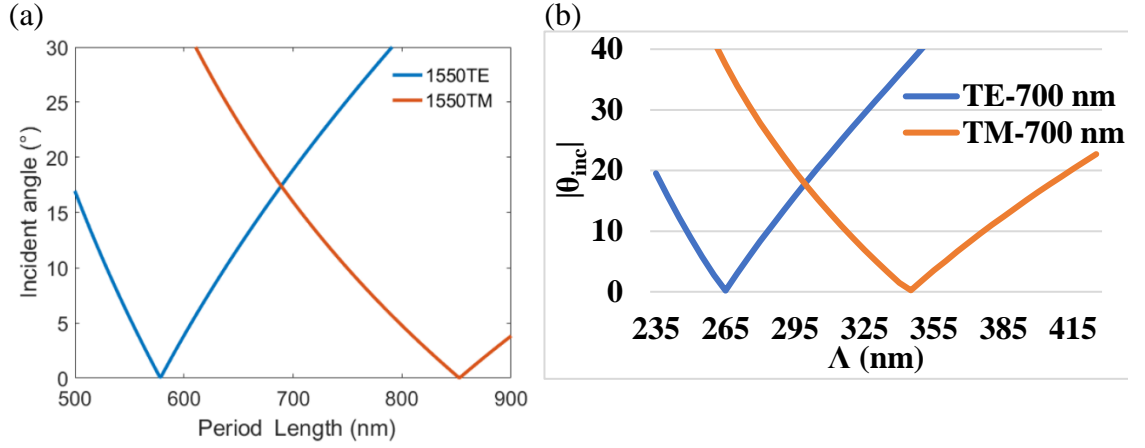


Figure 4.24: The $|\theta_{inc}|$ against the Λ for the GC in (a) [99], (b) Section (4.3.2)

Figure (4.24.b) shows that the optimum Λ is 300 nm with a θ_{inc} of 17.75° supports the coupling of both TE and TM cases of the light. However, the described approach is valid for a 3D GC with four output branches to split the incident light into different propagation directions based on the light's polarization. Therefore, the θ_{inc} 's sign was not taken into account in [99] because the light could be propagating in a forward or backward direction as shown in Figure (4.25) [99].

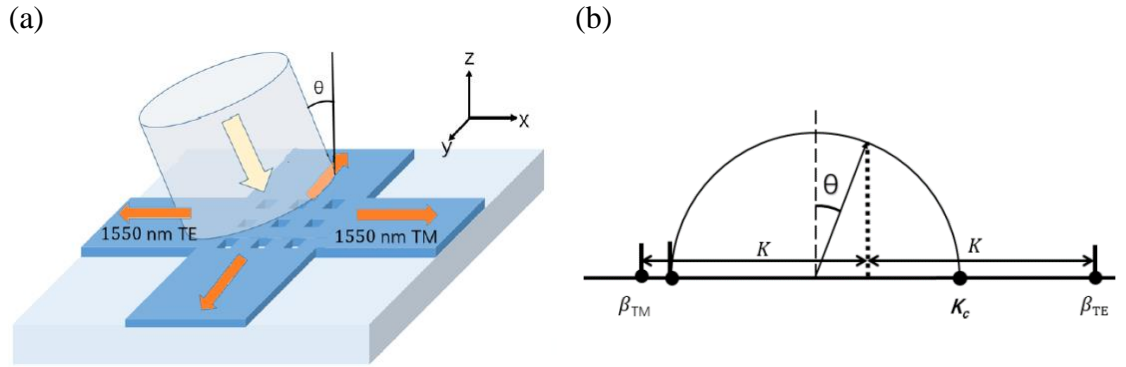


Figure 4.25: The 3D GC proposed in [99], (a) The schematic, (b) The Bragg's conditions

Nevertheless, there is a single propagation direction in 1D GC and, hence, the θ_{inc} should not be taken as an absolute value. Consequently, the variation of θ_{inc} against the Λ without taking the absolute value of θ_{inc} is shown in Figure (4.26.a).

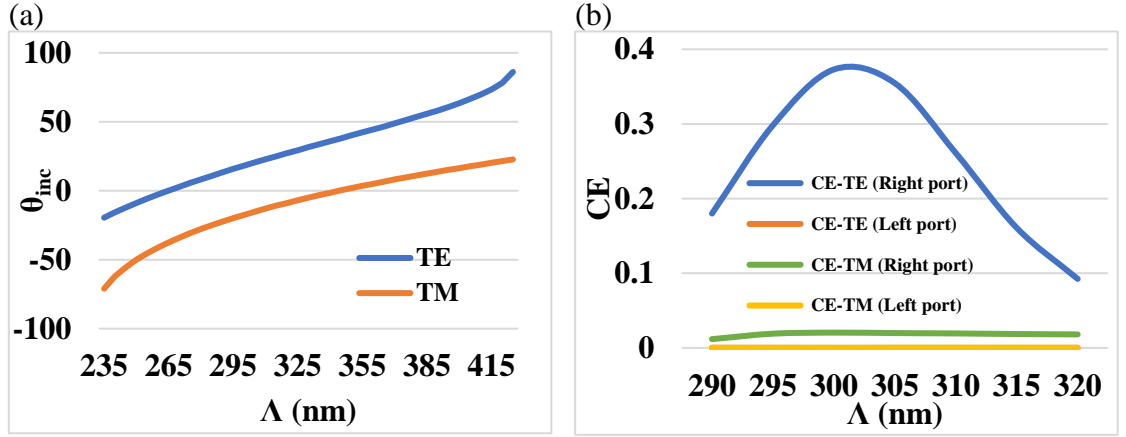


Figure 4.26: (a) The θ_{inc} against Λ , (b) The CE against the Λ for a θ_{air} of 17.75° on the 150 nm GC described in Section (4.3.2)

Figure (4.26.a) shows no intersection points under any values of θ_{inc} and Λ . Therefore, the CE at the right port of Figure (4.17.a) is 37% for a TE polarized light and 2% for a TM polarized light at the left port. The wide difference of CE for TE and TM polarized light using the described methodology is because of Λ . The design rules for the 3D GC described in [99] have differences compared to the design rules of 1D GC. Therefore, different Λ and θ_{inc} should be obtained based on their corresponding design rules in [99] to achieve high CE at both ends of the GC described in Figure (4.17.a).

Up to this level, the investigation of this methodology is enough because the aim of Chapter 4 is not to split the polarization of incident light. However, the efficient coupling of the light between the optical fiber source and the GaP waveguide is more important. The described methodology in this section could be followed as future work to design a polarization splitter GC needed at the detector side in integrated QKD systems.

4.4.2. The Λ intersection and union method [95]

Another design methodology used in 220 nm Si waveguides is the intersection or union of the GCs designed for TE and TM polarization coupling as demonstrated by [95] shown in Appendix (A).

The resultant GC structure has a nonuniform (apodized) distribution that results in equal effective indices for both TE and TM polarization and, consequently, satisfies Bragg's condition to support the coupling of both polarization cases. The optimal Λ_{TE} and Λ_{TM} should be determined as starting Λ s as explained in [95]. Hence, the 290 nm and 390 nm are taken as starting Λ s for TE and TM GC, respectively, with the same 2D simulation framework environment and parameters (x-position and the edge depth) explained in Section (4.3.2). A contour plot that shows a common CE for both TE and TM polarization cases could be plotted by sweeping their corresponding Λ s by 20 nm above and below their optimum values as in [95]. Figure (4.27) shows the contour plots for the methodology performed in [95] and that results from implementing the same methodology to the proposed 150 nm GaP waveguide in Chapter 2. The contour plots for the GC based on a 150 nm GaP waveguide are plotted by a MATLAB code shown in Appendix (E).

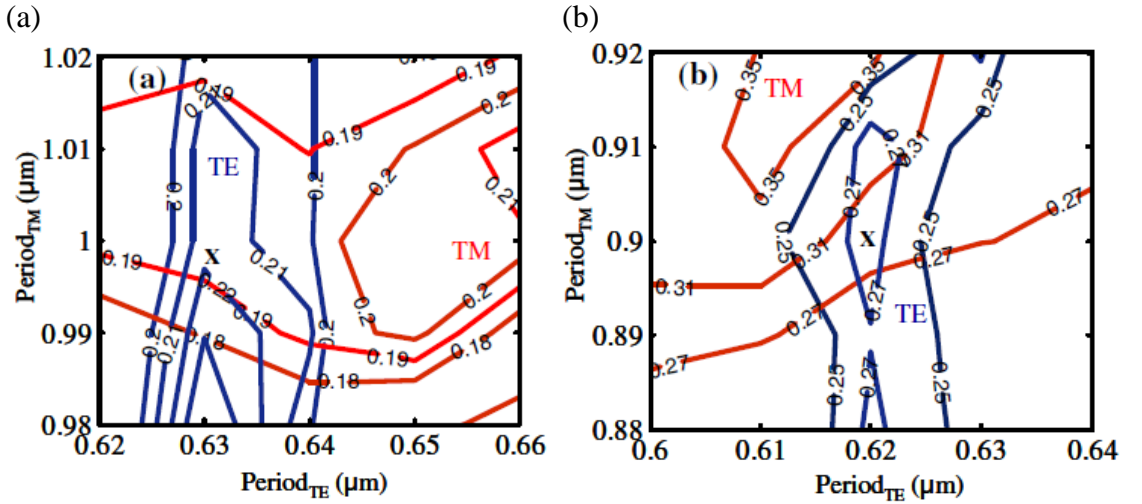


Figure 4.27: Contour plots showing the CE for (a) Intersection, and (b) Union methods based on a 220 nm Si waveguide performed by [95], (c) Intersection, and (d) Union methods based on a 150 nm GaP waveguide, where the solid line is the TE's CE and the dashed line is the TM's CE

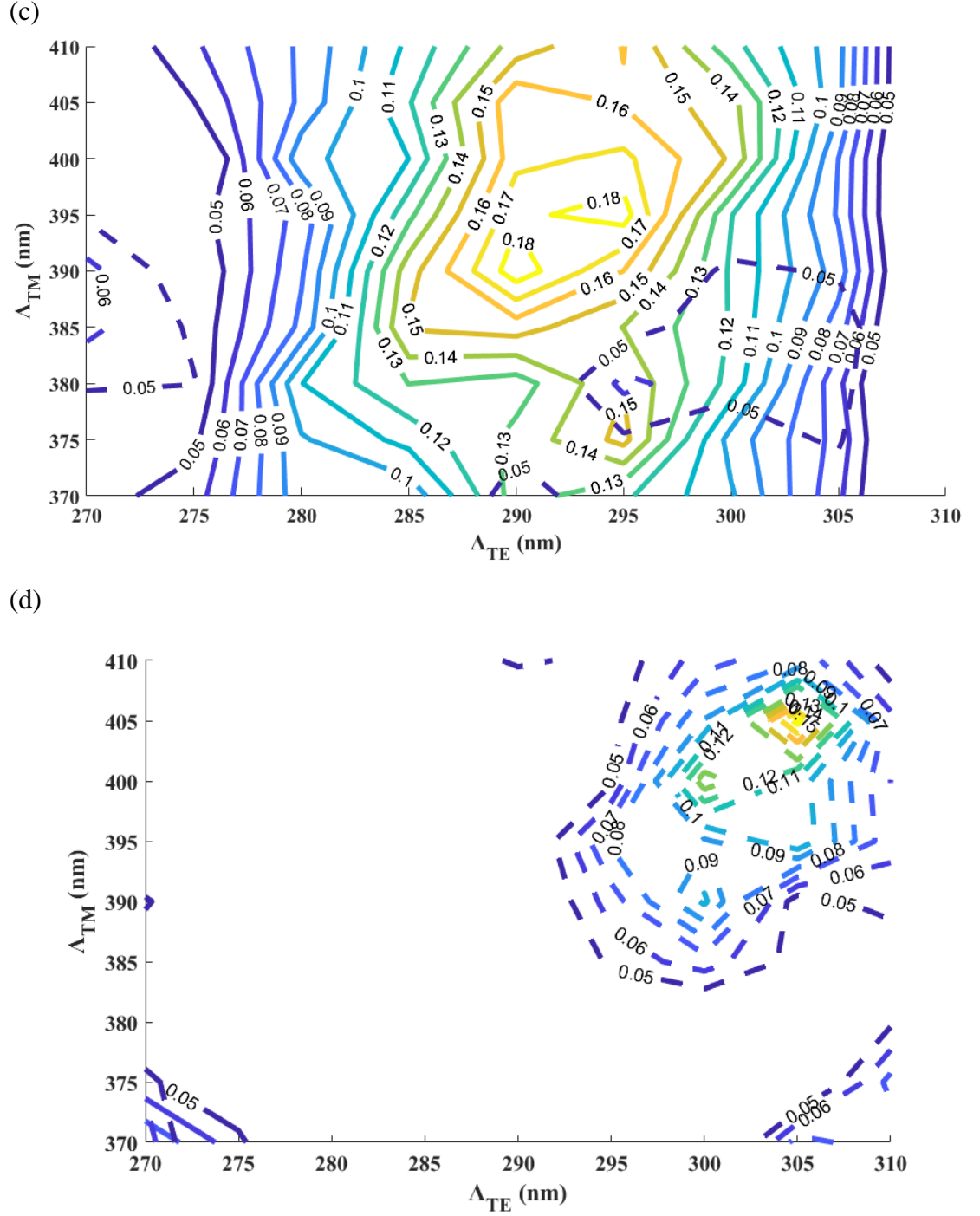


Figure 4.27: Continued.

The intersection and union methodology exhibited a maximum CE of 20.4% and 28.8%, respectively, at 1550 nm for both TE and TM polarized light as shown in Figures (4.27.a) and (4.27.b) [95]. However, the intersection method showed a maximum CE of only 5% while the union method failed to achieve a common CE for both TE and TM polarized light for a 150 nm GaP waveguide at 700 nm as shown in Figure (4.27.c) and (4.27.d),

respectively. The intersection and union method requires a thicker waveguide channel to achieve a better apodization pattern that could confine and guide the light efficiently. Therefore, the intersection and union methods failed to design an efficient GC based on a 150 nm GaP waveguide for the TE and TM polarized light. However, the intersection and union methodology could be pursued as future work to design efficient GCs based on a thicker waveguide channel.

4.5. The proposed GC design

In this section, a novel, and simple approach is proposed to design a compact four-state polarization-independent GC based on a double-layer approach utilizing a 150 nm GaP waveguide. The 1st layer is designed to couple a TE polarized light while the 2nd layer is designed to couple a TM polarized light. The deposition of the 2nd GaP layer above the 1st GaP layer emits the light efficiently regardless of its polarization state. Furthermore, the described approach yields uniform grating periods instead of thin or apodized grating structures. Consequently, the fabrication process is easier with multiple depositions and etching processes.

Before describing the proposed methodology, COMSOL's 2D simulation framework is modified to mimic the experimental environment for the 150 nm GaP waveguide described in Chapter 2. Section (4.5.1) describes the modifications to COMSOL's 2D simulation framework, which are taken as a basis to simulate the proposed GC design.

4.5.1. The modifications to COMSOL's 2D simulation framework

This section simplifies COMSOL's 2D simulation framework described in Section (4.3.1) and [118] and considers more experimental environment issues. Firstly, the used PML layer is substituted by a 2nd-order scattering boundary condition to decrease the mesh elements of the simulation domain and, consequently, reduces the simulation time with the

same performance. Section (4.3.1)'s simulation domain had 827986 mesh elements while the same simulation domain but with a 2nd-order boundary condition exhibits 799970 mesh elements with a CE of 44% as shown in Figure (4.28).

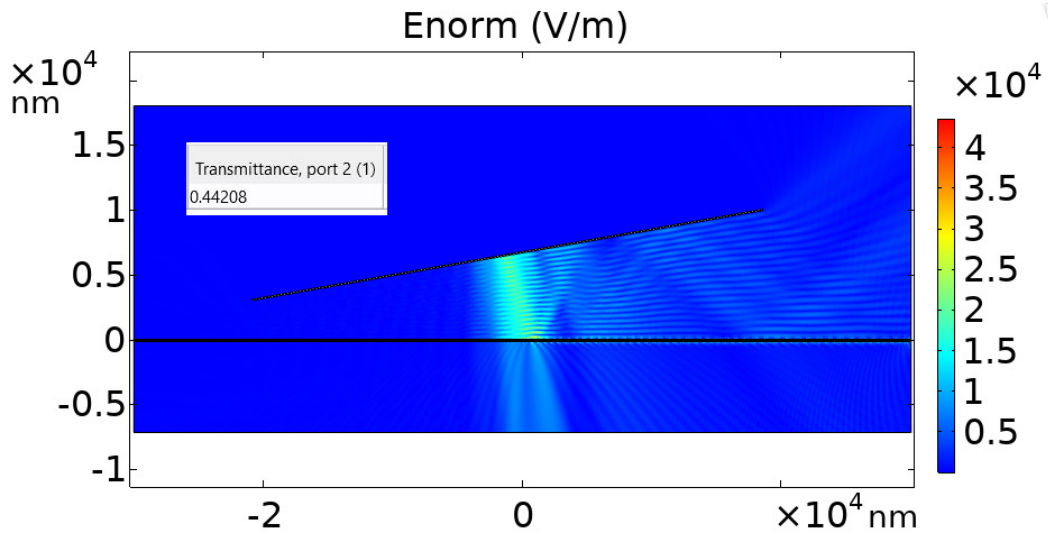


Figure 4.28: The scattering of the normal electric field in Section (4.3.1)'s simulation framework with a 2nd-order scattering boundary condition instead of the PML layer

Figure (4.17.a) and Figure (4.28) show a bouncing scattering of the light between the waveguide structure and the optical fiber source. Also, there is a considerable amount of light that penetrates the waveguide's structure. The light penetration is considered a loss because it is not confined properly within GC's structure. The bouncing scattering might lead to constructive or destructive interference of the light and result in a misleading value of the CE. The misleading CE was highlighted in [118], where the simulated and experimental CE values were 44% and 19%, respectively. It is possible to reduce the wide difference between the simulated and experimental CE by setting a Physics-controlled mesh (automated mesh by COMSOL) with Extremely-fine size. The automated mesh reduced the CE to 26%, which is closer to the experimental CE than 44%. Furthermore, the automated mesh reduces the mesh's elements number to 723385 with a more accurate result of the CE. Therefore, the automated mesh with Extremely-fine resolution is considered for the following simulations.

To mitigate these unwanted light scatterings, the fiber length is reduced to $3.5\ \mu\text{m}$, which is the core diameter of the HP-PM630 fiber, because no light propagates outside the core region. The shortening of the fiber source's length might lead to an inefficient collection of the scattered photons from the GC if it was kept at the same distance from the GC. Consequently, the fiber source height is reduced to $1\ \mu\text{m}$, while the fiber source height above the GC was $3\ \mu\text{m}$ in Section (4.3.1)'s simulation framework. The $1\ \mu\text{m}$ length of the tilted optical fiber assures that its bottom end does not hit the GC structure as indicated in Section (4.5.2), Figure (4.29).

Another important consideration is that the optical fiber function is to detect and collect (not inject) the scattered single photons emitted from a QE inside the $150\ \text{nm}$ GaP photonic waveguide proposed in Chapter 2. Hence, the settings of ports are changed such that the optical fiber source is a numeric port that detects the scattered photons, while port 2 (the right port) is set as a user-defined power source.

4.5.2. The proposed GC design methodology

The proposed GC is based on a double-layer approach as shown in Figure (4.29).

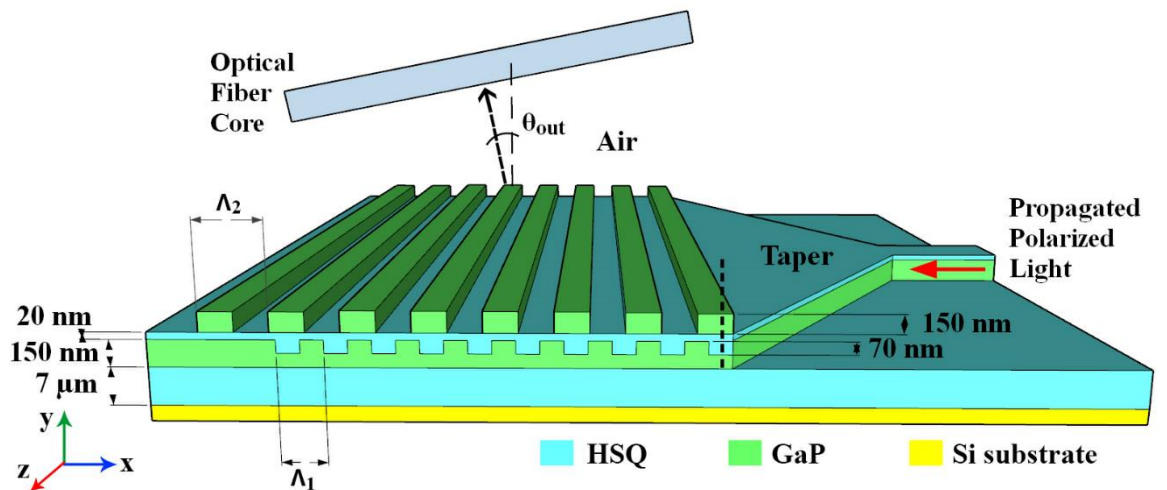


Figure 4.29: The proposed double-layer GC

The goal is to maximize the collection efficiency of the diffracted polarized light by a PMF. The PMF is tilted by an angle ($\theta_{\text{out}} = 10^\circ$) in the air region to avoid higher diffraction orders from the GC. Besides, an HSQ layer

with an optimum thickness of 20 nm is deposited above the 1st GC layer to act as a separator between the two GCs layers. The optimum thickness of the HSQ layer is explained in Figure (2.7).

The principle of the proposed GC is based on applying Equation (4.8) to multi sections of the GaP waveguide to achieve a unified n_{eff} for all four cases of light polarization. The implementation of Equation (4.8) on a single layer GaP waveguide is shown in Figure (4.30). $n_{(\text{eff}-\text{full channel})}$ is the effective index of the 150 nm GaP region, ff_{high} is the fill factor of the 150 nm GaP region, and $n_{(\text{etched channel})}$ is the effective index of the optimized 80 nm GaP channel. In this case, the GaP photonic waveguide is separated into two different regions to calculate the total effective index by using Equation (4.8), which supports the coupling of a TE polarized light. The effective indices for each structure are calculated by the slab waveguide approximation [117] using the 2D mode analysis tool in COMSOL as shown in Figure (4.30).

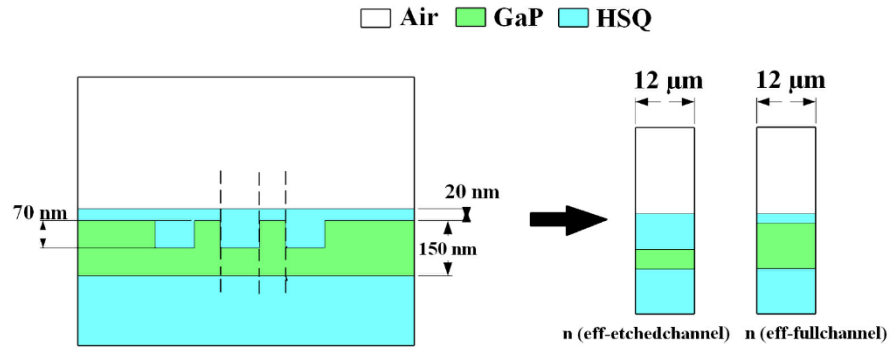


Figure 4.30: The separation of the GC into two slab waveguides to estimate the effective index for the full channel and etched channel waveguides

The effective index for the TM polarization is smaller than the effective index in the TE polarization resulting in a larger grating period to efficiently couple the TM polarized light to the PMF. However, it is possible to equalize the effective indices for both TE and TM polarization cases by depositing a second layer composed of 150 nm GaP gratings above the 20 nm HSQ separator. The 2nd layer deposition results in a modification in the effective index, as shown in Equation (4.8), that makes the GC compatible

to transmit the TE or the TM light with the same CE. The new GC structure should be divided into four regions as shown in Figure (4.31) to calculate the overall effective index.

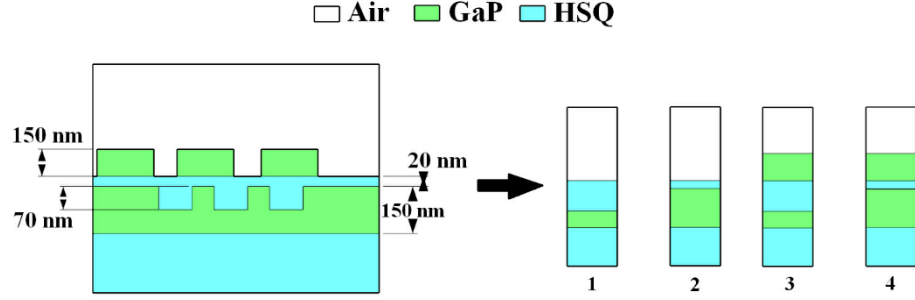


Figure 4.31: The new separation of the GC into four slab waveguides

Consequently, Equation (4.8) is modified as:

$$n_{(\text{eff})} = \sum_{i=1}^n ff_i n_{(\text{eff}-i)} , \quad (4.11.a)$$

$$\sum_{i=1}^n ff_i = 1, \quad (4.11.b)$$

where $n_{(\text{eff})}$ is the total effective index of the new GC, $ff_{1,2,3,4}$ are the fill factors of the regions from 1 to 4, respectively, and $n_{(\text{eff}-1,2,3,4)}$ are the effective indices for each region shown in Figure (4.31), respectively. Moreover, the resultant new structure is not periodic and Equations (4.11.a) and (4.11.b) should include all the resultant random fill factors over all the GC's corrugations.

With the proposed modification, it is possible to tune the grating periods and the fill factors for the double layers to achieve the optimum values for maximum CE for four polarization cases. This approach simplifies the fabrication process since it yields a uniform GC for both layers. Non-uniform or apodized GCs approaches might face difficulties in fabrication processes or optimizations since their geometries are based on thin waveguide grooves or summits that could not be fabricated with current technologies [118]. The diagram presented in Figure (4.32) describes the proposed design strategy.

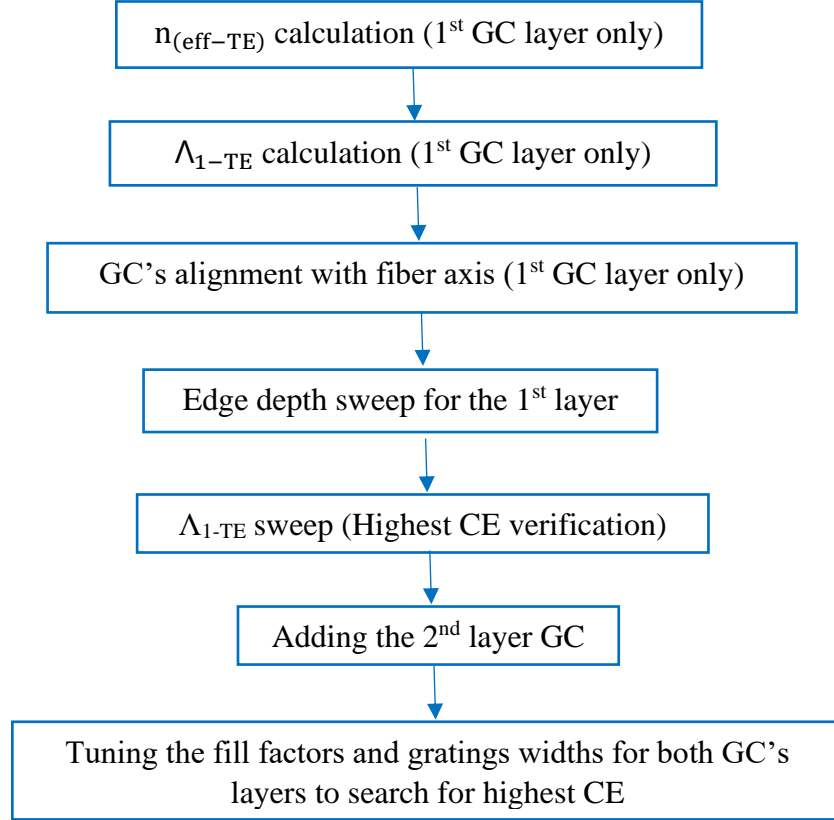


Figure 4.32: The proposed double-layer GC's design strategy

Before the deposition of the 2nd GC layer, which is composed of 150 nm GaP gratings, the 1st GC layer should be designed to support the coupling of a TE polarized light. The 1st GC layer's period (Λ_1) could be calculated from Equation (4.5) and was equal to 283.27 nm in Section (4.3.2). The initial Λ_1 is selected as 280 nm because the short and sub-nm lengths could occur due to fabrication error. The etching depth of the 1st layer is taken as 75 nm as an initial value.

The optical fiber port is a numeric port that detects the scattered photons from the GC. A numeric source is used at the right port to excite the light at different polarizations. The TE light is excited by setting E_z to 1 V/m while the TM light is excited by setting the H_z to 1 V/m. A linearly polarized light with 45° could be excited by setting both E_z and E_y to 1 V/m while a -45° linearly polarized light is excited by setting E_z and E_y to -1 V/m and 1

V/m, respectively. The aforementioned port settings simulate the field directions for each polarization case as explained in Chapter 2.

The following design step does not consider the existence of the 2nd 150 nm GaP layer. The 1st layer is designed to couple a TE polarized light with a grating period of 280 nm. The alignment of the GC to the fiber in the simulation domain is necessary to find the optimum spatial x-position coordinate (the dotted line in Figure (4.29)) to achieve a maximum CE.

The spatial x-axis position (the center of the first grating tooth) of the GC under the optical fiber is swept from 0.5 μm to 2 μm with a 10 nm step size to align the optical fiber for maximum CE of the TE polarized light, only, as shown in Figure (4.33). The TM and 45°/-45° light polarization cases are considered later in Figure (4.37) because Figure (4.33) used a lot of memory for simulation.

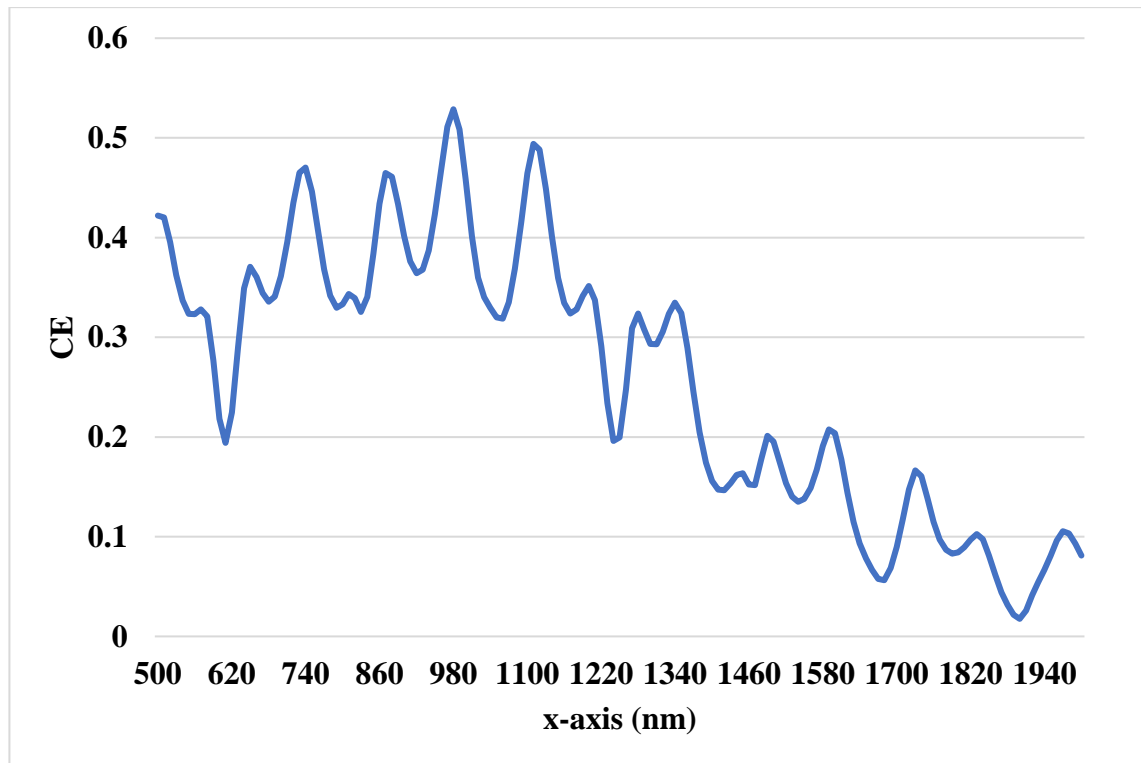


Figure 4.33: The CE against the x-shift in the GC position (1st layer only)

Figure (4.33) shows a maximum CE of 53% at $x = 980$ nm, which is fixed in the following simulation steps. The new fiber source parameters show higher CE than in Section (4.3.2) indicating the accuracy of the new

proposed simulation environment. The x-axis position is fixed at 980 nm and the etching depth is swept from 30 nm to 90 nm with a 5 nm step size for maximum CE as shown in Figure (4.34).

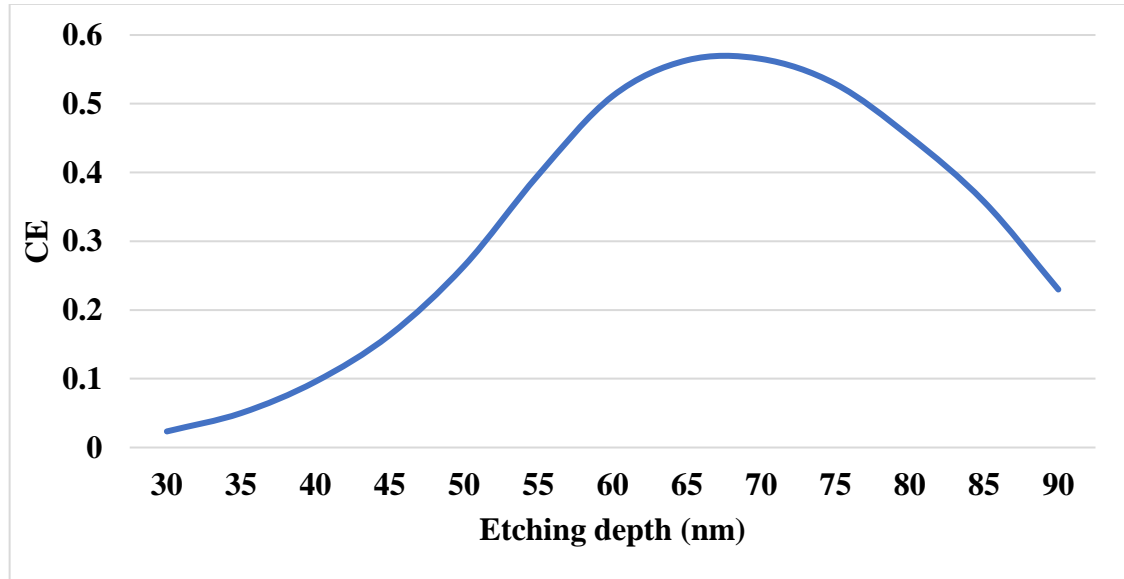


Figure 4.34: The CE against the etch depth of the 1st layer only

Figure (4.34) shows a maximum CE of 56.52% for an etch depth of 70 nm. By setting the etch depth and the x-position to their optimal values, the GC period is swept from 275 nm to 300 nm with a 5 nm step size to search for maximum CE as shown in Figure (4.35).

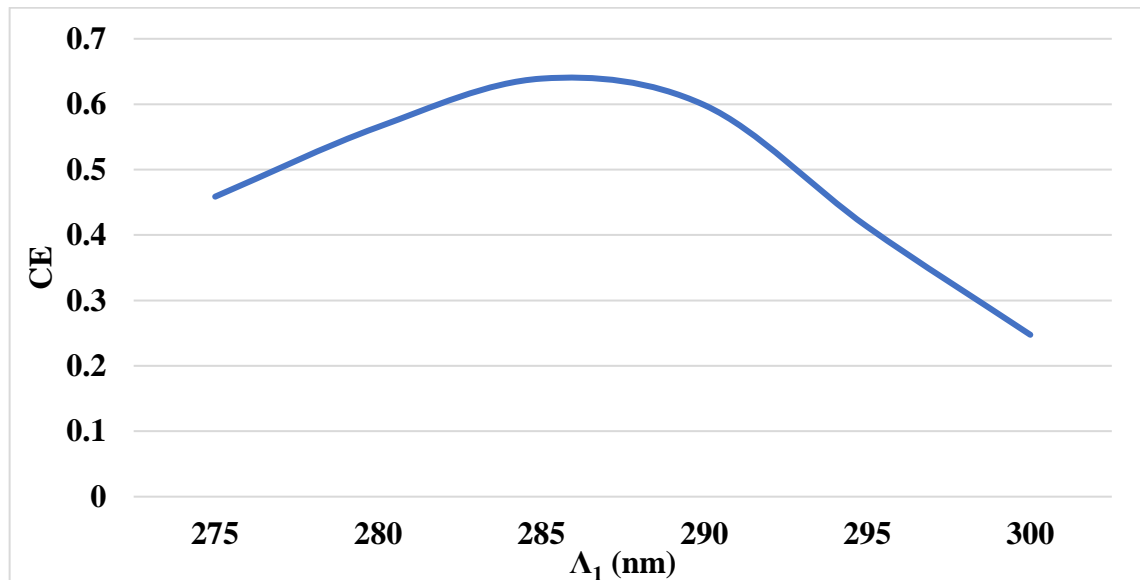


Figure 4.35: The CE against Λ_1

Figure (4.35) shows a maximum CE of 64% for a Λ_1 equals 285 nm. By setting all the optimal parameters of Λ_1 , etch depth, and the GC's x spatial

position of the 1st layer only, the CE for a TE-polarized light against the operation wavelength is shown in Figure (4.36) with a maximum CE of 64% at 700 nm.

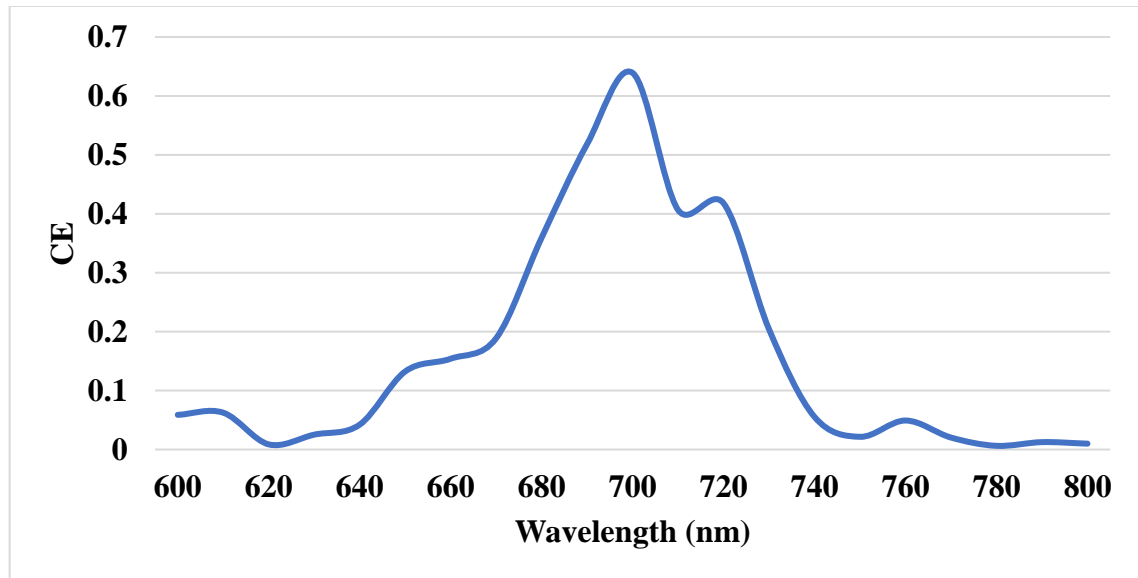


Figure 4.36: The CE against the operation wavelength for a TE polarization excitation from the right port

To observe the CE behavior for all the light polarization cases, Figure (4.37) shows the CE of the GC against the x-axis spatial coordinate between 920 nm and 1060 nm for the TE, TM, and a 45°/-45° light polarization.

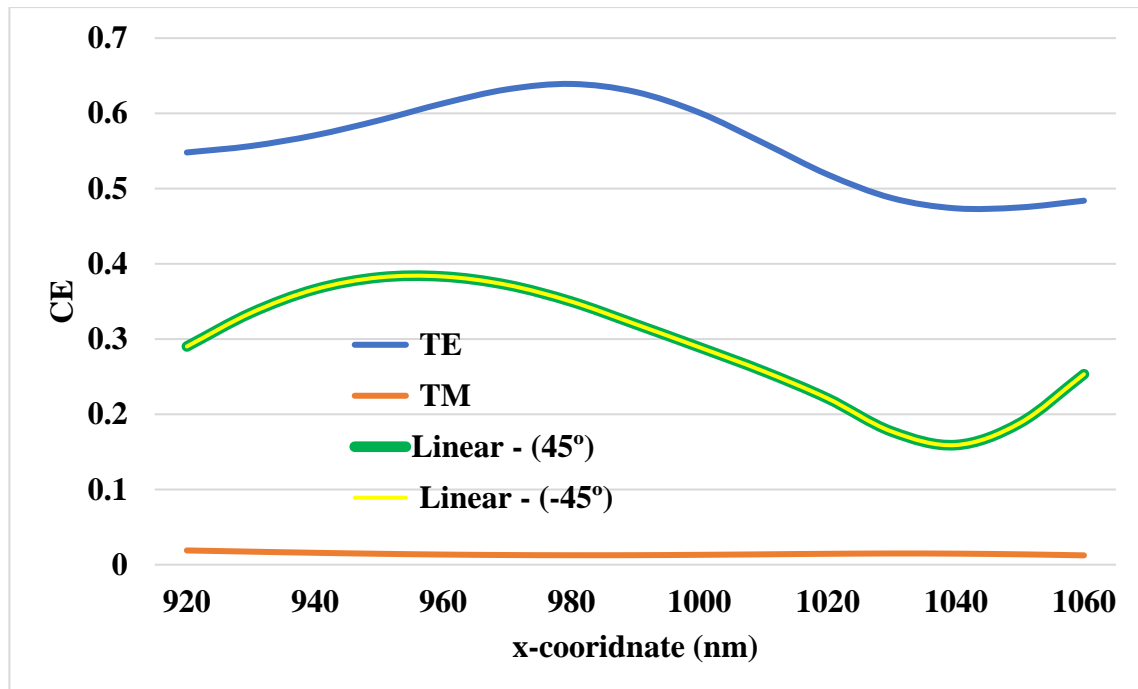


Figure 4.37: The CE of a GC against the x-coordinate to a fixed position of a PMF in the simulation domain

For an ff of 50%, the Λ_2 is obtained from Figure (4.19), Equations (4.5), and (4.8), which equals 376.45 nm. The 2nd layer is deposited above the 20 nm HSQ layer that covers the 1st layer as shown in Figure (4.29).

The number of gratings to the left side from the optimum x-position is selected such that the GC with a minimum Λ covers the entire core of the PMF. Consequently, 11 gratings of 285 nm for the 1st layer and a similar number of gratings for the 2nd layer. Figure (4.38) shows the CE spectra for each case of excitation polarization using the single-layer approach and the double-layer approach.

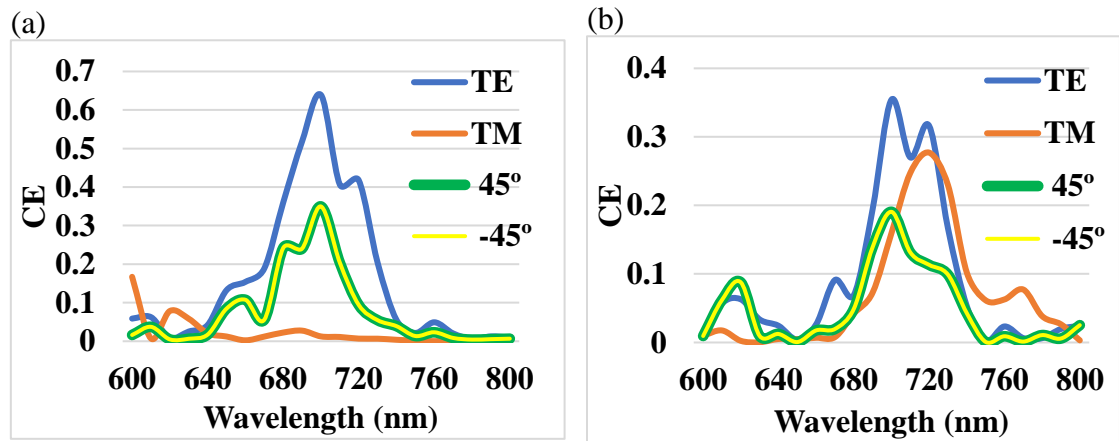


Figure 4.38: The CE spectra of the proposed GC with (a) a single-layer approach, (b) a double-layer approach

The single-layer approach of the GC achieved a CE of 64% for a TE polarized light, a CE of 35% for a linearly polarized light at 45°/-45°, and a CE of 1% for a linearly polarized light at 90° as shown in Figure (4.38.a).

A higher CE for TM polarized light could be achieved by depositing a second layer of 150 nm GaP with a grating period of 375 nm above the first layer with the same thickness as shown in Figure (4.29). However, the CEs for TE and 45°/-45° linearly polarized light deteriorate. CEs of 35%, 16%, and 19% for the TE, TM, and 45°/-45° linearly polarized light, respectively, are achieved as shown in Figure (4.38.b).

By tuning the filling factors, the 1st layer grating period, and the 2nd layer grating period, better performance for the proposed GC could be

achieved. The fill factor for each layer is tuned from 0.1 to 0.9 with a 0.1 step size, while the grating periods of the first layer and the second layer are tuned from 260 nm to 310 nm and from 350 nm to 400 nm, respectively. The corresponding CEs for each polarization case are recorded in separate EXCEL sheets for each case. For example, for an ff of 0.5 for the 1st layer, an ff of 0.6 for the 2nd layer, and the grating period for the first and second layer are tuned to 285 nm and 380 nm, respectively, the CEs are 39.2%, 31% and 23.3% for a TE, TM and 45°/-45° linearly polarized light, respectively, as shown in Figure (4.39).

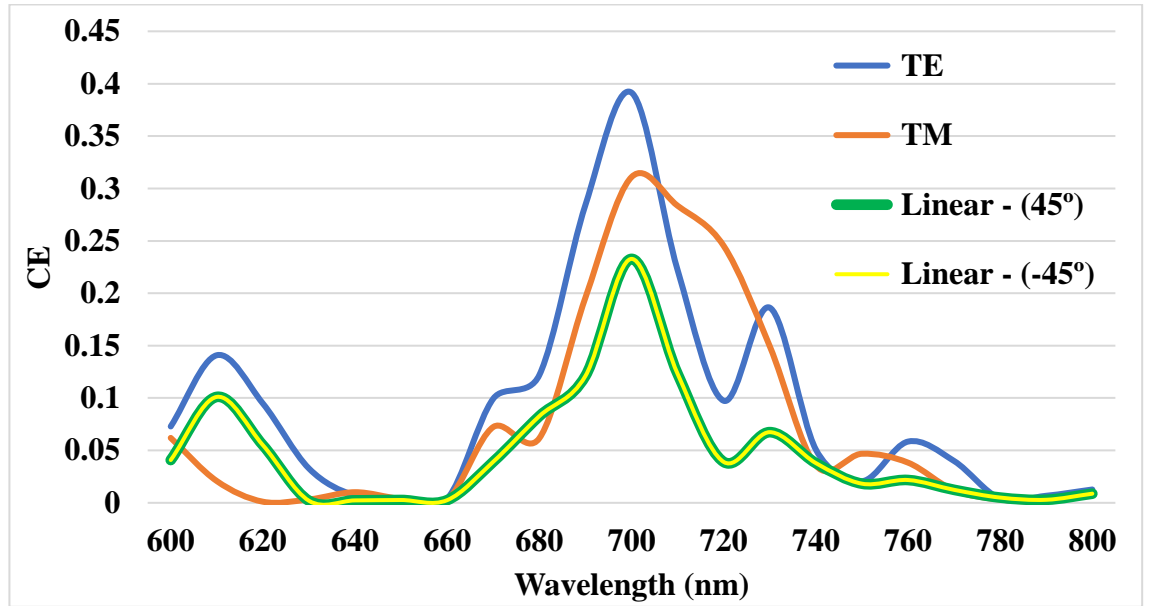


Figure 4.39: The CE spectra of the four polarization cases for the optimum double-layer GC

The polarization-dependent loss (PDL) identifies the polarization-independence of the GC and is defined as [96,97]:

$$\text{PDL} = 10\log \left| \frac{\text{CE}_{\text{TE}}}{\text{CE}_{\text{TM}}} \right| \quad (4.12. a)$$

$$\text{PDL} = 10\log \left| \frac{\text{CE}_{\text{TM}}}{\text{CE}_{45^\circ/-45^\circ}} \right| \quad (4.12. b)$$

$$\text{PDL} = 10\log \left| \frac{\text{CE}_{\text{TE}}}{\text{CE}_{45^\circ/-45^\circ}} \right| \quad (4.12. c)$$

Accordingly, the optimum double-layer GC shows a PDL of 1 dB, 1.25 dB, and 2.26 dB for TE-TM, TM-45°/-45°, and TE-45°/-45°, respectively, at 700 nm as shown in Figure (4.40).

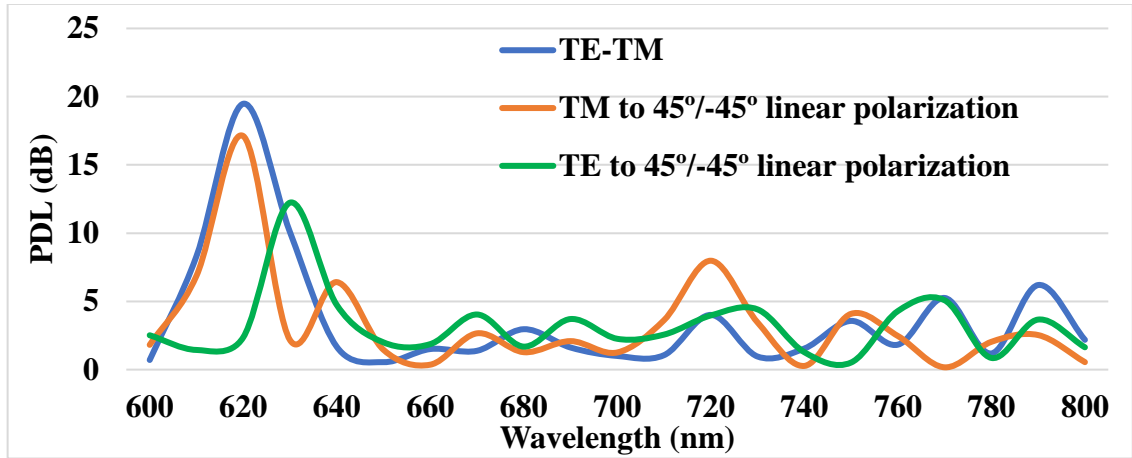


Figure 4.40: The PDL performance of the optimum double-layer GC for different polarization cases

The observation of the intensity in the simulation domain is necessary to show how the fields are scattered. Figure (4.41) shows the intensity distribution of the light for each case of polarization of the excitation source (Right port).

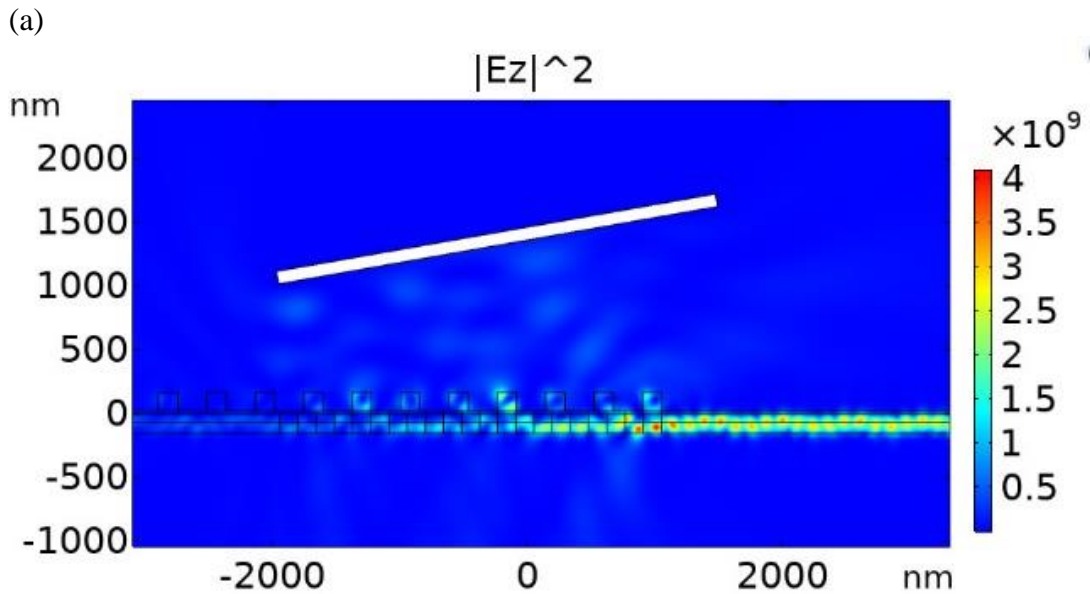


Figure 4.41: The intensity distribution in the simulation domain for (a) a TE excitation, (b) a TM excitation, (c), and (d) a 45° linear excitation.

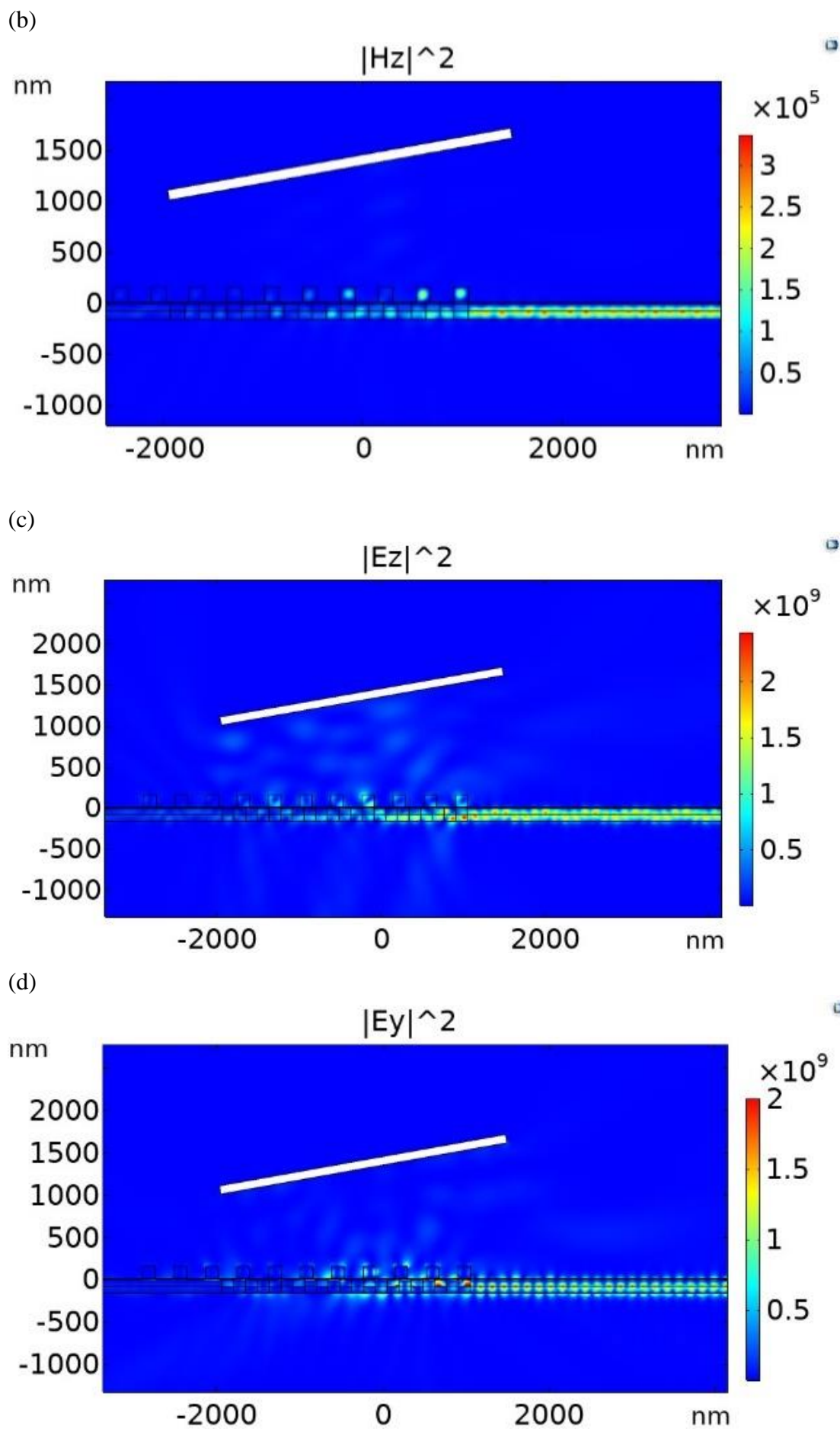


Figure 4.41: Continued.

Figure (4.41.a) shows the scattering of the $|E_z|^2$ in the case of 0° polarization excitation from the right port. The out-of-plane component of the field, which is E_z , generates both H_x and H_y components inside the GaP region. However, the H_y component is the major field in the selected mode of propagation and, consequently, this is a clear indication that 39% of the propagating photons polarized at 0° inside the GaP region are coupled to the PMF. Similarly, Figure (4.41.b) shows the scattering of the $|H_z|^2$ in the case of 90° excitation. For a 45° linearly polarized light, the excitation of the right port is performed with both E_y and E_z components of the light.

Accordingly, Figure (4.41.c) and Figure (4.41.d) show the scattering of the z-component and y-component of the intensity, respectively. Moreover, for a -45° linearly polarized light, the excitation of the right port is similar to that in the 45° polarization case except that the z-component of the excitation source becomes negative. As a result, the scattering of the field in the simulation domain is similar to that shown in Figures (4.41.c) and (4.41.d) except for the negativity of the E_z component to Figure (4.41.c). Consequently, the intensity distribution for the -45° polarization case was not included in Figure (4.41) to concise. Moreover, there is a negligible scattering of the intensity field in the space of the simulation domain (air region) for all the polarization cases. Table (4.1) compares the performance of the proposed double-layer GC approach with other polarization-independent GCs approaches.

Table 4.1: A summary of the simulation performance of the polarization-independent GCs approaches

Publication	Wavelength (nm)	Waveguide channel width (nm)	CE (%)
[92]	1550	340	64
[93]	1550	750	52.5
[94]	1550	370	60
[95]	1550	220	20
[96]	1550	400	60
[97]	1550	460	60
[98]	1550	220	32.5
[99]	1550	220	35.5
Our work	700	150	39.2 [*] /31 ^{**} /23.3 ^{***}

^{*} For a TE polarization

^{**} For a TM polarization

^{***} For a 45°/-45° linear polarization

4.5.3. The excitation requirements

The calculation of the CE for the optimized GC structure using a 532 nm excitation source is necessary to determine its minimum power requirement. The optical fiber source port injects a 532 nm laser light with a Gaussian distribution into the GC's structure and the right port of the 2D simulation framework is used to monitor the CE. The excitation power that reaches the QE after being coupled to the GC and propagated along the HPWs designed in Chapter 2 is calculated by

$$P_{QE} = P_{exc} \times CE_{532nm} \times (1 - \gamma_{HPW}), \quad (4.13)$$

where P_{exc} is the 532 nm laser source excitation power, CE_{532nm} is the CE of the GC at 532 nm, and γ_{HPW} is the attenuation loss of the HPW. The γ_{HPW} of the HPW is calculated by repeating Table (2.2) at 532 nm as shown in Table (4.2). The γ_{HPW} of each HPW is calculated at positions listed in Table (4.3) as the following

$$\frac{L_{\text{propagation at 532 nm}}}{(1/e)} = \frac{L_{\text{rotation at 700 nm}}}{\gamma_{HPW}} \quad (4.14)$$

For example, the propagation length (1/e losses) for 45° output polarization is calculated as 11.05 μm . However, the required conversion length is 3.333 μm . Consequently, by a proportion and ratio calculation

shown in Equation (4.14), the loss factor is calculated to be 0.111 which yields a transmission of $1 - 0.111 = 0.889$. Table (4.3) shows a minimum excitation power of 4.87 mW at the end of 0° HPW when using a TM polarized excitation light source.

Table 4.2: The two orthogonal modes effective indices for the four HPWs designed at Chapter 2 at 532 nm

Output polarization angle	Tuned Al width (nm)	$n_{\text{eff-TM1}}$	$n_{\text{eff-TM2}}$	$L_{\text{eff-TM1}}$ (μm)	$L_{\text{eff-TM2}}$ (μm)
0°	5	2.8743-0.0043944i	2.9636-0.0032487i	9.77845	17.15
90°	90	2.8927-0.0042777i	2.9606-0.0036438i	9.897	11.62
45°	62	2.8845-0.0038325i	2.963-0.0032759i	11.05	12.9
-45°	62	2.8845-0.0038326i	2.963-0.0032759i	11.05	12.9

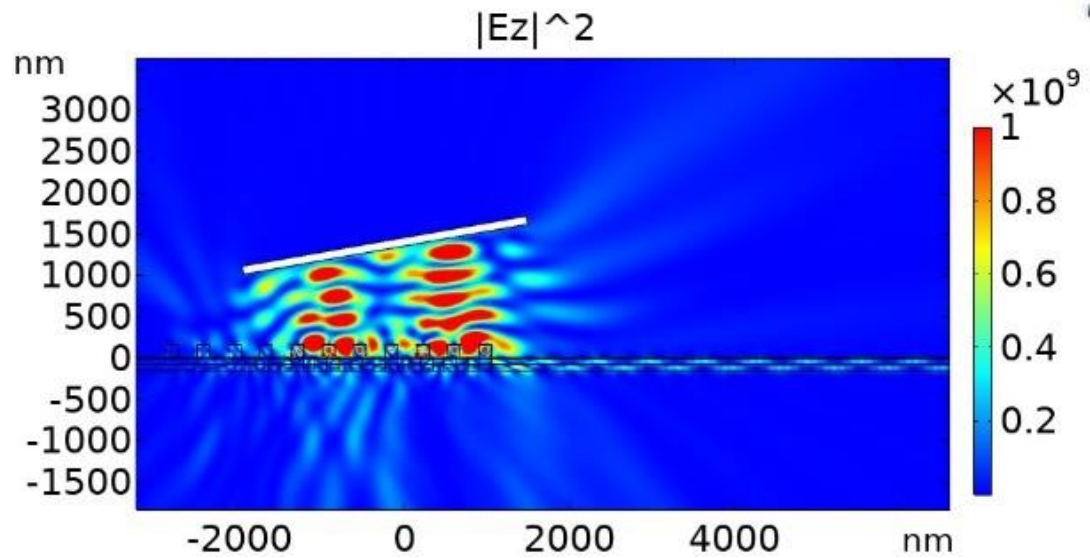
Table (4.3) shows the corresponding CE for each case of the excitation source's polarization where the excitation power is assumed to be 1 W.

Table 4.3: The CE of the GC after being excited by a 532 nm laser light having 0° , 90° , and $45^\circ/-45^\circ$ (Green) and the output power at the end of HPWs mentioned in Table (4.2) (Orange)

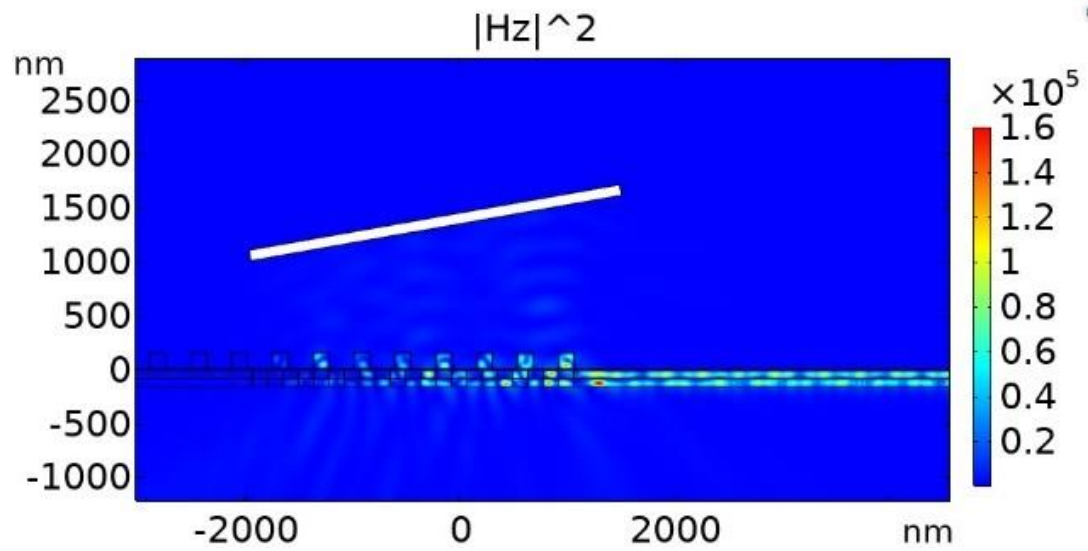
The polarization of the excitation source and the HPW	CE	γ_{HPW}	0° HPW's output (mW)	90° HPW's output (mW)	45° HPW's output (mW)	-45° HPW's output (mW)
0°	0.011	0.1881	8.93	9.416	9.78	9.78
90°	0.006	0.144	4.87	5.14	5.33	5.33
45°	0.011	0.111	8.93	9.416	9.78	9.78
-45°	0.011	0.111	8.93	9.416	9.78	9.78

Therefore, a 1 W excitation power source is enough to excite the QE that needs only 0.5 mW to achieve a $g^{(2)}(\tau)$ smaller than 0.5 as indicated in Table (3.1). The 1 W excitation power source could be decreased by an optical attenuator to achieve the required excitation power. Finally, Figure (4.42) shows the excitation field distribution for each case of excitation polarization.

(a)



(b)



(c)

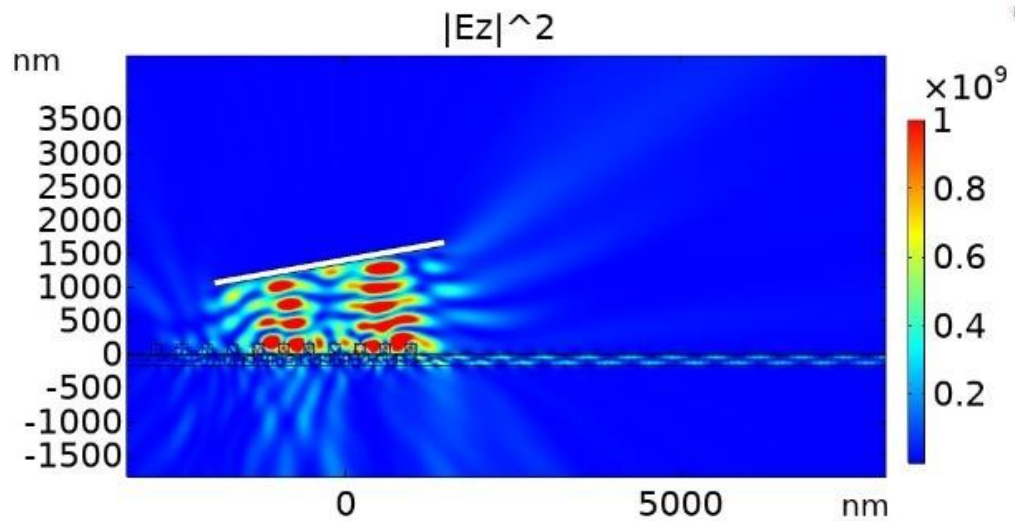


Figure 4.42: The intensity distribution of the excitation light source in the simulation domain for (a) a TE excitation, (b) a TM excitation, (c), and (d) a 45° linear excitation.

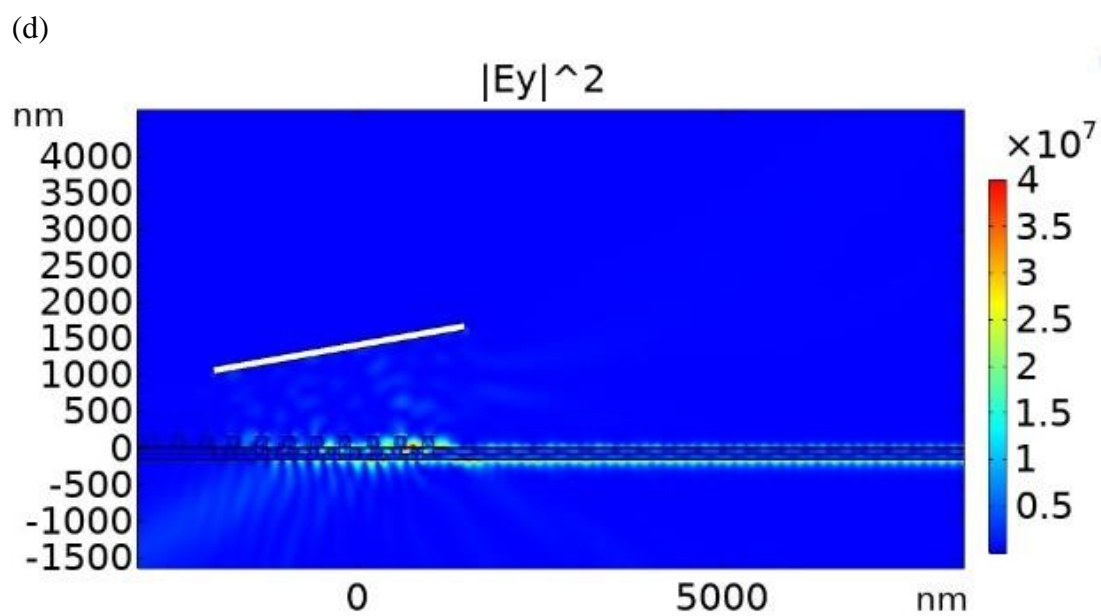


Figure 4.42: Continued.

Chapter Five

Conclusions and Suggestions for the Future Work

Chapter 5

Conclusions and Suggestions for Future Work

5.1. Conclusions

Four HPWs, which have an embedded QE, were designed to emit single photons with a definite polarization at 0° , 45° /- 45° , and 90° . The proposed HPWs provided a high energy extraction efficiency for the QE in the optimum position inside them for each HPW. The proposed structure with a specified output polarization could be implemented in a practical on-chip QKD system based on BB84 protocol or other related protocols and, consequently, reduces the system complexity.

The experimental photophysics parameters, which are unique to every QE, were used in the suggested MATLAB modeling scripts. Besides, the effect of coupling on a model for the two-level QE was presented using QuTiP. The proposed work predicted the experimental behavior of the QE before and after coupling to a nanostructure, i.e., DLSPP waveguide or nanoantenna. Although the theoretical modeling has its limitations since it does not include all the experimental framework parameters, however, the prediction of the experimental data provides sufficient information to evaluate the approximate performance of the QE before and after coupling to a nanostructure.

A novel and, simple approach is proposed to design a compact and polarization-independent GC. The proposed method simplifies the fabrication process through consecutive deposition and etching processes. Furthermore, the proposed design methodology could be followed as a general design methodology for any emission wavelength or waveguide dimensions. The CE of the proposed GC is comparable to other GCs presented in the literature survey with larger channel width.

5.2. Future work

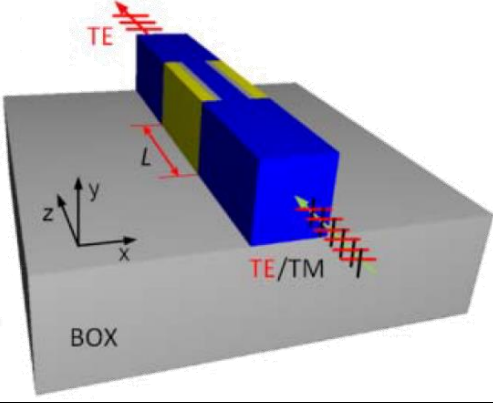
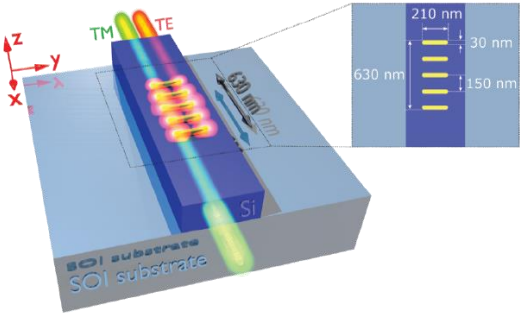
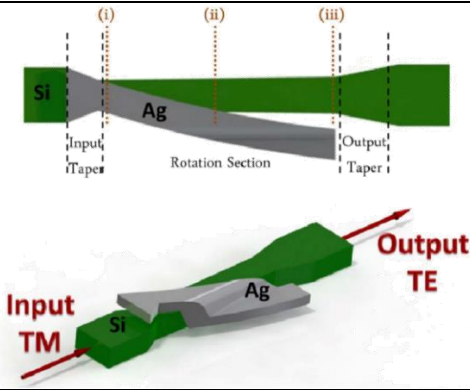
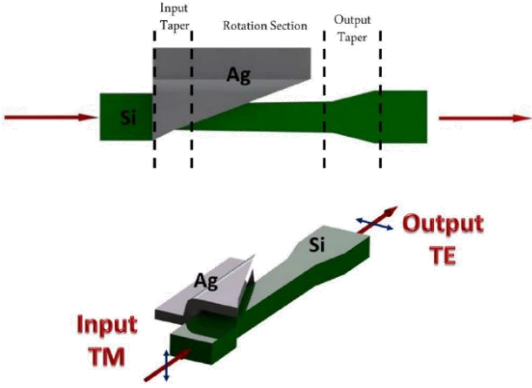
The high performance of coupling the QE to an HPW with low loss and compact footprint facilitates the way toward further developments. For example:

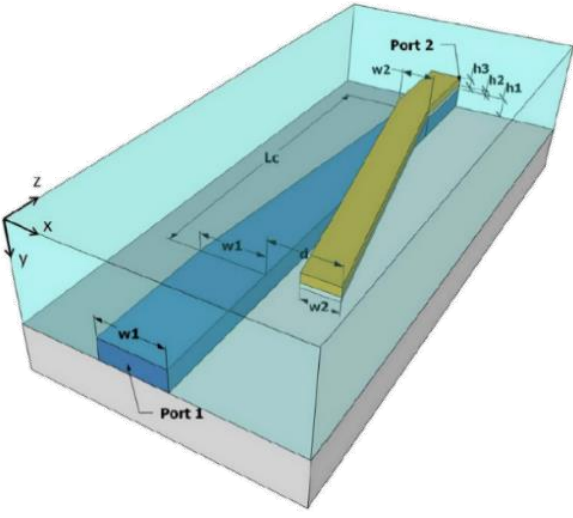
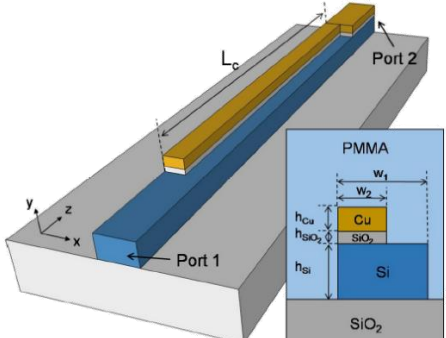
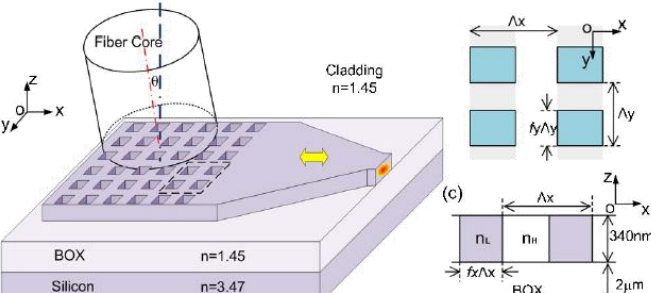
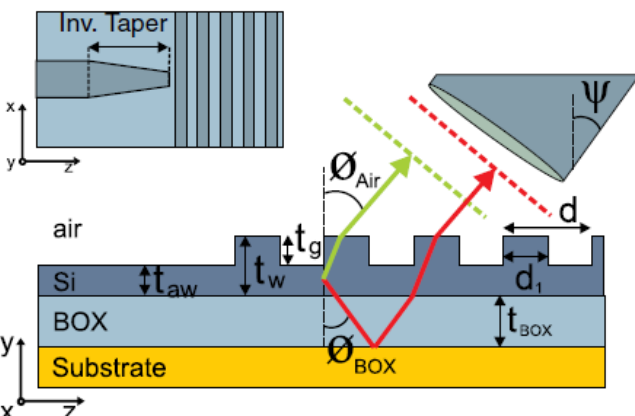
1. The design of an HPW that supports different orientations for the QE embedded inside the HPW with enhanced Purcell factor.
2. The utilization of tapered structures might lead to more advanced performance.
3. The photophysics parameters of QEs other than NV center, such as SiV, GeV, SnV, PbV, semiconductor QDs, etc, are still not determined. The modeling of $g^{(2)}(\tau)$ for other QEs could be determined once the photophysics parameters of these QEs will be known.
4. Different approaches could be followed to improve the performance of the proposed GC. For example, the second layer gratings' shape could be altered to obtain equal CEs and PDL for the four polarization cases. Consequently, the new shape might result in equal brightness for all polarization cases.
5. Studying the performance of QEs that emit at 1550 nm.

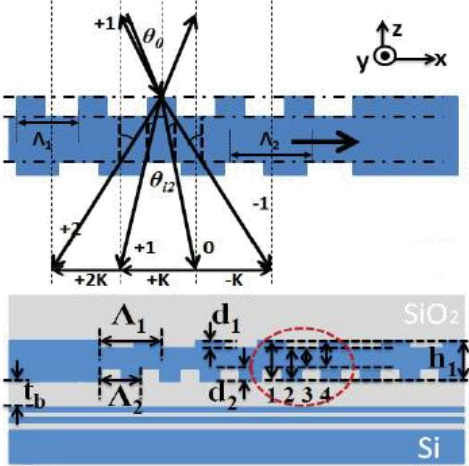
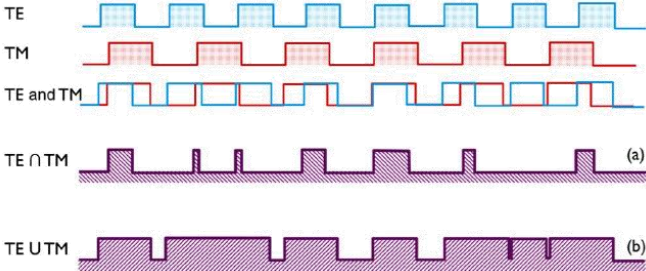
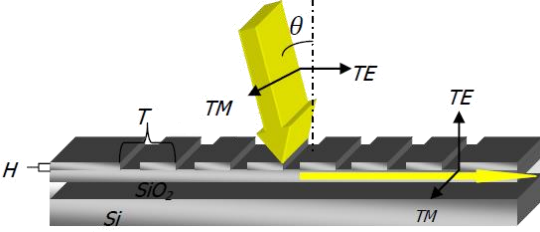
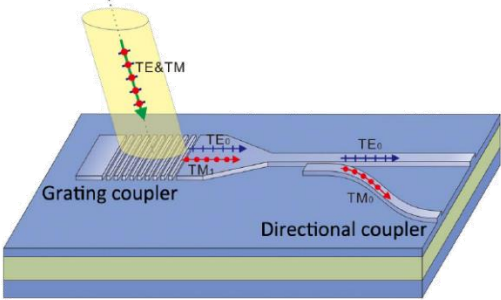
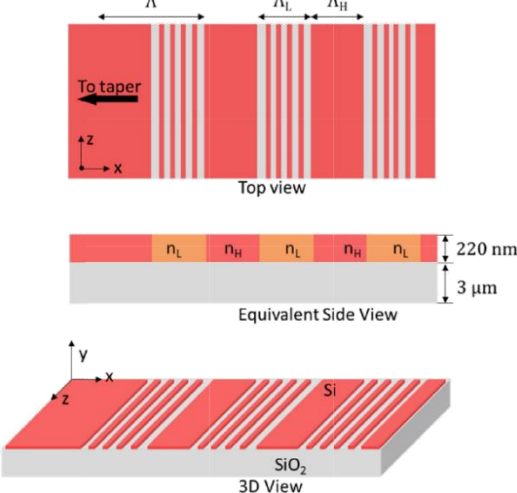
Appendices

A. Graphical literature survey

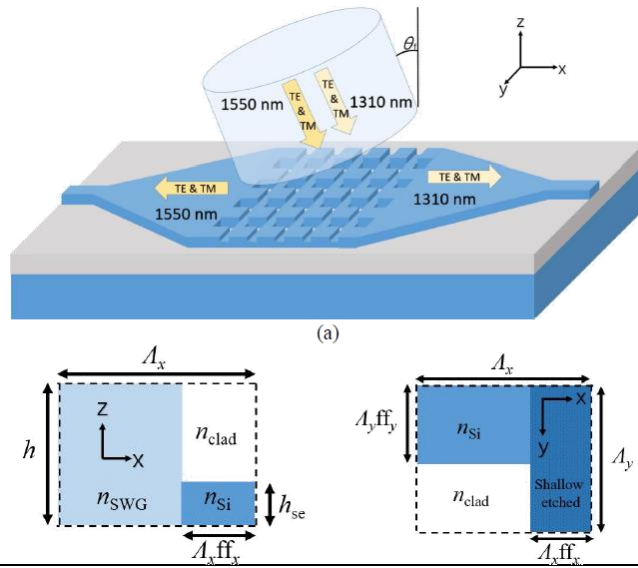
Reference	Structure	Comments
H. Zbinden et al. [64,65]		A Typical system for quantum cryptography using polarization coding based on BB84 protocol
Siampour et al. (2017) [78]		<ul style="list-style-type: none"> • QE: NV • DLSPP • $\beta = 63\%$ • 42-fold • Enhanced $\frac{\Gamma_{\text{tot}}}{\Gamma_0} = 42$
Kumar et al. (2019) [79]		<ul style="list-style-type: none"> • QE: QDs • HPW • $\beta = 87\%$ • $\frac{\Gamma_{\text{tot}}}{\Gamma_0} = 37$
Siampour et al. (2020) [80]		<ul style="list-style-type: none"> • QE: GeV, NV • DLSPP • $\beta = 66\%$ • $\frac{\Gamma_{\text{tot}}}{\Gamma_0} = 10, 12$
T. Heindel et al. (2020) [81]		<ul style="list-style-type: none"> • On-chip polarized single-photon source

<p>Y. Zhang et al. (2015) [83]</p>		<ul style="list-style-type: none"> • Length = 800 nm • Insertion loss = 2.5 dB • Extinction ratio = 25 dB • BW = 300 nm
<p>R. Salas-Montiel et al. (2019) [84]</p>		<ul style="list-style-type: none"> • Extinction ratio = 23 dB μm^{-1} • Insertion loss = 2.4 dB μm^{-1} • $\lambda = 1.59 \mu\text{m}$ • Length = 630 nm
<p>M. Mojahedi et al. (2012) [86]</p>		<ul style="list-style-type: none"> • Length = 5 μm • $\lambda = 1.55 \mu\text{m}$ • Extinction ratio > 14 dB • Insertion loss = 2.1 dB
<p>M. Mojahedi et al. (2013) [85]</p>		<ul style="list-style-type: none"> • Length = 3.7 μm • $\lambda = 1.55 \mu\text{m}$ • Insertion loss = 1.5 dB • Extinction ratio > 13.5 dB

<p>M. Qi et al. (2015) [87]</p>		<ul style="list-style-type: none"> • High coupling factors of 92%, 78%, 75%, and 73% are achievable using Ag, Au, Al, and Cu as the metal cap, respectively. • Length = 5 μm • $\lambda = 1300\text{--}1800\text{ nm}$ • Reflection < -40 dB
<p>M. Qi et al. (2015) [88]</p>		<ul style="list-style-type: none"> • $\lambda = 1550\text{ nm}$ • BW = 200 nm • Length = 5 μm • Coupling factor = 78%
<p>H.K. Tsang (2011) [92]</p>		<ul style="list-style-type: none"> • $\lambda = 1550\text{ nm}$ • CE = 64% • Channel thickness = 340 nm
<p>P. Cheben et al. (2012) [93]</p>		<ul style="list-style-type: none"> • $\lambda = 1550\text{ nm}$ • CE = 52.5% • Channel thickness = 1 μm

<p>F. Luan et al. (2012) [94]</p>		<ul style="list-style-type: none"> • $\lambda = 1550$ nm • CE = 60% • Channel thickness = 370 nm
<p>F.R. Libsch et al. (2015) [95]</p>		<ul style="list-style-type: none"> • $\lambda = 1550$ nm • CE = 20% • Channel thickness = 220 nm
<p>S. Chang et al. (2015) [96]</p>		<ul style="list-style-type: none"> • $\lambda = 1550$ nm • CE = 50% • Channel thickness = 400 nm
<p>S. Chang et al. (2015) [97]</p>		<ul style="list-style-type: none"> • $\lambda = 1550$ nm • CE = 60% • Channel thickness = 460 nm
<p>W.N. Ye (2019) [98]</p>		<ul style="list-style-type: none"> • $\lambda = 1550$ nm • CE = 32.5% • Channel thickness = 220 nm

W.N. Ye
(2020) [99]



- $\lambda = 1330$ nm, 1550 nm
- CE = 35.5%
- Channel thickness = 220 nm

B. The MATLAB code for Section (3.2)

```

clear all;
tow = (-100E-9:0.001E-9:100E-9); %the time delay for the autocorrelator
pf =0.88; %Emission probability of the QE
k12 = 1/(400E-9); %Pump rate
k21 = 1/(20.1E-9); %Radiative rate before coupling
k211 = 3/(20.1E-9); %Radiative rate after coupling
k32 = 1/(127E-9); %Nonradiative transition before coupling
k321 = 2/(127E-9); %Nonradiative transition after coupling
k23 = 1/(31E-9); %Nonradiative transition before coupling
k231 = 2/(31E-9); %Nonradiative transition before coupling
A1 = k12 + k21 + k32 + k23;
A2 = k12 + k211 + k321 + k231;
B1 = k12*k23 + k12*k32 + k21*k32;
B2 = k12*k231 + k12*k321 + k211*k321;
towtwo1 = 2/(A1-(sqrt(A1*A1 - 4*B1)));
towtwo2 = 2/(A2-(sqrt(A2*A2 - 4*B2)));
towthree1 = 2/(A1+(sqrt(A1*A1 - 4*B1)));
towthree2 = 2/(A2+(sqrt(A2*A2 - 4*B2)));
c21 = (1-(towtwo1*k32))/(k32*(towtwo1-towthree1));
c22 = (1-(towtwo2*k321))/(k321*(towtwo2-towthree2));
c31 = -1 - c21;
c32 = -1 - c22;
g21 = 1-(pf^2)+(pf^2)*((1 + (c21 .* exp(-abs(tow)./towtwo1)) + (c31 .* exp(-
abs(tow)./towthree1)))); %g2 before coupling
g22 = 1-(pf^2)+(pf^2)*((1 + (c22 .* exp(-abs(tow)./towtwo2)) + (c32 .* exp(-
abs(tow)./towthree2)))); %g2 after coupling
hold on
plot (tow,g21,'b-')
plot (tow,g22,'r-')
hold off

```

C. The MATLAB code for Section (3.3)

```

clear all;
tow = (-100:0.001:100);
row=0.864406779;
gamma1=0.03;
gamma2=0.005;
beta=1.36;
k21 = 0.046;
k12 = gamma1 - k21;
k31 = gamma2/beta;
k23 = (gamma1*gamma2*(beta-1))/(beta*k12);
k21after = 5.8*k21;
k23after = 1*k23;
k31after = 1*k31;
k12after = 1*k12;
gamma12 = k12 + k21;
gamma22 = k31 + ((k12*k23)/(k12+k21));
beta2 = 1 + ((k12*k23)/(k31*(k21+k12)));
gamma12after = k12after + k21after;
gamma22after = k31after + ((k12after*k23after)/(k12after+k21after));
beta2after = 1 + ((k12after*k23after)/(k31after*(k21after+k12after)));
g2b1 = 1-(row*row)+((row*row)*(1 - (beta * exp(-gamma1*abs(tow))) + ((beta -
1)*exp(-gamma2*abs(tow)))));
g2b2 = 1-(row*row)+((row*row)*(1 - (beta2 * exp(-gamma12*abs(tow))) + ((beta2 -
1)*exp(-gamma22*abs(tow)))));
g2b3 = 1-(row*row)+((row*row)*(1 - (beta2after * exp(-gamma12after*abs(tow))) +
((beta2after - 1)*exp(-gamma22after*abs(tow)))));
hold on
plot(tow,g2b1,'b')
plot(tow,g2b2,'r')
plot(tow,g2b3,'black')
hold off

```

D. The QuTiP code for Section (3.4)

```

import numpy as np
import matplotlib.pyplot as plt
from scipy.interpolate import interp2d
from qutip import *
plt.rcParams["font.size"] = "18"
plt.rcParams["font.family"] = "Times New Roman"
plt.rcParams["font.weight"] = "bold"
# shared parameters
gamma1 = 1 # decay rate
gamma2 = 5 # Enhanced decay rate
tlist = np.linspace(0, 13, 300)
taulist = tlist
# parameters for TLS with exponential shape wavepacket (short pulse)
tp_e = 0.060 # Gaussian pulse parameter
Om_e = 19.40 # driving strength
t_offset_e = 0.405
pulse_shape_e = Om_e/2 * np.exp(-(tlist - t_offset_e) ** 2 / (2 * tp_e ** 2))
# parameters for TLS with Gaussian shape wavepacket (long pulse)
tp_G = 2.000 # Gaussian pulse parameter
Om_G = 0.702 # driving strength
t_offset_G = 5
pulse_shape_G = Om_G/2 * np.exp(-(tlist - t_offset_G) ** 2 / (2 * tp_G ** 2))
# initial state
psi0 = fock(2, 0) # ground state
# operators
sm = destroy(2) # atomic lowering operator
n = sm.dag()*sm # number operator
# Hamiltonian
H_I = sm + sm.dag()
H_e = [[H_I, pulse_shape_e]]
H_G = [[H_I, pulse_shape_G]]
# collapse operator that describes dissipation
c_ops1 = [np.sqrt(gamma1) * sm] # represents spontaneous emission
c_ops2 = [np.sqrt(gamma2) * sm] # represents spontaneous emission
n_e1 = mesolve(H_e, psi0, tlist, c_ops1, n).expect[0]
n_G1 = mesolve(H_G, psi0, tlist, c_ops1, n).expect[0]
n_e2 = mesolve(H_e, psi0, tlist, c_ops2, n).expect[0]
n_G2 = mesolve(H_G, psi0, tlist, c_ops2, n).expect[0]
fig, ax = plt.subplots(figsize=(5, 8))
ax.plot(tlist, n_e1, 'r', label = "Exponential pulse,Before coupling")
ax.plot(tlist, n_G1, 'b', label = "Gaussian pulse,Before coupling")
ax.plot(tlist, n_e2, 'c', label = "Exponential pulse,After coupling")
ax.plot(tlist, n_G2, 'g', label = "Gaussian pulse,After coupling")
ax.legend()
ax.set_xlim(0, 13)
ax.set_ylim(0, 1)
ax.set_xlabel('Time, $t$ [$1/\gamma$]')
ax.set_ylabel('Emission flux [$\gamma$]')
#ax.set_title('Two-level system emission shapes')
# specify relevant operators to calculate the correlation for decay rate =1
# <A(t)B(t+tau)C(t)>

```

```

a_op = sm.dag()
b_op = sm.dag() * sm
c_op = sm
# calculate two-time correlations for decay rate = 1
G2_t_tau_e1 = correlation_3op_2t(H_e, psi0, tlist, taulist, c_ops1, a_op, b_op, c_op)
G2_t_tau_G1 = correlation_3op_2t(H_G, psi0, tlist, taulist, c_ops1, a_op, b_op, c_op)
# specify relevant operators to calculate the correlation for decay rate = 5
# <A(t)B(t+tau)C(t)>
a_op = sm.dag()
b_op = sm.dag() * sm
c_op = sm
# calculate two-time correlations for decay rate = 5
G2_t_tau_e2 = correlation_3op_2t(H_e, psi0, tlist, taulist, c_ops2, a_op, b_op, c_op)
G2_t_tau_G2 = correlation_3op_2t(H_G, psi0, tlist, taulist, c_ops2, a_op, b_op, c_op)
fig = plt.figure(figsize = (4, 9))
ax_e = fig.add_subplot(121)
p_e = ax_e.pcolor(tlist*gamma1, taulist*gamma1, abs(G2_t_tau_e1).transpose())
ax_e.set_xlim(0, 13)
ax_e.set_ylim(0, 13)
ax_e.set_xlabel('Time, $t$ [$1/\gamma$]')
ax_e.set_ylabel('Delay, $\tau$ [$1/\gamma$]')
ax_e.set_title('$G^{(2)}(t,\tau)$ for exponential output pulse, decayrate = 1');
fig.colorbar(p_e, ax = ax_e)
ax_G = fig.add_subplot(122)
p_G = ax_G.pcolor(tlist*gamma1, taulist*gamma1, abs(G2_t_tau_G1).transpose())
ax_G.set_xlim(0, 13)
ax_G.set_ylim(0, 13)
ax_G.set_xlabel('Time, $t$ [$1/\gamma$]')
ax_G.set_ylabel('Delay, $\tau$ [$1/\gamma$]')
ax_G.set_title('$G^{(2)}(t,\tau)$ for Gaussian output pulse, decayrate = 1');
fig.colorbar(p_G, ax = ax_G)
fig = plt.figure(figsize = (4, 9))
ax_e = fig.add_subplot(121)
p_e = ax_e.pcolor(tlist*gamma1, taulist*gamma1, abs(G2_t_tau_e1).transpose())
ax_e.set_xlim(0, 13)
ax_e.set_ylim(0, 13)
ax_e.set_xlabel('Time, $t$ [$1/\gamma$]')
ax_e.set_ylabel('Delay, $\tau$ [$1/\gamma$]')
ax_e.set_title('$G^{(2)}(t,\tau)$ for short pulse, Before coupling');
fig.colorbar(p_e, ax = ax_e)
ax_G = fig.add_subplot(122)
p_G = ax_G.pcolor(tlist*gamma1, taulist*gamma1, abs(G2_t_tau_G1).transpose())
ax_G.set_xlim(0, 13)
ax_G.set_ylim(0, 13)
ax_G.set_xlabel('Time, $t$ [$1/\gamma$]')
ax_G.set_ylabel('Delay, $\tau$ [$1/\gamma$]')
ax_G.set_title('$G^{(2)}(t,\tau)$ for long output pulse, Before coupling');
fig.colorbar(p_G, ax = ax_G)
fig = plt.figure(figsize=(4, 9))
ax_e = fig.add_subplot(121)
p_e = ax_e.pcolor(tlist*gamma2, taulist*gamma2, abs(G2_t_tau_e2).transpose())
ax_e.set_xlim(0, 36)

```

```

ax_e.set_ylim(0, 36)
ax_e.set_xlabel('Time, $t$ [$1/\gamma$]')
ax_e.set_ylabel('Delay, $\tau$ [$1/\gamma$]')
ax_e.set_title('$G^{(2)}(t,\tau)$ for short output pulse, After coupling');
fig.colorbar(p_e, ax = ax_e)
ax_G = fig.add_subplot(122)
p_G = ax_G.pcolor(tlist*gamma2, taulist*gamma2, abs(G2_t_tau_G2).transpose())
ax_G.set_xlim(0, 36)
ax_G.set_ylim(0, 36)
ax_G.set_xlabel('Time, $t$ [$1/\gamma$]')
ax_G.set_ylabel('Delay, $\tau$ [$1/\gamma$]')
ax_G.set_title('$G^{(2)}(t,\tau)$ for long output pulse, After coupling');
fig.colorbar(p_G, ax = ax_G)
G2_tau_e1 = np.trapz(G2_t_tau_e1.transpose(), tlist)
G2_tau_G1 = np.trapz(G2_t_tau_G1.transpose(), tlist)
G2_tau_e2 = ((gamma2)^2) * np.trapz(G2_t_tau_e2.transpose(), tlist)
G2_tau_G2 = ((gamma2)^2) * np.trapz(G2_t_tau_G2.transpose(), tlist)
fig, ax = plt.subplots(figsize = (5, 8))
ax.plot(taulist, G2_tau_e1, 'r', label = "Exponential pulse, Before coupling")
ax.plot(taulist, G2_tau_G1, 'b', label = "Gaussian pulse, Before coupling")
ax.plot(taulist, G2_tau_e2, 'c', label = "Exponential pulse, After coupling")
ax.plot(taulist, G2_tau_G2, 'g', label="Gaussian pulse, After coupling")
ax.legend()
ax.set_xlim(0, 13)
ax.set_ylim(0, 0.07)
ax.set_xlabel('Time delay, $\tau$ [$1/\gamma$]')
ax.set_ylabel('$G^{(2)}(\tau)$ [$\gamma^2$]')
#ax.set_title('Integrated second-order coherence');
g20_e1 = 2*abs(np.trapz(G2_tau_e1, taulist))
g20_G1 = 2*abs(np.trapz(G2_tau_G1, taulist))
g20_e2 = 2*abs(np.trapz(G2_tau_e2, taulist))/((gamma2)^2)
g20_G2 = 2*abs(np.trapz(G2_tau_G2, taulist))/((gamma2)^2)

>>>g20_e1 (For exponential pulse with decayrate = 1)
0.034335904555071774
>>>g20_G1(For Gaussian pulse with decay rate = 1)
0.436043415331417
>>>g20_e2 (For exponential pulse with decay rate = 5)
0.0054122364617288764
>>>g20_G2 (For Gaussian pulse with decay rate = 5)
0.0034828382166751607

```

E. MATLAB code to generate the contour plots

```

clc
clear all;
TE=xlsread('Probe-Te.csv');
TM=xlsread('Probe-Tm.csv');
x1=TE(1,2:18);
y1=TE(2:25,1);
z1=TE(2:25,2:18);
x2=TM(1,2:18);
y2=TM(2:25,1);
z2=TM(2:25,2:18);
zlev=0.18:0.01:0.22;
hold on
contour (x1,y1,z1,zlev,'showtext','on')
contour (x2,y2,z2,zlev,'--','showtext','on')
hold off

```

#The Excel file (Probe-Te.csv) is arranged as shown:

	A	B	C	D	E	F	G	H	I	J	K	L	M	N	O	P	Q	R
1	TE/TM	250	255	260	265	270	275	280	285	290	295	300	305	310	315	320	325	330
2	335	0.008884	0.01155	0.025697	0.021571	0.014717	0.006626	0.020081	0.082075	0.12502	0.1541	0.11282	0.071546	0.044888	0.060982	0.041737	0.014135	0.0062
3	340	0.017088	0.005036	0.015518	0.017389	0.013852	0.007277	0.010594	0.062007	0.154	0.16206	0.13747	0.086732	0.044566	0.051322	0.047106	0.025751	0.006809
4	345	0.007833	0.01906	0.01839	0.018942	0.007476	0.007971	0.012437	0.045597	0.14071	0.21034	0.11853	0.07995	0.036625	0.033145	0.050917	0.02964	0.017147
5	350	0.018744	0.009936	0.023312	0.019387	0.012503	0.015194	0.010247	0.059636	0.12763	0.1829	0.14087	0.075317	0.045864	0.019263	0.036067	0.035937	0.024412
6	355	0.020463	0.015309	0.012299	0.018508	0.025119	0.008288	0.042513	0.059971	0.14699	0.18613	0.16122	0.072238	0.036151	0.016607	0.016995	0.037454	0.024899
7	360	0.024095	0.021232	0.015805	0.020848	0.019244	0.007247	0.044166	0.089155	0.16006	0.20264	0.18352	0.090331	0.035522	0.006113	0.004553	0.024582	0.027614
8	365	0.01956	0.032877	0.014189	0.021481	0.033684	0.025037	0.024128	0.11537	0.17746	0.19588	0.17468	0.16276	0.049319	0.010677	0.000481	0.009109	0.0277
9	370	0.01237	0.007207	0.02455	0.012169	0.015703	0.020188	0.037982	0.099845	0.19723	0.18174	0.17767	0.10111	0.052104	0.017243	0.000234	0.006007	0.023258
10	375	0.051635	0.025943	0.021531	0.007309	0.011849	0.032166	0.040113	0.084271	0.18895	0.1943	0.12478	0.11455	0.045881	0.019927	0.003785	0.007478	0.015692
11	380	0.036215	0.042943	0.015284	0.036633	0.004837	0.015028	0.031254	0.093358	0.14441	0.19597	0.15951	0.069145	0.056937	0.021417	0.009094	0.006409	0.021856
12	385	0.026988	0.03227	0.031621	0.028823	0.011656	0.006494	0.034447	0.10249	0.14563	0.17939	0.14377	0.073348	0.028127	0.02534	0.009027	0.002228	0.016902
13	390	0.018228	0.048247	0.01973	0.019858	0.034318	0.006727	0.034463	0.090368	0.17338	0.14239	0.13014	0.072201	0.026428	0.009219	0.005964	0.001897	0.007704
14	395	0.035195	0.035431	0.033269	0.01935	0.032274	0.010344	0.027599	0.11141	0.14234	0.19773	0.11866	0.077951	0.023382	0.009815	0.001352	0.000459	0.002092
15	400	0.030169	0.02336	0.023268	0.037608	0.01576	0.014696	0.0141	0.09631	0.18021	0.19361	0.14662	0.0655	0.026298	0.00606	0.002107	0.000649	0.000231
16	405	0.002117	0.018439	0.020299	0.015588	0.032913	0.031197	0.019217	0.061322	0.18096	0.20698	0.16249	0.09572	0.02606	0.007922	0.001331	0.001121	0.00098
17	410	0.023073	0.000703	0.032659	0.018627	0.048291	0.039443	0.017604	0.060813	0.18015	0.19356	0.16307	0.11556	0.036862	0.008455	0.000184	0.003143	0.002274
18	415	0.047384	0.032354	0.014604	0.008181	0.027537	0.041556	0.024337	0.042054	0.13642	0.20401	0.15762	0.097327	0.04523	0.009776	0.005965	0.00159	0.003876
19	420	0.033	0.021433	0.04485	0.012617	0.035878	0.031669	0.024674	0.038147	0.11716	0.19889	0.16061	0.094206	0.060338	0.008745	0.008347	0.007445	0.005403
20	425	0.046509	0.018798	0.0147	0.014619	0.020754	0.035447	0.049198	0.06638	0.10816	0.20526	0.16407	0.10065	0.048303	0.013128	0.006396	0.006115	0.007911
21	430	0.059982	0.03253	0.017107	0.033902	0.021526	0.029793	0.052018	0.087611	0.13496	0.2025	0.16887	0.10718	0.050782	0.028445	0.006332	0.003147	0.006967
22	435	0.045875	0.023526	0.010725	0.040478	0.01628	0.018848	0.034623	0.069735	0.16624	0.20322	0.18254	0.11902	0.056012	0.033607	0.004958	0.000449	0.001827
23	440	0.031256	0.023391	0.014509	0.028511	0.021024	0.029284	0.039586	0.049378	0.15066	0.21386	0.20657	0.14276	0.058132	0.021072	0.014278	0.000721	0.006425
24	445	0.056066	0.025265	0.013493	0.032157	0.03738	0.035294	0.039607	0.045038	0.11598	0.18765	0.22848	0.17031	0.085361	0.036622	0.009356	0.006003	0.005905
25	450	0.036804	0.08211	0.020819	0.019589	0.062814	0.046319	0.046053	0.11315	0.12877	0.16661	0.17128	0.17005	0.11081	0.055758	0.003949	0.002405	0.000243

Figure (E-1): The Excel file shows the CE arrangements for different TE and TM periods

F. Publications:

Photonics and Nanostructures - Fundamentals and Applications 45 (2021) 100925



Contents lists available at ScienceDirect

Photonics and Nanostructures - Fundamentals and Applications

journal homepage: www.elsevier.com/locate/photonics



The spontaneous emission performance of a quantum emitter coupled to a hybrid plasmonic waveguide with specified output polarization for on-chip plasmonic single-photon source

Farooq A. Khaleel^{*}, Shelan K. Tawfeeq

Institute of Laser for Postgraduate Studies, University of Baghdad, Iraq

ARTICLE INFO

Keywords:
Polarization rotator
Hybrid plasmonic waveguide
Single-photon source
Purcell enhancement
Quantum emitter
COMSOL

ABSTRACT

Nowadays, most of the on-chip plasmonic single-photon sources emit an unpolarized stream of single photons that demand a subsequent polarizer stage in a practical quantum cryptography system. In this paper, we numerically demonstrated the coupling of the light emitted from a quantum emitter (QE) at 700 nm wavelength to the propagation mode supported by an on-chip hybrid plasmonic waveguide (HPW) polarization rotator. Our results proved that the light emitted is linearly polarized at 0° , 45° , and 90° with propagation lengths of 5 μm , 3.3 μm , and 3.9 μm , respectively. Moreover, high power-conversion efficiency was obtained from an applied transverse magnetic (TM) mode (0-polarization) to a transverse electric (TE) (90°-polarization) and a linearly polarized light at 45° of 97% and a 98%, respectively. Furthermore, we obtained almost a 3-fold enhancement of the total decay rate of the QE with high emission coupling efficiency (β -factor) of 88%, 80%, and 87% to the corresponding waveguide mode for 0° , 45° , and 90° , respectively. Our work paves the way towards more efficient, compact, and less complicated on-chip plasmonic single-photon sources with a specified output polarization.

1. Introduction

The single-photon source is one of the main building blocks in any quantum cryptography system that realizes a certain encryption protocol [1,2]. A typical experimental realization of the single-photon source depends on the generation of weak coherent pulses (WCP) that mimic the behavior of single-photon pulses [3,4]. However, the probability of multiphoton generation in WCP results in leakage of information, reduction of the transmission rate, and decreases the security of the system [5]. Therefore, highly efficient quantum key distribution (QKD) systems prefer the utilization of a truly efficient single-photon source instead of WCP [6].

Recently, the most efficient single-photon sources with pure single-photon emission reported the use of different types of QEs including quantum dots [7,8], defect centers in diamonds [9,10], and molecules [11,12]. The integration possibility of these single-photon sources on silicon chips urged the development of "plug and play" single-photon sources for QKD transmitters where the coupling techniques between the waveguide mode and the optical fiber are used to simplify the alignment and extract the single-photon efficiently for free-space

transmission [13].

The spontaneous emission rate of on-chip QEs can be changed by varying the QE environment via the Purcell effect [14]. Many recent published works simulated the enhancement of Purcell factor as well as the enhancement of the radiative emission coupling efficiency (β -factor) by coupling the QE emission to a plasmonic waveguide (PW) due to the high confinement of its fundamental propagation mode. For example, Siampour et al. [15] proposed an on-chip single-photon source that achieved a 42 fold enhancement of the spontaneous emission for a nitrogen-vacancy (NV) coupled to a dielectric-loaded surface plasmon polariton (DLSP) waveguide with β equals 63%. Furthermore, Kumar et al. [16] achieved a 37 total decay rate enhancement and β -factor of 87% when they coupled quantum dots emission to the proposed HPW for on-chip single-photon applications. A recent work of Siampour et al. [17] achieved an outstanding performance of 10-fold Purcell enhancement for a germanium vacancy (GeV) center and 12-fold Purcell enhancement for NV center coupled to their proposed DLSP waveguide structure, which can also act as an efficient on-chip single-photon source for QKD systems.

The polarization of the output light for the aforementioned

^{*} Corresponding author.

E-mail address: farooq.abd1101a@ilps.uobaghdad.edu.iq (F.A. Khaleel).

<https://doi.org/10.1016/j.photonics.2021.100925>

Received 26 November 2020; Received in revised form 9 March 2021; Accepted 28 April 2021

Available online 11 May 2021

1569-4410/© 2021 Elsevier B.V. All rights reserved.



Design and numerical verification of a polarization-independent grating coupler using a double-layer approach for visible wavelengths applications

Farooq Abdulghafoor Khaleel¹ · Shelan Khasro Tawfeeq¹

Received: 23 July 2021 / Accepted: 6 November 2021

© The Author(s), under exclusive licence to Springer Science+Business Media, LLC, part of Springer Nature 2021

Abstract

In this paper, a double-layer approach is proposed to design a compact four states polarization-independent grating coupler (GC). The proposed polarization-independent GC is designed to couple a 700 nm polarized light propagated in a 150 nm Gallium Phosphide (GaP) waveguide to a polarization-maintaining fiber. The double-layer approach is based on the deposition of GaP gratings designed to couple the transverse magnetic (TM) light over the GaP gratings designed to couple the transverse electric (TE) light. The two layers are separated by a Hydrogen silsesquioxane (HSQ) with an optimum thickness of 20 nm. The grating periods and the fill factors of the two layers are optimized to achieve maximum possible coupling efficiency (CE). The proposed method resulted in relatively high CEs of 39.2, 31.1, and 23.3% for the TE, TM, and 45°/-45° linearly polarized light, respectively. The polarization-dependent loss (PDL) is 1 dB, 1.26 dB, and 2.26 dB corresponding to TE-TM, TM-45°/-45°, and TE-45°/-45°, respectively. The performance of the double-layer approach is numerically verified by the two-dimensional (2D) finite element algorithm (FEM) using COMSOL software. The proposed method suggests a novel and simple approach to design a compact four states polarization-independent GC that could be used in integrated (on-chip) photonic communication circuits.

Keywords Polarization-independent · Grating coupler · Photonic waveguide · Integrated photonic · COMSOL · Subwavelength structures

1 Introduction

The optical fibers are widely used to transfer light over long distances with minimum propagation losses. The photonic waveguides perform the same function in on-chip photonic circuits. However, the coupling of the light between the optical fibers and the photonic circuits is a major issue because of the difference in their waveguide modes (Chrostowski and Hochberg 2015). The GC is one of the best solutions that managed

✉ Farooq Abdulghafoor Khaleel
 Farook.abd1101a@ilps.uobaghdad.edu.iq

¹ Department of Engineering and Industrial Applications, Institute of Laser for Postgraduate Studies, University of Baghdad, Baghdad, Iraq

Received: 18 November 2021 | Revised: 28 January 2022 | Accepted: 5 April 2022

DOI: 10.1002/jnm.3013

RESEARCH ARTICLE

WILEY

The modeling techniques of the second-order correlation function $g^{(2)}(\tau)$ for a quantum emitter

Farooq Abdulghafoor Khaleel  | Shelan Khasro Tawfeeq 

Department of Engineering and Industrial Applications, Institute of Laser for Postgraduate Studies, University of Baghdad, Baghdad, Iraq

Correspondence

Farooq Abdulghafoor Khaleel,
Department of Engineering and Industrial Applications, Institute of Laser for Postgraduate Studies, University of Baghdad, Baghdad, Iraq.
Email: farooq.abd1101a@ilps.uobaghdad.edu.iq

Abstract

The numerical techniques required to prove the single-photon emission from any type of quantum emitter (QE) after being coupled to any nanostructure are presented in this paper. The Purcell effect modifies the emission characteristics of QEs, such as color centers in nanodiamonds, for example, nitrogen-vacancy (NV) centers, silicon vacancy (SiV) centers, and so forth, or semiconductor quantum dots. Our numerical approach is based on the unique QEs' experimental photophysics parameters and numerical analysis software, which are MATLAB and Quantum Toolbox in Python (QuTiP). Our results show a comparable $g^{(2)}(\tau)$ behavior between our proposed numerical model and the other two experimental results for the QE before and after coupling to a plasmonic waveguide with subwavelength dimensions. Our proposed method is essential to prove the single-photon emission of modeled single-photon source (SPS) in an on-chip polarization-dependent quantum key distribution system (QKD).

KEYWORDS

numerical modeling, photophysics, purcell effects, QuTiP, second-order correlation function, single-photon source

1 | INTRODUCTION

Multiple fast quantum photonic processes could be integrated into built-in rigid circuits, which could be realized by stable and compact schemes known as Photonic Integrated Circuits (PICs). PICs facilitate designing quantum building blocks with different materials and geometries at a lithographic scale to achieve accurate demands of QKD applications.^{1,2} An essential building block in PICs is a controlled source of indistinguishable single photons.³ These single photons could be achieved either with a probability-dependent source, that could be heralded or multiplexed for high efficiency⁴ or by coupling a single QE to a nanocavity⁵ or nanowaveguide⁶ designed to gather single photons emitted by spontaneous emission. The coupling of the QE into nanostructures enhances the spontaneous emission rate of the QE due to the Purcell effect.⁷ The coupling of a single QE, for example, a color center in nanodiamond,⁸ semiconductor quantum dot (QD),⁹ or a molecule¹⁰ to a plasmonic waveguide (PW) is an important field of study. Its importance resulted from the subwavelength confinement of the light, decay rate enhancement of the QE, and efficient routing of the emitted photons on the same PIC.^{11,12} By applying the emitted photons from the QE and from the PWs end to a Hanbury Brown and Twiss (HBT) detection setup, the single-photon emission is proved before and after the coupling, respectively.^{13,14} From the HBT experiment, a measured value of $g^{(2)}(\tau = 0)$ less than 0.5 is clear proof that the QE's radiation and, consequently, the excited plasmons are emitted on a photon-by-photon basis.^{15,16}



On the use of Aluminium as a plasmonic material in polarization rotators based on a hybrid plasmonic waveguide

Farooq Abdulghafoor Khaleel^{1*}, Shelan Khasro Tawfeeq¹

*Corresponding author: farooq.abd1101a@ilps.uobaghdad.edu.iq

1. Institute of Laser for Postgraduate Studies, University of Baghdad, Iraq, Baghdad, Iraq.

(Received 21/11/2021; accepted 29/12/2021)

Abstract: The Aluminium (Al) material emerged as a plasmonic material in the wavelength ranges from the ultraviolet to the visible bands in different on-chip plasmonic applications. In this paper, we demonstrate the effect of using Al on the electromagnetic (EM) field distribution of a compact hybrid plasmonic waveguide (HPW) acting as a polarization rotator. We compare the performance of Al with other familiar metals that are widely used as plasmonic materials, which are Silver (Ag) and Gold (Au). Furthermore, we study the effect of reducing the geometrical dimensions of the used materials on the EM field distributions inside the HPW and, consequently, on the efficiency of the polarization rotation. We perform the study based on the Finite Element Method (FEM) using COMSOL software at an operation wavelength of 700 nm. This paper verifies that the Al could be used as an efficient plasmonic material in integrated single-photon sources for quantum key distribution systems.

Key words:

1. Introduction

The photonic applications at the visible and infrared wavelengths depend widely on plasmonics. Recent researches showed considerable progress in plasmon-based light trapping [1, 2], surface-enhanced spectroscopy [3, 4], sensors [5, 6], optoelectronic devices [7, 8], nonlinear optics [9, 10], and photocatalysis [11, 12]. In nanoscale devices, extending the plasmonic excitation effect from infrared, visible to the ultraviolet wavelengths range is a major challenge. The challenge arises from the limited performance (i.e. weak resonance effect) of the common plasmonic metals, which are Au and Ag, at the visible and UV wavelengths ranges [13, 14]. The Ag exhibited rapid oxidation that deteriorates the plasmonic effects, while the interband transitions in Au increase at the visible wavelength ranges and below and act as a dissipative channel that weakens the plasmonic effect [15, 16]. However, the Al emerged as a preferable plasmonic metal at the visible and UV wavelengths because of its strong resonance at these wavelengths, natural

availability, low cost, and fabrication easiness and accuracy down to 5 nm linewidth [17, 18].

One of the most important integrated plasmonic devices is the polarization rotators [19]. Recently, the polarization rotators are applied in integrated single-photon sources in polarization-based quantum key distribution systems [20]. The aim of [20] was to control the output polarization of the emitted photons from a quantum emitter (QE) coupled to an HPW acting as a polarization rotator. Moreover, the emission wavelength of most QEs is 700 nm, where the Au and Ag plasmonic metals begin to lose their plasmonics properties [21].

This paper compares the performance of using Au, Ag, and Al as plasmonic metals in polarization rotators based on HPW. Furthermore, the effect of using different plasmonic metals on the miniaturization of the integrated HPW will also be discussed. This paper is arranged as follows: Section (2) demonstrates the principles of the polarization rotators. Section (3) compares the performance of the polarization rotator using different plasmonics metals. Finally, Section (4) concludes our findings.

References

- [1] T. Vogl, Next-generation single-photon sources using two-dimensional hexagonal boron nitride, 2019.
- [2] E.M. Purcell, Spontaneous Emission Probabilities at Radio Frequencies, in: E. Burstein, C. Weisbuch (Eds.), *Confin. Electrons Photons New Phys. Appl.*, Springer US, Boston, MA, 1995: p. 839. https://doi.org/10.1007/978-1-4615-1963-8_40.
- [3] L. Liebermeister, Photonic waveguides evanescently coupled with single NV-centers, (2015). <http://nbn-resolving.de/urn:nbn:de:bvb:19-191017>.
- [4] D.E. Chang, A.S. Sørensen, E.A. Demler, M.D. Lukin, A single-photon transistor using nanoscale surface plasmons, *Nat. Phys.* 3 (2007) 807–812. <https://doi.org/10.1038/nphys708>.
- [5] A. Gonzalez-Tudela, D. Martin-Cano, E. Moreno, L. Martin-Moreno, C. Tejedor, F.J. Garcia-Vidal, Entanglement of Two Qubits Mediated by One-Dimensional Plasmonic Waveguides, *Phys. Rev. Lett.* 106 (2011) 20501. <https://doi.org/10.1103/PhysRevLett.106.020501>.
- [6] D.E. Chang, A.S. Sørensen, P.R. Hemmer, M.D. Lukin, Quantum Optics with Surface Plasmons, *Phys. Rev. Lett.* 97 (2006) 53002. <https://doi.org/10.1103/PhysRevLett.97.053002>.
- [7] P. Kok, W.J. Munro, K. Nemoto, T.C. Ralph, J.P. Dowling, G.J. Milburn, Linear optical quantum computing with photonic qubits, *Rev. Mod. Phys.* 79 (2007) 135–174. <https://doi.org/10.1103/RevModPhys.79.135>.
- [8] M. Leifgen, T. Schröder, F. Gädeke, R. Riemann, V. Métillon, E. Neu, C. Hepp, C. Arend, C. Becher, K. Lauritsen, et al., Evaluation of nitrogen- and silicon-vacancy defect centres as single photon sources in quantum key distribution, *New J. Phys.* 16 (2014) 23021.

<https://doi.org/10.1088/1367-2630/16/2/023021>.

- [9] M. Arcari, I. Söllner, A. Javadi, S. Lindskov Hansen, S. Mahmoodian, J. Liu, H. Thyrestrup, E.H. Lee, J.D. Song, S. Stobbe, P. Lodahl, Near-Unity Coupling Efficiency of a Quantum Emitter to a Photonic Crystal Waveguide, *Phys. Rev. Lett.* 113 (2014) 93603. <https://doi.org/10.1103/PhysRevLett.113.093603>.
- [10] J. Riedrich-Möller, L. Kipfstuhl, C. Hepp, E. Neu, C. Pauly, F. Mücklich, A. Baur, M. Wandt, S. Wolff, M. Fischer, S. Gsell, M. Schreck, C. Becher, One- and two-dimensional photonic crystal microcavities in single crystal diamond, *Nat. Nanotechnol.* 7 (2012) 69–74. <https://doi.org/10.1038/nnano.2011.190>.
- [11] J. Claudon, J. Bleuse, N.S. Malik, M. Bazin, P. Jaffrennou, N. Gregersen, C. Sauvan, P. Lalanne, J.-M. Gérard, A highly efficient single-photon source based on a quantum dot in a photonic nanowire, *Nat. Photonics.* 4 (2010) 174–177. <https://doi.org/10.1038/nphoton.2009.287x>.
- [12] D.K. Gramotnev, S.I. Bozhevolnyi, Plasmonics beyond the diffraction limit, *Nat. Photonics.* 4 (2010) 83–91. <https://doi.org/10.1038/nphoton.2009.282>.
- [13] S. Kumar, A. Huck, U.L. Andersen, Efficient Coupling of a Single Diamond Color Center to Propagating Plasmonic Gap Modes, *Nano Lett.* 13 (2013) 1221–1225. <https://doi.org/10.1021/nl304682r>.
- [14] G.E. Moore, Cramming more components onto integrated circuits, Reprinted from *Electronics*, volume 38, number 8, April 19, 1965, pp.114 ff., *IEEE Solid-State Circuits Soc. Newsl.* 11 (2006) 33–35. <https://doi.org/10.1109/N-SSC.2006.4785860>.
- [15] P.B. Zantye, A. Kumar, A.K. Sikder, Chemical mechanical planarization for microelectronics applications, *Mater. Sci. Eng. R*

Reports. 45 (2004) 89–220.

<https://doi.org/https://doi.org/10.1016/j.mser.2004.06.002>.

- [16] M. Haurylau, G. Chen, H. Chen, J. Zhang, N.A. Nelson, D.H. Albonesi, E.G. Friedman, P.M. Fauchet, On-Chip Optical Interconnect Roadmap: Challenges and Critical Directions, IEEE J. Sel. Top. Quantum Electron. 12 (2006) 1699–1705.
<https://doi.org/10.1109/JSTQE.2006.880615>.
- [17] M.L. Brongersma, V.M. Shalaev, The Case for Plasmonics, Science (80-.). 328 (2010) 440–441.
<https://doi.org/10.1126/science.1186905>.
- [18] T. Lavrinenko, A.V., Lægsgaard, J., Gregersen, N., Schmidt, F., & Søndergaard, Numerical Methods in Photonics, 1st ed., CRC Press, 2015. <https://doi.org/https://doi.org/10.1201/b17408>.
- [19] A. Taflove, S.C. Hagness, Computational electrodynamics : the finite-difference time-domain method, Artech House, Boston, 2005.
- [20] K. Yee, Numerical solution of initial boundary value problems involving maxwell’s equations in isotropic media, IEEE Trans. Antennas Propag. 14 (1966) 302–307.
<https://doi.org/10.1109/TAP.1966.1138693>.
- [21] P. Bienstman, Rigorous and efficient modelling of wavelength scale photonic components, Ghent University, 2001.
- [22] D. Pisssoort, B. Denecker, P. Bienstman, F. Olyslager, D. De Zutter, Comparative study of three methods for the simulation of two-dimensional photonic crystals, J. Opt. Soc. Am. A. 21 (2004) 2186–2195. <https://doi.org/10.1364/JOSAA.21.002186>.
- [23] P.D. J. N. Reddy, Introduction to the Finite Element Method, 4th editio, McGraw-Hill Education, New York, 2019.

<https://www.accessengineeringlibrary.com/content/book/9781259861901>.

- [24] L. Novotny, B. Hecht, Principles of Nano-Optics, Cambridge University Press, 2006. <https://doi.org/10.1017/CBO9780511813535>.
- [25] S.I. Bozhevolnyi, L. Martin-Moreno, F. Garcia-Vidal, Quantum Plasmonics, Springer, Cham, 2017.
<https://doi.org/https://doi.org/10.1007/978-3-319-45820-5>.
- [26] Y. Chen, T.R. Nielsen, N. Gregersen, P. Lodahl, J. M\ork, Finite-element modeling of spontaneous emission of a quantum emitter at nanoscale proximity to plasmonic waveguides, Phys. Rev. B. 81 (2010) 125431. <https://doi.org/10.1103/PhysRevB.81.125431>.
- [27] S. Buckley, K. Rivoire, J. Vučković, Engineered quantum dot single-photon sources, Reports Prog. Phys. 75 (2012) 126503.
<https://doi.org/10.1088/0034-4885/75/12/126503>.
- [28] B. Lounis, M. Orrit, Single-photon sources, Reports Prog. Phys. 68 (2005) 1129–1179. <https://doi.org/10.1088/0034-4885/68/5/r04>.
- [29] M. Fox, Quantum optics: an introduction, Oxford Univ. Press, Oxford, 2006. <https://cds.cern.ch/record/1001868>.
- [30] S. DEY, Plasmonic Effect on Exciton and Multiexciton Dynamics of Quantum Dots near Metal Nanostructures, University of Connecticut, 2017. <https://opencommons.uconn.edu/dissertations/1511>.
- [31] S. Takeuchi, Recent progress in single-photon and entangled-photon generation and applications, Jpn. J. Appl. Phys. 53 (2014) 30101. <https://doi.org/10.7567/jjap.53.030101>.
- [32] O. Chen, J. Zhao, V.P. Chauhan, J. Cui, C. Wong, D.K. Harris, H. Wei, H.-S. Han, D. Fukumura, R.K. Jain, M.G. Bawendi, Compact high-quality CdSe–CdS core–shell nanocrystals with narrow

emission linewidths and suppressed blinking, *Nat. Mater.* 12 (2013) 445–451. <https://doi.org/10.1038/nmat3539>.

- [33] P. Lodahl, S. Mahmoodian, S. Stobbe, Interfacing single photons and single quantum dots with photonic nanostructures, *Rev. Mod. Phys.* 87 (2015) 347–400. <https://doi.org/10.1103/RevModPhys.87.347>.
- [34] A. V Akimov, A. Mukherjee, C.L. Yu, D.E. Chang, A.S. Zibrov, P.R. Hemmer, H. Park, M.D. Lukin, Generation of single optical plasmons in metallic nanowires coupled to quantum dots, *Nature*. 450 (2007) 402–406. <https://doi.org/10.1038/nature06230>.
- [35] S.J.P. Kress, F. V Antolinez, P. Richner, S. V Jayanti, D.K. Kim, F. Prins, A. Riedinger, M.P.C. Fischer, S. Meyer, K.M. McPeak, D. Poulikakos, D.J. Norris, Wedge Waveguides and Resonators for Quantum Plasmonics, *Nano Lett.* 15 (2015) 6267–6275. <https://doi.org/10.1021/acs.nanolett.5b03051>.
- [36] M.W. Doherty, N.B. Manson, P. Delaney, F. Jelezko, J. Wrachtrup, L.C.L. Hollenberg, The nitrogen-vacancy colour centre in diamond, *Phys. Rep.* 528 (2013) 1–45. <https://doi.org/https://doi.org/10.1016/j.physrep.2013.02.001>.
- [37] H. Bernien, L. Childress, L. Robledo, M. Markham, D. Twitchen, R. Hanson, Two-Photon Quantum Interference from Separate Nitrogen Vacancy Centers in Diamond, *Phys. Rev. Lett.* 108 (2012) 43604. <https://doi.org/10.1103/PhysRevLett.108.043604>.
- [38] A. Sipahigil, M.L. Goldman, E. Togan, Y. Chu, M. Markham, D.J. Twitchen, A.S. Zibrov, A. Kubanek, M.D. Lukin, Quantum interference of single photons from remote nitrogen-vacancy centers in diamond., *Phys. Rev. Lett.* 108 (2012) 143601. <https://doi.org/10.1103/PhysRevLett.108.143601>.
- [39] E. Togan, Y. Chu, A.S. Trifonov, L. Jiang, J. Maze, L. Childress,

M.V.G. Dutt, A.S. Sørensen, P.R. Hemmer, A.S. Zibrov, M.D. Lukin, Quantum entanglement between an optical photon and a solid-state spin qubit, *Nature*. 466 (2010) 730–734.
<https://doi.org/10.1038/nature09256>.

- [40] H. Bernien, B. Hensen, W. Pfaff, G. Koolstra, M.S. Blok, L. Robledo, T.H. Taminiau, M. Markham, D.J. Twitchen, L. Childress, R. Hanson, Heralded entanglement between solid-state qubits separated by three metres, *Nature*. 497 (2013) 86–90.
<https://doi.org/10.1038/nature12016>.
- [41] W. Pfaff, B.J. Hensen, H. Bernien, S.B. van Dam, M.S. Blok, T.H. Taminiau, M.J. Tiggelman, R.N. Schouten, M. Markham, D.J. Twitchen, R. Hanson, Unconditional quantum teleportation between distant solid-state quantum bits, *Science* (80-.). 345 (2014) 532–535.
<https://doi.org/10.1126/science.1253512>.
- [42] B. Hensen, H. Bernien, A.E. Dréau, A. Reiserer, N. Kalb, M.S. Blok, J. Ruitenber, R.F.L. Vermeulen, R.N. Schouten, C. Abellán, W. Amaya, V. Pruneri, M.W. Mitchell, M. Markham, D.J. Twitchen, D. Elkouss, S. Wehner, T.H. Taminiau, R. Hanson, Loophole-free Bell inequality violation using electron spins separated by 1.3 kilometres, *Nature*. 526 (2015) 682–686. <https://doi.org/10.1038/nature15759>.
- [43] L. Rondin, J.-P. Tetienne, T. Hingant, J.-F. Roch, P. Maletinsky, V. Jacques, Magnetometry with nitrogen-vacancy defects in diamond, *Reports Prog. Phys.* 77 (2014) 56503. <https://doi.org/10.1088/0034-4885/77/5/056503>.
- [44] F. Dolde, H. Fedder, M.W. Doherty, T. Nöbauer, F. Rempp, G. Balasubramanian, T. Wolf, F. Reinhard, L.C.L. Hollenberg, F. Jelezko, J. Wrachtrup, Electric-field sensing using single diamond spins, *Nat. Phys.* 7 (2011) 459–463.

<https://doi.org/10.1038/nphys1969>.

- [45] P. Neumann, I. Jakobi, F. Dolde, C. Burk, R. Reuter, G. Waldherr, J. Honert, T. Wolf, A. Brunner, J.H. Shim, D. Suter, H. Sumiya, J. Isoya, J. Wrachtrup, High-Precision Nanoscale Temperature Sensing Using Single Defects in Diamond, *Nano Lett.* 13 (2013) 2738–2742. <https://doi.org/10.1021/nl401216y>.
- [46] G. Kucsko, P.C. Maurer, N.Y. Yao, M. Kubo, H.J. Noh, P.K. Lo, H. Park, M.D. Lukin, Nanometre-scale thermometry in a living cell, *Nature*. 500 (2013) 54–58. <https://doi.org/10.1038/nature12373>.
- [47] A. Mohtashami, A.F. Koenderink, Suitability of nanodiamond nitrogen-vacancy centers for spontaneous emission control experiments, *New J. Phys.* 15 (2013) 43017. <https://doi.org/10.1088/1367-2630/15/4/043017>.
- [48] F. Masiello, X-ray diffraction and imaging with a coherent beam : application to X-Ray optical elements and crystal exhibiting phase inhomogeneities, Université de Grenoble ; Università degli studi (Torino, Italia), 2011. <https://tel.archives-ouvertes.fr/tel-00609216>.
- [49] G. Davies, M.F. Hamer, W.C. Price, Optical studies of the 1.945 eV vibronic band in diamond, *Proc. R. Soc. London. A. Math. Phys. Sci.* 348 (1976) 285–298. <https://doi.org/10.1098/rspa.1976.0039>.
- [50] M.K. Boll, Photophysics of Quantum Emitters in Diamond and Hexagonal Boron Nitride, Technical University of Denmark, 2019.
- [51] A.T. Collins, M.F. Thomaz, M.I.B. Jorge, Luminescence decay time of the 1.945 {eV} centre in type Ib diamond, *J. Phys. C Solid State Phys.* 16 (1983) 2177–2181. <https://doi.org/10.1088/0022-3719/16/11/020>.
- [52] C. Kurtsiefer, S. Mayer, P. Zarda, H. Weinfurter, Stable Solid-State

Source of Single Photons, *Phys. Rev. Lett.* 85 (2000) 290–293.
<https://doi.org/10.1103/PhysRevLett.85.290>.

- [53] L.J. Rogers, K.D. Jahnke, M.W. Doherty, A. Dietrich, L.P. McGuinness, C. Müller, T. Teraji, H. Sumiya, J. Isoya, N.B. Manson, F. Jelezko, Electronic structure of the negatively charged silicon-vacancy center in diamond, *Phys. Rev. B.* 89 (2014) 235101.
<https://doi.org/10.1103/PhysRevB.89.235101>.
- [54] U.F.S. D’Haenens-Johansson, A.M. Edmonds, M.E. Newton, J.P. Goss, P.R. Briddon, J.M. Baker, P.M. Martineau, R.U.A. Khan, D.J. Twitchen, S.D. Williams, EPR of a defect in CVD diamond involving both silicon and hydrogen that shows preferential alignment, *Phys. Rev. B.* 82 (2010) 155205.
<https://doi.org/10.1103/PhysRevB.82.155205>.
- [55] E. Neu, C. Hepp, M. Hauschild, S. Gsell, M. Fischer, H. Sternschulte, D. Steinmüller-Nethl, M. Schreck, C. Becher, Low-temperature investigations of single silicon vacancy colour centres in diamond, *New J. Phys.* 15 (2013) 43005. <https://doi.org/10.1088/1367-2630/15/4/043005>.
- [56] A. Sipahigil, K.D. Jahnke, L.J. Rogers, T. Teraji, J. Isoya, A.S. Zibrov, F. Jelezko, M.D. Lukin, Indistinguishable Photons from Separated Silicon-Vacancy Centers in Diamond, *Phys. Rev. Lett.* 113 (2014) 113602. <https://doi.org/10.1103/PhysRevLett.113.113602>.
- [57] L.J. Rogers, K.D. Jahnke, T. Teraji, L. Marseglia, C. Müller, B. Naydenov, H. Schauffert, C. Kranz, J. Isoya, L.P. McGuinness, F. Jelezko, Multiple intrinsically identical single-photon emitters in the solid state, *Nat. Commun.* 5 (2014) 4739.
<https://doi.org/10.1038/ncomms5739>.
- [58] E. Neu, M. Agio, C. Becher, Photophysics of single silicon vacancy

centers in diamond: implications for single photon emission, *Opt. Express*. 20 (2012) 19956–19971.
<https://doi.org/10.1364/OE.20.019956>.

- [59] S.J. Orfanidis, *Electromagnetic Waves and Antennas*, Sophocles J. Orfanidis, 2016. <https://books.google.iq/books?id=4n5ezQEACAAJ>.
- [60] S.A. Maier, *Plasmonics: Fundamentals and Applications*, 1st ed., Springer US, 2007. <https://doi.org/10.1007/0-387-37825-1>.
- [61] M.A. Ordal, R.J. Bell, R.W. Alexander, L.L. Long, M.R. Query, Optical properties of fourteen metals in the infrared and far infrared: Al, Co, Cu, Au, Fe, Pb, Mo, Ni, Pd, Pt, Ag, Ti, V, and W., *Appl. Opt.* 24 (1985) 4493–4499. <https://doi.org/10.1364/AO.24.004493>.
- [62] F. Dieleman, *Quantum properties of plasmonic waveguides*, Imperial College London, 2017. <https://doi.org/10.25560/49436>.
- [63] S. V Gaponenko, *Introduction to Nanophotonics*, Cambridge University Press, 2010. <https://doi.org/10.1017/CBO9780511750502>.
- [64] S. K. Tawfeeq, A. I. Khalil, Generation of Truly Random QPSK Signal Waveforms for Quantum Key Distribution Systems Based on Phase Coding, *Iraqi J. Laser*. 10 (2011) 1–7.
- [65] N. Gisin, G. Ribordy, W. Tittel, H. Zbinden, Quantum cryptography, *Rev. Mod. Phys.* 74 (2002) 145–195.
<https://doi.org/10.1103/RevModPhys.74.145>.
- [66] A. I. Khaleel, S. K. Tawfeeq, Real Time Quantum Bit Error Rate Performance Test for a Quantum Cryptography System Based on BB84 protocol, *Iraqi J. Laser*. 8 (2009) 29–35.
- [67] S. Pirandola, U.L. Andersen, L. Banchi, M. Berta, D. Bunandar, R. Colbeck, D. Englund, T. Gehring, C. Lupo, C. Ottaviani, J.L. Pereira, M. Razavi, J.S. Shaari, M. Tomamichel, V.C. Usenko, G. Vallone, P.

- Villoresi, P. Wallden, Advances in quantum cryptography, *Adv. Opt. Photon.* 12 (2020) 1012–1236. <https://doi.org/10.1364/AOP.361502>.
- [68] N. Lütkenhaus, Security against individual attacks for realistic quantum key distribution, *Phys. Rev. A.* 61 (2000) 52304. <https://doi.org/10.1103/PhysRevA.61.052304>.
- [69] P. Jiang, N. Ma, P. Liu, W. Wu, K. Zhang, An Easy-Implemented On-Chip Waveguide Coupled Single Photon Source Based on Self-Assembled Quantum Dots Membrane, *Appl. Sci.* 11 (2021). <https://doi.org/10.3390/app11020695>.
- [70] C.W. Wong, J. Gao, J.F. McMillan, F.W. Sun, R. Bose, Quantum information processing through quantum dots in slow-light photonic crystal waveguides, *Photonics Nanostructures - Fundam. Appl.* 7 (2009) 47–55. <https://doi.org/https://doi.org/10.1016/j.photonics.2008.11.007>.
- [71] H. Wang, Y.-M. He, T.-H. Chung, H. Hu, Y. Yu, S. Chen, X. Ding, M.-C. Chen, J. Qin, X. Yang, R.-Z. Liu, Z.-C. Duan, J.-P. Li, S. Gerhardt, K. Winkler, J. Jurkat, L.-J. Wang, N. Gregersen, Y.-H. Huo, Q. Dai, S. Yu, S. Höfling, C.-Y. Lu, J.-W. Pan, Towards optimal single-photon sources from polarized microcavities, *Nat. Photonics.* 13 (2019) 770–775. <https://doi.org/10.1038/s41566-019-0494-3>.
- [72] A. Beveratos, R. Brouri, T. Gacoin, A. Villing, J.-P. Poizat, P. Grangier, Single Photon Quantum Cryptography, *Phys. Rev. Lett.* 89 (2002) 187901. <https://doi.org/10.1103/PhysRevLett.89.187901>.
- [73] H. Siampour, S. Kumar, S.I. Bozhevolnyi, Nanofabrication of Plasmonic Circuits Containing Single Photon Sources, *ACS Photonics.* (2017). <https://doi.org/10.1021/acsphotonics.7b00374>.
- [74] K.G. Lee, X.W. Chen, H. Eghlidi, P. Kukura, R. Lettow, A. Renn, V.

Sandoghdar, S. Götzinger, A planar dielectric antenna for directional single-photon emission and near-unity collection efficiency, *Nat. Photonics*. 5 (2011) 166–169.
<https://doi.org/10.1038/nphoton.2010.312>.

- [75] P. Lombardi, M. Trapuzzano, M. Colautti, G. Margheri, I. Pietro Degiovanni, M. López, S. Kück, C. Toninelli, A Molecule-Based Single-Photon Source Applied in Quantum Radiometry, *Adv. Quantum Technol.* 3 (2020) 1900083.
<https://doi.org/https://doi.org/10.1002/qute.201900083>.
- [76] K. Mnaymneh, D. Dalacu, J. McKee, J. Lapointe, S. Haffouz, J.F. Weber, D.B. Northeast, P.J. Poole, G.C. Aers, R.L. Williams, On-Chip Integration of Single Photon Sources via Evanescent Coupling of Tapered Nanowires to SiN Waveguides, *Adv. Quantum Technol.* 3 (2020) 1900021. <https://doi.org/10.1002/qute.201900021>.
- [77] S. Hughes, S. Franke, C. Gustin, M. Kamandar Dezfouli, A. Knorr, M. Richter, Theory and Limits of On-Demand Single-Photon Sources Using Plasmonic Resonators: A Quantized Quasinormal Mode Approach, *ACS Photonics*. 6 (2019) 2168–2180.
<https://doi.org/10.1021/acsp Photonics.9b00849>.
- [78] H. Siampour, S. Kumar, S.I. Bozhevolnyi, Chip-integrated plasmonic cavity-enhanced single nitrogen- vacancy center emission, *Nanoscale*. (2017). <https://doi.org/10.1039/C7NR05675C>.
- [79] S. Kumar, S.I. Bozhevolnyi, Excitation of Hybrid Plasmonic Waveguide Modes by Colloidal Quantum Dots, *ACS Photonics*. (2019). <https://doi.org/10.1021/acsp Photonics.9b00379>.
- [80] H. Siampour, O. Wang, V.A. Zenin, S. Boroviks, P. Siyushev, Y. Yang, V.A. Davydov, L.F. Kulikova, V.N. Agafonov, Ultrabright single-photon emission from germanium-vacancy zero-phonon lines :

deterministic emitter-waveguide interfacing at plasmonic hot spots, *Nanophotonics*. (2020) 1–10. <https://doi.org/10.1515/nanoph-2020-0036>.

- [81] T. Kupko, M. von Helversen, L. Rickert, J.-H. Schulze, A. Strittmatter, M. Gschrey, S. Rodt, S. Reitzenstein, T. Heindel, Tools for the performance optimization of single-photon quantum key distribution, *Npj Quantum Inf.* 6 (2020) 29. <https://doi.org/10.1038/s41534-020-0262-8>.
- [82] Y. He, H. Wang, S. Gerhardt, K. Winkler, J. Jurkat, Y. Yu, M.-C. Chen, X. Ding, S. Chen, J. Qian, Z.-C. Duan, J. Li, L. Wang, Y. Huo, S. Yu, S. Hofling, C. Lu, J. Pan, Polarized indistinguishable single photons from a quantum dot in an elliptical micropillar., *ArXiv Opt.* (2018).
- [83] Z. Ying, G. Wang, X. Zhang, Y. Huang, H. Ho, Y. Zhang, Ultracompact TE-Pass Polarizer Based on a Hybrid Plasmonic Waveguide, *IEEE Photonics Technol. Lett.* 27 (2015) 201–204. <https://doi.org/10.1109/LPT.2014.2365029>.
- [84] B. Wang, S. Blaize, R. Salas-Montiel, Nanoscale plasmonic TM-pass polarizer integrated on silicon photonics, *Nanoscale*. 11 (2019) 20685–20692. <https://doi.org/10.1039/C9NR06948H>.
- [85] J.N. Caspers, J.S. Aitchison, M. Mojahedi, Experimental demonstration of an integrated hybrid plasmonic polarization rotator, *Opt. Lett.* 38 (2013) 4054–4057. <https://doi.org/10.1364/OL.38.004054>.
- [86] J.N. Caspers, M.Z. Alam, M. Mojahedi, Compact hybrid plasmonic polarization rotator, *Opt. Lett.* 37 (2012) 4615–4617. <https://doi.org/10.1364/OL.37.004615>.
- [87] S. Kim, M. Qi, Mode-evolution-based polarization rotation and

coupling between silicon and hybrid plasmonic waveguides, *Sci. Rep.* 5 (2015) 18378. <https://doi.org/10.1038/srep18378>.

- [88] S. Kim, M. Qi, Polarization rotation and coupling between silicon waveguide and hybrid plasmonic waveguide, *Opt. Express*. 23 (2015) 9968–9978. <https://doi.org/10.1364/OE.23.009968>.
- [89] R.F. Oulton, V.J. Sorger, D.A. Genov, D.F.P. Pile, X. Zhang, A hybrid plasmonic waveguide for subwavelength confinement and long-range propagation, *Nat. Photonics*. 2 (2008) 496–500. <https://doi.org/10.1038/nphoton.2008.131>.
- [90] N.T. Huong, N.D. Vy, M.-T. Trinh, C.M. Hoang, Tuning SPP propagation length of hybrid plasmonic waveguide by manipulating evanescent field, *Opt. Commun.* 462 (2020) 125335. <https://doi.org/https://doi.org/10.1016/j.optcom.2020.125335>.
- [91] M.A. Butt, N.L. Kazanskiy, S.N. Khonina, Modal Characteristics of Refractive Index Engineered Hybrid Plasmonic Waveguide, *IEEE Sens. J.* 20 (2020) 9779–9786. <https://doi.org/10.1109/JSEN.2020.2991215>.
- [92] X. Chen, H.K. Tsang, Polarization-independent grating couplers for silicon-on-insulator nanophotonic waveguides, *Opt. Lett.* 36 (2011) 796–798. <https://doi.org/10.1364/OL.36.000796>.
- [93] C. Alonso-Ramos, L. Zavargo-Peche, A. Ortega-Moñux, R. Halir, I. Molina-Fernández, P. Cheben, Polarization-independent grating coupler for micrometric silicon rib waveguides, *Opt. Lett.* 37 (2012) 3663–3665. <https://doi.org/10.1364/OL.37.003663>.
- [94] Z. Xiao, T.-Y. Liow, J. Zhang, S.T.H. Silalahi, P. Shum, F. Luan, Mode Control in Planar Waveguide Grating Couplers With Double Surface Corrugation, *IEEE Photonics Technol. Lett.* 24 (2012) 1722–1725. <https://doi.org/10.1109/LPT.2012.2213300>.

- [95] J.H. Song, F.E. Doany, A.K. Medhin, N. Dupuis, B.G. Lee, F.R. Libsch, Polarization-independent nonuniform grating couplers on silicon-on-insulator, *Opt. Lett.* 40 (2015) 3941–3944.
<https://doi.org/10.1364/OL.40.003941>.
- [96] J. Zhang, J. Yang, H. Lu, W. Wu, J. Huang, S. Chang, Subwavelength TE/TM grating coupler based on silicon-on-insulator, *Infrared Phys. Technol.* 71 (2015) 542–546.
<https://doi.org/https://doi.org/10.1016/j.infrared.2015.06.018>.
- [97] J. Zhang, J. Yang, H. Lu, W. Wu, J. Huang, S. Chang, Polarization-independent grating coupler based on silicon-on-insulator, *Chin. Opt. Lett.* 13 (2015) 91301. <http://col.osa.org/abstract.cfm?URI=col-13-9-091301>.
- [98] N. Purwaha, A. Atieh, W.N. Ye, Broadband and polarization flexible SOI grating coupler based on sub-wavelength gratings with low back reflections, *OSA Contin.* 2 (2019) 1350–1357.
<https://doi.org/10.1364/OSAC.2.001350>.
- [99] T. Hao, A. Sánchez-Postigo, P. Cheben, A. Ortega-Moñux, W.N. Ye, Dual-Band Polarization-Independent Subwavelength Grating Coupler for Wavelength Demultiplexing, *IEEE Photonics Technol. Lett.* 32 (2020) 1163–1166. <https://doi.org/10.1109/LPT.2020.3014640>.
- [100] K. Hajim, S. Tawfiq, A. Meki, Quantum Cryptography and a Quantum Key Distribution Protocol, *Iraqi J. Laser.* 3 (2004) 1–10.
<https://ijl.uobaghdad.edu.iq/index.php/IJL/article/view/151>.
- [101] P. Sibson, J.E. Kennard, S. Stanisic, C. Erven, J.L. O’Brien, M.G. Thompson, Integrated silicon photonics for high-speed quantum key distribution, *Optica.* 4 (2017) 172–177.
<https://doi.org/10.1364/OPTICA.4.000172>.
- [102] B. Tilmann, G. Grinblat, R. Berté, M. Özcan, V.F. Kunzelmann, B.

Nickel, I.D. Sharp, E. Cortés, S.A. Maier, Y. Li, Nanostructured amorphous gallium phosphide on silica for nonlinear and ultrafast nanophotonics, *Nanoscale Horiz.* 5 (2020) 1500–1508.
<https://doi.org/10.1039/D0NH00461H>.

[103] K. Schneider, P. Welter, Y. Baumgartner, H. Hahn, L. Czornomaz, P. Seidler, Gallium Phosphide-on-Silicon Dioxide Photonic Devices, *J. Light. Technol.* 36 (2018) 2994–3002.
<https://doi.org/10.1109/JLT.2018.2829221>.

[104] Refractive index database, (n.d.). www.refractiveindex.info (accessed June 10, 2021).

[105] Dow Corning® XR-1541 E-Beam Resist, (2008).

[106] M.W. Knight, N.S. King, L. Liu, H.O. Everitt, P. Nordlander, N.J. Halas, Aluminum for Plasmonics, *ACS Nano*. 8 (2014) 834–840.
<https://doi.org/10.1021/nn405495q>.

[107] T. Morgan-Wall, H.J. Hughes, N. Hartman, T.M. McQueen, N. Marković, Fabrication of sub-15 nm aluminum wires by controlled etching, *Appl. Phys. Lett.* 104 (2014) 173101.
<https://doi.org/10.1063/1.4874137>.

[108] M. Kjaergaard, F. Nichele, H.J. Suominen, M.P. Nowak, M. Wimmer, A.R. Akhmerov, J.A. Folk, K. Flensberg, J. Shabani, C.J. Palmstrøm, C.M. Marcus, Quantized conductance doubling and hard gap in a two-dimensional semiconductor–superconductor heterostructure, *Nat. Commun.* 7 (2016) 12841.
<https://doi.org/10.1038/ncomms12841>.

[109] L. Gao, Y. Huo, J.S. Harris, Z. Zhou, Ultra-Compact and Low-Loss Polarization Rotator Based on Asymmetric Hybrid Plasmonic Waveguide, *IEEE Photonics Technol. Lett.* 25 (2013) 2081–2084.
<https://doi.org/10.1109/LPT.2013.2281425>.

- [110] C. Perera, K.C. Vernon, Simulation of the gap plasmon coupling with a quantum dot, in: J. Friend, H.H. Tan (Eds.), *Micro/Nano Mater. Devices, Syst.*, SPIE, 2013: pp. 161–168.
<https://doi.org/10.1117/12.2033300>.
- [111] C. Wang, A Solid-State Single Photon Source Based on Color Centers in Diamond, (2007). <http://nbn-resolving.de/urn:nbn:de:bvb:19-72761>.
- [112] M. Berthel, O. Mollet, G. Dantelle, T. Gacoin, S. Huant, A. Drezet, Photophysics of single nitrogen-vacancy centers in diamond nanocrystals, *Phys. Rev. B.* 91 (2015) 35308.
<https://doi.org/10.1103/PhysRevB.91.035308>.
- [113] S. Schietinger, M. Barth, T. Aichele, O. Benson, Plasmon-Enhanced Single Photon Emission from a Nanoassembled Metal–Diamond Hybrid Structure at Room Temperature, *Nano Lett.* 9 (2009) 1694–1698. <https://doi.org/10.1021/nl900384c>.
- [114] D.A. Steck, *Quantum and Atom Optics*, (2014). <http://atomoptics-nas.uoregon.edu/~dsteck/teaching/quantum-optics/quantumoptics-%0Anotes.pdf>.
- [115] K.A. Fischer, QuTiP Lecture: Pulse-wise second-order optical coherences of emission from a two-level system, *Dyn. Model. Pulsed Two-Phot. Interf.* (2016).
<https://nbviewer.jupyter.org/github/qutip/qutip-notebooks/blob/master/examples/pulse-wise-second-order-coherence-g2.ipynb>.
- [116] M.A. Antón, F. Carreño, O.G. Calderón, S. Melle, E. Cabrera, Radiation emission from an asymmetric quantum dot coupled to a plasmonic nanostructure, *J. Opt.* 18 (2016) 25001.
<https://doi.org/10.1088/2040-8978/18/2/025001>.

- [117] L. Chrostowski, M. Hochberg, *Silicon Photonics Design: From Devices to Systems*, Cambridge University Press, 2015.
<https://doi.org/10.1017/CBO9781316084168>.
- [118] L.O. Skrebergene, *Optimization and fabrication of a fiber-to-waveguide silicon-on-insulator grating coupler*, NTNU, 2020.
- [119] Corning, *SMF-28 Ultra Optical Fiber*, (2014) 1–2.
<http://www.corning.com/WorkArea/showcontent.aspx?id=65789>.
- [120] A. Ghatak, K. Thyagarajan, *An Introduction to Fiber Optics*, Cambridge University Press, 1998.
<https://doi.org/10.1017/CBO9781139174770>.

الخلاصة

تبعث معظم المصادر البلازمونية المتكاملة احادية الفوتون سילاً من الفوتونات الاحادية غير محددة القطبية. هذه الفوتونات تحتاج الى مرحلة المستقطب في اي نظام عملي يستخدم للتجفير الكمي. لهذا السبب، حددت هذه الاطروحة قطبية الفوتونات المنبعثة عن طريق دراسة ثلاثة مواضيع اساسية.

في البداية، تم استعراض مقارنة الضوء المنبعث من باعث كمي يعمل بطول موجي 700 نانومتر الى نسق الانتشار المدعوم من قبل مدور للقطبية مبني على دليل موجي بلازموني هجين. أثبتت النتائج ان الضوء المنبعث كانت له قطبية خطية بزوايا 0، 45، -45، و 90 درجة باطوال انتشار 5، 3.3، و 3.9 مايكرومتر، على التتابع. علاوة على ذلك، تم الحصول على كفاءة عالية لتحويل القدرة من الضوء المطبق ذا عرضية مغناطيسية (قطبية تعادل 0 درجة) الى عرضية كهربائية (قطبية تعادل 90 درجة) و ضوء ذا قطبية خطية بزوايتين 45/-45 درجة تعادل 97% و 98%، على التتابع. حسن العمل المقترح معامل الانحدار للبائع الكمي 3 اضعاف تقريبا مع كفاءات انبعاث مقارنة عالية تساوي 88%، 80%، و 87% الى نسق الدليل الموجي للقطبيات 0، 45/-45، و 90 درجة، على التتابع. تمهد الطريقة المقترحة الطريق للحصول على مصادر بلازمونية متكاملة احادية الفوتون كفوءة، مدمجة، اقل تعقيداً، وذات قطبية محددة. حسب معلومات الباحث، هذه الدراسة هي اول دراسة صممت باعث احادي الفوتون متكامل ذا قطبية محددة ومبني على الدليل الموجي البلازموني المدمج في جهة البائع لنظام ناقل للمفتاح الكمي محققا قطبية محددة بنفس الطول الموجي للبائع الكمي وبكفاءة استخراج عالية.

ثانياً، تم استعراض الطرق العددية التي تثبت احادية انبعاث الفوتونات من اي باعث كمي بعد اقترانه الى اي بناء نانوي. يعدل معامل برسيل مواصفات الانبعاث للبواعث الكمية كمراكز الالوان في الكرستال النانوي (فراغات النتروجين وفراغات السليكون) او نقاط اشباه الموصلات الكمية. ان الطريقة العددية المقترحة مبنية على استخدام معاملات الفيزياء الضوئية المختبرية الفريدة الخاصة بكل باعث كمي و برامج التحليل العددي (الماتلاب واداة الكم بوساطة البايتون). اظهرت النتائج تصرف مشابه لدالة الارتباط من الدرجة الثانية بين الطريقة العددية المقترحة وتجربتين عمليتين قبل وبعد اقتران البائع الكمي الى دليل موجي بلازموني بابعاد دون الطول الموجي. ان الطريقة المقترحة ضرورية لاثبات الانبعاث الاحادي للفوتونات لبائع احادي الفوتون نظريا في نظام توزيع المفتاح الكمي المتكامل المعتمد على القطبية.

اخيراً، تم اقتراح تقنية الطبقات الثنائية لتصميم مشبك مقارن مدمج غير معتمد على القطبية وبدعم اربع حالات للقطبية. تم تصميم المشبك المقارن ليقرن الضوء القطبي ذا الطول الموجي 700 نانومتر المنتشر في دليل موجي مكون من فوسفات الكاليوم بعرض 150 نانومتر الى فايبر محافظ

للقطبية. ان تقنية الطبقات الثنائية مبنية على ترسيب مشبكات مكونة من فوسفات الكالسيوم مصممة لاقتزان الضوء ذا العرضية المغناطيسية فوق مشبكات مكونة من فوسفات الكالسيوم مصممة لاقتزان الضوء ذا العرضية الكهربائية. تعزل الطبقتان عن بعضهما بطبقة من بولي ميثيل الهيدروجين بعرض مثالي يساوي 20 نانومتر. حققت الطريقة المقترحة كفاءات اقتزان عالية نسبيا بحدود 39.2%، 31.1%، و 23.3% للقطبية ذات العرض الكهربائي، المغناطيسي، 45-/45 درجة قطبية خطية، على التتابع. كانت الخسائر المعتمدة على القطبية بحدود 1 ديسبل، 1.26 ديسبل، و 2.26 ديسبل بين ضوء ذا مقطع عرضي كهربائي الى مغناطيسي، مغناطيسي الى قطبي خطي بزاوية 45-/45 درجة، و كهربائي الى قطبي خطي بزاويتين 45-/45 درجة، على التتابع. تم التحقق عدديا من اداء تقنية الطبقات الثنائية باستخدام خوارزمية نظرية العناصر المحدودة ثنائية الابعاد باستخدام برنامج الكومسول. تقترح الطريقة الجديدة المقترحة خوارزمية بسيطة لتصميم مشبك اقتزان غير معتمد على القطبية ويدعم اقتزان اربع حالات للقطبية ومن الممكن استخدامها في دوائر الاتصالات المتكاملة الكمية والفوتونية.



وزارة التعليم العالي والبحث العلمي

جامعة بغداد

معهد الليزر للدراسات العليا

التصميم والتحقيق العددي لمصدر متكامل احادي الفوتون مبنياً على
البلازمونيات الكمية

أطروحة مقدمة الى

معهد الليزر للدراسات العليا / جامعة بغداد لاستكمال متطلبات نيل شهادة دكتوراة
فلسفة في تطبيقات الليزر / الهندسة الالكترونية والاتصالات

الطالب

فاروق عبد الغفور خليل

المشرف

الاستاذ المساعد الدكتوراة

شيلان خسرو توفيق